

Doctoral Dissertation

Modeling of field and thermal  
magnetization reversal in nanostructured  
magnetic materials

Felipe García Sánchez

Dpto de Física Teórica de la Materia Condensada  
Universidad Autónoma de Madrid

Advisor: Oksana Fesenko Morozova

Tutor: Enrique Velasco Caravaca

Madrid, November 2007



*A María Pilar Esteban*



# Contents

<b>Resumen</b>	<b>9</b>
<b>1 Introduction</b>	<b>11</b>
1.1 Magnetic nanotechnology and magnetic nanostructures . . . . .	11
1.2 Magnetic recording crisis and challenges . . . . .	14
1.3 The role of numerical modeling . . . . .	21
Bibliography . . . . .	23
<b>2 Numerical methods: towards multiscale description</b>	<b>27</b>
2.1 Multiscale character of magnetism . . . . .	27
2.2 Linking different spatial scales . . . . .	29
2.2.1 Ab-initio calculation of magnetic properties. . . . .	30
2.2.2 Atomistic models in magnetism . . . . .	32
2.2.3 Micromagnetics: classical approach to model magnetization distribution . . . . .	34
2.2.4 Passing atomistic information to micromagnetics: a multiscale model . . . . .	40
2.3 Linking different timescales . . . . .	42
2.3.1 The magnetization dynamics and the Landau-Lifshitz-Gilbert equation . . . . .	44
2.3.2 Non-thermal adiabatic approximation . . . . .	48
2.3.3 Short-time thermal description: stochastic LLG equations . . . . .	50
2.3.4 Long-time behavior: Arrhenius-Néel law . . . . .	52
2.3.5 Monte Carlo methods . . . . .	53
2.3.6 Energy barriers calculations . . . . .	55
2.3.7 Acceleration methods: Victora and Voter methods . . . . .	61
2.3.8 Victora method . . . . .	61
2.3.9 Voter method . . . . .	65
Bibliography . . . . .	71

<b>3</b>	<b>Multiscale modeling of magnetization reversal in soft/hard bilayer for magnetic recording applications</b>	<b>79</b>
3.1	Introduction . . . . .	79
3.2	Theoretical background . . . . .	82
3.3	Atomistic models . . . . .	85
3.4	Simulations of one grain of FePt/FeRh . . . . .	86
3.5	Coercivity reduction in FePt/FeRh film: necessity of multiscale modeling . . . . .	91
3.6	Multigrain FePt/FeRh material . . . . .	97
3.7	Magnetization dynamics of an FePt/FeRh bilayer . . . . .	101
3.8	Generic Soft/Hard material: one grain simulation . . . . .	103
3.9	Energy barriers of individual grains . . . . .	105
3.10	Multigrain simulations in generic soft/hard magnetic material . . . . .	109
3.11	Figures of merit . . . . .	112
3.12	Conclusions . . . . .	114
3.13	Conclusiones en castellano . . . . .	116
	Bibliography . . . . .	118
<b>4</b>	<b>Magnetization reversal in textured Fe particles with different aspect ratios</b>	<b>123</b>
4.1	Experimental motivation . . . . .	123
4.2	Simulational model . . . . .	125
4.3	Magnetization reversal in ideal Fe elongated particles . . . . .	126
4.4	Angular dependence of coercivity . . . . .	132
4.5	Coercivity of Fe particles with surface anisotropy . . . . .	134
4.6	Coercivity of Fe particles with magnetoelastic anisotropy . . . . .	135
4.7	Thermal switching mechanism in Fe particles . . . . .	136
4.8	Conclusions . . . . .	140
4.9	Conclusiones en castellano . . . . .	142
	Bibliography . . . . .	144
<b>5</b>	<b>Modeling of hysteresis processes in antidot Fe films</b>	<b>145</b>
5.1	Introduction . . . . .	145
5.2	Coercivity dependence on the geometrical parameters . . . . .	148
5.2.1	Experimental results . . . . .	149
5.2.2	Previous simulations . . . . .	150
5.2.3	Damaged zone simulations . . . . .	151
5.3	Angular dependence of coercivity . . . . .	153
5.3.1	Experimental Results . . . . .	154
5.3.2	Coherent Reversal Model . . . . .	156

---

5.3.3	Periodic Model . . . . .	158
5.3.4	Domain Wall Model . . . . .	160
5.4	Conclusions . . . . .	163
5.5	Conclusiones en castellano . . . . .	164
	Bibliography . . . . .	165
<b>List of publications</b>		<b>167</b>



# Resumen<sup>1</sup>

Las simulaciones numéricas se han mostrado como una herramienta útil para predecir las propiedades de materiales magnéticos en relación a los parámetros intrínsecos y extrínsecos. En particular, las simulaciones numéricas son especialmente importantes para predecir el comportamiento magnético en distintos materiales nanoestructurados, tales como bicapas magnéticas, "dots", nanopartículas etc. La relevancia de las simulaciones se demuestra en su enorme importancia en la evaluación del rendimiento de los candidatos para futuros medios de grabación magnética. La tendencia hacia mayores densidades de grabación implica una reducción en las dimensiones del tamaño de bit. Los requisitos de la grabación magnética incluyen permanencia de los datos para tiempos mayores de 20 años. En estas condiciones es preciso evaluar la estabilidad térmica de los sistemas propuestos. Los materiales propuestos tienen una elevada anisotropía magnetocristalina, como por ejemplo el FePt, para obtener la estabilidad térmica requerida. Otra propuesta es la utilización de bicapas magnéticas compuestas de blando duro que aumentan la estabilidad térmica pero manteniendo el campo coercitivo por debajo del campo magnético máximo que puede crear las cabezas grabadoras. La técnica más extendidamente usada para simular las propiedades de histéresis, dinámicas y térmicas está basada en el micromagnetismo. Aunque también es usado para simular materiales nanoestructurados, el micromagnetismo ha sido desarrollado esencialmente como una aproximación continua limitada a tamaños de sistema mayores que la longitud de intercambio; una longitud característica cuyo valor típicamente está entre 5 y 100 nm. Cabe destacar que en materiales de alta anisotropía la pared de dominio se reduce a pocas distancias atómicas por lo que el micromagnetismo no es apropiado en tales materiales con lo que es necesario tratarlos modelos atomísticos.

La investigación se centra en propiedades de histéresis, dinámicas y térmicas de sistemas magnéticos nanométricos y en el desarrollo de distintos métodos de cálculo. Más concretamente se pretende estudiar:

- La posibilidad de acelerar los cálculos de dinámica y cálculos de estabilidad térmica a largo plazo. Así mismo se pretende desarrollar los modelos multi-

---

<sup>1</sup>Las conclusiones en castellano se hayan después de cada capítulo

escala para mejorar los cálculos micromagnéticos. Este modelo incluye características atomísticas y micromagnéticas permitiendo incluir datos atomísticos en la simulación pero con tamaños simulados de muestra mesoscópicos.

- Los procesos de imanación en bicapas magnéticas compuesto de un material blando sobre un material duro en relación con aplicaciones de grabación magnética. En especial se estudiará el efecto de la intercara en la histéresis del material. Adicionalmente y con el objeto de comprobar su posible utilización como medio de grabación de magnético se calcularán las barreras de energía en dichos sistemas. Además se simularán sistemas compuestos de granos con distintas intensidades del acoplo entre ellos, dado que las muestras reales tienen forma granular.
- El efecto de la energía magnetostática en materiales de alta imanación y dimensiones reducidas y su comparación con medidas experimentales. Los sistemas incluyen películas tratadas mediante litografía (agujeros “antidots” de Fe) y nanopartículas de Fe embebidas en una matriz de Cu. En estos sistemas se evaluará la dependencia de la histéresis con respecto al ángulo que forma el campo aplicado y en el caso de las láminas con red de agujeros se comparará con el comportamiento observado experimentalmente.
- La inclusión de propiedades magnéticas diferentes de las del material masivo en el modelo y su influencia en las propiedades magnéticas así como la evaluación de posibles contribuciones energéticas responsables del comportamiento observado y no tenido en cuenta en los modelos estándar.

# Chapter 1

## Introduction

### 1.1 Magnetic nanotechnology and magnetic nanostructures

Nowadays advanced technologies rely on research in materials performance and on developing new materials with novel superior properties. Nanotechnology is the engineering of materials of sizes less than microns and involves physics, chemistry, material science, biology and other fields. The interest in nanotechnology in our days is based on the promise of significant social implications, which include better understanding of nature, efficient manufacturing techniques for almost every human-made object and a new world of products beyond what has been possible with other technologies. Nanomaterials constitute an emerging sub discipline in materials sciences due to the use of devices with smaller dimensions for which a new physical behavior naturally appears. The fabrication of nanodevices is feasible since we have a close example: life itself. Some of the proposed paradigms can be found in nature. An example of molecular motors is kinesin and a form of nanoassembling is RNA replication. The prospects of nanotechnology are still not clear: whether it will generate a completely new technology. However, nanotechnology has been up to date a new form of understanding science.

Magnetism has been from its origins one of the more fertile fields of science. A historically important magnetic device such as the compass has stimulated the curiosity for centuries. Analogously, the nanomagnetism is between the most successful fields of nanotechnology. The special role of nanomagnetism is due to the fact that magnetic properties depend uniquely on both dimensionality and length-scales. The reduced size of the nanostructures originates properties different from the bulk ones, as for example surface properties, due to the different surrounding of the magnetic atom. Generally speaking, new phenomena occur always when one of the dimensions of the nanostructure becomes comparable to some characteristic

length, defining the magnetic behavior, such as the magnetostatic correlation length.

The magnetic nanostructured materials could be divided into two groups: (i) naturally occurring nanostructured materials such as polycrystalline magnetic films and (ii) artificially prepared nanostructures. The control of the magnetic properties of polycrystalline magnetic materials emerges via understanding of physical processes related to their granular structure and preparation techniques which can control the grain properties. The new materials for permanent magnets, SmCo and NiFeB, as well as the materials for magnetic recording, CoCrPt, are examples of nanostructured materials where the correct combination of different phases allows to achieve the desired performance.

From the point of view of fabrication of artificial nanostructured materials, the different methods can be grouped coarsely in:

- Top-down. Top-down approach has been the traditional approach to miniaturization via lithographic tools [Sheats 98]. One of other possible fabrication methods includes the extrusion as the example examined in Chapter 4.
- Bottom-up. The sample is assembled from small building units. A typical example is chemical synthesis from solution containing the precursors [Sellmyer 02]. The procedure allows to create 2D disposition of the nanoelements or 3D disposition, as for example Co particles in alumina matrix [Luis 02].

Top-down approach offers more external control of the geometry and properties of the nanostructures. On the other hand, bottom-up is less expensive than its counterpart and is preferred for applications where the cost is an important factor. Beside of these two methods to fabricate nanostructures, and complementing them, the use of simulations allows to predict and to design new materials in the virtual laboratory.

Fig. 1.1 shows some of the possible magnetic nanostructure geometries. These include chain of fine particles [He 07], arrays of striped nanowires [Shearwood 94], arrays of cylindrical nanowires [Zhan 02], nanojunctions [Rüster 03], arrays of nanodots [Novosad 02], etc.

The nanomagnets have a vast field of application and exhibit very interesting new properties. Nanomagnetism is already central to data storage, sensor and device technologies. The nanostructured magnetic materials have improved the performance in traditional applications as sensors, actuators, permanent magnets and transformer cores. Besides, the nanomagnetism is increasingly being used in the life sciences and medicine. For example, the magnetic nanoparticles can be used as a method for cell labeling, drug delivery and hyperthermia [Pankhurst 03]. The fundamental requirement is the biocompatibility of the nanoparticles in order to avoid

toxicity. From more traditional technological point of view the exciting new phenomena include spin injection [Jedema 01], giant magnetoresistance (GMR) (the subject of the Nobel Price in Physics this year) [Baibich 88], tunnelling magnetoresistance (TMR) [Moodera 95], half metallic magnets [de Groot 83], etc. All this phenomena open a new field known as spintronics. The semiconductor devices could potentially be substituted by spin-aware devices as the spin transistor [Wolf 01]. The microelectronics has played a crucial and innovative role in driving the scientific and technological progress that has made a major contribution to social and economic growth worldwide for many decades. One can imagine the tremendous possibilities that can be offered by nanoelectronics, a natural extension of microelectronics in the present trend of miniaturization. However, this extension must be accompanied by a deeper understanding and control of the various aspects of nanoelements. Finally, spintronics and high density recording require fast magnetic switching processes. It is therefore of great interest to obtain a thorough understanding of the spin dynamics and magnetic relaxation on nano-second time scales.

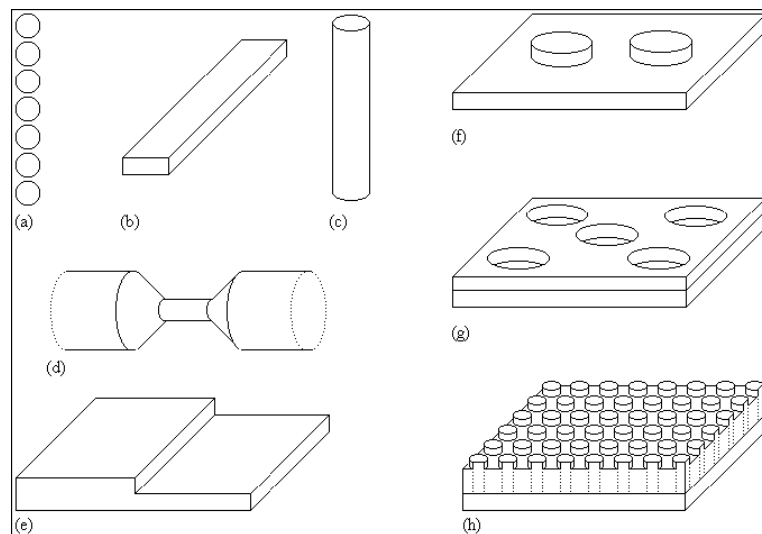


**Figure 1.1:** Typical nanostructure geometries: (a) chain of fine particles, (b) striped nanowire, (c) cylindrical nanowire, (d) nanojunction, (e) vicinal surface step, (f) nanodots, (g) antidots and (h) particulate medium. From R. Skomski [Skomski 03].

Besides of industrial applications, patterned magnetic structures are very attractive as model systems to study fundamental physical properties of small magnetic particles. The magnetization state of magnetic nanostructures is different from that of the bulk. In the bulk material the sample is divided into domains separated by domain walls. Nevertheless, if the size of the nanostructure is small compared to the domain wall or the geometry of the sample favors some disposition of the magnetization, this is not longer true. Examples of this are single domain particles

[Puntes 01] or vortex state in circular nanodots [Novosad 02]. Magnetic thin films and multilayers, which can also be considered nanostructures, can exhibit a number of interesting properties, as for example thickness-dependent domain wall and coercive phenomena [Zhao 01]. The interlayer exchange interactions within magnetic multilayer structures is a very important property leading to different static, dynamic and thermal properties of magnetic multilayers and nanostructures (see Chapter 3 to see an example). Another example constitutes the phenomenon of exchange bias [Kodama 99]. The latter is widely used in current read head devices, for example.

To conclude, magnetic nanostructures exhibit various scientifically interesting and technologically important deviations from bulk magnets. The number of phenomena and the potential applications indicate a promising future for the nanomagnetism. The creation, understanding and exploitation of artificial nanostructures and the study of their magnetic properties remains a challenge for future research.

## 1.2 Magnetic recording crisis and challenges

Magnetic recording is one of the most important examples of working nanotechnology. Here we will mostly be concerned with the hard disk magnetic storage. The magnetic information in the hard disk is stored in “bits” which are patterns of magnetization in a magnetizable material to store data. The present-day bit size is of the order of 100 *nm*.

The magnetic recording started more than one hundred years ago. In 1888 Oberlin Smith suggested the possibility of magnetic recording using cotton threads in which steel dust would be suspended. Ten year later, in 1898, Valdemar Poulsen recorded the sound of his own voice in a steel wire extended between two walls, inclined in order to allow a small magnet to slide down the wire with constant velocity. While the electromagnet went down the wire the sound was recorded and it was replayed changing the magnet by a telephone earphone. This experiment originated the patent of the Telegraphone the same year. Posteriorly, in 1956 IBM created the IBM 305 RAMAC the first computer that incorporated a hard drive, the IBM 350. This hard disk had a total capacity of 5 *Mbytes* consisting of 50 disks with an areal density of 0.002 *Mb/in*<sup>2</sup>.

During the recent past the data density stored on rigid disk media (see Fig. 1.2), which is the highest density format, has been increasing at the rate of 60% per annum, following an exponential law equivalent to the Moore law for the integration of transistors in a chip (see Fig. 1.3). In the nineties and due to the introduction of advanced GMR spin-valve heads this rate of advance has increased to 100% per annum and in the last years this growth rate is slowed down. Until several

years ago the evolution of magnetic recording was based on the “scaling” principle: the dimensions of recording heads, head-media separation, magnetic grain size were proportionally reduced in order to achieve higher areal density. Today the situation is different. Scaling is no longer applicable. These days, a good understanding of basic physics of recording phenomena is a necessity for an engineer working in magnetic recording. It is pertinent at this time to enquire as to where the fundamental physical limitations of magnetic recording may lie. In this context there are several principle areas of interest: the first of these is limitations to data rate. These are concerned with the fundamental physics of the maximum rate at which a magnetic moment may reverse from one direction to the other. The theoretical calculation of these limits is complex and not well understood. Secondly, and of principle concern, it is the limit to the density at which information can be stored in a magnetic thin film. This latter limitation is based on the signal to noise ratio and also on the question of the thermal stability of increasingly small written bits.

Thermal stability of a bit of information is of critical importance particularly as bits are made smaller and media are made thinner. In conventional magnetic recording, the medium is a granular film and a bit consists of several ( $N = 500 \div 1000$ ) almost non-interacting magnetic grains. Signal to noise considerations are extremely complex and derive from factors such as the shape of bits and cross-talk between neighboring bits or even neighboring tracks but from simple statistical estimation the signal-to-noise ratio (SNR) is proportional to  $\sqrt{N}$  [Mallinson 91]. Therefore, the number of grains included in a bit can not be reduced in order to preserve SNR and, consequently, the increasing bit density implies a reduction of the grain size.

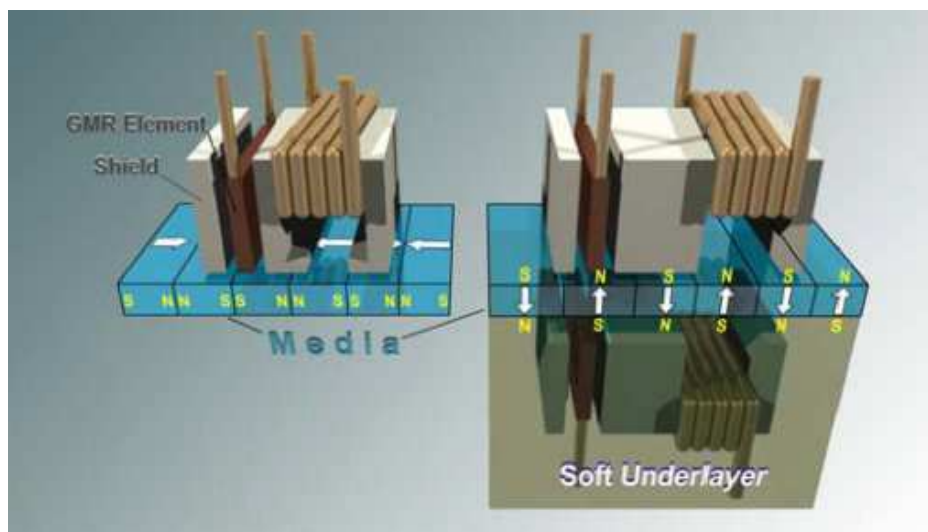


**Figure 1.2:** Diagram showing the differences between longitudinal and perpendicular magnetic recording (from D. Weller of Seagate Research).

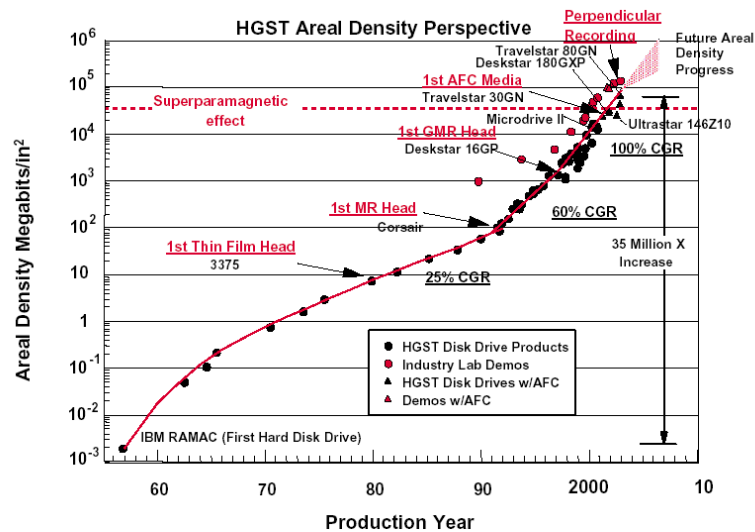


**Figure 1.3:** Historical evolution of the bit density in magnetic recording media (from Hitachi).

However, a reduction in the grain size leads to a reduction in the energy barrier  $KV$ , separating two magnetization states, where  $K$  is the anisotropy constant and  $V$  the grain volume, which determines the thermal stability of the written information. When the energy barrier is comparable to the thermal energy (see Fig. 1.4), the magnetization becomes unstable and the inversion of the magnetization by thermal fluctuations is likely to occur. This effect is known as superparamagnetism and the corresponding limitation of the density as superparamagnetic limit. Essentially, values of  $KV/k_B T > 60$  ( $k_B$  is the Boltzmann's constant and  $T = 300 K$  is the temperature) are required to ensure the long-term stability of written information. According to this, H.Charap established that the maximum achievable density, considering a stability of at least tens years for the stored information, was  $40 Gb/in^2$  [Charap 97]. This limit has been shortly overcome after this prediction, showing the necessity of more realistic modeling of the superparamagnetic behavior. Additionally, after the overrun of this limit, the challenge of the magnetic recording industry is to surpass the density of  $1 Tb/in^2$  within a thermal stable medium.

At present longitudinal magnetic recording systems are the basis of all low cost high-density information storage systems. Toshiba was the first company to fabricate a perpendicular recording based hard drive in 2004 [Toshiba 04]. In January 2006, Seagate Technology [Seagate 06] began shipping its first laptop sized, 2.5 inch hard drive using perpendicular recording technology, the Seagate Momentus 5400.3. At this time the majority of its hard disk storage devices utilizes the new technology. In October 2007 Seagate Technology announced a new record of magnetic recording density of 421 Gb (gigabits) per square inch. The company announced the results

of a magnetic recording demonstration that used perpendicular recording heads and media created with currently available production equipment. The difference between longitudinal and perpendicular recording is the orientation of the anisotropy of media grains. Fig. 1.2 shows schematically the difference between both recording solutions. In the case of longitudinal recording the grains magnetization is lying in the plane of the magnetic medium. When the medium is magnetized by the recording head, the average magnetization is pointing in the down-track direction (see Fig 1.2). When perpendicular head and media are used, the media anisotropy is oriented perpendicular to the thin film and its magnetization is pointing either “up” or “down”.

The advantages of the perpendicular recording system over the longitudinal recording are multiple: (i) Higher thermal stability can be achieved by small in-plane grain diameter with cylindrical grain structure. (ii) A vertical pole head in a recording media with a soft underlayer can generate twice the field of longitudinal recording head. This allows writing higher coercivity medium, further decreasing grain size and maintaining media thermal stability. (iii) The read-back signal amplitude from perpendicular medium with soft underlayer is larger compared with equivalent longitudinal medium, improving signal-to-noise ratio. (iv) Perpendicular media grains are strongly oriented. This results in smaller medium noise and a sharper recorded transition. (v) The demagnetization field in the perpendicular medium is small at the transition region. This allows writing narrower magnetic transitions and improves thermal stability of high density data. The most optimistic scenarios predicted that the optimized perpendicular system may achieve a factor of 4-5 over the best longitudinal areal density.

The introduction of perpendicular recording technology comes to ease the su-

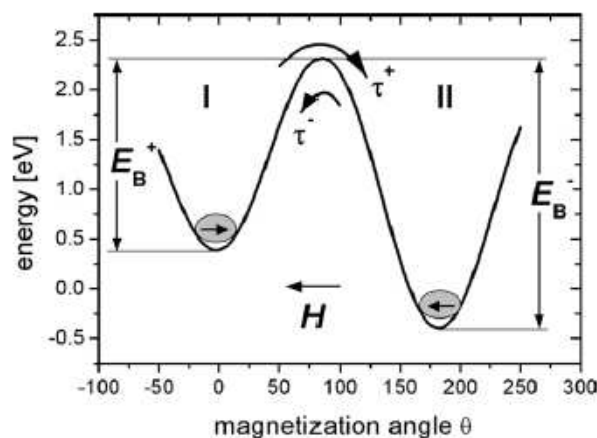


**Figure 1.4:** Energy of a single domain particle under applied field. The reversal modes and its corresponding energy barriers are indicated. From Ref. [Weller 99].

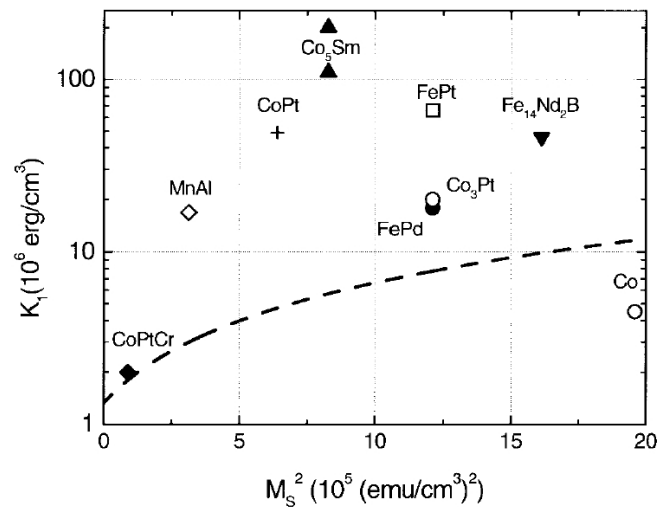


**Figure 1.5:** The magnetocrystalline anisotropy versus the square of the saturation magnetization for different magnetic materials. Extracted from Ref. [Weller 99].

perparamagnetic problem. However, this solution only delays the problem. On the other hand, clearly, a reduction in the grain size can be compensated for by an increase in the magnetocrystalline anisotropy constant  $K$ . Fig. 1.5 shows the magnetocrystalline anisotropy of different materials as compiled by D. Weller [Weller 99]. The saturation magnetization is also indicated, due to the destabilizing role of the magnetostatic interaction in thin films. The material used for current recording media is the *CoPtCr*, in which the *Cr* is segregated in the grain boundaries, reducing the interaction between grains. The two materials with highest magnetocrystalline

### Media Design Constraints - “Trilemma”

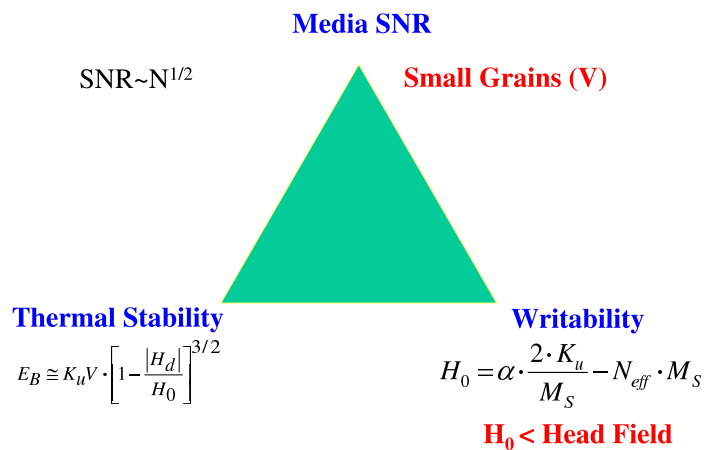


**Figure 1.6:** The different requirements composing the magnetic recording “trilemma”.

anisotropy constant are *FePt* and *SmCo*. Nevertheless, the *SmCo* alloys present problems of oxidation of the *Sm* [Kardelky 05], which effectively reduces the potentiality as material for magnetic recording, due to the deterioration of the performance of the medium with time. The  $L1_0$  chemically ordered *FePt* alloy, which is less susceptible to oxidation, has attracted much attention, and is considered, together with *CoPt* as the most promising candidate for a recording medium of new generation. The *FePt* has been successfully produced in several forms: epitaxially grown single-crystal films [Farrow 96], chemically synthesized nanoparticles [Sun 00] (SOMA “self-organized magnetic array” project) and isolated island particles [Takahashi 04]. On the other hand, stable, high perpendicular anisotropy media with no size dispersion non-interacting grains is still a challenge.

Moreover, associated with an increase in  $K$  is a consequent increase in the anisotropy field of the medium, given by  $H_k = 2K/M_s$  with  $M_s$ - the saturation magnetization value. This leads to increasing medium coercivity and the requirement of larger write fields. Unfortunately, the maximum field of the writing heads is bounded by the current technology and this poses a difficulty to the use of high anisotropy fields, since it is impossible to write in them. This constitutes a well known magnetic recording trilemma (see Fig. 1.6). At the present time the research centers of magnetic recording are actively working searching for new solutions for the future. In the following we mention different solutions that have been suggested:

- Heat assisted magnetic recording.

HAMR is a Seagate-based acronym for Heat-Assisted Magnetic Recording. Alternatively, Hitachi uses an acronym TAR (“Temperature-assisted recording”). It describes a technology that magnetically records data on high-stability media such as an FePt alloy, using laser thermal assistance to first heat the material. These materials can store single bits in a much smaller area without being limited by the same superparamagnetic effect that limits the current technology used in hard disk storage. The anisotropy constant decreases with increasing temperature at a faster rate than the magnetization, leading to a reduction in the anisotropy field and coercivity with increasing temperature. The idea is to heat with a laser spot in the bit during the writing process as shown in Fig. 1.7, achieving low coercive fields. Posteriorly and after the cooling of the bit, the storing of the magnetization is at room temperature, when the material presents high anisotropy values and, correspondingly, large thermal stability. HAMR could increase the limit of magnetic recording by more than a factor of 100. This could result in storage capacities as great as 50 Tera bits per square inch. Seagate believes it can produce 300 Tera bit (37.5 Tera byte) Hard disk drives using HAMR technology [Wired 07].

- Patterned media.

Patterned media is a technology that allows to record data in a uniform array of magnetic grains, storing one bit per grain, as opposed to regular hard-drive technology, where each bit is stored in a few hundred magnetic grains. The media consists of a periodic array of discrete magnetic elements either prepared artificially by different lithography techniques or self-organized spontaneously. Each element is a bit that is almost isolated from other elements but the magnetization inside the bit is strongly exchange coupled, compared to the conventional recording media. Therefore, the corresponding energy barrier is larger than the corresponding for the equivalent bit in conventional media and the thermal stability is improved. Another advantage of patterned media is the elimination of the transition noise between bits since the bits are completely separated. The major obstacle to smaller bit size using lithography is finding a low cost means of making media. One of the recent possibilities, already used by Toshiba in their laboratory demonstration is the pre-patterned media for hard disks in which different recording tracks are separated by trenches using imprinted lithography.

One of the most promising proposals is the combination of *FePt* SOMA with HAMR.

- Tilted media.

The coercivity of a single domain particle presents a minimum at an applied field angle of  $45^\circ$  while the thermal stability is preserved. Therefore, a medium in which the grains are tilted with this angle will allow less switching field and larger area density. However, the design of the reading heads is very complicated since the magnetization will be inclined with respect to the film normal.

Other proposals are related to the use of technologies different to hard-disk one which by their own possibilities approach the characteristics of hard disk media. For example, a new type of magnetic storage, called MRAM, is being produced that stores data in arrays of magnetic bits and reads the state of the bits using the GMR effect on the bits. Its advantage is non-volatility, low power usage, and good shock robustness. However, with storage density and capacity orders of magnitude smaller than the hard disk one, MRAM is a nice application for situations where small amounts of storage with a need for very frequent updates ( $10^{15}$  writes) are required. Other proposals can be also found in Chapters 3 and 5.

The research for future magnetic recording media is a very challenging task that includes material science and simulation of the performance of the material. The

work of this thesis has been carried out in collaboration with Seagate Research, which has also provided me with a four year studentship.

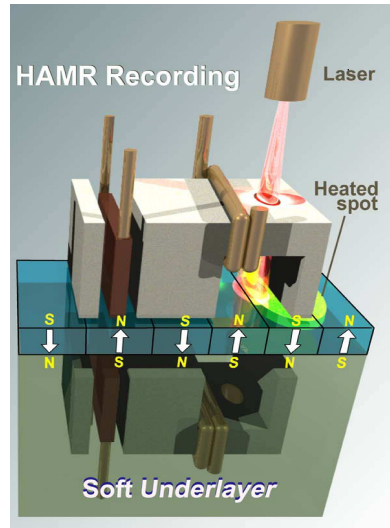


**Figure 1.7:** Diagram showing a writing head for Heat Assisted Magnetic Recording (HAMR) (from D. Weller of Seagate Research)

### 1.3 The role of numerical modeling

A quantitative treatment of the correlation between the microstructure and magnetic properties in nanostructured materials requires numerical and computational techniques. These techniques, in many senses, are complimentary to the experimental ones, specially in understanding of the magnetization reversal mechanisms, which define the nanostructured material performance. The experimental studies, such as magnetic imaging, have serious difficulties in controlling the magnetic properties down to several nanometers scale in space or down to nanosecond scale in time. At the same time, the modeling of reversal modes propagation both in space and time in this scale is possible. The use of computational techniques such as micromagnetics provides a way to obtain a realistic relation between the microstructure and magnetic properties in many cases.

By using this technique, the magnetic properties of a nanostructured material, relevant to its application, such as coercivity and remanence, dynamical switching time and thermal stability could be predicted qualitatively in relation to nanostructure. The rapid variation of many extrinsic and intrinsic parameters is accessible by using numerical techniques and is useful in understanding the qualitative tendency in the material behavior when one aims the design of materials with determined properties. As an example, the micromagnetic simulations have been shown to be

extremely useful techniques in the study of the performance of magnetic media used for magnetic recording [Bertram 94].

In general, many factors influence the magnetic properties of a nanocrystalline magnetic film, e.g., the grain size and shape, anisotropy distribution, the grain boundary properties, magnetic impurities, etc. The potential of an analytical approach is limited to a small number of very simplified cases. The simulations represent the only alternative to experimental techniques. At the same time, the micromagnetic simulations require an input of the intrinsic media parameters in the micromagnetic code from measurements. However, in many cases and especially in granular materials, the experimental techniques are unable to provide the knowledge of the microstructure with the desired details. This is especially true for the treatment of the grain boundary or the interface in nanostructured materials where normally there is no detailed knowledge of many intrinsic parameters such as exchange or anisotropy. This limits the potential accuracy of micromagnetic predictions. For example, the coercivity value, which is a result of very complicated interplay between intrinsic and extrinsic magnetic medium parameters, calculated numerically, rarely coincides with the experimental value. At the same time, this also constitutes a strong point of the numerical simulations since it allows the flexibility and control in varying the intrinsic parameters (such as different intergrain boundary models).

## Bibliography

- [Baibich 88] M. N. Baibich, J. M. Broto, A. Fert, F. N. Van Dau, F. Petroff, P. Eitenne, G. Creuzet, A. Friederich and J. Chazelas. *Giant magnetoresistance of (001)Fe/(001)Cr magnetic superlattices*. Phys. Rev. Lett., vol. 61, pages 2472–2475, 1988.
- [Bertram 94] H. N. Bertram. Theory of magnetic recording. Cambridge, UK: Cambridge University Press, 1994.
- [Charap 97] S. H Charap, P.-L. Lu and Y. He. *Thermal stability of recorded information at high densities*. IEEE Trans. Mag., vol. 33, pages 978–983, 1997.
- [de Groot 83] R. A. de Groot, F. M. Mueller, P. G. van Engen and K. H. J. Buschow. *New class of materials: Half-metallic ferromagnets*. Phys. Rev. Lett., vol. 50, pages 2024–2027, 1983.
- [Farrow 96] R. F. C. Farrow, D. Weller, R. F. Marks, M. F. Toney, S. Hom, G. R. Harp and A. Cebollada. *Growth temperature dependence of long-range alloy order and magnetic properties of epitaxial  $Fe_xPt_{1-x}$  ( $x \sim 0.5$ ) films*. Appl. Phys. Lett., vol. 69, pages 1166–1168, 1996.
- [He 07] L. He, W. Zheng, W. Zhou, H. Du, C. Chen and L. Guo. *Size-dependent magnetic properties of nickel nanochains*. J. Phys.: Condens. Matter, vol. 19, page 036216, 2007.
- [Jedema 01] F. J. Jedema, A. T. Filip and B.J. van Wees. *Electrical spin injection and accumulation at room temperature in an all-metal mesoscopic spin valve*. Nature, vol. 410, pages 345–348, 2001.
- [Kardelky 05] S. Kardelky, A. Gebert, O. Gutfleisch, V. Hoffmann and L. Schultz. *Prediction of the oxidation behaviour of Sm-Co-based magnets*. J. Magn. Magn. Mater., vol. 290–291, pages 1226–1229, 2005.
- [Kodama 99] R. H. Kodama and A. E. Berkowitz. *Atomic-scale magnetic modeling of oxide nanoparticles*. Phys. Rev. B, vol. 59, pages 6321–6336, 1999.
- [Luis 02] F. Luis, F. Petroff, J. M. Torres, L. M. García, J. Bartolomé, J. Carrey and A. Vaurès. *Magnetic relaxation of interacting Co clusters: Crossover from two- to three-dimensional lattices*. Phys. Rev. Lett., vol. 88, page 217205, 2002.

- [Mallinson 91] J. C. Mallinson. *A new theory of recording media noise*. IEEE Trans. Mag., vol. 27, pages 3519–3531, 1991.
- [Moodera 95] J. S. Moodera, L. R. Kinder, T. M. Wong and R. Meservey. *Large magnetoresistance at room temperature in ferromagnetic thin film tunnel junctions*. Phys. Rev. Lett., vol. 74, pages 3273–3276, 1995.
- [Novosad 02] V. Novosad, K. Yu. Guslienko, H. Shima, Y. Otani, S. G. Kim, K. Fukamichi, N. Kikuchi, O. Kitakami and Y. Shimada. *Effect of interdot magnetostatic interaction on magnetization reversal in circular dot arrays*. Phys. Rev. B, vol. 65, page 060402, 2002.
- [Pankhurst 03] Q. A. Pankhurst, J. Connolly, S. K. Jones and J. Dobson. *Applications of magnetic nanoparticles in biomedicine*. J. Phys. D: Appl. Phys., vol. 36, pages R167–R181, 2003.
- [Puntes 01] V. F. Puntes, K. M. Krishnan and A. P. Alivisatos. *Colloidal nanocrystal shape and size control: the case of cobalt*. Science, vol. 291, pages 2115–2117, 2001.
- [Rüster 03] C. Rüster, T. Borzenko, C. Gould, G. Schmidt, L. W. Molenkamp, X. Liu, T. J. Wojtowicz, J. K. Furdyna, Z. G. Yu and M. E. Flatté. *Very large magnetoresistance in lateral ferromagnetic (Ga,Mn)As wires with nanoconstrictions*. Phys. Rev. Lett., vol. 91, page 216602, 2003.
- [Seagate 06] Seagate. [www.seagate.com/cda/newsinfo/newsroom/releases/article/0,1121,2949,00.html](http://www.seagate.com/cda/newsinfo/newsroom/releases/article/0,1121,2949,00.html), 2006.
- [Sellmyer 02] D. J. Sellmyer, C. P. Luo, Y. Qiang and J. P. Liu. Nanomaterials and magnetic thin films. handbook of thin film material, ed. h.s. nalwa vol 5. New York: Academic Press, 2002.
- [Shearwood 94] C. Shearwood, S. J. Blundell, M. J. Baird, J. A. C. Bland, M. Gester, H. Ahmed and H. P. Hughes. *Magnetoresistance and magnetization in submicron ferromagnetic gratings*. J. Appl. Phys., vol. 75, pages 5249–5256, 1994.
- [Sheats 98] J. R. Sheats and B. W. Smith. Microlithography science and technology. New York: Marcel Dekker, 1998.
- [Skomski 03] R. Skomski. *Nanomagnetics*. J. Phys.: Condens. Matter, vol. 15, pages R841–R896, 2003.

- [Sun 00] S. Sun, C. B. Murray, D. Weller, L. Folks and A. Moser. *Monodisperse FePt nanoparticles and ferromagnetic FePt nanocrystal superlattices*. *Science*, vol. 287, pages 1989–1992, 2000.
- [Takahashi 04] Y. K. Takahashi, T. Koyama, M. Ohnuma, T. Ohkubo and K. Hono. *Size dependence of ordering in FePt nanoparticles*. *J. Appl. Phys.*, vol. 95, pages 2690–2696, 2004.
- [Toshiba 04] Toshiba. [http://www.toshiba.co.jp/about/press/2004\\_12/pr1401.htm](http://www.toshiba.co.jp/about/press/2004_12/pr1401.htm), 2004.
- [Weller 99] D. Weller and A. Moser. *Thermal effect limits in ultrahigh-density magnetic recording*. *IEEE Trans. Mag.*, vol. 35, pages 4423–4439, 1999.
- [Wired 07] Wired. <http://www.wired.com/science/discoveries/news/2007/01/72387>, 2007.
- [Wolf 01] S. A. Wolf, D. D. Awschalom, R. A. Buhrman, J. M. Daughton, S. von Molnár, M. L. Roukes, A. Y. Chtchelkanova and D. M. Treger. *Spintronics: a spin-based electronics vision for the future*. *Science*, vol. 294, pages 1488–1495, 2001.
- [Zhan 02] Q. Zhan, Z. Chen, D. Xue, F. Li, H. Kunkel, X. Zhou, R. Roshko and G. Williams. *Structure and magnetic properties of Fe-Co nanowires in self-assembled arrays*. *Phys. Rev. B*, vol. 66, page 134436, 2002.
- [Zhao 01] Y.-P. Zhao, R. M. Gamache, G.-C. Wang, T.-M. Lu, G. Palasantzas and J. Th. M. De Hosson. *Effect of surface roughness on magnetic domain wall thickness, domain size, and coercivity*. *J. Appl. Phys.*, vol. 89, pages 1325–1330, 2001.



# Chapter 2

## Numerical methods: towards multiscale description

“It is difficult to make predictions, especially about the future”  
Yogi Berra, baseball coach

In this chapter we present numerical methods for magnetic material modeling. Some of these methods can be considered in our days as standard for micromagnetic modeling. Special attention is paid to the methods which were developed by the author of the thesis (Sections 2.2.4, 2.3.6 and 2.3.7). Several of them were taken from the modeling in other branches of physics and firstly applied to magnetic properties, as for example, the A.Voter method for dynamics acceleration. Other methods, as for example, the Lagrangian multiplier technique was previously applied in magnetism to small nanoparticles only. The development of methods has been done in collaboration with Seagate Technology with the aim to find ways to predict correctly long-time thermal stability.

### 2.1 Multiscale character of magnetism

Several length scales of different nature participate nontrivially in the magnetic phenomena. A good example is the magnetization reversal in a magnetic material that contains different kinds of defects as interfaces, voids, twins, etc. The reversal starts by nucleation near a defect, which is few nanometers and even angstroms in size. Posteriorly, a domain wall is formed that has a width of tens or hundreds of nanometers. The reversal creates a full spectrum wave length magnon distribution that transfers the energy across the sample [Suhl 98]. Additionally, the microstructure (which includes the defect profile) and the extrinsic parameters (e.g sample shape) determine the behavior of the material and the maximum domain size. The

microstructure has a length scale from few nanometers to micrometers. The interactions have also different range in magnetism: from the long range dipolar interaction to the rapidly decaying exchange interaction.

Since the atomic magnetism has a quantum origin, we need quantum tools to describe it. Even assuming permanent magnetic moments, classical physics is not able to predict ferromagnetism [Hernando 01, Page 35]. Ab-initio calculations can be used to calculate the intrinsic parameters as magnetic moment, exchange energies, lattice sizes, etc. together with the energy reduction due to defect presence. The most widely used formalism is Density Functional Theory (DFT) [Dreizler 90] and its different approximations. However, it is extremely expensive in computational requirements and largest computationally affordable systems in our days consist of hundred of atoms. Simulation sizes comparable to domain wall width are not reachable for a large range of magnetic materials.

On the other hand micromagnetics, a continuum approximation, can be used in a range of systems in which the main length is comparable to the domain wall width as in artificially nanostructured elements (e.g. magnetic dots). Quite extended regions with the size of up to one hundred times the domain wall width can be simulated with this technique. In order to be more realistic the micromagnetic simulations must go hand in hand with the growing processes and characterization, since they need as input parameters the structural material parameters, such as the distribution of grain sizes, the presence of different chemical phases, the texture, etc. The tendency in the last years is to perform simulation with the greatest level of complexity of the media. However, other necessary parameters, such as the intergranular exchange and local values of magnetization, can not be obtained from standard magnetometric techniques and only ab-initio calculations could provide them, although in idealized situations.

In nowadays the trend is multiscale modeling, with the aim of using the ab-initio parameters in large scale calculations. Both in the European Union and in the United States multiscala modeling programs have been regarded as an scientific priority for the next years [DoE USA , Cordis Europa ]. The notion of multiscale modeling stems from the necessity to treat inherently multiscale problems, as the magnetic systems. A nice example of such a modeling is the study of domain wall pinning by antiphase boundary in CoPt [Antropov 03]. Different schemes of multiscale model can be implemented depending on the simulation purposes. Fig. 2.1 shows a hierarchical model. In this model the small scale simulation(ab-initio) provides data for the final inclusion in the largest scale simulation. Additional finite temperature atomistic simulations are performed to obtain temperature dependent parameters. Other implementations are possible (see Section 2.2.4), in which two regions at different discretization levels are simulated at the same time to account

for a defect on an atomistic scale.

The main problem of multiscale modeling is to link together different types of models. For example, the link between ab-initio calculations and the atomistic model is not obvious when magnetic moments are not localized or the exchange interactions are not of the Heisenberg type. The link between atomistic and micromagnetic model presents difficulties because the high-frequency part of the spinwave spectrum is truncated in micromagnetics. A related model is coarse grained modeling [Dobrovitski 00] that includes an intermediate region that is neither atomistic nor micromagnetic. The aim of the region is the correct propagation of spin waves that otherwise would be reflected by the interface.

Furthermore, different time scales appear in magnetism. From the femto seconds ultrafast magnetic dynamics [Beaurepaire 96] a vast range of magnetic processes appear, each of them with a different time scale. The magnetization precession occurs at picoseconds. The processes corresponding to the relaxation of energy into the lattice vibrations have time scales of  $10^{-10} - 10^{-11}$  s. If a domain wall is propagating driven by current in a pinning media, its velocity can be as slow as  $0.3$  m/s [Kläui 05]. Finally, larger time scales corresponding to slow relaxation are interesting from the point of view of magnetic recording media stability and magnetic viscosity experiments.

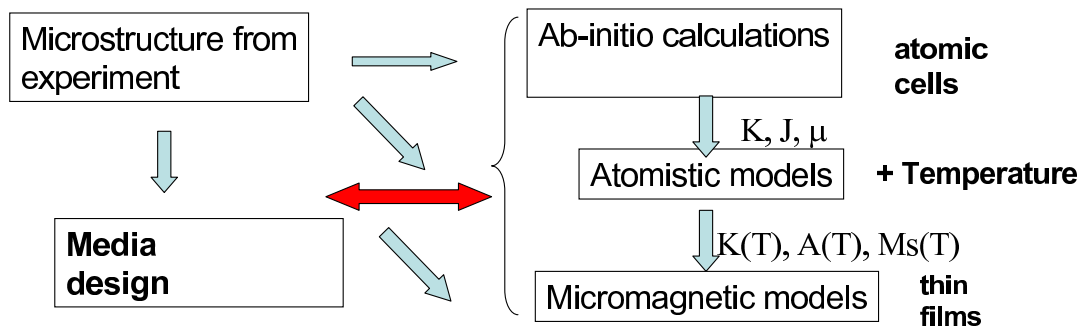


**Figure 2.1:** Diagram showing a hierarchical multiscale model and its relation with experiments.

## 2.2 Linking different spatial scales

In the following sections different approaches to the simulation of magnetic systems are presented, each at different spatial scale. Therefore, the problem is sliced in different models depending on the physical problem. Finally, we describe a mul-

tiscale model that can include several characteristics of different length scales in a single simulation.

### 2.2.1 Ab-initio calculation of magnetic properties.

Spin  $S$  and orbital  $L$  moments, its coupling and the exchange interaction are pure quantum phenomena responsible for the ferromagnetism. With simple quantum statistical models we can explain some observed effects as the magnetocrystalline anisotropy  $l(l + 1)/2$  temperature dependence exponent [Callen 66], where  $l$  is the order of the spherical harmonics describing the angular dependence of the local anisotropy, known as Callen-Callen or Akulov law. Another example is the  $T^{3/2}$  temperature dependence of magnetization deviation from its 0  $K$  value or Bloch law [Bloch 30]. However, analytical models are not able to treat complex systems and to extract the intrinsic parameters of magnetic materials. In the mentioned above example of the magnetic anisotropy temperature dependence the analytical calculation is not able to provide the zero temperature value, needed in order to complete the whole temperature dependence. First principles numerical calculations are the tool needed to provide the strength of the interactions and the structure of the material at the atomic level. Unfortunately, the full Hamiltonian eigenvalue problem is still only solvable in few cases and extra approximations are needed. The first of them is the Born-Oppenheimer approximation in which only the electronic degrees of freedom are taken into account quantically and the nuclei move in the resulting ionic potential. Another very useful approximation is to consider only the outer electrons and to treat the inner electrons as pseudopotential acting on the outer electrons. A powerful and amply used tool is found in the density functional theory (DFT) which has its origin in the Hohenberg-Kohn Theorem that transforms the complex many-body problem of interacting electrons and nuclei into a coupled set of one-particle Kohn-Sham equations. The problem changes from a eigenvalue problem to a variational problem, which is computationally much more manageable. The energy becomes a functional of the electronic density  $n(r)$ . The exact functional is not known, because the exchange and correlation terms are not, and additional approximation have to be invoked: Local Density Approximation(LDA), General Gradient Approximation(GGA) , etc.

In the magnetic systems variations have to be included: our scheme has to be spin aware (instead of LDA the local spin density(LSDA) is used). The relativistic spin-orbit coupling has to be added to the functional in order to calculate the magnetocrystalline anisotropy. This term is very weak and can be considered as a perturbation but provokes the need to change the representation from  $LS$  to the total angular moment  $J, J_z$  because  $L$  and  $S$  are no longer good quantum numbers.

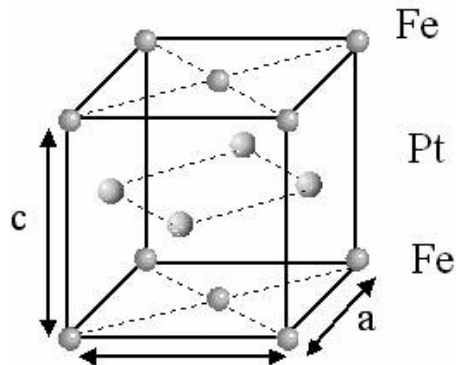


**Figure 2.2:** FePt  $L1_0$  lattice cell showing the planes of Fe and Pt.

An example of ab-initio calculations is the work on the magnetic anisotropy of FePt  $L1_0$  [Mryasov 05], which is one of the principle materials under investigation in this thesis. In what follows, we will use the FePt parameters, estimated in this work. The high anisotropy fct FePt  $L1_0$  phase consists of alternated atomic layers of Fe and Pt (see Fig. 2.2). The magnetocrystalline anisotropy is mainly due to the contribution from the 5d element (Pt) having large spin-orbit coupling whereas the 3d element (Fe) provides the large magnetic moment. The work uses the constrained LSDA (CLSDA) method, which allows to treat non-collinear magnetic order [Dederichs 84]. The Pt, normally non-magnetic, has an induced non-localized magnetic moment (see Fig. 2.3) proportional to the exchange field from the Fe moments. Treating the Pt moments as independent degrees of freedom gives incorrect results (low  $T_c$  and ‘soft’ Pt layers). The exchange of the Fe sites is not limited to nearest neighbors and can be ferromagnetic (positive) or antiferromagnetic (negative) (see Fig. 2.4). Based on those facts and the ab-initio calculated parameters, the authors of Ref. [Mryasov 05] introduced an effective hamiltonian that includes only the Fe magnetic moment degrees of freedom:

$$H = - \sum_{i \neq j} \tilde{J}_{ij} \mathbf{m}_i \cdot \mathbf{m}_j - \sum_i d_i^{(0)} (\mathbf{m}_i^z)^2 - \sum_{i \neq j} d_{ij}^{(2)} \mathbf{m}_i^z \cdot \mathbf{m}_j^z \quad (2.1)$$

where  $d^{(0)}$  is the single ion anisotropy,  $d_{ij}^{(2)}$  is a new two ion anisotropy and  $\tilde{J}_{ij}$  is the effective exchange interaction parameter. Here  $\mathbf{m}_i$  denote Fe sublattice spin moments which can be treated as unit vector as will be explained in the next subsection. The contribution of the Pt moments is the new effective parameters for the exchange and the single ion anisotropy and a new term in the hamiltonian: the two ion anisotropy. The result of this mechanism is a large uniaxial out-of-plane anisotropy and the authors obtained a bulk value  $K_1(T = 0) = 7.7 \cdot 10^7 \text{ erg/cm}^3$ .

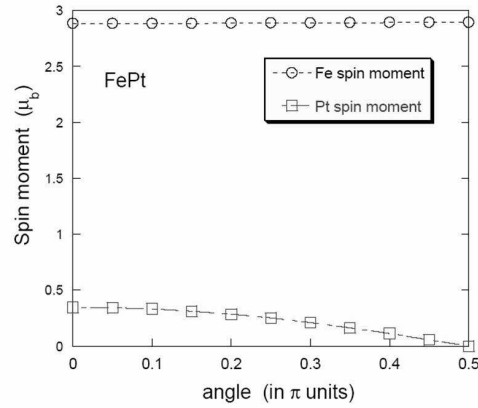


**Figure 2.3:** Fe and Pt magnetic moment in FePt as a function of the angle between them. Courtesy of U. Nowak.

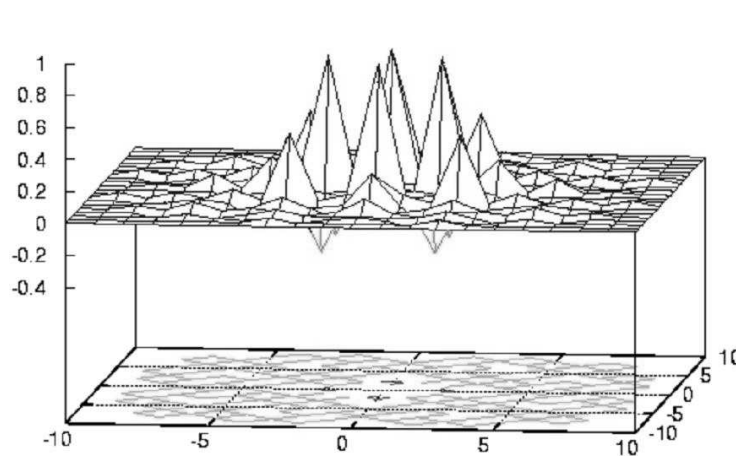


**Figure 2.4:** In-plane exchange strength for Fe sites in FePt normalized to the nearest neighbors value. Courtesy of U. Nowak.

## 2.2.2 Atomistic models in magnetism

In this approach every physical magnitude has its value in the atom sites and atomic-level information, such as interatomic distance or magnetic moment, is explicitly used. Although the ab-initio simulations are also atomistic, this paragraph only refers to the simulation based on semiclassical energy. The spin is a vector whose components can have any value. In fact the true classical approach is strictly speaking valid for  $S \rightarrow \infty$ , being  $S$  the spin. However, in this kind of atomistic simulations some quantum features can be added, for example discrete values for the spin projection, a classical example for this is the Ising model that represents a spin  $S = 1/2$ . Contrary to the ab-initio models, the atomistic simulations do not consider the electronic structure. The atomistic models have been extensively used

in other fields of the materials science as in film growth dynamics [Rahman 04], solid-liquid systems [Hoyt 02], etc.

The atomistic sites have a localized magnetic moment  $\mu_s$ , whose value is obtained from experiments or ab-initio calculations. The natural unit is the Bohr magneton  $\mu_B = 9.274 \cdot 10^{-21} \text{ erg/G}$  and the moment constitutes usually few magnetons. Instead of the vector  $\boldsymbol{\mu}$ , it is more convenient to work in reduced magnetic moment  $\mathbf{m} = \boldsymbol{\mu}/\mu_s$ .

From the magnetic point of view, the main energy contributions are the Zeeman energy, the magnetic dipole-dipole energy, the exchange energy and the magnetic anisotropy energy.

The anisotropy reflects the existence of preferred spatial directions in which the magnetization will align. There are different sources of anisotropy, but their contribution to the energy can always be written in similar functional dependence on  $\mathbf{m}$ . The principal source is the magnetocrystalline anisotropy that has its origin in the spin-orbit (LS) coupling and the ionic crystal field. Due to this fact, the magnetocrystalline anisotropy has the same symmetry as the lattice of the material. For uniaxial materials the anisotropy energy is an expansion of even powers of  $m$  that usually reduces to its first term:

$$(\text{Uniaxial anisotropy}) \quad E_{ani} = -d_1(\mathbf{m} \cdot \mathbf{e})^2. \quad (2.2)$$

Its main effect is to align the magnetic moment in the direction of  $\mathbf{e}$ , which is known as easy axis. If the material has a cubic lattice the anisotropy is an expansion of terms with cubic symmetry and considering only its first term is equal to:

$$(\text{Cubic anisotropy}) \quad E_{ani} = d_1(m_x^2 m_y^2 + m_x^2 m_z^2 + m_y^2 m_z^2). \quad (2.3)$$

The other sources of magnetic anisotropy are: surface anisotropy, magnetoelastic anisotropy and shape anisotropy.

The Zeeman energy is the energy of a magnetic dipole in a magnetic field:

$$E_{ext} = -\mu_s \mathbf{m} \cdot \mathbf{H}_{ext}. \quad (2.4)$$

The applied field tends to align the magnetization in its direction. Both the anisotropy and the Zeeman energies are local and are easy to calculate.

The exchange interaction is an electronic interaction whose origins are the Pauli exclusion principle and the Coulomb repulsion. The exchange interaction requires the integration of the electronic wave function. A more convenient evaluation of the exchange generally involves calculating the exchange explicitly using the Heisenberg form:

$$E_{ex} = -\frac{1}{2} \sum_{i \neq j} J_{ij} \mathbf{m}_i \cdot \mathbf{m}_j \quad (2.5)$$

with  $J_{ij}$  the exchange integral. This definition of the Heisenberg exchange energy will be used throughout the thesis. This sum extends to all the moment pairs in the material, but due to the short range of the exchange interaction, the sum is usually restricted to nearest neighbors:

$$E_{ex} = -\frac{J}{2} \sum_{i \neq j} \mathbf{m}_i \cdot \mathbf{m}_j. \quad (2.6)$$

A positive value of exchange parameter yields ferromagnetism and a negative value antiferromagnetism. The main effect of exchange is the alignment of all the magnetic moments in the case of ferromagnetism and it is usually the strongest interaction that dominates locally. However, the exchange interaction is isotropic and can not alone account for the ferromagnetism, thus needing the anisotropic energy term. We should note here that the Heisenberg form of exchange explicitly implies the direct exchange formation. Other forms of exchange interactions (indirect, RKKY, etc...) in same cases could be mapped into the Heisenberg form with some correction. Generally speaking, this is not true.

The interaction energy between two moments in the material is the classical dipole-dipole energy:

$$E_{dip} = \frac{\mathbf{m}_i \cdot \mathbf{m}_j}{r_{ij}^3} - \frac{3(\mathbf{m}_i \cdot \mathbf{r}_{ij})(\mathbf{m}_j \cdot \mathbf{r}_{ij})}{r_{ij}^5}. \quad (2.7)$$

The contribution of each of the individual terms is the least important of the energies. However, this does not mean that the dipolar interactions can be neglected because, being long-ranged, they are a sum over the whole magnetic material. The dipolar interaction is responsible for magnetic inhomogeneities, the foremost of them is the domain wall. The exchange controls the details of the microscopic magnetic structure, while the magnetostatic energy is responsible for the magnetization distribution over the whole system.

### 2.2.3 Micromagnetics: classical approach to model magnetization distribution

#### General principles of micromagnetics

The process of demagnetization in a standard hysteresis experiment consists basically of a series of stationary states. The time of measurement (typically milliseconds) is as large as to disregard rapid dynamic effects (occurring at pico - nanoseconds). For this kind of process the micromagnetic approach, firstly introduced by W.F. Brown [Brown 63a], is used. The micromagnetism is a semiclassical approach that considers the magnetization  $\mathbf{M}(\mathbf{r})$  as a vector function of the spatial coordinates,

but with constant module  $M_s$ . This implies a continuous approximation that ignores any discrete effect. The magnitude  $M_s$  is the saturation magnetization and it is defined as the density of magnetic moments (per unit of volume in the material). It is more useful to work with the magnetization unit vector  $\mathbf{m}(\mathbf{r}) = \mathbf{M}(\mathbf{r})/M_s$ . The energies appearing in the atomistic level are substituted by a functional of  $\mathbf{m}(\mathbf{r})$ :

$$E_{tot} = E_{ex} + E_{ani} + E_{ext} + E_{dem}, \quad (2.8)$$

$$E_{ex} = \int_V A(\mathbf{r})[(\nabla m_x)^2 + (\nabla m_y)^2 + (\nabla m_z)^2]dV, \quad (2.9)$$

$$E_{ani} = - \int_V [K(\mathbf{r})\mathbf{m}(\mathbf{r}) \cdot \mathbf{e}(\mathbf{r})^2]dV, \quad (2.10)$$

$$E_{ext} = - \int_V \mathbf{M}(\mathbf{r}) \cdot \mathbf{H}_{ext}(\mathbf{r})dV, \quad (2.11)$$

$$E_{dem} = - \frac{1}{2} \int_V \mathbf{M}(\mathbf{r}) \cdot \mathbf{H}_{dem}(\mathbf{r})dV. \quad (2.12)$$

The micromagnetic exchange energy is a continuous version of the atomistic exchange. The expression is the square of a derivative and, therefore, the minimum value corresponds to the saturated state. Therefore, the micromagnetic exchange also favors all the moments to be parallel. For granular magnetic material the exchange constant is often phenomenological.

The atomistic magnetic moment and the saturation magnetization are related through

$$M_S = \frac{c\mu_s}{V_{cell}} \quad (2.13)$$

where  $V_{cell}$  is the volume of the unit cell and  $c$  the number of moments per cell ( $c = 1$  for sc,  $c = 2$  for bcc,  $c = 4$  for fcc). The anisotropy constant is an energy density, whose origin is equivalent to the atomistic anisotropy and their relation is:

$$K = \frac{cd_1}{V_{cell}}. \quad (2.14)$$

The magnetization state is found by minimizing the total energy with respect to the function  $\mathbf{m}(\mathbf{r})$ . Namely, we must solve  $\min E_{tot}(\mathbf{m}(\mathbf{r}))$  with the restriction  $\|\mathbf{m}(\mathbf{r})\| = 1$ . The minimum found by this procedure is normally a relative minimum of the total energy. The minimization procedure depends on the initial conditions and the final state is dependent of the initial state. On the other hand, this is also the case in the experiments. The variational problem solution satisfies  $\delta E_{tot}/\delta \mathbf{m}(\mathbf{r})=0$

with the addition of a Lagrange multiplier term, proportional to  $\mathbf{m}(\mathbf{r})$ . Therefore, the solution of variational problem also satisfies the Brown condition for minimum:

$$\frac{\delta E}{\delta \mathbf{m}(\mathbf{r})} \times \mathbf{m}(\mathbf{r}) = 0.$$

We can define an effective field as

$$\mathbf{H}_{\text{eff}} = -\frac{1}{M_S V} \frac{\delta E}{\delta \mathbf{m}} \quad (2.15)$$

and to rewrite the Brown condition as

$$\mathbf{m} \times \mathbf{H}_{\text{eff}} = 0. \quad (2.16)$$

From Eq. (2.8) the total effective field is a sum of exchange, anisotropy, external and magnetostatic fields:

$$\mathbf{H}_{\text{eff}} = \mathbf{H}_{\text{ex}} + \mathbf{H}_{\text{ani}} + \mathbf{H}_{\text{ext}} + \mathbf{H}_{\text{dem}} \quad (2.17)$$

with

$$\mathbf{H}_{\text{ex}} = \frac{2A}{M_S} \nabla^2 \mathbf{m}, \quad (2.18)$$

$$\mathbf{H}_{\text{ani}} = \frac{2K}{M_S} (\mathbf{m} \cdot \mathbf{e}) \mathbf{e}. \quad (2.19)$$

It is often useful to define the anisotropy field  $H_K = 2K/M_S$  and normalize all the fields to this parameter.

Until the rapid development of the computers, the micromagnetics was an analytical theory and many analytical results were derived. However, normally all of them are based on simplifications and have very limited regions of applicability. In numerical approaches we divide or discretize the sample by the discretization length  $\Delta$ , considering a constant magnetization inside each element.

There are two physically relevant parameters that we need to take in account in order to select the size of the discretization length  $\Delta$ : the wall-width parameter

$$\delta = \sqrt{\frac{A}{K}} \quad (2.20)$$

and the exchange length

$$l_{ex} = \sqrt{\frac{A}{M_S^2}}. \quad (2.21)$$

The domain wall width parameter determines the thickness of the domain wall separating magnetic domains of different magnetization directions. This parameter corresponds to the width of a Bloch wall that is found in materials in which the main source of anisotropy is magnetocrystalline anisotropy (hard materials). The

exchange length is the length below which atomic exchange interactions dominate typical magnetostatic fields. The exchange length is proportional to the Néel domain wall width. This type of domain wall that only contains volume charges appears in thin films of soft magnetic material. In order to describe correctly the domain wall the discretization length must be less than its width but include enough atoms to be valid as the continuous approximation.

In the literature there are two main methods of discretization: Finite Differences (FD) [Berkov 93] and Finite Elements Method (FEM) [Fidler 00]. The advantage of the finite differences method is its easy implementation but its main disadvantage is its inability to describe irregular shapes. To overcome this problem Gibbons proposed the Embedded Curved Boundary (ECB) method as an alternative based on the interpolation of the boundary elements [Gibbons 00]. For curved surfaces FEM is best suited because its elements are tetrahedra with variable size, although any numerical approach will fail to describe real surfaces. At the present, there are several software packages available for micromagnetic simulations. Most of them are commercial programs, but also there have been efforts to release free source codes in particular Oommf [OOMMF], which uses FD method with Fast Fourier Transform, and magpar [Magpar], which uses FEM simulations. In our calculations in the following chapters we used codes developed inside the group that use the finite differences method.

In the numerical solution of Eq. (2.16) the right term can never be zero due to numerical convergence problem. We want this value to be as low as possible, but in practice we finish our calculation when a tolerance value has been reached. In our calculation we use the following definition for the micromagnetic error:

$$error = \max \frac{\|\mathbf{m} \times \mathbf{H}_{\text{eff}}\|}{\|\mathbf{m}\| \|\mathbf{H}_{\text{eff}}\|} = \max \sin \widehat{\mathbf{m} \mathbf{H}_{\text{eff}}}. \quad (2.22)$$

We will consider that calculations are properly converged when  $error < \epsilon$ . A reasonable value of  $\epsilon$  is  $10^{-4}$ .

Finally, we will return to the micromagnetic exchange constant  $A$ . Its relation with the atomistic exchange parameter can be easily calculated if we compare the finite difference version of Eq. (2.18) and the effective field arising from Eq. (2.5) and making  $\Delta$  equal to the lattice distance. Thus in a tetragonal with lattice size parameters  $a_x = a_y = a_{\text{par}}$  and  $a_z = a_{\text{perp}}$ :

$$A_{\text{perp}} = \frac{J_{\text{perp}} a_{\text{perp}}}{2a_{\text{par}}^2}, \quad (2.23)$$

$$A_{\text{par}} = \frac{J_{\text{par}}}{2a_{\text{perp}}}. \quad (2.24)$$

In the case of a cubic cell the equivalence becomes

$$A = \frac{cJ}{2a}. \quad (2.25)$$

### Magnetostatic potential. The DADI method

The micromagnetism poses particular emphasis in the exact calculation of the demagnetizing field. In the continuous micromagnetic approach it is described by the Maxwell equation in the absence of currents  $\nabla \times \mathbf{H} = 0$  and, therefore, there exists a potential called scalar magnetostatic potential that satisfies:

$$\mathbf{H}_{\text{dem}} = -\nabla U_{\text{mag}}. \quad (2.26)$$

This potential satisfies the Laplace equation outside the material and the Poisson one inside the material:

$$\begin{aligned} \nabla^2 U_{\text{mag}} &= 0 && \text{Outside ferromagnetic material} \\ \nabla^2 U_{\text{mag}} &= 4\pi \nabla \cdot \mathbf{M}(\mathbf{r}) && \text{Inside ferromagnetic material} \end{aligned} \quad (2.27)$$

with the boundary conditions:

$$\frac{\partial U_{\text{mag},in}}{\partial \mathbf{n}} - \frac{\partial U_{\text{mag},out}}{\partial \mathbf{n}} = 4\pi \mathbf{M} \cdot \mathbf{n} \quad (2.28)$$

where  $\mathbf{n}$  is the unit normal to surface of the ferromagnetic sample.

The sources of the magnetostatic field are called magnetostatic charges. The surface charge is defined as  $\sigma = \mathbf{M} \cdot \mathbf{n}$  and the volume charge as  $\rho = -\nabla \cdot \mathbf{M}$ . The magnetostatic energy integral extends to all the space, not only the ferromagnetic body, and the minimization of the magnetostatic energy will seek the reduction of the field outside the ferromagnetic body. This can be achieved reducing of the magnetic charges and that fact is stated as the pole avoidance principle. This field gives origin to domains and magnetization inhomogeneities. The generic solution of a field from its sources is found in traditional electromagnetism

$$U_{\text{mag}} = \int_V \frac{\rho(\mathbf{r}')}{|\mathbf{r} - \mathbf{r}'|} d^3 r' + \oint_S \frac{\sigma(\mathbf{r}')}{|\mathbf{r} - \mathbf{r}'|} d^3 r' \quad (2.29)$$

and from Eq. (2.26)

$$\mathbf{H}_{\text{dem}} = - \int_V \frac{(\mathbf{r} - \mathbf{r}')\rho(\mathbf{r}')}{|\mathbf{r} - \mathbf{r}'|^3} d^3 r' - \oint_S \frac{(\mathbf{r} - \mathbf{r}')\sigma(\mathbf{r}')}{|\mathbf{r} - \mathbf{r}'|^3} d^3 r'. \quad (2.30)$$

In micromagnetic calculations most of the computation time is spent in the calculation of the magnetostatic field. The dipolar interaction is non-local and long ranged. The field in dipole-dipole representation is a sum of  $3N$  elements, where  $N$  is the number of atomic moments and the numerical integration of Eq. (2.30) scales

like  $N^2$  and this represents too much computational time even for today advanced computers. Due to this reason, several advanced methods have been used to solve the magnetostatic problem. The methods used are Fast Fourier Transform (FFT) [Yuan 92], Finite Element Method (FEM) [Chen 97], hybrid FEM - Boundary Element Method (FEM-BEM) [Fredkin 90], Fast Multipole Method (FMM) [Brown 04] and other advanced methods. The efficiency of each method depends on the implementation and on the simulated physical problem. We use a different method called the Dynamic Alternating Direction Implicit (DADI) [Gibbons 98]. The underlying principle of this method is to add a fictitious time derivative to Eq. (2.27):

$$-\frac{\partial\psi}{\partial t} = L\psi + \rho \quad (2.31)$$

with  $L = \nabla^2$ . Next, we integrate the resulting equation forward in time to the time-asymptotic state. At this point the fictitious time derivative goes to zero and we have the desired solution  $\psi = U_{mag}$ . The ideal case would be the performance of only one step of integration of Eq. (2.31). The time step  $1/\omega$  should be chosen to achieve the convergence in as few steps as possible. In a hysteresis loop the solution is obtained from the solution of the previous field step, thus the test potential is very close to the solution and the method converges in few steps. Near coercivity large changes of magnetization and scalar potential are expected. In this situation, the complete convergence is needed.

The operator  $L$  is replaced by its finite difference equivalent. For example the  $L_x$  contribution is

$$L_x = \frac{\psi_{i+1,j,k} + \psi_{i-1,j,k} - 2\psi_{i,j,k}}{\Delta^2} \quad (2.32)$$

with  $\Delta$  - the size of the spatial discretization and  $\psi_{i,j,k}$  the value of the scalar potential in the element on the node  $(i, j, k)$ . The method consists of three passes

$$\begin{aligned} (-\omega + L_x/2)\psi^{n+1/3} &= (-\omega + L_x/2 - L_y - L_z)\psi^n + \rho & \textit{xpass} \\ (-\omega + L_y/2)\psi^{n+2/3} &= -\omega\psi^{n+1/3} + (L_y/2)\psi^n & \textit{ypass} \\ (-\omega + L_z/2)\psi^{n+1} &= -\omega\psi^{n+2/3} + (L_z/2)\psi^n & \textit{zpass}. \end{aligned} \quad (2.33)$$

The magnetostatic volume charges are included replacing the operator divergence by its finite difference equivalent. In the surface cells we have to change this term by the surface charges. For example the contribution of a cell which occupy the position  $(i,j,k)$  will be:

$$\rho = \frac{1}{2}(M_{i+1,j,k} - M_{i-1,j,k} + M_{i,j+1,k} - M_{i,j-1,k} + M_{i,j,k+1} - M_{i,j,k-1}). \quad (2.34)$$

The solution of these equations involve tridiagonal matrices, which are linear systems easy to solve. This can be easily seen from Eq. (2.32) because the left hand side only includes the values of  $\psi_{i+1,j,k}, \psi_{i-1,j,k}$  and  $\psi_{i,j,k}$ . The evaluation of the potential is

the successive solution of Eqs. (2.33). From the current value  $\psi^n$ , we obtain  $\psi^{n+1/3}$ , and this yields the value  $\psi^{n+2/3}$  and, finally, the value of the potential in the next step  $\psi^{n+1}$ .

This method needs the addition of free (zero magnetization) space in the simulated region to allow the potential to slowly tend to its infinity value. This value is arbitrary because the equation is differential and we choose it, for convenience, to be zero. This is also the case in FEM and FFT methods (zero-padding). The hybrid FEM-BEM method presents the advantage of not requiring discretization elements outside the simulated sample. In the DADI method periodic boundary is easily implemented if we consider  $\psi(1) = \psi(N + 1)$ . The resulting tridiagonal system is replaced then by a periodic tridiagonal system, which is also very simple to solve.

#### 2.2.4 Passing atomistic information to micromagnetics: a multiscale model<sup>1</sup>

The multiscale calculations involve the use of several models of different length scales in the same calculations. There is more than one approach to include the ab-initio, atomistic and micromagnetic (mesoscopic) calculations. Unfortunately, the simulations can not reach the scale of real samples, that is up to  $mm$ , but it is able to simulate the small size systems produced by nowadays technology. As a first example of multiscale modeling we examine again the work of O.N. Mryasov [Mryasov 05]. The motivation of the work is the temperature dependence of the anisotropy of FePt. In the case of a two ion anisotropy Skomski et al. have shown that the Callen-Callen law has to be changed by a  $M(T)^2$  dependence [Skomski 03]. The experimental factor in the low-temperature range in FePt is 2.1 [Okamoto 02, Thiele 02]. From Langevin Dynamics atomistic calculations using the effective Hamiltonian (see Eq. (2.1)) with the parameters obtained from ab-initio it was possible to reproduce this temperature dependence. Posteriorly, based on the same model D. Hinzke [Hinzke 07] has calculated the temperature dependence of the domain wall width, thus obtaining the micromagnetic exchange parameter  $A(T)$ . Those data can be included in a micromagnetic simulation to obtain values at finite temperature and this procedure is equivalent to the method shown in Fig. 2.1.

Other method, in parallel to the previous one, will be used in the next chapter to calculate magnetization processes in soft/hard bilayers. The necessity of the multiscale approach for small intergranular exchange values has been suggested in Refs. [Kronmüller 97, Kronmüller 01]. The multiscale model is based on the partitioning of the computational cell into atomistic and micromagnetic regions, as shown schematically in Fig. 2.5. The atomistic scale discretization is used in the inter-

<sup>1</sup>based on author's work Ref. [Garcia-Sanchez 05]

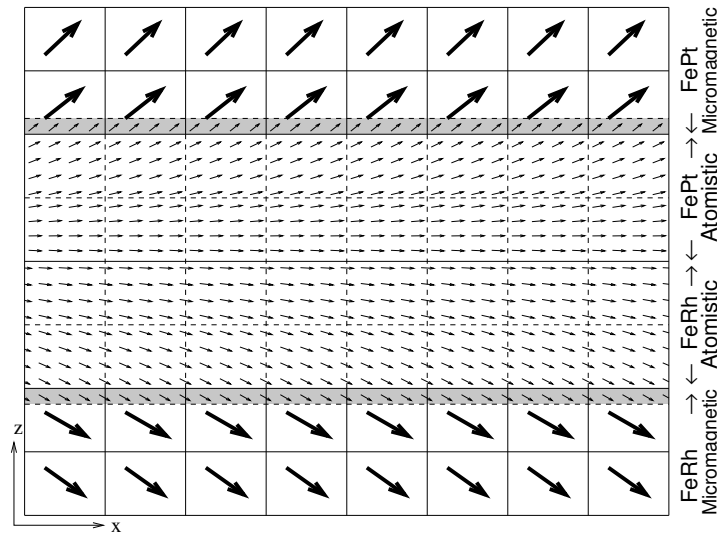


**Figure 2.5:** Schematic diagram showing the basis of the multi-scale model in terms of the partitioning of the system into micromagnetic and atomistic regions. The model will be used in the next chapter to model FePt/FeRh interface.

face regions, where spatially rapid changes in magnetization might be expected. In this region, the exchange is treated exactly within the Heisenberg model, allowing the system to access to the entire spectrum of magnetic excitations. The lattice structure is taken into account explicitly. For the calculation of the magnetostatic field, the atomistic region is partitioned into “macrocells” of the same size as the micromagnetic region. Inside each macrocell the volume charges are neglected. For computational simplicity the thickness of the atomistic region is commensurate with the size of the micromagnetic cells. The average magnetization of each macrocell is calculated and used in the micromagnetic evaluation of the magnetostatic field. The magnetostatic field is calculated using DADI. Finally, we have to consider the interface between the atomistic and micromagnetic region. On this boundary we first used [Garcia-Sanchez 05] Heisenberg exchange between the actual atoms in the atomistic region and virtual atoms in the micromagnetic region having the direction of the average magnetization in the micromagnetic cell projected onto the physical lattice, corresponding to the gray region in Fig. 2.5.

The averaging method to obtain the micromagnetic macrocells from atomistic moments has drawbacks, as for example in the case of the hysteresis loops presented in Fig. 2.6 those correspond to FePt/FeRh bilayer with easy axis perpendicular to the plane ( $Z$  direction) and applied field in the  $Z$  direction and dimensions  $6 \text{ nm} \times 6 \text{ nm} \times 12 \text{ nm FePt} + 12 \text{ nm FePt}$ . The calculation using averaging overestimates the coercive field due to the fact that averaging does not result in a continuous variation of the magnetization. In this case the best method is the interpolation of

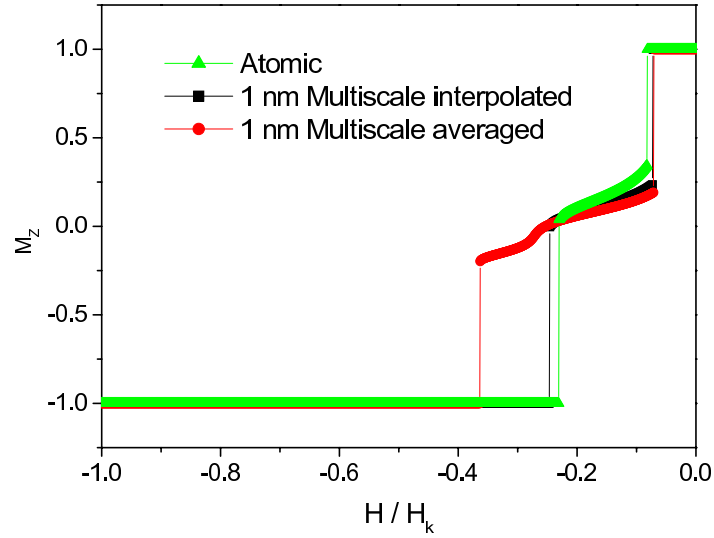


**Figure 2.6:** Hysteresis loops of a bilayer with parameters  $A = 10^{-6} \text{ erg/cm}$ ,  $K^{FePt} = 7 \cdot 10^7 \text{ erg/cm}^3$ ,  $K^{FeRh} = 0$ ,  $M_s^{FePt} = 1100 \text{ emu/cm}^3$  and  $M_s^{FeRh} = 1270 \text{ emu/cm}^3$  using atomistic model and two different schemes of multiscale model.

the micromagnetic moment from the nearest atomistic moments. The used method is a trilinear interpolation. The spatial coordinates are expressed as:

$$t = \frac{x - x_{min}}{x_{max} - x_{min}}, \quad (2.35)$$

$$u = \frac{y - y_{min}}{y_{max} - y_{min}}, \quad (2.36)$$

$$v = \frac{z - z_{min}}{z_{max} - z_{min}}, \quad (2.37)$$

and the magnetization is obtained from the following equation:

$$M = [m_1(1-t)(1-u) + m_2t(1-u) + m_3tu + m_4(1-t)u](1-v) + [m_5(1-t)(1-u) + m_6t(1-u) + m_7tu + m_8(1-t)u]v. \quad (2.38)$$

The notations are shown in Fig. 2.7. The interpolation gives the proper micromagnetic magnetization values at the center. After interpolation we obtain the correct coercive field as we can see in Fig. 2.6.

## 2.3 Linking different timescales

The magnetization dynamics simulations have to be able to deal with different time scales. Experimentally, the magnetization dynamics occur at different time scales starting from femtoseconds (recent pump-probe experiments [Cinchetti 06]),

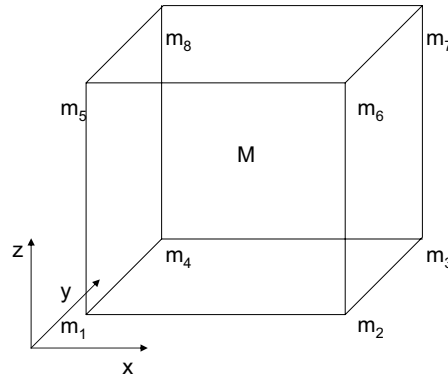


**Figure 2.7:** Drawing showing the labeling of the atomic sites used to interpolate the magnetization value in  $M$ .

and from fast magnetization dynamics (fast-magneto-optical measurements [Bauer 00]). At seconds-hours range, slow thermal magnetization dynamics are measured in standard magnetometers as magnetic viscosity [Wegrowe 97]. Finally, long-time magnetization stability up to decades is relevant to magnetic recording applications [Weller 99].

From the point of view of simulation, the main parameter is the time-step of the numerical integration of the basic equation of motion (the Landau-Lifshitz-Gilbert equation). In the atomistic modeling, the time step is defined by the exchange interaction and is of the order of  $10^{-16}$  s. Therefore, integrating the equation of motion at atomistic level, one can afford the description of small system up to the time of 1 ns. In the micromagnetic systems the time-step has to be at least two orders of magnitude less than the frequency of precession of the magnetization. The resulting time-step is about  $10^{-13}$  s and the reachable time simulations of tens of nanoseconds, far from interval of interest in most of the experimental situations. These limits depend on the system size and in the computer technology advances.

The zero-temperature dynamics are deterministic. Different techniques are available to extend the simulation time scale by improving the numerical integration of the dynamical equation [Suess 02] and even trying to solve analytically simple systems under some assumptions (see Section 2.3.2 and [Serpico 04]). However, the temperature effects are very important in dynamics and produce magnetization random walk and eventually thermal decay of initial magnetization state. The deterministic behavior becomes stochastic at finite temperature and the system will evolve from state to state overcoming energy barriers due to thermal fluctuations. At long time scale in this situation statistical methods have to be used in order to simulate the dynamic of the magnetization. Fig. 2.8 summarizes different methods in the presence of temperature. The stability of the magnetization can be studied with the

Kinetic Monte Carlo method, energy barrier calculations and the Arrhenius-Néel law. In between several methods can be used to accelerate the thermal dynamics, as for example, Victora method [Xue 00] or Time Quantified Metropolis Monte Carlo [Chubykalo 03a] reaching ranges of several seconds. Here we will describe several of these methods, which we tried to implement in magnetic systems and check their performance.

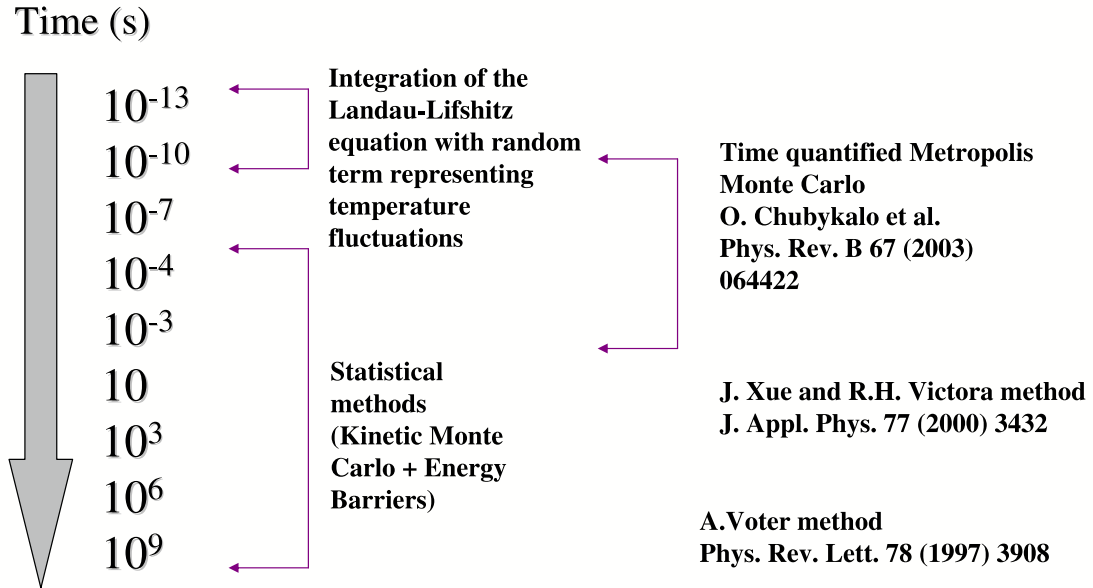


**Figure 2.8:** Numerical methods for the thermal dynamics of the magnetization and their characteristic time scales.

### 2.3.1 The magnetization dynamics and the Landau-Lifshitz-Gilbert equation

The equation of motion of a magnetic moment under an applied field is

$$\frac{d\boldsymbol{\mu}}{dt} = -\gamma\boldsymbol{\mu} \times \mathbf{H} \quad (2.39)$$

where  $\gamma = 1.7609 \cdot 10^7 (Oe \text{ s})^{-1}$  is the gyromagnetic ratio for a Landé factor  $g = 2$ . The moment precesses around the field with the Larmor frequency  $\gamma H/2\pi$  and never reaches the equilibrium position unless it already points in the same direction. The equation conserves both the energy and the magnetic moment magnitude. The macroscopic magnetization vector  $\mathbf{M}$  also satisfies a similar equation, recalling Eq. (2.13). The equation is valid from both the micromagnetic and the atomistic point of view and the way to include any interaction in the equation is to use instead of

the external field the effective field calculated by means of

$$H_{eff} = -\frac{1}{V} \frac{\partial E}{\partial \mathbf{M}}. \quad (2.40)$$

Eq. (2.39) does not explain the absorption line in resonance experiments and the fact that the magnetic moment eventually aligns with field direction. The motion is modified by the interaction with crystal lattice vibrations, conduction electrons and other external sources. L.D Landau and E.M. Lifshitz [Landau 35] proposed to add a term proportional to  $[\mathbf{M} \times [\mathbf{M} \times \mathbf{H}]]$ , which conserves the magnitude, in order to obtain a phenomenological equation of the spin dynamics. Posteriorly, T. Gilbert suggested to add a viscous force  $-\mathbf{M} \times \partial \mathbf{M} / \partial t$  to the equation of motion (2.39) [Gilbert 55]. The Gilbert and the Landau-Lifshitz equations are equivalent with the renormalization of the precession and dissipation terms. The Gilbert version is preferred because it predicts slower motion with increasing damping. The Gilbert equation, converted to Landau-Lifshitz form, is known as the Landau-Lifshitz-Gilbert(LLG) equation and has the expression:

$$\frac{d\mathbf{M}}{dt} = -\frac{\gamma}{1 + \alpha^2} (\mathbf{M} \times \mathbf{H}_{eff}) - \frac{\alpha\gamma}{(1 + \alpha^2)M_s} \mathbf{M} \times (\mathbf{M} \times \mathbf{H}_{eff}) \quad (2.41)$$

where  $\alpha$  is the phenomenological damping constant, which represents all the relaxation mechanisms. For longitudinal magnetic recording media the damping parameter measured by ferromagnetic resonance lays in the range of 0.01 – 0.04 [Inaba 97]. The equation is dissipative and does not conserve the energy, albeit conserving the magnitude of the magnetization. An example of dissipative LLG dynamics can be seen in Fig. 2.9. The precession frequency in the absence of external field is  $\gamma H_k / (1 + \alpha^2)$ , therefore, sometimes it is useful to express the equation in reduced units

$$\frac{d\mathbf{m}}{d\tau} = -(\mathbf{m} \times \mathbf{h}_{eff}) - \alpha \mathbf{m} \times (\mathbf{m} \times \mathbf{h}_{eff}) \quad (2.42)$$

where  $\tau = ((1 + \alpha^2) / \gamma H_k) t$  is the reduced time,  $\mathbf{h}_{eff} = \mathbf{H}_{eff} / H_k$  is the reduced field and  $\mathbf{m} = \mathbf{M} / M_s$  the reduced magnetization.

The second term of right side of Eq. (2.41), the damping term, makes the magnetization rotate towards the direction of the effective field and eventually to be parallel to its direction, reaching the equilibrium. That represents a minimum of the energy. Accordingly, we can use the integration of LLG equation to minimize the energy [Berkov 93] and this is the method we mostly use in this thesis. For this purpose, it is better to use a large value of the damping constant and to remove the precession term.

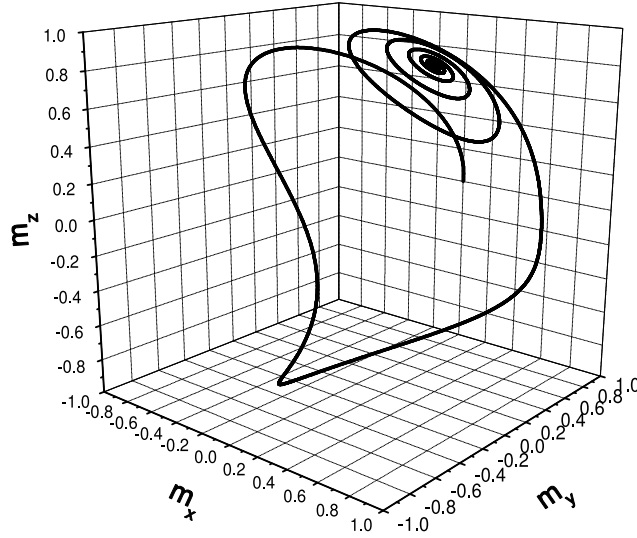


**Figure 2.9:** Trajectory of the magnetization of a single domain particle with easy axis in the Z direction under applied field  $h_{app} = \{0.5, 0, 0\}$  with initial condition  $m_0 = \{0, 1, 0\}$  and  $\alpha = 0.1$ .

### Nonlinear dynamics<sup>2</sup>

The Landau-Lifshitz-Gilbert equation is nonlinear. Therefore, the magnetic systems will present phenomena associated with nonlinearity such as stochastic resonance, nonlinear bifurcations or chaos [Fernández 00]. Furthermore, it is not possible to find exact analytical solutions except in very simple cases. The dissipation term is explicitly nonlinear, but even in the absence of this term the dynamics are nonlinear, because the effective field is dependent on the magnetization value.

To illustrate we can examine the case of a single domain particle with uniaxial anisotropy and easy axis in the Z direction under constant applied field. The energy of such particle is:

$$E/2KV = -\frac{1}{2}m_z^2 - H_x m_x - H_y m_y - H_z m_z \quad (2.43)$$

where the first term is uniaxial anisotropy and the external field is measured in units of  $H_K$ . We can choose  $H_y = 0$  without loss of generality and the applied field becomes  $\mathbf{H} = (H \sin \vartheta_H, 0, H \cos \vartheta_H)$  where  $\vartheta_H$  is the field angle with the axis Z. The energy minimum makes an angle  $\vartheta_0$  with the Z axis. We can change from the laboratory reference frame  $\{m\}$  to a reference frame  $\{m'\}$  where the minimum position always corresponds to the Z' axis. The transformation is a rotation of angle  $\vartheta_0$  around the Y axis. In the small amplitude approximation, where the components  $m'_x$  and  $m'_y$  of the magnetization vector are supposed to be small in comparison to

<sup>2</sup>based on author's work Ref. [Usatenko 06]

component  $m'_z \sim 1$ , the equation of motion in the new frame of reference  $\{m'\}$  is:

$$\dot{m}'_x = -(A - \dot{\vartheta}_0)m'_y - 2Cm'_xm'_y + \frac{1}{2}(A - D)m'_y(m'^2_x + m'^2_y) - \alpha Bm'_x \quad (2.44)$$

$$\dot{m}'_y = (B - \dot{\vartheta}_0)m'_x + 3Cm'^2_x + Cm'^2_y + \frac{1}{2}(D - B)m'_x(m'^2_x + m'^2_y) - \alpha Am'_y \quad (2.45)$$

and the variables  $A$ ,  $B$ ,  $C$  and  $D$  are determined by equations:

$$A = \cos^2 \vartheta_0 + H \cos(\vartheta_H - \vartheta_0), \quad B = \cos 2\vartheta_0 + H \cos(\vartheta_H - \vartheta_0), \quad (2.46)$$

$$C = -\frac{1}{4} \sin 2\vartheta_0, \quad D = H \cos(\vartheta_H - \vartheta_0). \quad (2.47)$$

In the frictionless case, the solution up to second harmonic of Eq. (2.44) is  $m'_x = a_0 + a \cos \omega_{NL}t + a_2 \cos 2\omega_{NL}t$  where  $\omega_{NL}$  is the nonlinear instantaneous frequency,  $a$  is the amplitude of motion,  $a_0$  is the zero harmonic and  $a_2$  is the second harmonic. The zero harmonic  $a_0$ , which value can be obtained from

$$a_0 = -2a_2 = \frac{|C|a^2}{4} \sqrt{\frac{2B}{\omega}} \left( \frac{1}{A} + \frac{3}{B} \right) \quad (2.48)$$

describes the displacement of the center of the magnetization vector rotation due to the nonlinear effect and is always positive.

In the considered case of constant applied field,  $\dot{\vartheta}_0 = 0$ , we arrive to an expression for the instantaneous frequency

$$\begin{aligned} \omega_{NL} = \omega - \frac{3\omega a^2 C^2}{8} \left( \frac{1}{A} + \frac{3}{B} \right)^2 \\ + \frac{Ba^2}{2} \left[ \frac{\omega D}{8} \left( \frac{3}{A^2} + \frac{3}{B^2} + \frac{2}{AB} \right) - 1 \right] \end{aligned} \quad (2.49)$$

where  $\omega = \sqrt{AB}$ . The comparison of Eq. (2.49) with numerical simulations shows good agreement for small values of the amplitude of the precessional cycle  $a$  (see Fig. 2.10). This can be expected since our approximation is only valid for small amplitudes. In the case of  $H_x = 0$  we have an axially symmetric case and Eq. (2.49) reduces to  $\omega_{NL} = 1 + H - \frac{1}{2}a^2$ .

The applicability of the solution can be extended including additional terms. The existence of corrections to the orbit center allows us to conclude that under numerical simulation of the LLG equation the precessional terms should not be neglected at long simulation times in the micromagnetic simulations.

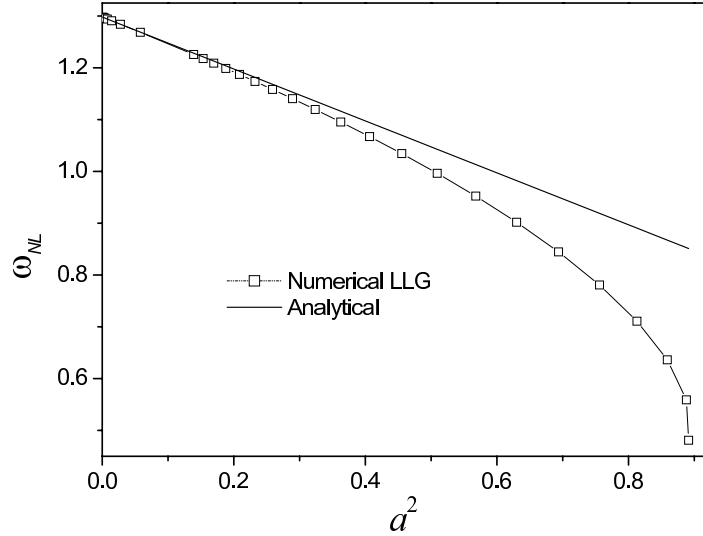


**Figure 2.10:** The nonlinear rotation frequency  $\omega_{NL}$  of the magnetization vector for a small ferromagnetic particle under the applied magnetic field  $\mathbf{H} = (0.1, 0, 0.3)$  versus the square of amplitude  $a^2$  comparing the analytical result, Eq. (2.49), and the numerical simulation of the LLG equation.

### 2.3.2 Non-thermal adiabatic approximation<sup>3</sup>

At timescales in the range of pico - nano seconds, the magnetic response is determined by the characteristic frequency of the magnetization precession and corresponds to typical ferromagnetic resonance experiment (FMR) [Slichter 89], where the small external perturbation is applied to the systems with the frequency typically of the order  $10^9$  to  $10^{11}$   $s^{-1}$ . In the theory of FMR the dynamic Landau-Lifshitz-Gilbert (LLG) equation is linearized and the solution is being sought as a linear dynamic response to the small perturbation in terms of the trigonometric functions proportional to that of the external excitation. However, at this timescale the system is in a dynamical regime, and if the external perturbation is not small, it possesses many characteristics inherent to the dynamics of nonlinear systems.

Typical magnetometer measurements of the magnetization response to external fields are on the opposite end of the timescale range. At this scale, the frequency of excitation is much smaller than that of precession frequency or the typical inverse relaxation time, determined by the damping parameter. From the computational point of view, the corresponding response could be calculated in the stationary approximation, i.e. minimizing the total magnetic energy at each external magnetic field value. The intermediate timescale corresponds to that of the adiabatic dynamics in which the dynamical information could be taken on average. In this regime the precession time is faster than the external perturbation, but the relaxation is not

<sup>3</sup>based on author's work Ref. [Usatenko 06]

fast enough to consider the system as stationary at each point. An example of such dynamics is illustrated in Fig. 2.11. One of the attempts to describe the adiabatic dynamics of single domain particles is due to G. Bertotti et al. [Bertotti 04], who calculated a slow magnetic energy variation in the presence of constant applied field.

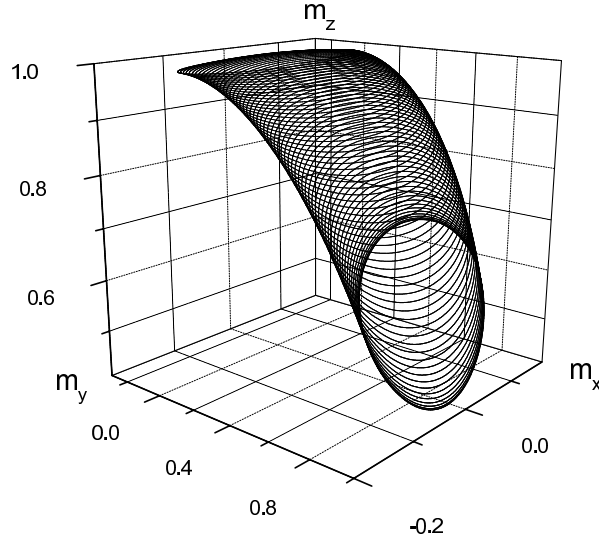


**Figure 2.11:** The adiabatic dynamics of single domain particle without friction in the slowly varying perpendicular magnetic field  $H_x = H_0 \sin(\pi t/T)$ ,  $H_y = H_z = 0$ , with  $H_0 = 0.8$ ,  $T = 200$ ,  $t \in [0, 100]$  with initial conditions  $m_x = 0.15$ ,  $m_y = 0$  and  $m_z = 0.99$ .

We study the motion of a single domain particle under an adiabatically varying magnetic field in the small amplitude approximation. The system is the same described in the previous section, but in this case the position of the minimum will also slowly change with time and the equations,

$$2H \sin(\vartheta - \vartheta_H) + \sin 2\vartheta = 0, \quad \varphi = 0 \quad (2.50)$$

determine the coordinates  $(\vartheta_0, \varphi_0)$  of the stationary points, including minima. The number of minima is two if the applied field is less than the critical field determined by the Stoner-Wohlfarth astroid [Stoner 48] and only one if it does not.

In this case the amplitude of precession  $a$  is no more constant. It can be found from the Eqs. (2.44) and (2.45) in a linear approximation and the supposition that the applied field is a slow varying function of time, i.e  $\dot{H} \sim \epsilon H$  with  $\epsilon \ll \sqrt{AB}$ . Consequently,  $A$  and  $B$  are also slowly varying functions of time. The solution for the magnetic moment motion is then:

$$\begin{aligned} m'_x &= a \cos \Phi, & m'_y &= \frac{a\dot{\Phi}}{A} \left( 1 + \frac{\dot{\vartheta}_0}{A} \right) \sin \Phi \\ &+ \left[ \frac{\alpha}{2} \left( 1 - \frac{B}{A} \right) + \frac{\dot{A}}{4A^2} \right] a \cos \Phi, & m'_z &\cong 1, \end{aligned} \quad (2.51)$$

$$a = \sqrt{\frac{IA}{\dot{\Phi}}} \exp\left(-\frac{\alpha}{2} \int_{t_0}^t (A+B) dt\right), \quad (2.52)$$

$$\dot{\Phi}^2 = AB - \frac{\alpha^2}{4}(A-B)^2 - (A+B)\dot{\vartheta}_0 + \mathcal{O}(\epsilon\alpha A)$$

where  $I$  is a constant dependent of the initial conditions. The quantity  $\dot{\Phi}^2$  is the square of the instantaneous frequency of rotations and its first term,  $\omega = \sqrt{AB}$ , is the ferromagnetic resonance frequency, the second term represents the renormalization by the friction. The third term is a geometrical Berry-Hannay [Berry 85] phase that depends on the trajectory. In order to know the current phase, we need to know the trajectory in the space of parameters and even in the case of equal initial and final applied fields (case that includes a periodic applied field) there will be an additional phase in the moment motion.

The adiabaticity condition that the variation of the field has to be less than the ferromagnetic resonance frequency can be rewritten as  $\epsilon \ll \sqrt{AB} = \omega$ . However, the variable magnetic field contains two components in the plane and can be dependent on two adiabatic parameters having different rates of variation. Therefore, the former inequality must be complemented by the additional conditions  $|\dot{\vartheta}_0| \ll |A|$ ,  $|\dot{\vartheta}_0| \ll |B|$ .

### 2.3.3 Short-time thermal description: stochastic LLG equations

From a general point of view, the dynamics of a system described by the variable  $X$  in contact with a heat bath of temperature  $T$  are called Langevin dynamics(LD) and are described by the stochastic equations:

$$\frac{dX}{dt} = a(X, t) + b(X, t)\eta(t) \quad (2.53)$$

where  $\eta(t)$  is the noise term,  $a(X, t)$  the drift and  $b(X, t)$  the diffusion term.

In the magnetic systems it is customary to introduce thermal fluctuations as additional random field  $\mathbf{H}_{th}$ . The noise is supposed to be uncorrelated in time due to the fact that magnons are slower than phonons. It can be proven [Chubykalo 03b] that there are no correlations between components  $x,y,z$  and different particles. Therefore, the thermal field  $\mathbf{H}_{th}$  is a gaussian distributed noise with the following properties:

$$\langle H_{th,i} \rangle = 0 \quad (2.54)$$

$$\langle H_{th,i}(t)H_{th,j}(t') \rangle = \sigma\delta_{ij}\delta(t-t') \quad (2.55)$$

The fluctuation-dissipation theory, which states that the system response to an external excitation is equal to the response to a fluctuation, yields a value  $\sigma = 2\alpha k_B T / M_S V (1 + \alpha^2)$  [Brown 63b] that explicitly depends on  $\alpha$ .

The stochastic equation has to be numerically integrated. The general noise is represented by a function  $W_k$ , which is continuous everywhere but not differentiable and its integral  $\Delta W_k = \int_t^{t+\Delta t} W_k$  can not be interpreted as a calculus integration. In the stochastic LLG equation this variable is the thermal field. The implementation of the integration gives rise to different calculi: the use of the value at the beginning of the step is known as Ito stochastic calculus and a midpoint integration as Stratonovich stochastic calculus and other implementations are also possible. Between the different schemes to integrate the stochastic equation, it has been argued that only the Heun scheme, which implies a midpoint integration and will be used here, gives the proper thermal properties [García-Palacios 98]. Posteriorly, D. Berkov [Berkov 02] demonstrated that in cartesian coordinates all the schemes are equivalent because a normalization is needed after each step in order to conserve the magnitude. E. Martínez et al. [Martínez 04] arrived to an equivalent conclusion in spherical coordinates. The Heun scheme is a predictor-corrector method. The first step or predictor is

$$\bar{M}_i = M_i(t) + a_i(\mathbf{M}, t)\Delta t + b_{ik}(\mathbf{M}, t)\Delta W_k \quad (2.56)$$

and the second or corrector is

$$M_i(t + \Delta t) = M_i(t) + \frac{1}{2} [a_i(\bar{\mathbf{M}}, t + \Delta t) + a_i(\mathbf{M}, t)] \Delta t + \frac{1}{2} [b_{ik}(\bar{\mathbf{M}}, t + \Delta t) + b_{ik}(\mathbf{M}, t)] \Delta W_k. \quad (2.57)$$

The magnetization value will correspond in average to a minimum, but its actual position never rests in the minimum, the position that would reach without the thermal fluctuations. The numerical integration of the stochastic LLG equation does not allow, similar to its deterministic equivalent, simulation times larger than few nanoseconds and has also the inconvenience that prevents the use of advanced numerical schemes used in ordinary differential equations. Nevertheless, new schemes have been recently suggested [Martínez 07], which allow a longer timestep. The inclusion of the temperature in the micromagnetism is not straightforward and is focus of much interest. Namely, the micromagnetic integration of the stochastic LLG shows strong dependence on the discretization length [Tsiantos 02] and results in an overestimation of the Curie temperature [Grinstein 03].

### 2.3.4 Long-time behavior: Arrhenius-Néel law

Thermal fluctuations cause a random walk of the system in a multidimensional energy space, which ultimately produces a decay of the initial magnetization state. If the value of the thermal energy is comparable to the relevant energy barriers the system will be unstable and will randomly oscillate between the energy minima, presenting superparamagnetism. If this energy is small compared to the energy barrier value, the magnetization will stay in a local minimum during many precession periods and eventually will surmount the energy crest separating two energy minima and appear in the valley of another minimum. This phenomenon is known as thermal activation and is always present in any finite temperature experiment [Basso 00]. Due to the fact that the thermal switching over large energy barriers occurs rarely, the switching events are also known as infrequent events. Thermal activation can be also responsible for domain wall motion on pinning potentials due to defects [Chen 99]. The magnetization thermal stability poses an important problem and is a limitation from the point of view of magnetic-based technologies such as MRAM and magnetic recording. Due to this, the study of thermal activation is a subject of current interest. Moreover, the thermal activation is important in order to understand the magnetic relaxation and the dynamical coercivity phenomena from a fundamental point of view.

In the most general case, when temperature fluctuations are small as compared to energy barriers, the probability of magnetic switching is governed by the Arrhenius-Néel law:

$$f = f_0 \exp(-\Delta E/k_B T). \quad (2.58)$$

The prefactor  $f_0$  is known as the attempt frequency and its inverse as switching time  $\tau = 1/f_0$  constant and has a value between  $f_0 = 10^9 \text{ Hz}$  and  $f_0 = 10^{11} \text{ Hz}$  for magnetic systems.  $\Delta E$  is the energy barrier and its value is the energy of the saddle point minus the energy at the minimum. In a Stoner-Wohlfarth particle the energy barrier is  $\Delta E = KV$ , but in the general case, the calculation has to be done numerically in a multidimensional space (see Section 2.3.6). In experiments the attempt frequency is often taken as constant, but in general  $f_0 = f_0(T, H, V, \alpha)$ .

To calculate the prefactor we need some simplifications. The Transition State Theory (TST) simplifies the thermodynamics of the system assuming that the trajectories pass through the saddle point. This theory has its origin in chemical reaction kinetics and was originally developed by H. Kramers [Kramers 40], who demonstrated that the prefactor can be calculated from the probability diffusion equation or Fokker-Planck equation (FPE). Due to this, the original energy minimum is known as reactive state and the final minimum as product state. The first evaluation in a magnetic system was for a single domain particles with uniaxial

anisotropy and applied field parallel to the easy axis [Brown 63b]. In this case an asymptotic analytical expression was obtained from the smallest eigenvalue of the FPE equation:

$$\frac{1}{\tau} = \frac{2K^{3/2}V^{1/2}\alpha\gamma}{M_s(1+\alpha^2)(k_B T\pi)^{1/2}}(1-h^2)\left\{(1+h)\exp\left[-\frac{KV(1+h)^2}{k_B T}\right]+(1-h)\exp\left[-\frac{KV(1-h)^2}{k_B T}\right]\right\} \quad (2.59)$$

Posteriorly, additional eigenvalues of the FPE equation were evaluated for a more accurate attempt frequency of a single domain particle [Coffey 95b] and applied field not parallel to the easy axis was included [Coffey 95a].

For a general system and Intermediate to High Damping (IHD) case Langer developed an expression for the escape rate [Langer 68]:

$$\frac{1}{\tau} = \frac{\mathcal{V}}{(2\pi)^{3/2}(k_B T)^{1/2}} \frac{|k|}{\sqrt{|\lambda_-|}} \prod_l \sqrt{\lambda_l^m} \prod_n \frac{1}{\sqrt{\lambda_n}} \exp\left(-\frac{\Delta E}{k_B T}\right) \quad (2.60)$$

where  $\lambda_l^m$  are the eigenvalues of the energy Hessian (matrix of second derivatives of the energy function) at the initial minimum,  $\lambda_-$  is the negative eigenvalue of the Hessian at the saddle point,  $\lambda_n$  are the positive eigenvalues of the Hessian at the saddle point,  $k$  is a dynamical term calculated linearizing the LLG equation and  $\mathcal{V}$  is the volume of the saddle-point subspace. The volume  $\mathcal{V}$  gives the correct escape rate in the cases where symmetry exists (e.g. axial symmetry). Thus, the evaluation of the prefactor requires the calculation of the eigenvalues of the energy Hessian at the initial state and at the saddle point, and, again, except for simple systems it has to be calculated numerically. The general procedure to do this is to find the points where the energy gradient vanishes and then to find the nature of the stationary points. This calculation is affordable in small systems only and methods have been developed to overcome this problem [Chubykalo-Fesenko 05].

### 2.3.5 Monte Carlo methods

The Monte Carlo Metropolis method has been widely used to obtain the equilibrium properties of a physical system in contact with a heat bath of temperature  $T$  [Binder 97]. Ising models with Monte Carlo constitute an ideal system from both learning and modeling point of view. In localized moments approximation the method has been used in conjunction with Heisenberg models [Hinze 98] and antiferromagnetism is studied with the same tools [Acharyya 00]. The method makes changes in the configuration and accept or reject the new configuration according to some probability based on the Boltzmann statistics. One iteration of this algorithm is called a Monte Carlo (MC) step. The method is known as Metropolis Monte Carlo method. The Metropolis Monte Carlo simulations generate configurations

with the system variables values according to the Boltzmann distribution, obtaining the equilibrium properties from the average of the configurations. However, the Monte Carlo method is also a viable method to obtain nonequilibrium properties. A classical example is the random walk of a Newtonian particle with thermal fluctuations. In magnetism the Metropolis method has been used to study the thermally induced magnetic collective magnetization relaxation [González 95]. The dynamics of magnetic systems with MC method do not consider the precession of the magnetic moment. The method will accept a configuration that decreases the energy but the moment will not describe the correct precession. Accordingly, the MC method will fail to describe the dynamics in the situations in which the precession is important and will succeed in case where it is not. This way we can expect good results of the method in cases of high temperature or large damping, where the diffusion prevails over the precession. Moreover, the MC step has not an associated timestep. To solve this problem the Time Quantified Metropolis Monte Carlo (TQMC) algorithm [Nowak 00, Chubykalo 03a] has been proposed. The main relation of TQMC is

$$R^2 = \frac{20k_b T \alpha \gamma}{(1 + \alpha^2) M_s V} \Delta t \quad (2.61)$$

where  $R$  is the radius of the cone around the current moment position inside which the trial moment lays and  $\Delta t$  is the equivalent timestep of the MC step. This timestep has to be chosen less than the characteristic time scale of the relaxation. From Eq. (2.61) it is clear that the advantage of this method is the possibility to increase the timestep with smaller temperatures that need a longer simulations in LD simulations. However, the associated acceleration is linearly proportional to  $KV$ , while an exponential acceleration is desirable, according to the Arrhenius-Néel law (2.58). More recently, X. Cheng et al. [Cheng 06] have reported a similar method that preserves the precession of the magnetic moment. To calibrate the timestep of the Monte Carlo step X. Cheng used the Fokker-Planck equation instead of a direct mapping to the Langevin dynamics. Nevertheless, if the magnetization precession has to be taken into account, the timestep associated with MC in this case is of the order of the timestep for the LD simulations.

A more successful method to calculate long time thermal magnetization dynamics is the Kinetic Monte Carlo method known in magnetism sometimes as Charap method [Kanai 91]. The method evaluates the rate of all the reversal modes, which link the minimum where the magnetization is presently located with other minimum in the system, and chooses the mode according to the probability:

$$P_i(t)dt = f_i \exp(-f_i t) dt \quad (2.62)$$

where  $f_i = 1/\tau_i$  is the rate and  $\tau_i$  is the time constant for the reversal mode  $i$ . The method requires the evaluation of the saddle point and the energy barrier for

each reversal mode. The method originally proposed by Charap calculated the switching rates of the reversal of the individual moments. This approach neglects the possible collective reversal modes appearing in strongly interacting systems. This was overcome by O. Chubykalo et al. [Chubykalo-Fesenko 05], who suggested an algorithm based on the combination of Langevin dynamics and Metropolis Monte Carlo in order to explore the possible reversal modes and used it to evaluate the stability of granular longitudinal magnetic recording media. Due to the exponential nature of the Arrhenius-Néel law used to calculate the switching rates, this method can predict the thermal relaxation in years scales.

### 2.3.6 Energy barriers calculations<sup>4</sup>

As exposed in the previous sections the determination of the stability of the magnetic materials needs the evaluation of the energy barrier or equivalently to find the relevant saddle point of the magnetic system. Numerical evaluation of the energy barrier should be done in a multidimensional space and is a difficult problem, especially when collective reversal modes are involved. The calculation of the energy barrier normally involves the search of the minimum energy path, a continuous path that joins two minima and provides the shortest path. An evaluation of energy barrier minimizing the action along the path was suggested in Ref. [Berkov 98]. In chemical physics the problem has been amply studied and several methods have been used, most of them based on elastic band method, an improved version of which is the Nudged Elastic Band method (NEB) that was first applied to the study of the adsorption of hydrogen on Cu surfaces [Mills 95]. In magnetic systems, the use of the nudged elastic band method has been extensively studied in nano-sized systems on the basis of the micromagnetic description [Dittrich 02, Suess 05]. The method uses a series of images, which move parallel to the  $-grad E$  direction, and introduces elastic constants between them. The later is done in order to maintain the separation between the images that otherwise accumulate near the minima resulting in a bad resolution of the saddle point. The saddle point is interpolated from the position of the nearest images, therefore, this kind of methods is known as interpolation methods.

In this thesis the method of the Lagrangian multiplier is used to determine energy barriers. This method can be used in simple magnetic elements such as nano-sized magnetic grains, particles, dots, wires etc. In these systems the occurrence of only one or several reversal modes could be expected. Consequently, the multidimensional space could be parametrized as a function of one “reaction coordinate”, as, for example, average magnetization vector. Previously, this method has been

---

<sup>4</sup>based on author's work Ref. [Paz 07]

proposed and successfully applied to determine the effective energy landscape and energy barriers of small magnetic particles with surface anisotropy [Garanin 03]. The implementation of the method on the basis of existing codes with energy minimization, using, for example, the Landau-Lifshitz-Gilbert equation integration is much simpler than that of the previously reported calculations of energy barriers using the nudged elastic band method. We have implemented the method on the basis of both micromagnetic and atomistic formalisms.

The method consists in projection of multidimensional energy landscape on one or several coordinates by guessing the character of the possible reversal mode. For example, in the case of small particles with surface anisotropy, dominated by the exchange interactions [Garanin 03], one can expect the type of the behavior corresponding to the rotation of the particle macrospin as the whole, so that the multidimensional space has been “projected” into one unit magnetization vector  $\boldsymbol{\nu}_0(\theta_0, \varphi_0)$ . This is done by adding to the total energy one more term,  $-N\boldsymbol{\lambda} \cdot (\boldsymbol{\nu} - \boldsymbol{\nu}_0)$ , where  $\boldsymbol{\lambda}$  is the Lagrangian multiplier,  $\boldsymbol{\nu}$  is the particle average magnetization direction:  $\boldsymbol{\nu} = \sum \mathbf{m}_i / |\sum \mathbf{m}_i|$ ,  $\mathbf{m}_i$  is the individual local magnetic spins and  $N$  is the number of spins inside the particle. This term produces an additional field and, therefore, the total magnetization is biased in the direction  $\boldsymbol{\nu}_0(\theta_0, \varphi_0)$ . To find the conditional minimum the total system magnetic energy is augmented with the Lagrangian multiplier term and its corresponding effective local field calculated from  $\mathbf{h}_i = -\partial E / \partial \mathbf{m}_i$ . The Landau-Lifshitz-Gilbert equations of motion for each individual spin without the precessional term is solved and concurrently one should add to them also three equations for the Lagrangian multiplier components:  $\dot{\boldsymbol{\lambda}} = \partial E / \partial \boldsymbol{\lambda}$ . The stationary points found in this approach are also the stationary points of the original Hamiltonian. However, if the system has many metastable states, only part of these points, compatible with the behavior assumed by the biased direction would be found. The method can produce highly non-collinear multidimensional stationary points.

The method allows to calculate the effective energy landscape for nanoelements in terms of the biased direction  $\boldsymbol{\nu}_0(\theta_0, \varphi_0)$ . An example of such a landscape is presented in Fig. 2.12 for a cylindrical magnetic grain, implemented on the basis of micromagnetic model with parameters corresponding to Fe with cubic anisotropy  $K = 50000 \text{ J/m}^3$ , the exchange parameter  $A = 8.3 \cdot 10^{-12} \text{ J/m}$  and the saturation magnetization value  $M_s = 2.15 \text{ T}$ . It is clearly seen that in this case there is a competition between magnetocrystalline and shape anisotropies.

The saddle point could be found as the one of the effective energy landscape. Alternatively, we notice that the stationary points coincide with the condition:  $|\boldsymbol{\lambda} \times \boldsymbol{\nu}_0| = 0$  and, therefore, they can be found minimizing the functional  $F(\theta_0, \varphi_0) = |\boldsymbol{\lambda}(\theta_0, \varphi_0) \times \boldsymbol{\nu}(\theta_0, \varphi_0)|$ , where  $\boldsymbol{\nu}(\theta_0, \varphi_0)$  is found as a result of the conditional minimization procedure, described above.

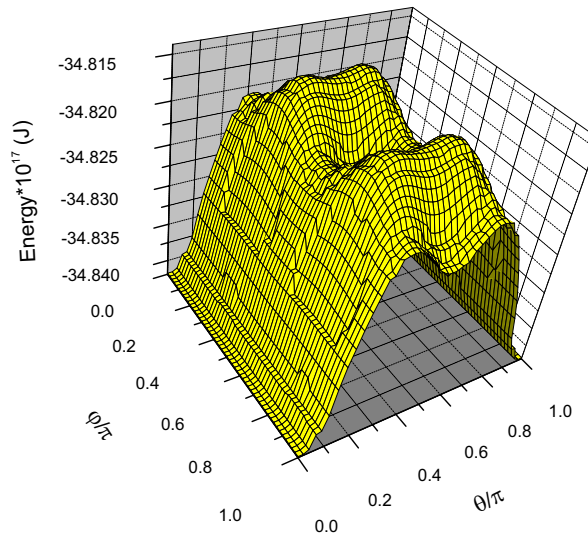


**Figure 2.12:** Effective energy landscape of an Fe cylindrical particle with the radius  $r = 5 \text{ nm}$  and the height  $h = 10 \text{ nm}$ .

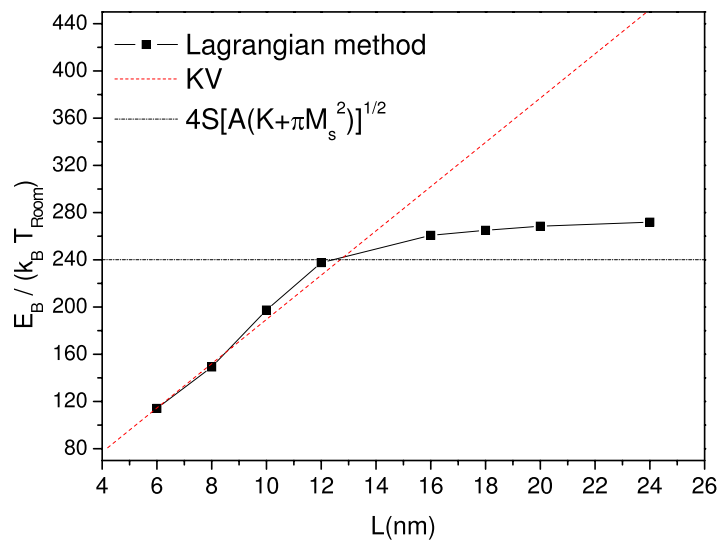


**Figure 2.13:** Energy barriers vs elongation of an isolated grain of FePt with a basis size of  $S = 6 \text{ nm} \times 6 \text{ nm}$

To illustrate the performance of the method, we have calculated the energy barriers of FePt rectangular magnetic grains as a function of their elongation. The general idea of these calculations is the same as in Ref. [Forster 03], however, the high-anisotropy grain was implemented on the basis of atomistic calculations with correct lattice structure and the Heisenberg exchange rather than finite element micromagnetic simulations. The parameters used for calculations were that corresponding to FePt: the anisotropy value  $K = 2 \cdot 10^7 \text{ erg/cm}^3$  and the saturation magnetization

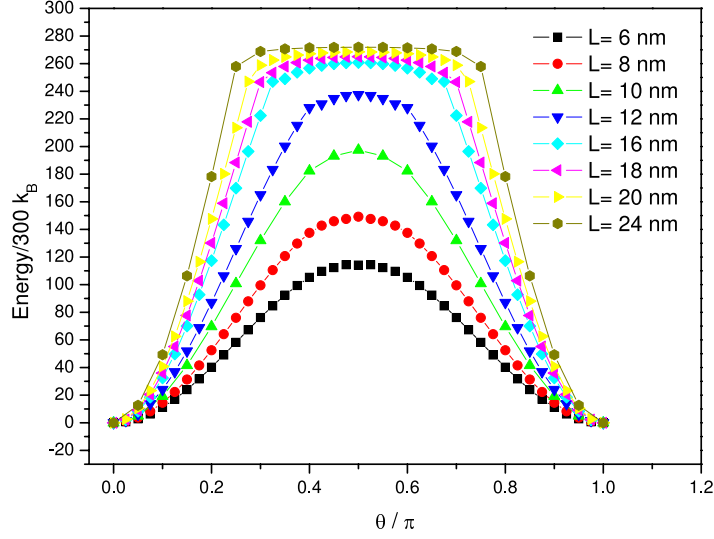


**Figure 2.14:** Effective energy as a function of the coordinate  $\theta$  ( $\nu_z = \cos \theta$ ) in an isolated grain of FePt with a basis size of  $S = 6 \text{ nm} \times 6 \text{ nm}$  and different lengths  $L$ .

$M_s = 1100 \text{ emu/cm}^3$ , the Heisenberg exchange constant  $J = 7.7 \cdot 10^{-14} \text{ erg}$ , the lattice parameters  $a = b = 0.272 \text{ nm}$  and  $c = 0.385 \text{ nm}$ . Fig. 2.13 represents energy barriers of an isolated grain with basis size  $S = 6 \text{ nm} \times 6 \text{ nm}$  as a function of elongation  $L$  and the corresponding effective energies obtained from the method as shown in Fig. 2.14. The configurations of the saddle points are presented in Figs. 2.15 (a-c). Varying the grain height, we have observed how the configuration of the saddle point changes from that corresponding to coherent rotation (the energy barrier value proportional to system volume) to the one related to the domain wall propagation (the energy barrier value independent on the system volume). The domain wall presence can be observed in Fig. 2.14 as a plateau in the effective energy because the energy of the domain wall is almost independent of the domain wall center position (as long as its center is far from the grain borders). The critical system size for which the propagation rather than that rotation mode occurs was determined in this case as  $12 \text{ nm}$ . The energy barrier tends to saturate to the domain wall energy. In the absence of the dipolar interaction this energy is  $E_{DW} = 4S\sqrt{AK}$ . The domain wall energy in this system will be determined mainly by the anisotropy and in order to compare with our results we can correct this value with the contribution of the ideal shape anisotropy of an infinite cylinder but its value has to be calculated numerically. The obtained values are in good agreement with  $E_{DW} = 4S[A(K + \pi M_s^2)]^{1/2}$  as can be seen in Fig. 2.13.

We should note here that the determination of the energy barriers in this method is based on the initial guess of the possible mode. The saddle point of the system may be not compatible with the condition assumed by the Lagrangian multiplier

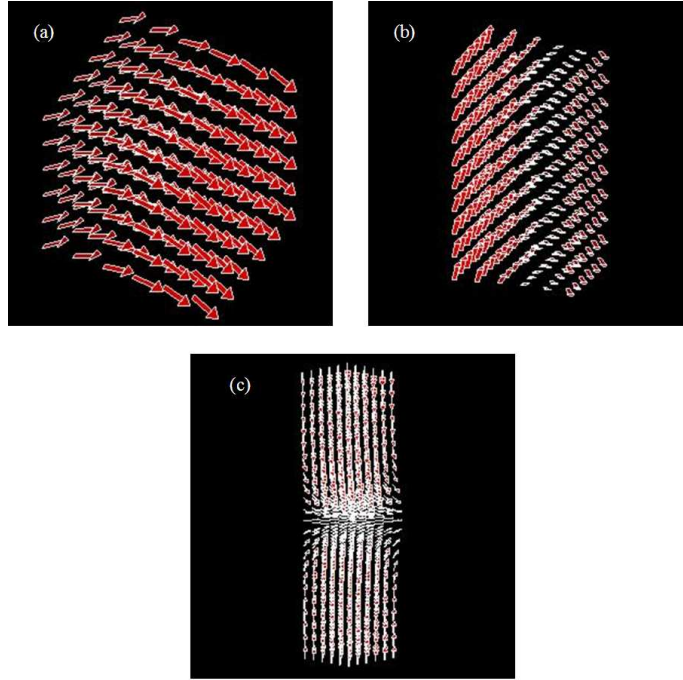


**Figure 2.15:** Configurations of the saddle points of an FePt particle with a basis size of  $S = 6 \text{ nm} \times 6 \text{ nm}$  and various elongations (a)  $L = 6 \text{ nm}$ , (b)  $L = 10 \text{ nm}$  and (c)  $L = 24 \text{ nm}$ .

term. In practice, the obtained point should be checked to fulfill the condition  $|\boldsymbol{\lambda} \times \boldsymbol{\nu}| = 0$ . In the opposite case the obtained effective energy landscape will not have stationary points. An example of this is the case of two equal grains coupled with phenomenological exchange parameter  $J_s$ . In the small coupling case, the use of the method with one single Lagrangian multiplier produces energy graph with a sharp peak instead of the saddle point. Alternatively, the method fails when the effective energy plot as a function of chosen parametrization coordinates, presents a sudden jump. We can compare these situations to the effective energy plots of Fig. 2.14 where the saddle point is obtained from a continuously differentiable curve. The failure of the method happens often as a consequence of the projection of a multidimensional space to only several degrees of freedom which produces a hysteresis in the energy minimization procedure.

In the case of two weakly coupled grains the best parametrization of the saddle point is the use of two Lagrangian multipliers, adding to the total energy the term:  $-N_1 \boldsymbol{\lambda}_1 \cdot (\boldsymbol{\nu}_1 - \boldsymbol{\nu}_{0,1}) - N_2 \boldsymbol{\lambda}_2 \cdot (\boldsymbol{\nu}_2 - \boldsymbol{\nu}_{0,2})$ , where  $N_i$  is the number of spins in the grain  $i$  and  $\boldsymbol{\nu}_i = \sum \mathbf{m}_j^i / |\sum \mathbf{m}_j^i|$  is the normalized magnetization vector of the  $i$ -th grain. This way, we obtain the effective energy contours of two FePt grains of dimension  $6 \text{ nm} \times 6 \text{ nm} \times 7.5 \text{ nm}$  as shown in Fig. 2.16 (a-b). For small values of the interfacial exchange parameter  $J_s$ , see Fig. 2.16 (a), we can observe the existence of

four minima, corresponding to the magnetization of each grain in the two possible opposite directions, which indicates almost independent reversal of the grains. Fig. 2.16 (b) represents the effective energy for values of  $J_s$  close to full coupling. In this case there are two minima and only one value of energy barrier corresponding to the two equivalent saddle points of the effective energy. Although the contour plots look similar to the case of two interacting magnetic moments, the saddle point configurations correspond to domain-wall structures pinned at the interface similar to Fig. 2.15(c).

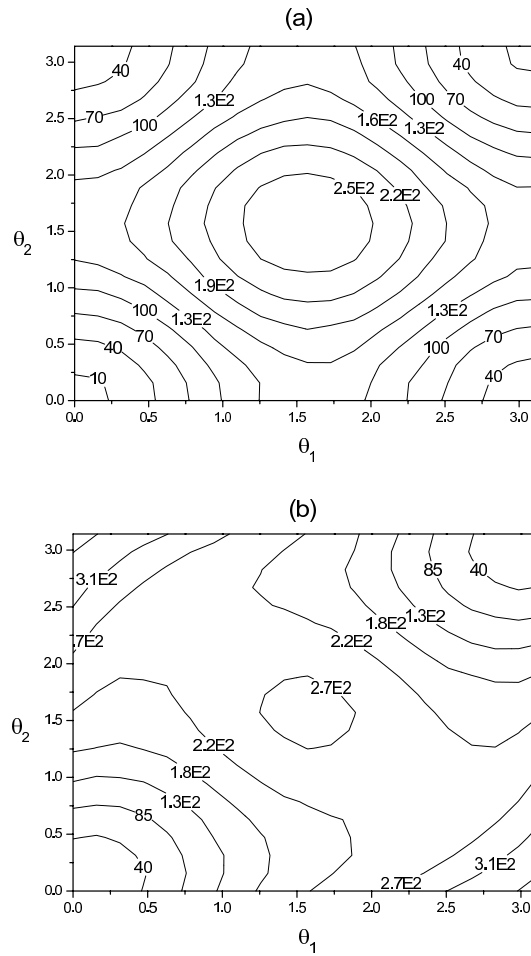


**Figure 2.16:** Contours of the effective energy (in terms of  $k_B T_{Room}$ ) as a function of the coordinates  $\theta_1, \theta_2$  (polar angles of average magnetization) of two exchange-coupled FePt grains with small  $J_s/J = 0.01$  (a) and almost full  $J_s/J = 0.8$  (b) exchange coupling strengths.

In conclusion, the method of the Lagrangian multiplier suggested in Ref. [Garanin 03] for evaluation of energy barriers in small particles with non-collinear structures has been successfully generalized for more complicated systems such as magnetic grains or dots. The method could be very useful in situations where

simple and unique reversal modes are expected and in the case that one can provide a suitable choice of parametrization of complicated multidimensional point in terms of several coordinates. Generally speaking, the same to some extent is true for the elastic band method [Dittrich 02], where one specifies the sense of direction of initial rotation. As for the potential to determine the possible reversal mode, provided that the initial guess is known, the elastic band method seems to be less restrictive. In other complicated situations where many metastable states with possible transitions between them exist, the method suggested in Ref. [Chubykalo-Fesenko 05], which uses the temperature acceleration to produce an initial reversal mode guess, seems to be a good choice.

### 2.3.7 Acceleration methods: Victora and Voter methods

In the following sections two different methods to extend the simulation time scale will be analyzed. The methods consists of the extrapolation of Langevin dynamics obtained in a short simulated time to a longer interval. Both methods need additional simulations and the effort of these simulations will determine the real performance of the method. This is specially true in the case of Voter method. We have checked in both cases the validity of the extrapolation in some simple cases.

### 2.3.8 Victora method<sup>5</sup>

In the cases where neither the energy barrier nor the attempt frequency is a function of the temperature the Arrhenius-Néel law is a simple relation between temperature and the time elapsed in the considered thermally activated process. Larger temperature corresponds to smaller elapsed time and the inverse also holds true. However, in the Arrhenius-Néel law there are two factors that are not easy to calculate, the attempt frequency and the energy barrier. In the axially symmetric case the attempt frequency is temperature dependent, but in other less simple cases the prefactor will be weakly dependent on temperature. If this happens, we can use a set of four equations to eliminate the prefactor and the energy barrier value from the problem. Based on that, J. Xue et al. [Xue 00] proposed a method to obtain simulation for larger times, not achievable numerically, calculating only small time intervals at higher temperatures. The method is applied to the calculation of the hysteresis loops and, therefore, it is more convenient to express the time scales as the inverse of the applied field sweep rate.

The method is as follows: we simulate a loop at a reference temperature and at a reference sweep rate, being this reference sweep rate as slow as feasible. Next we

---

<sup>5</sup>based on author's work

try to find the temperature of the fast sweep rate loop that matches the reference loop. The different variables will be related by the formula

$$\frac{T_{s-l} - T_l}{T_{s-r} - T_r} = \frac{T_l \ln(R_s/R_l)}{T_r \ln(R_s/R_r)} \quad (2.63)$$

where  $T_{s-l}$  is the temperature to perform the equivalent loop,  $T_l$  the temperature for the large time scale,  $T_r$  the reference temperature,  $T_{s-r}$  the temperature obtained from the matching of the loops,  $R_s$  the small time scale sweep rate,  $R_l$  the large time scale sweep rate and  $R_r$  the reference sweep rate. Finally, we calculate a loop at high temperature  $T_{s-l}$  and fast sweep rate  $R_s$ . The result of this last simulation is equivalent, according to the method, to the direct calculation of the desired loop at temperature  $T_l$  and slow sweep rate  $R_l$ . The total elapsed time in our system may reach seconds, scaling the performed simulations at nanoseconds, at the cost of a manageable computational time.

We will check the method in a system of 2048 non-interacting grains with  $K = 2 \cdot 10^6 \text{ erg/cm}^3$  and  $M_s = 350 \text{ emu/cm}^3$ . The average grain is supposed to be cylindrical in shape with radius 14 nm and height 10 nm. Additionally, there is a gaussian deviation of easy axis angles with standard deviation  $SD = 5$  and a gaussian deviation of volume centered in average volume and  $SD/V_{av} = 0.1$ . For the LLG integration we take the damping constant  $\alpha = 0.05$  and the timestep  $\Delta\tau = 0.01$  (in precessional period units). Every loop is the average of three loops in order to improve statistics. Our goal is to simulate a loop with a sweep rate  $R_l = 50 \text{ Oe/s}$  and temperature  $T_l = 300 \text{ K}$ .

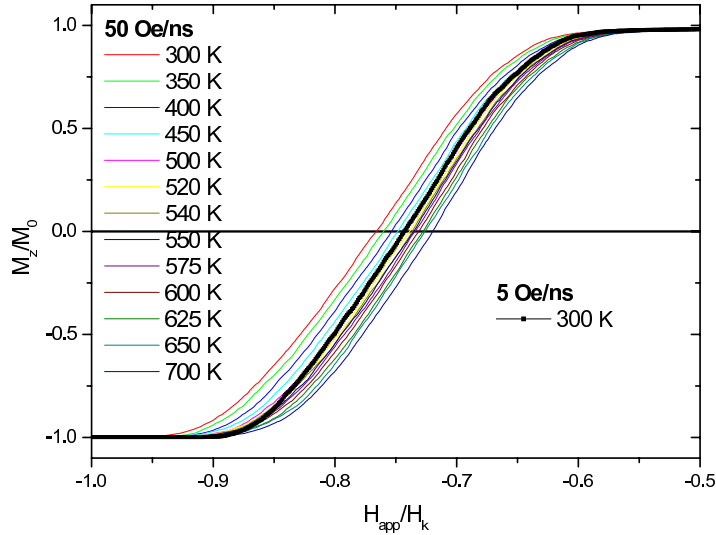


**Figure 2.17:** Hysteresis loops for the reference time scale,  $R_l = 5 \text{ Oe/ns}$ , and for the small time scale,  $R_s = 50 \text{ Oe/ns}$ , and different temperatures.

First, we calculate the hysteresis loop at reference time scale. In this case we

choose  $T_r = 300\text{ K}$  and  $R_r = 5\text{ Oe/ns}$ . Then we look for the small time scale loop  $R_s = 50\text{ Oe/ns}$  that best matches to the previous one. In the Fig. 2.17 it is found to be  $500\text{ K}$  loop, that is  $T_{s-r} = 500\text{ K}$ . From the Eq. (2.63) we obtain  $T_{s-l} = 2100\text{ K}$ . The method prediction for the loop of  $300\text{ K}$  and  $50\text{ Oe/s}$  is the simulation of the loop for  $2100\text{ K}$  and  $50\text{ Oe/ns}$ .

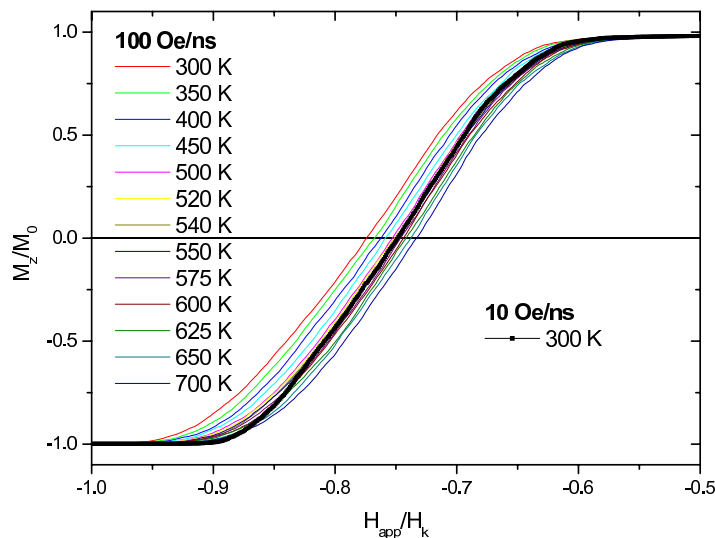


**Figure 2.18:** Hysteresis loops for the reference time scale,  $R_l = 10\text{ Oe/ns}$ , and for the small time scale,  $R_s = 100\text{ Oe/ns}$ , and different temperatures.

We can also try a different set of parameters to check the consistency. For example the reference time scale  $R_r = 10\text{ Oe/ns}$  and short time scale  $T_r = 100\text{ Oe/ns}$ . From the Fig. 2.18 we can extract  $T_{s-r} = 540\text{ K}$  and it yields  $T_{s-l} = 2532.5\text{ K}$ .

The loops resulting from the application of the method are shown in Fig. 2.19. The predicted  $H_c$  value from the  $R_s = 100\text{ Oe/ns}$  loops family is  $6797.26\text{ Oe}$  and from the  $R_s = 50\text{ Oe/ns}$  family is  $6865.83\text{ Oe}$ . There is good agreement between the values of coercivity in both set of parameters, however, we can not check them against simulations for the aimed time scales because the resulting computational time is far from being available.

The inverse problem can be used to check the method. If we use the reference time scale  $R_r = 10\text{ Oe/ns}$  and short time scale  $R_s = 100\text{ Oe/ns}$ , we can try to find the long time scale  $R_l$  that would match with one of the previous loops, for example  $700\text{ K}$ . That is to say what sweep rate has  $T_{s-l} = 700\text{ K}$ . The result is  $R_l = 2.15\text{ Oe/ns}$  and that time scale is reachable computationally. The results are shown in the Fig. 2.20.

The two loops should exactly match but we can see that the shapes differ specially near the saturation, although the switching fields agree reasonably. The predicted coercive field from the method is  $H_{c,pred} = 8385.6\text{ Oe}$  and the result from a direct

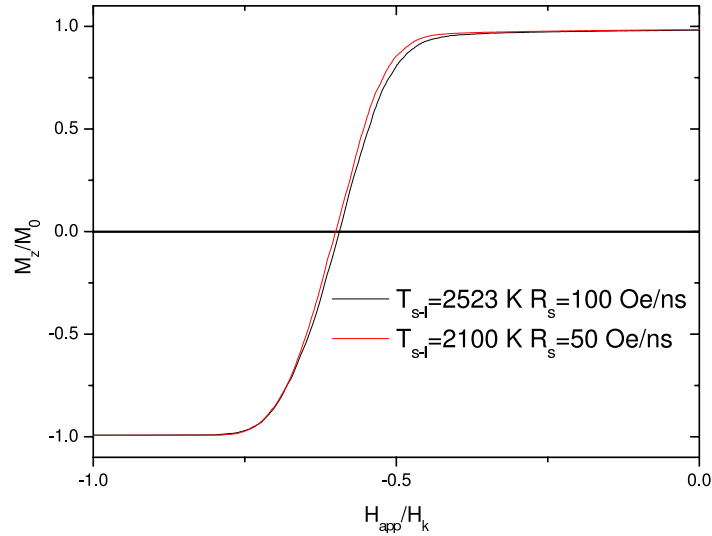


**Figure 2.19:** Comparison between the predictions of the method for  $R_l = 50 \text{ Oe/s}$  and temperature  $T_l = 300 \text{ K}$  for the same system with different values of  $R_s$ .

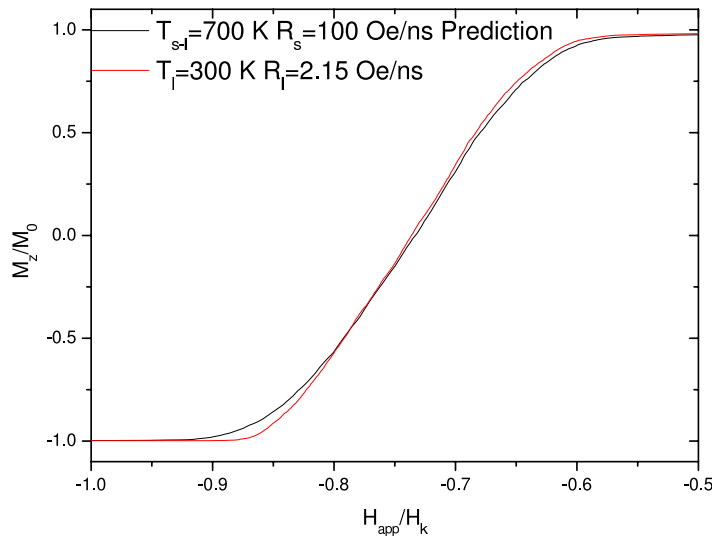


**Figure 2.20:** Comparison between the prediction of the method and the result from a standard simulation for a loop with  $R_l = 2.15 \text{ Oe/ns}$  and  $T_l = 300 \text{ K}$ .

LLG simulation  $H_c = 8422.86 \text{ Oe}$ .

The method allows to extend the reachable time scales several orders, although the method itself needs extra loops. The method has to be applied in a range of temperatures where the prefactor is constant or nearly constant. Basically, the method is a  $T \log(t)$  scaling [Labarta 93]. Although it is possible to obtain a quantitative agreement in coercivity, the method is not good in the nucleation field and in the near negative saturation, basically because the scaling law is not valid in these regimes.

### 2.3.9 Voter method<sup>6</sup>

The Voter method (also called “Hyperdynamics of the infrequent events”) was proposed in Refs. [Voter 97b, Voter 97a] and used to calculate the diffusional processes of Ag atoms on a Ag(111) surface, achieving an acceleration of the calculation up to 8000 times. For the first time we have applied the method to magnetic system and that is the motivation of the work presented in this section.

The method consists in modification of the external potential, basing on the Hessian energy matrix  $\partial^2 E/\partial x_i \partial x_j$ , where  $x_i$  are the system coordinates, so that the transition state (saddle point) remains unchanged. An additional external boost potential,  $\Delta V_b$  (see Fig. 2.21) is slowly switched on at the minimum, rising its value, and is switched off near the transition surface, i.e. where the first eigenvalue of the Hessian matrix  $\lambda_1$  becomes negative. This boost term is always positive making easier to escape from the potential minimum. The Langevin dynamics is then performed in this modified potential. The total time for the escape of the particle from the minimum can be evaluated as the sum of modified times at each timestep  $\Delta t_b$ , which could be computed from the Langevin dynamics timestep in the modified potential,  $\Delta t_{LD}$ , as the following:

$$\Delta t_b = \Delta t_{LD} \exp(\Delta V_b(t)/k_B T). \quad (2.64)$$

We have implemented the method for collection of non-interacting magnetic particles with external field applied at some angle to their anisotropy axis. According to the A.Voter’s suggestion, we have tried two forms of the boost potentials to accelerate the stochastic dynamical calculations:

$$\Delta V_{b1} = a\theta(\lambda_1)\lambda_1^2, \quad (2.65)$$

$$\Delta V_{b2} = b \frac{a\theta(\lambda_1)\lambda_1^2}{1 + 2a\theta(\lambda_1)\lambda_1^2}. \quad (2.66)$$

Here  $\theta$  is the standard Heaviside function and  $a$  and  $b$  are arbitrary parameters which could be tuned. On one hand, these parameters must be as large as possible to achieve the acceleration. On the other hand, the tuning of these parameters could be performed based on the fact that the equilibrium statistics should be achieved in the minimum, i.e. the number of LD time steps performed in the modified potential before the particle is escaped from the minimum must be large enough. The difference between the two potentials is that the second one, although more difficult to evaluate, produces much smoother modification and does not introduce a “crest” in the minimum, from which the particle could be scattered (see Fig. 2.21).

---

<sup>6</sup>based on author’s work Ref. [Chubykalo-Fesenko 04]

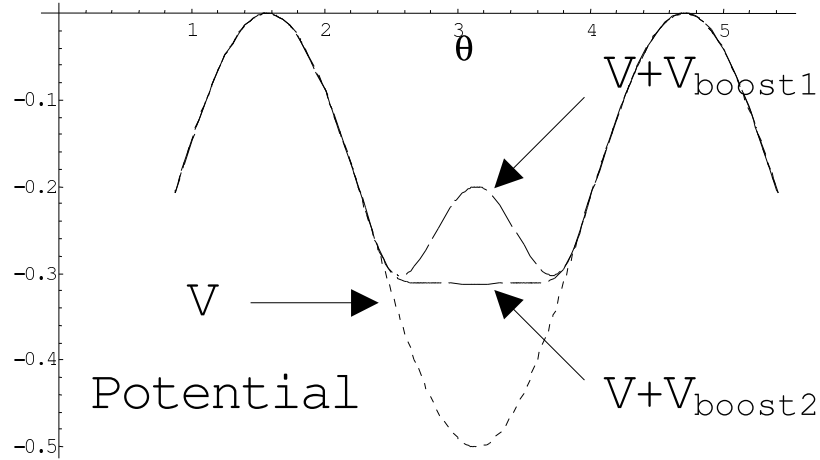


**Figure 2.21:** The initial potential for a magnetic moment, formula (2.43), and two possible boosting potentials (2.65) and (2.66), as function of magnetic moment angle  $\theta$  and in the absence of external applied field.

The implementation of the method requires the constant evaluation of the lowest eigenvalue of the correspondent Hessian matrix. The direct normal mode analysis is a time consuming procedure which depends strongly on the system size and would limit the acceleration achieved by the method. The direct evaluation of the eigenvalue problem scales like  $N^3$ , being  $N$  the number of moments in the system, whereas the number of operations in a Langevin dynamics steps scales like  $N$ . In order to obtain a good performance of the method, advanced methods that scale like  $N$  are desirable. The iterative methods, such as the Gauss-Siegel, which could use the previous value as initial guess, could be very helpful. A.Voter [Voter 97a] also suggested to replace the direct evaluation of  $\lambda_1$  by its approximate evaluation by means of the numerical minimization (with respect to the parameter  $s$ ) of the following expression:

$$\lambda^{num}(\mathbf{s}) = [E(\mathbf{x} + \eta\mathbf{s}) + E(\mathbf{x} - \eta\mathbf{s}) - 2E(\mathbf{x})]/\eta^2 \quad (2.67)$$

where  $\eta$  is a small parameter.

The averaged time for the particle to escape from the minimum is calculated using the A.Voter method and compared to that obtained from the direct integration of the LLG equation with a random term representing temperature fluctuations. Fig. 2.22 presents results of the calculations for switching time for an ensemble of uniaxial particles averaged over many realizations. The computation is stopped when the standard deviation from the average value is below 1%. It is clear that Voter's method for reasonable computational time is much faster than the direct LLG integration. Remarkably, the method reproduces correctly all the features

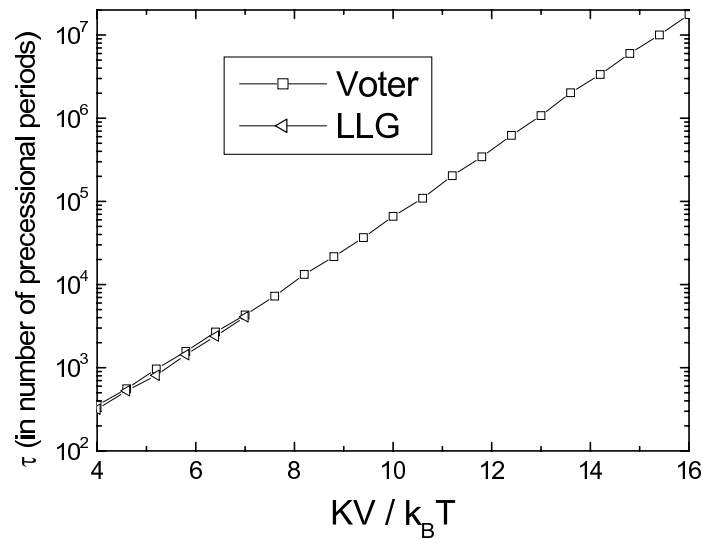


**Figure 2.22:** Switching time obtained with direct LLG calculations and with the Voter's method for a magnetic particle at zero applied field.

of the dynamics, including the precession. Fig. 2.23 presents the histogram for switching time of a particle for energy barrier value  $KV/k_B T = 4$ . It shows that the accelerated dynamics correctly reproduces the form of a  $t \exp(-t/\tau)$  distribution, where  $t$  is the reversal time, although the general tendency of the Voter distribution is the displacement to larger values.

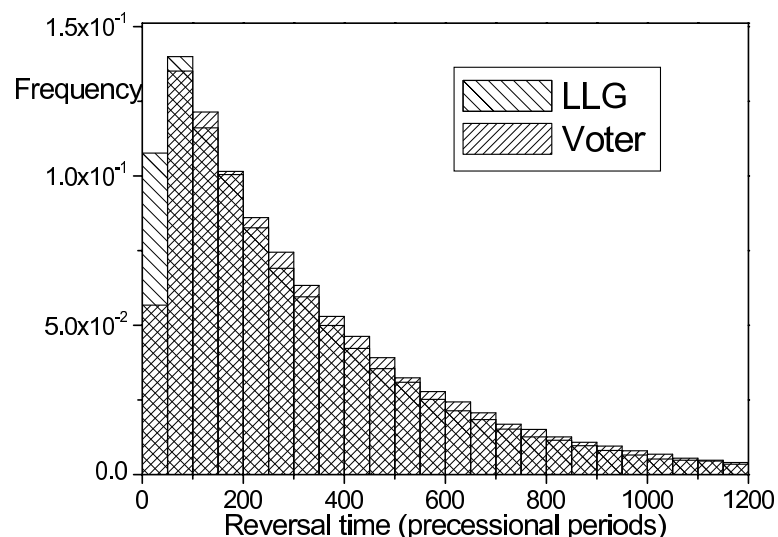


**Figure 2.23:** Histogram showing the distribution of reversal times for both LLG calculations and Voter's method with energy barrier value  $KV/k_B T = 4$ .

We have checked the results for different values of the damping parameters and different angles between the applied field and the anisotropy directions. Fig. 2.24

presents the results for an angle between the anisotropy direction and applied field of 45 degrees and for different values of the tuning parameter  $a$ . Therefore, unlike the TQMC method (see discussion in Section 2.3.5), the hyperdynamics method correctly reproduces the influence of the ellipticity of the precessional cone on the thermal switching statistics.

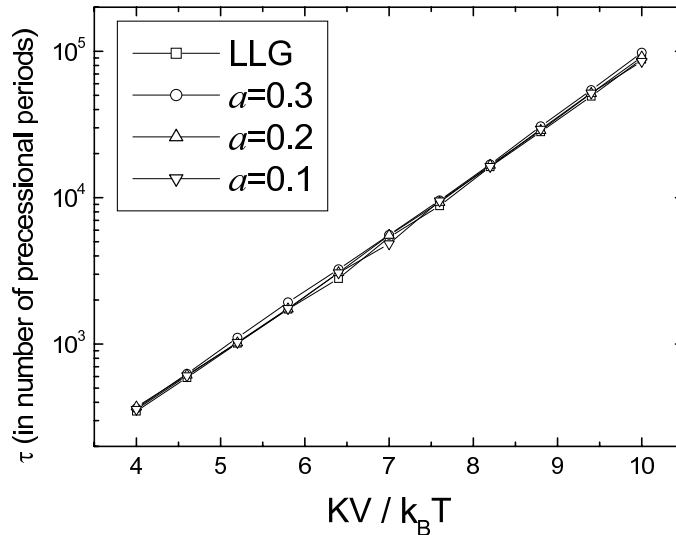


**Figure 2.24:** Average switching time for a magnetic moment with an applied field  $(0.2K/M_s, 0.2K/M_s, 0)$  and the easy axis parallel to  $z$  direction. Results for different values of parameter  $a$  are represented, as well as LLG direct calculations.

The real acceleration of the method depends on the efficiency to calculate the lowest eigenvalue of a complex large system. Therefore, for the small barriers case, the direct integration of the LLG equation is faster. To compare, we present in Fig. 2.25 the ratio between the average CPU time used in the Voter method (using direct lowest eigenvalue evaluation in system described by Eq. (2.67)) and the average CPU time used in the LD dynamics. The acceleration in calculation appears for barrier values larger than  $KV/k_B T = 7$ . For this “straightforward” implementation, the acceleration up to 24 times in CPU time has been reached. More sophisticated methods will improve this ratio. The method was also checked for a linear chain of 16 exchange coupled magnetic moments with open boundary condition without dipolar interactions. In this case the Hessian is a banded matrix, being a full matrix with dipolar interactions. The result is shown in Fig. 2.26. The disadvantages of a direct evaluation of the Hessian eigenvalue problem matrix become evident even in this relatively simple system.

In conclusion, we have implemented the method of “Hyperdynamics of infrequent events” to accelerate the molecular dynamics simulations in the case of magnetization dynamics achieving an acceleration up to 24 times. Higher acceleration seems

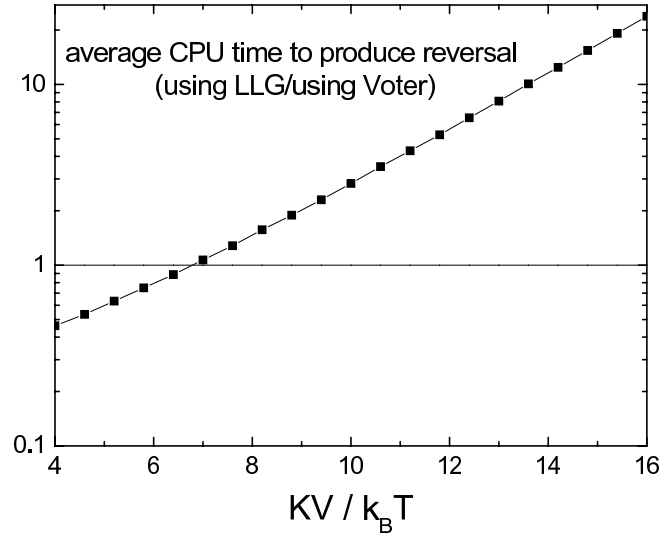


**Figure 2.25:** Comparison of real time performance: average total CPU time to produce reversal in LLG calculations divided by the same quantity using Voter’s method. The line  $y = 1$  represents equal performance and greater number reflects better efficiency of the tested method.

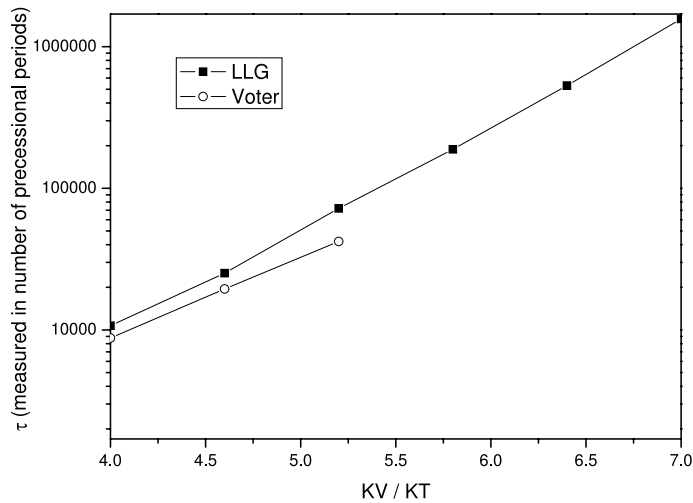


**Figure 2.26:** Switching time obtained with direct LLG calculations and with the Voter’s method for a linear chain of 16 exchange coupled magnetic moments at zero applied field and parameters  $J/KV = 0.4$  and  $\alpha = 0.3$

also possible if one uses more sophisticated modern methods to evaluate rapidly the lowest eigenvalue of the Hessian matrix. In comparison to the time-quantified Monte Carlo, the main advantage of the method is the correct description of the influence of the precession on the thermal switching process. In contrast to the Victora method this method does not suppose a priori the Arrhenius-Néel law with one unique temperature-independent attempt frequency. It may successfully be used

when various reversal modes, with different attempt frequencies, coexist during the thermal magnetization process. The limitations of the method make it useful for intermediate timescale, up to hundreds of nanoseconds, for example, for the dynamic coercivity calculations. Higher time scale seems not reachable.

## Bibliography

- [Acharyya 00] M. Acharyya, U. Nowak and K. D. Usadel. *Transverse ordering of an antiferromagnet in a field with oblique angle to the easy axis*. Phys. Rev. B, vol. 61, pages 464–469, 2000.
- [Antropov 03] V. P. Antropov and K. D. Belashchenko. *Multiscale modeling of hysteretic phenomena in magnets*. J. Appl. Phys., vol. 93, pages 6438–6443, 2003.
- [Basso 00] V. Basso, C. Beatrice, M. LoBue, P. Tiberto and G. Bertotti. *Connection between hysteresis and thermal relaxation in magnetic materials*. Phys. Rev. B, vol. 61, pages 1278–1285, 2000.
- [Bauer 00] M. Bauer, R. Lopusnik, J. Fassbender and B. Hillebrands. *Suppression of magnetic-field pulse-induced magnetization precession by pulse tailoring*. Appl. Phys. Lett., vol. 76, pages 2758–2760, 2000.
- [Beaurepaire 96] E. Beaurepaire, J.-C. Merle, A. Daunois and J.-Y. Bigot. *Ultrafast spin dynamics in ferromagnetic nickel*. Phys. Rev. Lett., vol. 76, pages 4250–4253, 1996.
- [Berkov 93] D. V. Berkov, K. Ramstöck, and A. Hubert. *Solving micromagnetic problems. Towards an optimal numerical method*. Phys. Stat. Sol. (a), vol. 137, pages 207–225, 1993.
- [Berkov 98] D. V. Berkov. *Numerical calculation of the energy barrier distribution in disordered many-particle systems: the path integral method*. J. Magn. Mater., vol. 186, pages 199–213, 1998.
- [Berkov 02] D. V. Berkov. *Fast switching of magnetic nanoparticles: Simulation of thermal noise effects using the Langevin dynamics*. IEEE Trans. Mag., vol. 38, pages 2489–2495, 2002.
- [Berry 85] M. V. Berry. *Classical adiabatic angles and quantal adiabatic phase*. J. Phys. A: Math. Gen., vol. 18, pages 15–27, 1985.
- [Bertotti 04] G. Bertotti, I. Mayergoyz and C. Serpico. *Averaging technique for the analysis of magnetization relaxations*. J. Appl. Phys., vol. 95, pages 6598–6600, 2004.
- [Binder 97] K. Binder and D. W. Heermann. Monte carlo simulation in statistical physics. Springer, 1997.

- [Bloch 30] F. Bloch. *Zur theorie des ferromagnetismus*. Z. Physik A, vol. 61, pages 206–219, 1930.
- [Brown 63a] W. F. Jr Brown. *Micromagnetics*. New York: Wiley, 1963.
- [Brown 63b] W. F. Jr. Brown. *Thermal fluctuations of a single-domain particle*. Phys. Rev., vol. 130, pages 1677–1686, 1963.
- [Brown 04] G. Brown, T. C. Schulthess, D. M. Apalkov and P. B. Visscher. *Flexible fast multipole method for magnetic simulations*. IEEE Trans. Mag., vol. 40, pages 2146–2148, 2004.
- [Callen 66] H. B. Callen and E. Callen. *The present status of the temperature dependence of magnetocrystalline anisotropy, and the  $l(l+1)/2$  power law*. J. Phys. Chem. Solids., vol. 27, pages 1271–1285, 1966.
- [Chen 97] Q. Chen and A. Konrad. *A review of finite element open boundary techniques for static and quasi-static electromagnetic field problems*. IEEE Trans. Mag., vol. 33, pages 663–676, 1997.
- [Chen 99] X. Chen and M. H. Kryder. *Thermal stability of Co/Pt multilayers*. J. Appl. Phys., vol. 85, pages 5006–5008, 1999.
- [Cheng 06] X. Z. Cheng, M. B. A. Jalil, H. K. Lee and Y. Okabe. *Mapping the Monte Carlo scheme to Langevin dynamics: A Fokker-Planck approach*. Phys. Rev. Lett., vol. 96, page 067208, 2006.
- [Chubykalo-Fesenko 04] O. A. Chubykalo-Fesenko, F. Garcia-Sanchez and R. W. Chantrell. *Implementation of the “Hyperdynamics of infrequent events” method for acceleration of thermal switching dynamics of magnetic moments*. IEEE Trans. Mag., vol. 40, pages 2140–2142, 2004.
- [Chubykalo-Fesenko 05] O. Chubykalo-Fesenko and R. W. Chantrell. *Modeling of long-time thermal magnetization decay in interacting granular magnetic materials*. IEEE Trans. Mag., vol. 41, pages 3103–3105, 2005.
- [Chubykalo 03a] O. Chubykalo, U. Nowak, R. Smirnov-Rueda, M. A. Wongsam, R. W. Chantrell and J. M. Gonzalez. *Monte Carlo technique with a quantified time step: Application to the motion of magnetic moments*. Phys. Rev. B, vol. 67, page 064422, 2003.

- [Chubykalo 03b] O. Chubykalo, R. Smirnov-Rueda, J. M. Gonzalez, M. A. Wongsam, R. W. Chantrell and U. Nowak. *Brownian dynamics approach to interacting magnetic moments*. J. Magn. Magn. Mater., vol. 266, pages 28–35, 2003.
- [Cinchetti 06] M. Cinchetti, M. Sánchez Albaneda, D. Hoffmann, T. Roth, J.-P. Wüstenberg, M. Krauß, O. Andreyev, H. C. Schneider, M. Bauer and M. Aeschlimann. *Spin-flip processes and ultrafast magnetization dynamics in Co: Unifying the microscopic and macroscopic view of femtosecond magnetism*. Phys. Rev. Lett., vol. 97, page 177201, 2006.
- [Coffey 95a] W. T. Coffey, D. S. F. Crothers, J. L. Dormann, L. J. Geoghegan, Yu. P. Kalmykov, J. T. Waldron and A. W. Wickstead. *The effect of an oblique magnetic field on the superparamagnetic relaxation time*. J. Magn. Magn. Mater., vol. 145, pages L263–L267, 1995.
- [Coffey 95b] W. T. Coffey, D. S. F. Crothers, Yu. P. Kalmykov and J. T. Waldron. *Constant-magnetic-field effect in Néel relaxation of single-domain ferromagnetic particles*. Phys. Rev. B, vol. 51, pages 15947–15956, 1995.
- [Cordis Europa ] Cordis Europa. <http://cordis.europa.eu/fp6/>.
- [Dederichs 84] P. H. Dederichs, S. Blügel, R. Zeller and H. Akai. *Ground states of constrained systems: Application to cerium impurities*. Phys. Rev. Lett., vol. 53, pages 2512–2515, 1984.
- [DoE USA ] Department of Energy USA. <http://www.energy.gov/news/1693.htm>.
- [Dittrich 02] R. Dittrich, T. Schrefl, D. Suess, W. Scholz, H. Forster and J. Fidler. *A path method for finding energy barriers and minimum energy paths in complex micromagnetic systems*. J. Magn. Magn. Mater., vol. 250, pages L12–L19, 2002.
- [Dobrovitski 00] V. V. Dobrovitski, M. I. Katsnelson and B. N. Harmon. *Statistical coarse-graining as an approach to multiscale problems in magnetism*. J. Magn. Magn. Mater., vol. 221, pages L235–L242, 2000.
- [Dreizler 90] R. M. Dreizler and E. K. U. Gross. *Density functional theory*. Berlin: Springer, 1990.
- [Fernández 00] L. Fernández, O. Pla and O. Chubykalo. *Quasiperiodicity, bistability, and chaos in the Landau-Lifshitz equation*. Phys. Rev. B, vol. 61, pages 11613–11617, 2000.

- [Fidler 00] J. Fidler and T. Schrefl. *Micromagnetic modelling—the current state of the art*. J. Phys. D: Appl. Phys., vol. 33, pages R135–R156, 2000.
- [Forster 03] H. Forster, N. Bertram, X. Wang, R. Dittrich and T. Schrefl. *Energy barrier and effective thermal reversal volume in columnar grains*. J. Magn. Magn. Mater., vol. 267, pages 69–79, 2003.
- [Fredkin 90] D. R. Fredkin and T. R. Koehler. *Hybrid method for computing demagnetizing fields*. IEEE Trans. Mag., vol. 26, pages 415–417, 1990.
- [Garanin 03] D. A. Garanin and H. Kachkachi. *Surface contribution to the anisotropy of magnetic nanoparticles*. Phys. Rev. Lett., vol. 90, page 065504, 2003.
- [García-Palacios 98] J. L. García-Palacios and F. J. Lazaro. *Langevin-dynamics study of the dynamical properties of small magnetic particles*. Phys. Rev. B, vol. 58, pages 14937–14958, 1998.
- [Garcia-Sanchez 05] F. Garcia-Sanchez, O. Chubykalo-Fesenko, O. Mryasov, R. W. Chantrell and K. Yu. Guslienko. *Exchange spring structures and coercivity reduction in FePt/FeRh bilayers: A comparison of multiscale and micromagnetic calculations*. Appl. Phys. Lett., vol. 87, page 122501, 2005.
- [Gibbons 98] M. R. Gibbons. *Micromagnetic simulation using the dynamic alternating direction implicit method*. J. Magn. Magn. Mater., vol. 186, pages 389–401, 1998.
- [Gibbons 00] M. R. Gibbons, G. Parker, C. Cerjan and D. W. Hewett. *Finite difference micromagnetic simulation with self-consistent currents and smooth surfaces*. Physica B, vol. 275, pages 11–16, 2000.
- [Gilbert 55] T. L. Gilbert. *A Lagrangian formulation of the gyromagnetic equation of the magnetization field*. Phys. Rev., vol. 100, page 1243, 1955.
- [González 95] J. M. González, R. Ramírez, R. Smirnov-Rueda and J. González. *Non-Arrhenius relaxation in micromagnetic models of systems with many degrees of freedom*. Phys. Rev. B, vol. 52, pages 16034–16040, 1995.
- [Grinstein 03] G. Grinstein and R. H. Koch. *Coarse graining in micromagnetics*. Phys. Rev. Lett., vol. 90, page 207201, 2003.
- [Hernando 01] A. Hernando and J.M. Rojo. Física de los materiales magnéticos. Madrid: Editorial Síntesis, 2001.

- [Hinze 98] D. Hinze and U. Nowak. *Magnetization switching in a Heisenberg model for small ferromagnetic particles*. Phys. Rev. B, vol. 58, pages 265–272, 1998.
- [Hinze 07] D. Hinze, U. Nowak, R. W. Chantrell and O. N. Mryasov. *Orientation and temperature dependence of domain wall properties in FePt*. Appl. Phys. Lett., vol. 90, page 082507, 2007.
- [Hoyt 02] J. J. Hoyt, M. Asta and A. Karma. *Atomistic simulation methods for computing the kinetic coefficient in solid-liquid systems*. Interface Science, vol. 10, pages 181–189, 2002.
- [Inaba 97] N. Inaba, Y. Uesaka, A. Nakamura, M. Futamoto and Y. Sugita. *Damping constants of Co-Cr-Ta and Co-Cr-Pt thin films*. IEEE Trans. Mag., vol. 33, pages 2989–2991, 1997.
- [Kanai 91] Y. Kanai and S. H. Charap. *Simulation of magnetic aftereffect in particulate recording media*. IEEE Trans. Mag., vol. 27, pages 4972–4974, 1991.
- [Kläui 05] M. Kläui, P.-O. Jubert, R. Allenspach, A. Bischof, J. A. C. Bland, G. Faini, U. Rüdiger, C. A. F. Vaz, L. Vila and C. Vouille. *Direct observation of domain-wall configurations transformed by spin currents*. Phys. Rev. Lett., vol. 95, page 026601, 2005.
- [Kramers 40] H. A. Kramers. *Brownian motion in a field of force and the diffusion model of chemical reactions*. Physica, vol. 7, pages 284–304, 1940.
- [Kronmüller 97] H. Kronmüller, R. Fischer, R. Hertel and T. Leineweber. *Micro-magnetism and the microstructure in nanocrystalline materials*. J. Magn. Magn. Mater., vol. 175, pages 177–192, 1997.
- [Kronmüller 01] H. Kronmüller and M. Bachmann. *Magnetization processes in nanocrystalline assemblies of particles*. Physica B, vol. 306, pages 96–101, 2001.
- [Labarta 93] A. Labarta, O. Iglesias, Ll. Balcells and F. Badia. *Magnetic relaxation in small-particle systems:  $T \ln(t/\tau_0)$  scaling*. Phys. Rev. B, vol. 48, pages 10240–10246, 1993.
- [Landau 35] L. D. Landau and E. M. Lifshitz. *On the theory of the dispersion of magnetic permeability in ferromagnetic bodies*. Phys. Z. Sowietunion, vol. 8, pages 153–169, 1935.

- [Langer 68] J. S. Langer. *Theory of nucleation rates*. Phys. Rev. Lett., vol. 21, pages 973–976, 1968.
- [Magpar ] Magpar. <http://magnet.atp.tuwien.ac.at/scholz/magpar/>.
- [Martínez 04] E. Martínez, L. López-Díaz, L. Torres and O. Alejos. *On the interpretations of Langevin stochastic equation in different coordinate systems*. Physica B, vol. 343, pages 252–256, 2004.
- [Martínez 07] E. Martínez, L. López-Díaz, L. Torres and C.J. García-Cervera. *Minimizing cell size dependence in micromagnetics simulations with thermal noise*. J. Phys. D: Appl. Phys., vol. 40, pages 942–948, 2007.
- [Mills 95] G. Mills, H. Jónsson and G. K. Schenter. *Reversible work transition state theory: application to dissociative adsorption of hydrogen*. Surf. Sci., vol. 324, pages 305–337, 1995.
- [Mryasov 05] O. N. Mryasov, U. Nowak, K. Y Guslienko and R. W. Chantrell. *Temperature-dependent magnetic properties of FePt: Effective spin Hamiltonian model*. Europhys Lett., vol. 69, pages 805–811, 2005.
- [Nowak 00] U. Nowak, R. W. Chantrell and E. C. Kennedy. *Monte Carlo simulation with time step quantification in terms of Langevin dynamics*. Phys. Rev. Lett., vol. 84, pages 163–166, 2000.
- [Okamoto 02] S. Okamoto, N. Kikuchi, O. Kitakami, T. Miyazaki, Y. Shimada and K. Fukamichi. *Chemical-order-dependent magnetic anisotropy and exchange stiffness constant of FePt(001) epitaxial films*. Phys. Rev. B, vol. 66, page 24413, 2002.
- [OOMMF ] OOMMF. <http://math.nist.gov/oommf/>.
- [Paz 07] E. Paz, F. Garcia-Sanchez and O. Chubykalo-Fesenko. *Numerical evaluation of energy barriers in nano-sized magnetic elements with Lagrange multiplier technique*. Physica B, vol. accepted, 2007.
- [Rahman 04] T. S Rahman, C. Ghosh, O. Trushin, A. Kara and A. Karim. *Atomistic studies of thin film growth*. PROC. SPIE ANNUAL MEETING, vol. 5509, page 1, 2004.
- [Serpico 04] C. Serpico, M. d’Aquino, G. Bertotti and I.D. Mayergoyz. *Quasiperiodic magnetization dynamics in uniformly magnetized particles and films*. J. Appl. Phys., vol. 95, pages 7052–7054, 2004.

- [Skomski 03] R. Skomski, A. Kashyap and D. J. Sellmyer. *Finite-temperature anisotropy of PtCo magnets*. IEEE Trans. Mag., vol. 39, pages 2917–2919, 2003.
- [Slichter 89] C. P. Slichter. Principles of magnetic resonance. Berlin: Springer, 1989.
- [Stoner 48] E. C. Stoner and E. P. Wohlfarth. *A mechanism of magnetic hysteresis in heterogeneous alloys*. Philos. Trans. R. Soc. Lond. A, vol. 240, pages 599–642, 1948.
- [Suess 02] D. Suess, V. Tsiantos, T. Schrefl, J. Fidler, W. Scholz, H. Forster, R. Dittrich and J. J. Miles. *Time resolved micromagnetics using a preconditioned time integration method*. J. Magn. Magn. Mater., vol. 248, pages 298–311, 2002.
- [Suess 05] D. Suess, T. Schrefl, S. Fahler, M. Kirschner, G. Hrkac, F. Dorfbauer and J. Fidler. *Exchange spring media for perpendicular recording*. Appl. Phys. Lett., vol. 87, page 012504, 2005.
- [Suhl 98] H. Suhl. *Theory of the magnetic damping constant*. IEEE Trans. Mag., vol. 34, pages 1834–1838, 1998.
- [Thiele 02] J.-U. Thiele, K. R. Coffey, M. F. Toney, J. A. Hedstrom and A. J. Kellock. *Temperature dependent magnetic properties of highly chemically ordered  $Fe_{55-x}Ni_xPt_{45}L_{10}$  films*. J. Appl. Phys., vol. 91, pages 6595–6600, 2002.
- [Tsiantos 02] V. Tsiantos, W. Scholz, D. Suess, T. Schrefl and J. Fidler. *The effect of the cell size in Langevin micromagnetic simulations*. J. Magn. Magn. Mater., vol. 242-245, pages 999–1001, 2002.
- [Usatenko 06] O. V. Usatenko, O. A. Chubykalo-Fesenko and F. Garcia-Sanchez. *Nonlinear adiabatic dynamics of small ferromagnetic particles*. Int. J. Mod. Phys. B, vol. 20, pages 5391–5404, 2006.
- [Voter 97a] A. F. Voter. *Hyperdynamics: Accelerated molecular dynamics of infrequent events*. Phys. Rev. Lett., vol. 78, pages 3908–3911, 1997.
- [Voter 97b] A. F. Voter. *A method for accelerating the molecular dynamics simulation of infrequent events*. J. Chem. Phys., vol. 106, pages 4665–4677, 1997.

- [Wegrowe 97] J.-E. Wegrowe, J. P. Meier, B. Doudin, J.-Ph. Ansermet, W. Wernsdorfer, B. Barbara, W. T. Coffey, Y.P. Kalmykov and J.-L. Déjardin. *Magnetic relaxation of nanowires: beyond the Néel-Brown activation process*. Europhys Lett., vol. 38, pages 329–334, 1997.
- [Weller 99] D. Weller and A. Moser. *Thermal effect limits in ultrahigh-density magnetic recording*. IEEE Trans. Mag., vol. 35, pages 4423–4439, 1999.
- [Xue 00] J. Xue and R. H. Victora. *Micromagnetic predictions for thermally assisted reversal over long time scales*. Appl. Phys. Lett., vol. 77, pages 3432–3434, 2000.
- [Yuan 92] S. W. Yuan and H. N. Bertram. *Fast adaptive algorithms for micromagnetics*. IEEE Trans. Mag., vol. 28, pages 2031–2036, 1992.

# Chapter 3

## Multiscale modeling of magnetization reversal in soft/hard bilayer for magnetic recording applications

### 3.1 Introduction

One approach proposed to circumvent the superparamagnetic limit in magnetic recording is thermally or Heat Assisted Magnetic Recording (HAMR) [Ruigrok 00]. However, as pointed out by J. Thiele et al. [Thiele 03], the exponents of the power law variations of  $K$  and  $M_s$  with temperature are such that the anisotropy field varies more slowly than  $K$ , requiring temperatures close to or above the Curie temperature to write information. This leads to significant practical problems associated with the head-disk interface, and especially the loss of lubricant [Hsia 02]. As a solution J. Thiele et al. [Thiele 03] proposed the idea of a composite medium of FePt and FeRh. It has been established that the ordered b.c.c. alloy FeRh belongs to the class of materials with a metamagnetic transition [Kouvel 66]: at room temperature  $Fe_xRh_{1-x}$  alloy ( $x > 0.5$ ) is antiferromagnetic, undergoing a transition to the ferromagnetic state at temperatures around 300 – 400K depending on concentration  $x$ . The remarkable property of FeRh is that it has a similar lattice parameter to FePt. Therefore, the two materials could be grown epitaxially with good interfacial properties [Goto 04]. The advantage of the composite medium is that the antiferromagnetic character of FeRh at room temperature could provide additional thermal stability while the coupling between FePt and FeRh after the metamagnetic transition has occurred, could be used to lower the switching field via an “exchange spring” mechanism. J. Thiele et al. [Thiele 03, Thiele 04b] have measured that a coercivity reduction of FePt in

2–3 times could be expected due to this coupling. The transition antiferro-ferro in FeRh has to be fast enough in order to implement a magnetic recording device. The heating through a laser pulse, in an similar way to 'pump-probe' experiments, yields transition times as low as 500 *fs* [Thiele 04a]. Therefore, it is possible to reverse the magnetization of the FePt in fields comparable to those provided by current write heads at temperatures considerably lower than the Curie point of FePt.

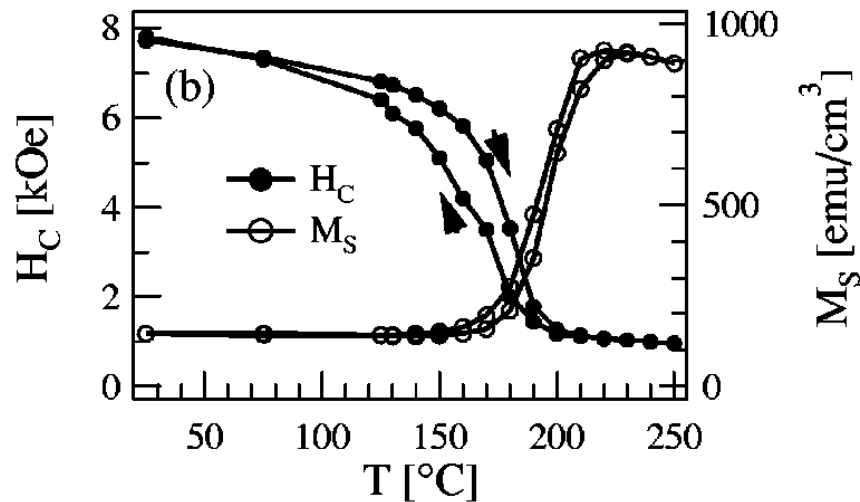


**Figure 3.1:** Temperature dependence of the coercive field and saturation magnetization of an FePt/FeRh bilayer. Extracted from [Thiele 03].

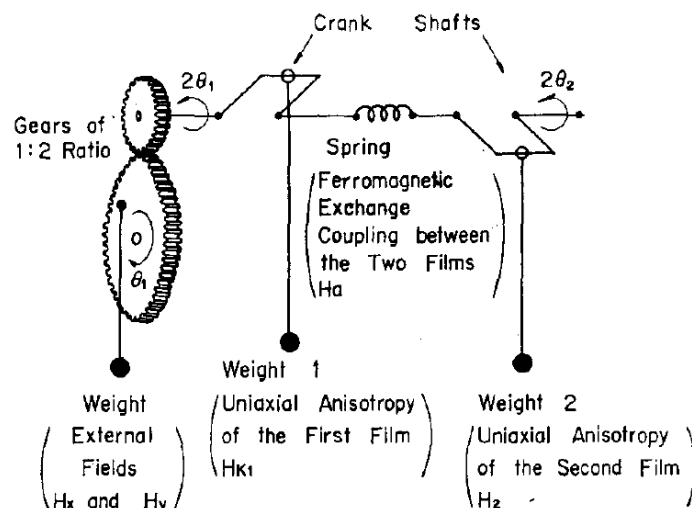


**Figure 3.2:** Mechanical analog of an “exchange spring” from [Goto 65].

On the other hand, exchange spring magnets have offered an extraordinary possibility to control hysteretic properties of composite media by tuning extrinsic and

intrinsic parameters of different magnetic phases. The first work that explained the coercivity of composite thin films with an exchange spring mechanism was due to E. Goto et al. [Goto 65] (see Fig. 3.2), but Goto did not coin the “exchange spring”. The fingerprint of an exchange spring is the reversible part of the hysteresis loop between the irreversible jumps that corresponds to the motion of the domain wall center towards the hard layer after the pinning of the domain wall at the interface. This reversible domain wall motion can be clearly observed in the experimental loop shown in Fig. 3.3. This part would be absent in the case of independent behavior of the two layers or strongly coupled bilayer. Posteriorly, the exchange spring mechanism was proposed by E. Kneller [Kneller 91] as a method to increase the energy product  $BH_{max}$  in permanent magnets. This quantity needs to be maximized in order to obtain a good permanent magnet. The enhancement of the energy product was previously reported in experiments in Ref. [Coehoorn 89]. The hard phase  $Nd_2Fe_{14}B$  was embedded in the soft phase  $Fe_3B$  matrix. Hence, an important application of exchange spring magnets includes permanent magnets such as  $SmCo$  or  $NdFeB$  where hard magnetic phase provides high coercivity and soft magnetic phase provides high saturation magnetization.

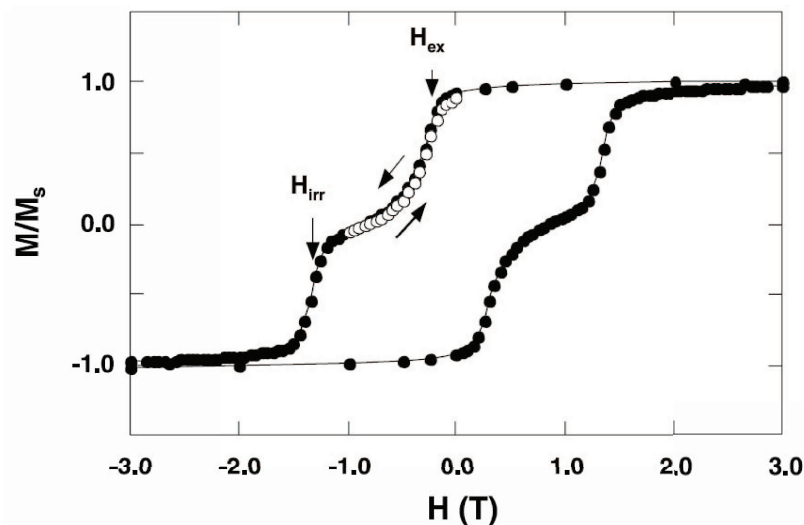


**Figure 3.3:** Measured hysteresis loop for a SmCo/Fe(10 nm) bilayer. The exchange spring behavior of the sample is manifested in the reversible part of the curve before the irreversible jump of the SmCo layer at  $H_{irr}$ . Extracted from Ref. [Jiang 02].

Recently, the use of a general composite magnetic bilayer has been suggested for magnetic recording applications [Thiele 03, Guslienko 04, Victora 05a, Suess 05b]. Unlike conventional exchange spring media, perpendicular magnetic recording requires a new type of exchange spring - perpendicular exchange spring (see Fig. 3.4). Differently from permanent magnets, the properties of this composite media

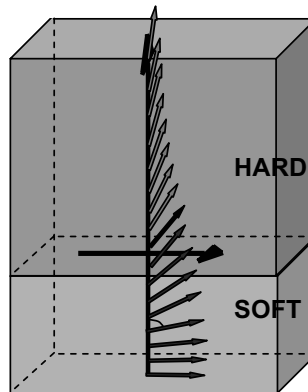


**Figure 3.4:** Schematic picture showing a perpendicular exchange spring in a soft/hard bilayer.

should be optimized to provide a relatively low coercive field suitable for conventional recording heads together with high thermal stability [Suess 05b, Dobin 06]. It has been shown that the properties of soft/hard phases could be optimized independently for coercive field and thermal energy barriers values, providing a real alternative for recording media of new generation [Suess 05b, Suess 07]. In comparison to FePt/FeRh material, this general proposal avoids heating process. However, there is an additional requirement of high energy barriers which does not exist in the FePt/FeRh case due to the anti-ferromagnetic character of FeRh at room temperature which itself provides additional thermal stability.

One can expect that the exchange spring mechanism depends on the coupling properties between the phases. Real concerns have been expressed on the possibility to grow soft/hard materials with grain matching in both layers [Thiele 04b]. Beside this, realistic interfaces between two materials present complicated properties, related to interface roughness, lattice parameters mismatch, diffusion of atoms across the interface, etc. All this situations contribute to the expectation of a reduced exchange value at the interface, which influences the exchange spring performance. The investigation of soft/hard magnetic layer performance as a function of the phenomenological interfacial exchange,  $J_s$  constitutes the main goal of the present chapter.

## 3.2 Theoretical background

The reduction of the coercivity in a soft/hard magnetic bilayer is explained by the formation of an exchange spring: the reversal starts in the soft phase (FeRh in our case), then a domain wall is formed, which later penetrates into the hard phase

(FePt) and helps to reverse its magnetization. This mechanism has also received recently the name of domain wall assisted magnetic recording (DWAMR) [Dobin 06]. In this case the size of the soft phase should be larger than the domain wall width  $L_{DW,soft} = \pi\sqrt{A_{Soft}/M_{Soft}^2}$  where  $A_{Soft}$  is the micromagnetic exchange constant in the soft layer and  $M_{Soft}$  the saturation magnetization. Alternatively, R. Victora and X. Shen [Victora 05a] have proposed a mechanism in which the domain wall is not formed, and the two layers behave essentially as two-spins: initially, the soft layer rotates towards the external field, which exerts an additional torque to the hard layer, helping to invert its magnetization. Both mechanisms are schematically represented in Fig. 3.5.

The standard approach to describe conventional in-plane exchange springs [Kneller 91, Hernando 92] used in many previous publications and generalized recently to the case of the perpendicular exchange spring [Guslienko 04] is a 1D model. Essentially, it assumes the homogeneous in-plane magnetization and considers a set of atomistic planes with the properties of soft or hard phase, each one represented by one magnetic moment. The magnetostatic contribution is taken into account in the demagnetization field approximation, which considers the in-plane dimensions as infinite. The model admits analytical treatment.

In the two macrospins model the coercive field is determined by an average anisotropy field [Fullerton 98]:

$$H_c = \frac{2(K_{Soft}L_{Soft} + K_{Hard}L_{Hard})}{M_{Soft}L_{Soft} + M_{Hard}L_{Hard}} \quad (3.1)$$

where  $L_{Soft}$  is the thickness of the soft layer,  $L_{Hard}$  is the thickness of the hard layer,  $M_{Hard}$  the saturation magnetization of the hard layer,  $K_{Soft}$  is the anisotropy constant of the soft layer and  $K_{Hard}$  is the anisotropy constant of the hard layer. In

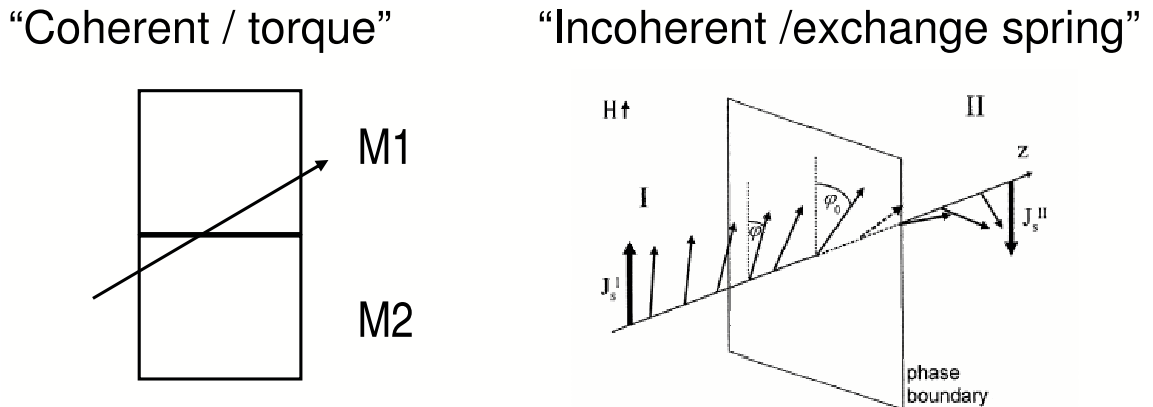


**Figure 3.5:** Proposed mechanisms for the coercivity in a composite medium: Two macrospins (left) and “exchange spring” (right).

the same model the corresponding energy barrier is:

$$E_B = K_{Soft}V_{Soft} + K_{Hard}V_{Hard} \quad (3.2)$$

where  $V_{Soft}$  is the volume of the soft layer,  $V_{Hard}$  is the volume of the hard layer. These formulae are valid if the thicknesses of both layers are below their respective domain wall widths.

For the exchange spring mechanism the magnetization process is determined by nucleation and depinning field. It has been shown [Goto 65], for example, that the nucleation field is determined in the strongly coupled case by:

$$H_N = \frac{2K_{Soft}}{M_{Soft}} - \frac{\pi^2 A_{Soft}}{2M_{Soft}L_{Soft}^2} = \frac{2K_{Soft}}{M_{Soft}} - \frac{M_{Soft}}{2} \left( \frac{L_{DW,Soft}}{L_{Soft}} \right)^2. \quad (3.3)$$

From this equation, it is clear that the nucleation field increases with the thickness of the soft layer. Namely, when  $L_{DW,Soft} \ll L_{Soft}$  we have  $H_N \approx H_k^{Soft}$ .

When the pinning is effective and the interfacial exchange strong enough the coercive field is determined by the pinning field [Kronmüller 02]:

$$H_c = \frac{K_{Hard}}{2M_{Hard}} \frac{1 - A_{Soft}K_{Soft}/A_{Hard}K_{Hard}}{\left(1 + \sqrt{A_{Soft}M_{Soft}/A_{Hard}M_{Hard}}\right)^2} \quad (3.4)$$

where  $A_{Hard}$  is the exchange constant in the hard layer. An interesting consequence of the pinning field equation is that the reduction of coercivity is larger when the difference of anisotropy constants between soft and hard materials is smaller. This fact has stimulated later the proposal of the graded media [Suess 06], using a multi-layer with increasing anisotropy constant in each layer. In this case large reduction of the coercive field together with large thermal stability have been predicted.

When the interfacial exchange is weak the soft layer nucleates but the domain wall is very sharp. For this case K. Guslienko has derived an expression for the coercive field [Guslienko 04]:

$$H_c = H_k^{Hard} - \frac{J_s M_s^{Soft}}{L_{Soft}} \left[ 1 + \frac{J_s M_s^{Hard}}{L_{Hard}(H_k^{Hard} - 4\pi M_s^{Soft})} \right]. \quad (3.5)$$

Although the equation is not valid for all interfacial exchange, it shows that the coercivity reduces with increasing interfacial exchange parameter. The coercivity will saturate for strong interfacial coupling and depending on the system parameters the behavior will reach that of an exchange spring mechanism (3.4) or two-macrospins (3.3).

The analytical and 1D numerical calculations from K. Guslienko et al. [Guslienko 04] have shown that the coercivity reduction in the FePt layer due to the exchange coupling to the FeRh layer strongly depends on the interfacial exchange

parameter and even for the exchange parameter as low as 10% of the bulk value, a coercivity reduction of the FePt of up to 50% could be expected.

However, although a 1D approach is probably justified in bilayers with a good in-plane film quality, the exact reversal mechanism and the degree of interfacial energy required for maximum coercivity reduction in a soft/hard magnetic material are questions requiring a 3D calculation [Suess 05a, Garcia-Sanchez 06]. With 3D simulations, which correctly include the magnetostatic fields, we can study the finite size effects and magnetization inhomogeneities, allowing noncoherent reversal, and variation of the parameters inside the plane, as for example granular structure.

### 3.3 Atomistic models

We will describe our atomistic model including the interface, the exchange interactions, the lattice structure, the saturation magnetization and the anisotropy constants. We consider only Fe sites possessing the total magnetic anisotropy and saturation magnetization in a similar way to the effective one-ion Hamiltonian presented in Ref. [Mryasov 05] and in Section 2.2.4. In our implementation the arrangement of the FeRh lattice with respect to FePt one was taken from Ref. [Goto 04] so that the fct FePt lattice is rotated 45 degrees with respect to bcc FeRh lattice and displaced half an FeRh lattice constant as shown in Fig. 3.6, with the  $c$  axis of the FePt lattice normal to the interface. Due to this rotation, it is more convenient to represent the FePt with a bct cell as shown in Fig. 3.7. Considering the bct lattice, the parameters for FePt are  $a = 0.272 \text{ nm}$  and  $c = 0.385 \text{ nm}$  and the lattice of the FeRh is matched according to the observed structure [Thiele 04b].

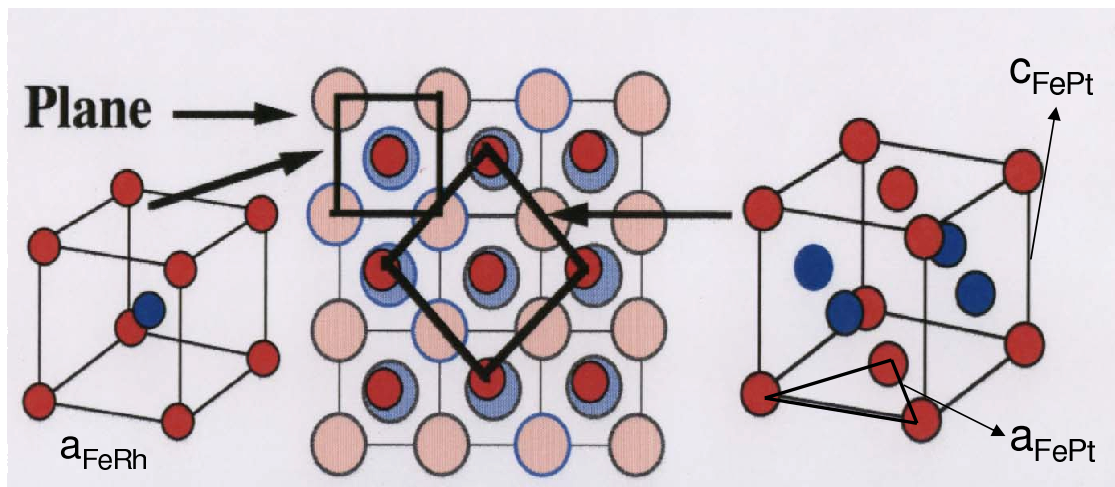


**Figure 3.6:** Lattice of FePt and FeRh and interface structure of FePt/FeRh as observed in the paper [Goto 04].

We have developed two models for exchange interaction in the FePt material. **The first model (I)** was developed to compare with the micromagnetic simulations. In this case we considered a model for FePt with exchange parameters  $J_{\perp} = J_{\parallel} = 7.7 \cdot 10^{-14} \text{ erg}$  calculated from Eqs. (2.23) and (2.24) and the corresponding micromagnetic exchange constant  $A$ . In **the second model (II)**, used in the Section 3.8, we used a representation of exchange interactions based on the first-principle calculations [Mryasov 05] but with an exchange interaction only until first neighbors. The exchange interaction has been renormalized in order to obtain the same thermal properties (i.e Curie temperature). This gives different exchange values perpendicular to the plane  $J_{\perp} = 3.139 \cdot 10^{-14} \text{ erg}$  and in-plane  $J_{\parallel} = 7.8476 \cdot 10^{-14} \text{ erg}$ , according to the layered structure of FePt .

For the simulations in the Section 3.8 the generic soft magnetic material was simulated using a generic model with cubic lattice with  $a = 0.272 \text{ nm}$ , exchange parameter  $J = 7.696 \cdot 10^{-14} \text{ erg}$  and varying saturation magnetization value. The interface in this simulation is such that in the Z direction there is a hard material atom just above the position of a soft material atom.

The saturation magnetization corresponding to the FeRh  $M_s^{FeRh} = 1270 \text{ emu/cm}^3$  is extracted from the experimental work of J. Thiele [Thiele 03]. In the case of the FePt anisotropy we have used the value measured in the perfectly ordered alloy,  $K^{FePt} = 7 \cdot 10^7 \text{ erg/cm}^3$ , and that for an FePt epitaxial film with a chemical order parameter of 0.7,  $K^{FePt} = 2 \cdot 10^7 \text{ erg/cm}^3$ . This parameter represents the number of atoms that occupy its proper position in the alloy and the magnetic anisotropy of the FePt alloy is strongly dependent on it [Okamoto 02]. The anisotropy axis of the hard material was directed perpendicular to the plane. The saturation magnetization of FePt  $M_s^{FePt} = 1270 \text{ emu/cm}^3$  was obtained from the last reference.

### 3.4 Simulations of one grain of FePt/FeRh

The switching field of the soft/hard bilayer depends on various microscopic and morphological parameters such as the saturation magnetization of soft layer, the exchange parameter at the interface or the thickness of soft and hard phases. We can appreciate this dependence in the formulae of Section 3.2. Since those formulae deal only with ideal and limiting cases, we have modeled a grain based on FePt/FeRh parameters to investigate the switching behavior of the composite media in different ranges of the parameters: thicknesses and interfacial exchange. The grain has a size of  $6 \text{ nm} \times 6 \text{ nm} \times L \text{ nm}$  consisting of an FePt grain above FeRh one with exact grain matching. We have used the atomistic model I with the following parameters:  $K^{FePt} = 7 \cdot 10^7 \text{ erg/cm}^3$  and  $K^{FeRh} = 0$ . The calculation finishes when the following condition is met  $\epsilon < 10^{-5}$  for the error (see Section 2.2.3).

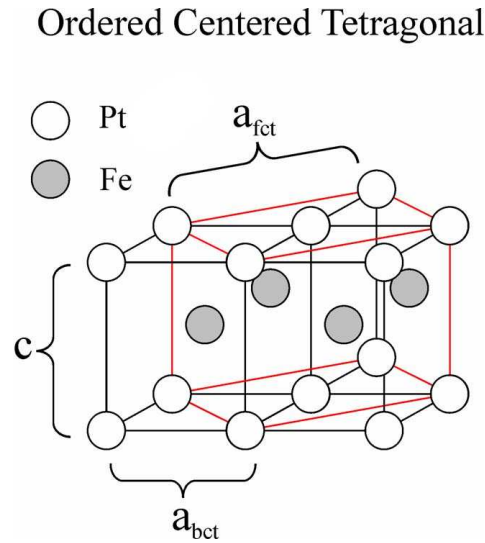


**Figure 3.7:** Relation between the unit cells of the fct and bct cells in  $L1_0$  phase.

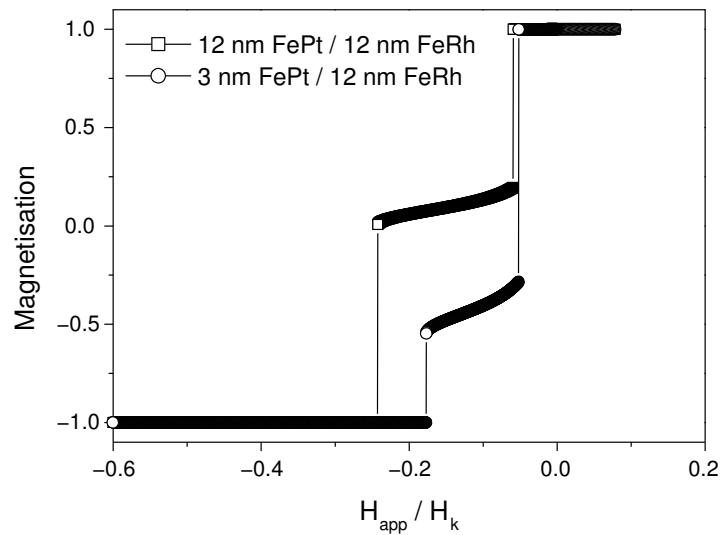


**Figure 3.8:** Magnetization as a function of the applied field for a singular grain of FePt/FeRh and two FePt thicknesses with  $J_s/J = 0.4$ .

Fig. 3.8 represents a hysteresis cycle of FePt/FeRh magnetic grain calculated for two different thicknesses of FePt. The nucleation process starts in FeRh grain, which is softer but has an additional shape anisotropy due to the grain elongation. The domain wall (exchange spring) of the Néel-type propagates and gets pinned at the FePt/FeRh interface. An additional field is necessary to push the center of the domain wall into the FePt (see Fig. 3.9). Associated with the movement of the domain wall, there is a change of the domain wall width illustrated in Fig. 3.10. The initial process is a compression of the domain wall against the interface [Dobin 06] that is reflected in the reduction of its width. Once the center of the domain wall penetrates

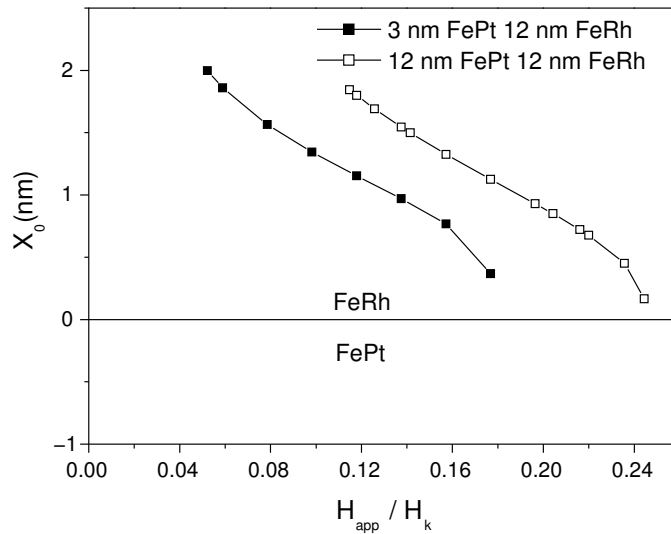


**Figure 3.9:** Domain wall center position as a function of the applied field for  $J_s/J = 0.4$ . The solid line represents the interface between FePt and FeRh.

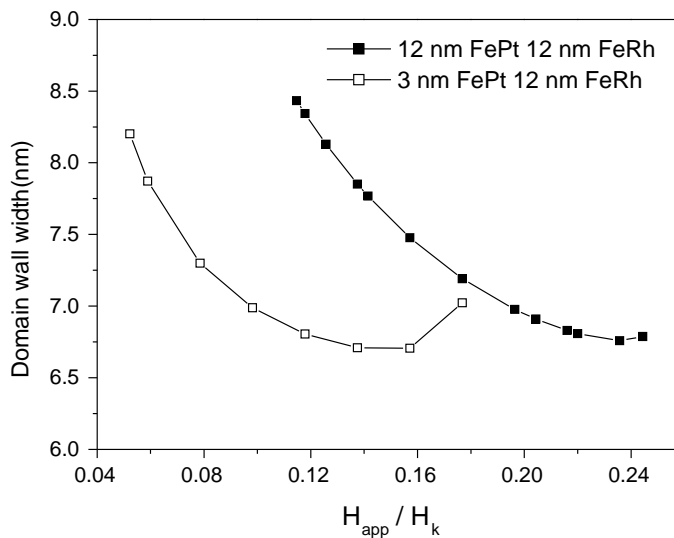
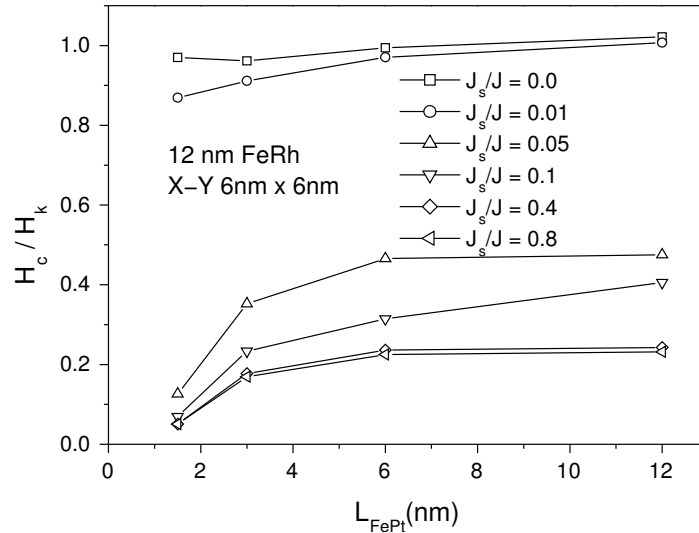


**Figure 3.10:** Domain wall width as a function of the applied field for  $J_s/J = 0.4$ .

inside the hard medium, this produces the complete magnetization reversal in FePt.

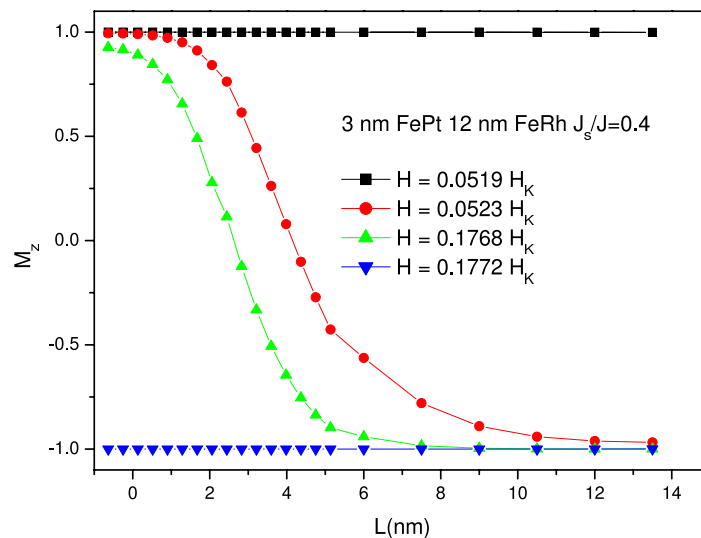
Fig. 3.11 represents the coercivity reduction in the case of the exchange spring medium as a function of the FePt thickness. For a thinner (3 nm) FePt layer, the domain wall could not be completely formed in the hard magnetic material (with the domain wall thickness 4 nm) as can be observed in Fig. 3.12. This is important since the total domain wall formation is an implicit assumption of some analytical models [Asti 06, Loxley 06, Kronmüller 02] that consider infinite thickness, included the one used to obtain the pinning field Eq. (3.4). This reduces the coercivity because the pinning is less effective. A remarkable reduction of the switching field (more than 5

times) than that of the pure FePt grain could be obtained even with small interfacial exchange value for thin FePt layer.



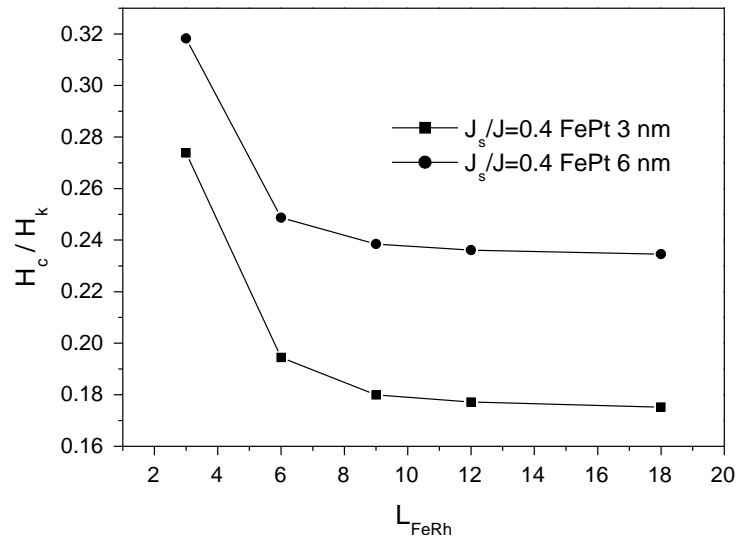
**Figure 3.11:** Coercivity reduction in an exchange spring medium with 12 nm FeRh, calculated in one-grain model as a function of FePt thickness for different reduced interfacial exchange parameters.

Fig. 3.13 represents the coercive field reduction as a function of the thickness of FeRh. It is clearly seen that the exchange spring formation (thick soft layer) is more efficient in decreasing the coercive field value than the case of thin soft layer. The coercivity saturates when the length of soft material is larger than its domain



**Figure 3.12:** Domain wall in an exchange spring medium with 3 nm FePt/12 nm FeRh and  $J_s/J = 0.4$  for different values of the applied field.

wall width. Fig. 3.14 represents the coercivity reduction as a function of interfacial exchange in grains with different thicknesses. Substantial reduction of the switching field could be achieved with interfacial exchange of the order of 10% of the bulk value. However, more interfacial exchange is necessary for thicker FePt layer as compared to a thinner one to get the same reduction.



**Figure 3.13:** Coercivity reduction calculated in one-grain model as a function of FeRh thickness for two different thickness of FePt and the value of the interfacial exchange parameter  $J_s/J = 0.4$ .

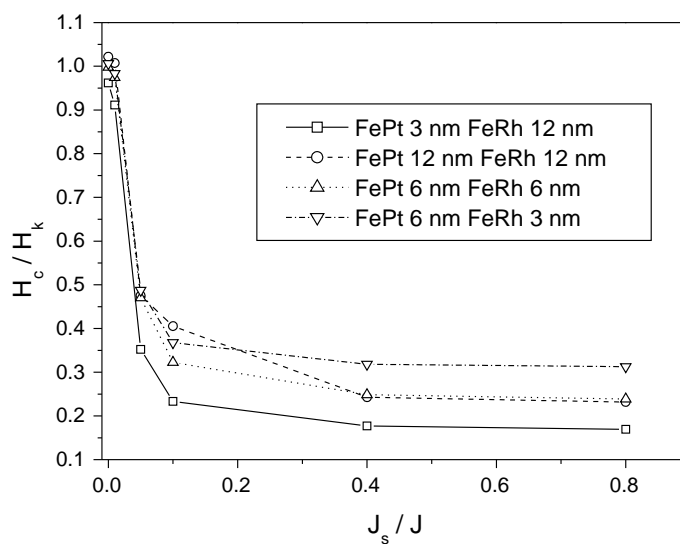


**Figure 3.14:** Coercivity reduction as a function of reduced interface parameter for grains with different FePt and FeRh thicknesses.

### 3.5 Coercivity reduction in FePt/FeRh film: necessity of multiscale modeling

We will study the switching properties of a soft/hard bilayer film using two different models. The first will be a standard micromagnetic model and the second the multiscale modeling already introduced in Section 2.2.4. From their comparison with the previous results of a 1-D model by K. Guslienko et al. [Guslienko 04], which will be referred in this section as “1D” model, we will show the necessity of multiscale modeling in the case of imperfect interfaces. The system modeled, represented in Fig. 3.15, has thicknesses of 15 nm of FePt and 30 nm of FeRh and the in-plane dimensions are 120 nm × 120 nm. Periodic boundary conditions in the magnetostatic potential as well as in the exchange interaction are used in x,y directions, but not in z direction where free boundary conditions are used. Due to the system configuration and the periodic boundary conditions, the magnetostatic interaction yields an in-plane shape anisotropy equivalent to that of an infinite film. The temperature is supposed to be higher than the transition temperature, therefore, the FeRh is in its ferromagnetic state. The magnetocrystalline anisotropy of the FeRh was neglected and due to its large saturation magnetization the shape anisotropy is predominant. The easy axis of the FePt was parallel to the z direction, normal to the film plane. The following value of the material constants were used:  $A^{FePt} = A^{FeRh} = 10^{-6}$  erg/cm and  $K^{FePt} = 2 \cdot 10^7$  erg/cm<sup>3</sup>.

In the micromagnetic simulations, as well as in the micromagnetic zones in the multiscale model, we used the discretization length of 1.5 nm (smaller than the domain wall width in FePt of 4 nm), therefore, the total number of cells in the film is 80 × 80 × 30. The validity of our micromagnetic simulations depends on the correct domain wall description. We have checked that the numerically calculated domain

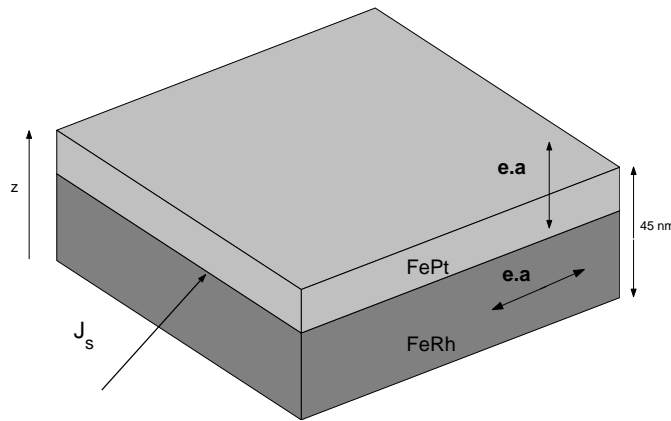


**Figure 3.15:** Schematic drawing of the system used to model FePt/FeRh films

wall profile in pure FePt has the correct width in comparison to the theoretical prediction. In Fig. 3.16 we present a comparison between a perpendicular exchange spring (the dependence  $M_z(z)$ ) calculated within 1-D atomistic approach and 3-D micromagnetic simulations when the exchange between the two layers has almost the bulk value. Although the two models give slightly different coercive fields, for applied fields close to the switching field the domain walls are almost identical. Therefore, our micromagnetic approach correctly describes the domain wall formation in this (strongly coupled) case.

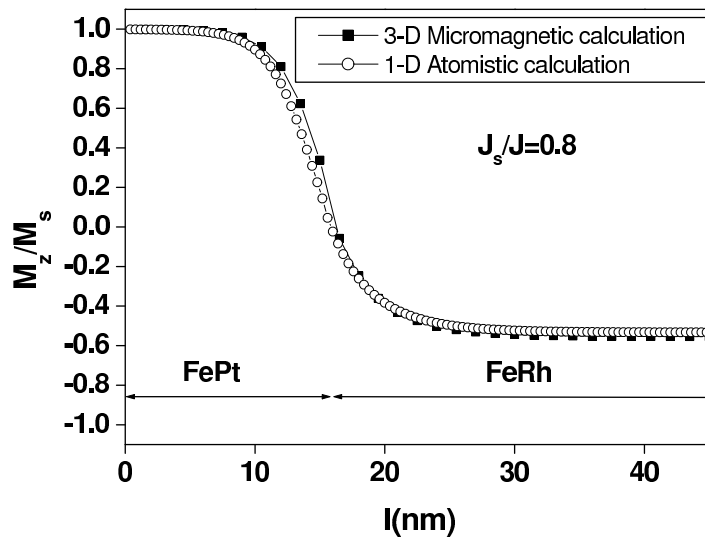


**Figure 3.16:** Comparison of the FePt/FeRh domain wall width for 3D micromagnetic and 1D atomistic approach for large interface exchange value and for applied field close to the switching field.

Now we will compare the calculations of the micromagnetic model with that of the multiscale model when the interfacial exchange is small. The multiscale model has been already described in Section 2.2.4, but in this case the atomistic region has twice the macromagnetic cell size in each material, giving a thickness of 3 nm treated atomistically on both the FePt and FeRh sides of the interface. The demagnetization curves for interfacial exchange value  $J_s/J = 0.1$  are shown in Fig. 3.17. Unlike the one-grain model, the hysteresis cycle of the FeRh part represents a rotation of the magnetization into the easy plane. In this case also an exchange spring is formed at the interface. However, this domain wall represents a magnetization rotation of 90 degrees rather than a 180 degree wall as in the isolated grain. This reversible rotation and the nucleation at positive fields is typical for a hard axis loop. The loops presents a jump corresponding to the depinning of the domain wall and the complete switching of the hard layer. We can observe that, in the multiscale model the complete reversal of the soft layer is not needed to reverse the hard layer. The results of

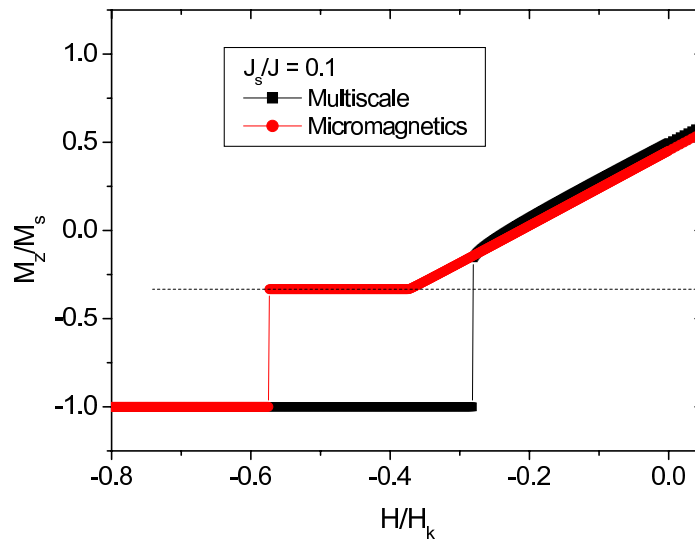


**Figure 3.17:** Magnetization curves calculated within the micromagnetic and multiscale models for an interfacial exchange coupling value of  $J_s/J = 0.1$ . The dashed line shows the total reversal of FeRh.

calculations of domain wall structures using the multi-scale model are shown in Fig. 3.18. It can be seen that there is a transition from the discontinuous domain wall structure at low  $J_s/J$  to a continuous wall at a critical value of  $J_c/J = 0.04$ . For  $J_s > J_c$  there is little evolution of the domain wall structure. The predictions of the multiscale model are in marked contrast to those of the micromagnetic approach. This is demonstrated comparing with Fig. 3.19, which shows the domain wall structures calculated using the micromagnetic model. Although the value  $J_s/J = 0.1$  is greater than the critical value  $J_c$  predicted by the multi-scale model, the micromagnetic calculation still predicts a discontinuous domain wall. This is because the micromagnetic determination of the exchange energy relies on a long-wavelength approximation, which underestimates the exchange energy associated with rapid spatial variation of the magnetization, thereby allowing discontinuous domain wall structures under conditions where these are not supported by the atomistic calculations. It appears that for the coercivity reduction, a continuous domain wall is necessary, as a consequence, the micromagnetic estimation of the critical exchange value is larger than the atomistic/multiscale estimation. Clearly, a discontinuous domain wall structure, which has an interfacial energy larger than that required to achieve a continuous domain wall, requires a larger field to initiate the propagation of the domain wall leading to magnetization reversal.

These limitations are also responsible for the failure of the micromagnetic model to predict saturation of the coercivity reduction until large values of interfacial exchange. The variation of the coercivity with interfacial exchange energy  $J_s$  for the

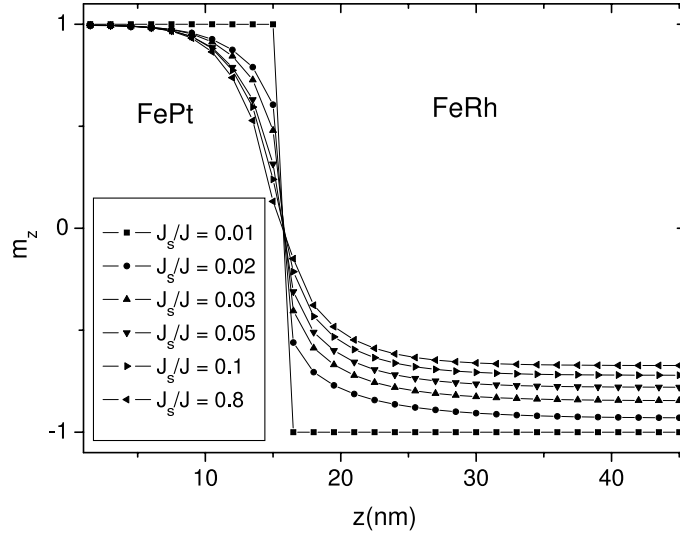


**Figure 3.18:** Domain wall structures calculated as a function of interfacial exchange ( $J_s$ ) given in units of bulk exchange ( $J$ ) using a multiscale model.

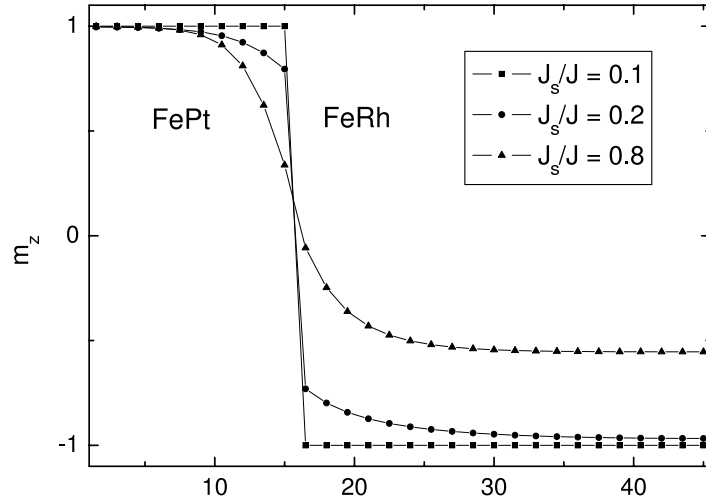


**Figure 3.19:** Domain wall structures calculated as a function of interfacial exchange using a micromagnetic model.

micromagnetic model is shown in Fig. 3.20. First we discuss the comparison with the “1D” model. Clearly, the micromagnetic model predictions differ significantly from the “1D” atomic scale model. It can be seen in Fig. 3.20, the “1D” model shows saturation in the coercivity reduction at around  $J_s/J = 0.2$ , whereas the micromagnetic model predicts a continuous (albeit slow) decrease up to the bulk value of exchange.

We can also compare our micromagnetic results with the analytical expressions of the pinning field Eq. (3.4). In our case  $K_{Soft} = 0$  yielding a pinning field

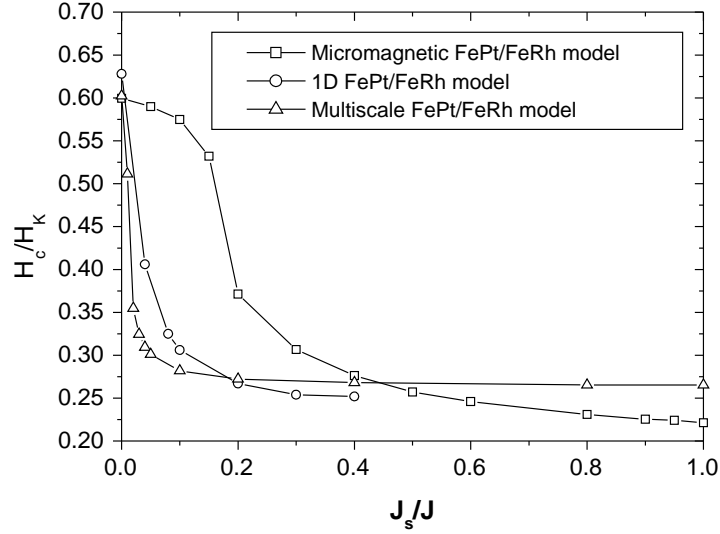


**Figure 3.20:** The variation of coercivity (given in units of anisotropy field  $H_k^{FePt}$ ) with interfacial exchange parameter for the micromagnetic and multiscale models in comparison with a “1D” atomic scale model.

$H_c/H_k^{FePt} = 1/4$  (cf. the value in Fig. 3.20). For the interfacial exchange value  $J_s = 0$  the coercive field of the FePt bilayer results from the shape and the magnetocrystalline anisotropies, whose contributions are opposite in sign:

$$H_c = \frac{2K^{FePt}}{M_s^{FePt}} - 4\pi M_s^{FePt}. \quad (3.6)$$

Using our model parameters, we obtain the switching field value  $H_c/H_k^{FePt} = 0.62$ . Our results from the simulations reasonably agree with these values (see Fig. 3.20).

In conclusion, we have demonstrated that the coercivity reduction in FePt/FeRh bilayers occurs via a complex reversal mechanism involving the penetration of an exchange spring from the soft FeRh into the hard FePt magnetic material. For weak interlayer coupling the standard micromagnetic approach cannot reproduce correctly this mechanism. We should notice here that several authors [Victoria 05b] incorporate in their micromagnetic model special boundary conditions resulting from the counting the number of atomistic magnetic moments at the interface. Namely, the interfacial exchange is supposed to be of the form:

$$J_s^* N_s \approx J_s^* (\Delta/d)^2 \quad (3.7)$$

where the  $J_s^*$  is the (reduced) atomistic exchange,  $N_s$  is the number of exchange-coupled magnetic moments across the interface,  $\Delta$ - the discretization size (cubic discretization is assumed for simplicity),  $d$  is the interatomic distance across the interface (cubic lattice is assumed for simplicity). It is clear that this approach gives a different strength of the micromagnetic exchange parameter used at the interface.

Since this parameter is in any case phenomenological, the results could be re-scaled. To illustrate this, we have also varied the discretization length in the micromagnetic approach. In this case we also used a square lattice with  $d = 0.4 \text{ nm}$  to simplify calculations. We modeled a grain of  $6 \text{ nm} \times 6 \text{ nm} \times 24 \text{ nm}$ , equal thicknesses of FePt and FeRh ( $12 \text{ nm}$ ) and anisotropy constant  $K^{\text{FePt}} = 7 \cdot 10^7 \text{ erg/cm}^3$ . The coercivities obtained for different discretization lengths are shown in comparison with the atomistic simulation in Fig. 3.21. The obtained coercivity presents an increasing reduction with a reducing discretization length, even for values of the discretization length below the lattice size. The fact that the coercivity curves do not saturate to a single curve for discretization lengths below a critical one is a failure of the micromagnetism to describe the soft/hard bilayer. However, all the micromagnetic curves collapse to a single curve if the interfacial exchange is rescaled by the factor  $d/(4\Delta)$ , which comes from the comparison of Eq. (2.25) and Eq. (3.7). Although the scaling is successful, it does not allow to make a limit of continuous exchange at the interface, and, therefore, the investigation of the whole range of interfacial exchange parameters. Additionally, this type of approach is essentially a multiscale approach for a step-like interface since it incorporates the atomistic knowledge at the interface assuming that all the parameters variations take place in one interatomic distance.

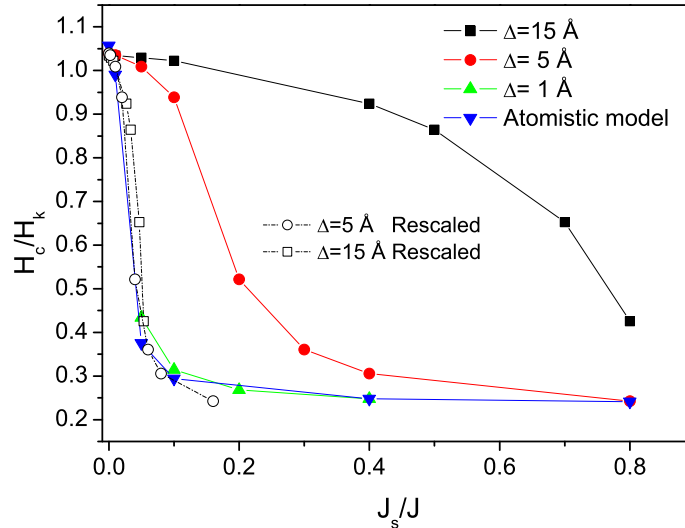


**Figure 3.21:** Comparison of the coercivity of a soft/hard grain in an atomistic model with a micromagnetic model with different discretization lengths  $\Delta$ . The dashed curves with hollow symbols are the rescaling of the interfacial exchange in micromagnetic simulations by the factor  $d/(4\Delta)$ .

### 3.6 Multigrain FePt/FeRh material

As has been pointed out in Ref. [Thiele 04b], the granular structure is an important feature of FePt recording medium and must be taken into account in the simulations. To reproduce this realistic feature, we have introduced granular structure in our multiscale model. We used the parameters and dimensions of Sections 3.4 and 3.5 to construct the multigrain material.

First, we will present the simulations based on the system of Section 3.5 ( $K^{FePt} = 2 \cdot 10^7 \text{ erg/cm}^3$ ) with the size of the FePt grain of 15 nm, grouping together  $10 \times 10 \times 10$  micromagnetic discretization units, which results in  $8 \times 8$  grains, as shown in Fig. 3.22. Since the grain size of FeRh may be much larger than that of FePt, the FeRh medium was considered to be continuous. The easy axes of FePt grains were considered to be distributed according to a Gaussian distribution with small dispersion  $5^\circ$ . The intergrain exchange parameter  $J_1^{FePt}$  was assumed to have a reduced value, with respect to the bulk value  $J$ . Fig. 3.23 represents hysteresis cycles corresponding to small, and intermediate intergrain exchange parameters and continuous FePt medium. The interfacial exchange parameter is also small in this case. The granular structure introduces additional nucleation centers so that the magnetization reversal process always starts earlier than that of the continuous medium. In the case of small intergrain exchange, the reversal process takes place “grain by grain”, while for intermediate intergrain exchange, once started, the reversal process proceeds in one collective reversal.

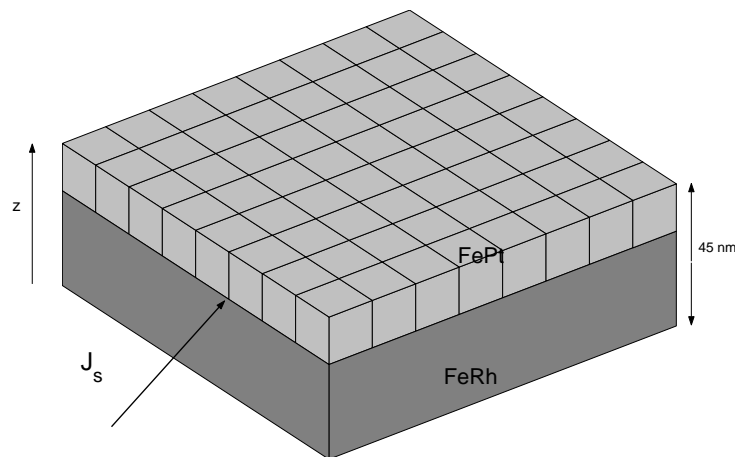


**Figure 3.22:** Diagram showing how the film is divided into grains.

In Fig. 3.24 we present the coercivity reduction for granular and continuum medium within the multiscale and micromagnetic approaches. Again, the micromagnetic approach shows that in order to achieve a significant coercivity reduction, a large interfacial exchange is necessary, whereas the multiscale approach shows a

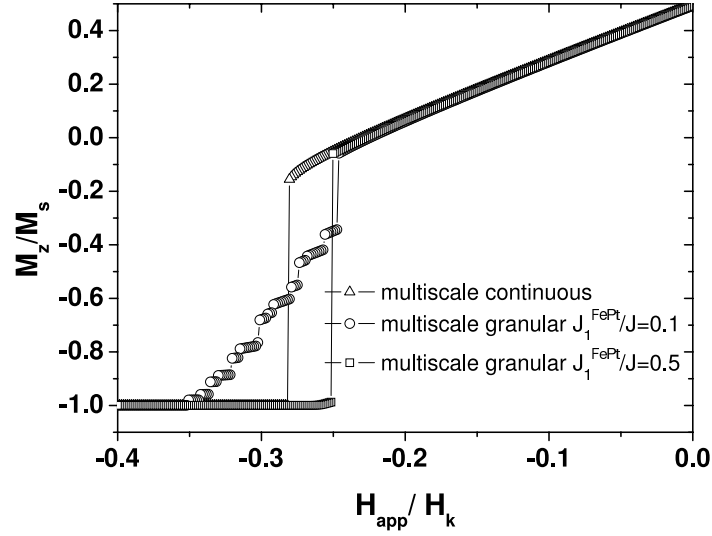


**Figure 3.23:** Simulated hysteresis cycles for 30 nm continuous FeRh/ 15 nm FePt granular media using multiscale model and  $K^{FePt} = 2 \cdot 10^7 \text{ erg/cm}^3$ .

significant coercivity reduction for interfacial exchange below 5% of the bulk value. This result is independent of the presence of the granular structure in FePt with or without appreciable intergrain exchange. It is clearly seen that for intermediate exchange values  $J_1^{FePt}/J$  the domain wall formed in FeRh penetrates in each grain at the same depinning field.

A remarkable reduction of the switching field (up to 20 times) could be achieved with thin hard layer (with thickness smaller than the exchange correlation length in hard material) and thick hard layer (with thickness higher than the exchange correlation length in soft material) and intermediate-to-full coupling. The reduction can be observed in the loop shown in Fig. 3.25 for an FePt thickness of 3 nm. However, this geometry also produces an effective coupling of hard grains through the exchange spring. A serious doubt may also arise on the signal-to-noise ratio in such implementation since the volume of soft material is much larger than that of the hard one.

Next, we will consider a thin film with the grain described in Section 3.4 ( $K^{FePt} = 7 \cdot 10^7 \text{ erg/cm}^3$ ) with granular structure for FePt (6 nm grain size) and continuous FeRh film. The FePt medium was considered granular with grain size of 6 nm. The system consisted of  $10 \times 10$  grains with periodic boundary conditions in X and Y directions. The soft magnetic layer was considered continuous in order to consider the possible coupling of hard magnetic medium through the soft one which could potentially deteriorate the recording medium performance. Fig. 3.26 represents a hysteresis cycle of 12 nm FePt/ 12nm FeRh thin film multilayer. For this small intergrain exchange value, distribution of switching fields has been observed suggesting

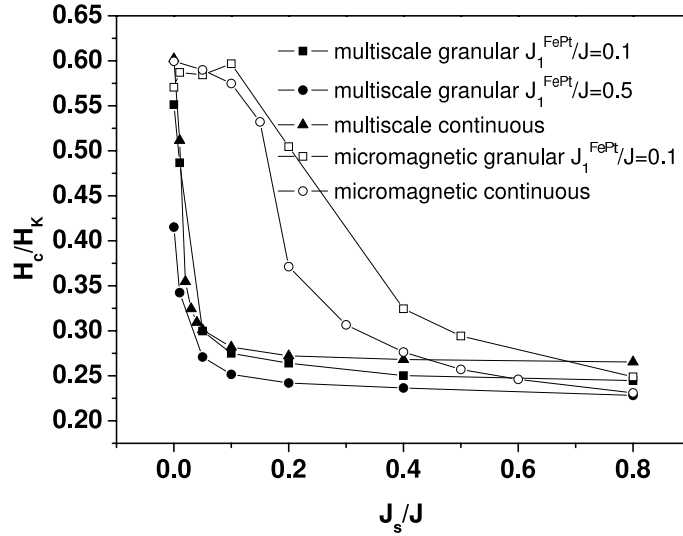


**Figure 3.24:** Coercivity reduction in granular and continuous medium within micromagnetic and multiscale approaches for  $K^{FePt} = 2 \cdot 10^7 \text{ erg/cm}^3$  and 30 nm FeRh/ 15 nm FePt.

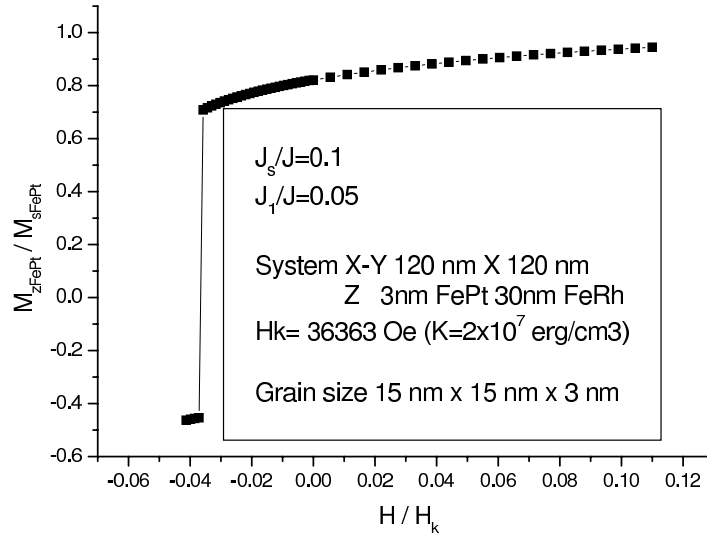


**Figure 3.25:** Hysteresis cycle of the continuous 30 nm FeRh/ granular 3 nm FePt thin film multilayer for  $K^{FePt} = 2 \cdot 10^7 \text{ erg/cm}^3$ ,  $J_1^{FePt}/J = 0.05$  and  $J_s/J = 0.1$ .

the almost independent grains behavior.

In the case where the thickness of FePt grain is 3nm, a large reduction in the coercivity of around 5 times has been observed for interfacial exchange parameter larger than 10% of the bulk value. This reduction is not as large as in Fig. 3.25 because of the difference in anisotropy value that determines a different pinning field. For small interfacial exchange value we observed again a distribution of the switching fields. However, for  $J_s/J \geq 0.1$  the demagnetization process of the granular medium

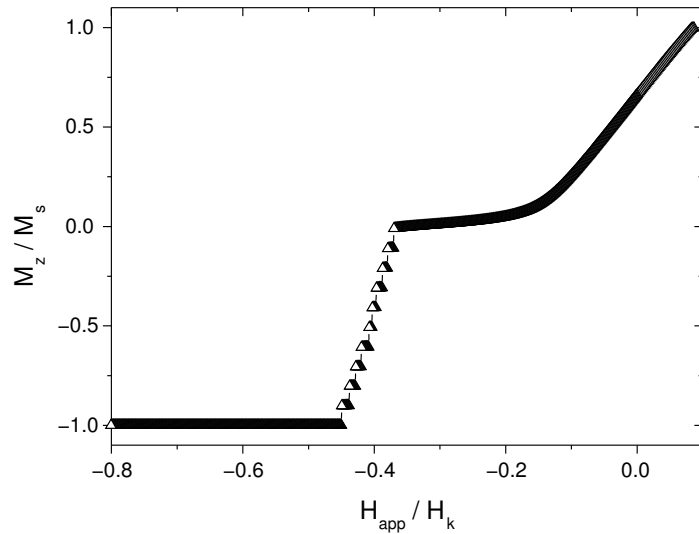


**Figure 3.26:** Hysteresis cycle for 12 nm granular FePt (with 6 nm grains) / 12 nm continuous FeRh thin film with for  $K^{FePt} = 7 \cdot 10^7 \text{ erg/cm}^3$ , and  $J_s/J = 0.05$  and  $J_1^{FePt}/J = 0.001$ .

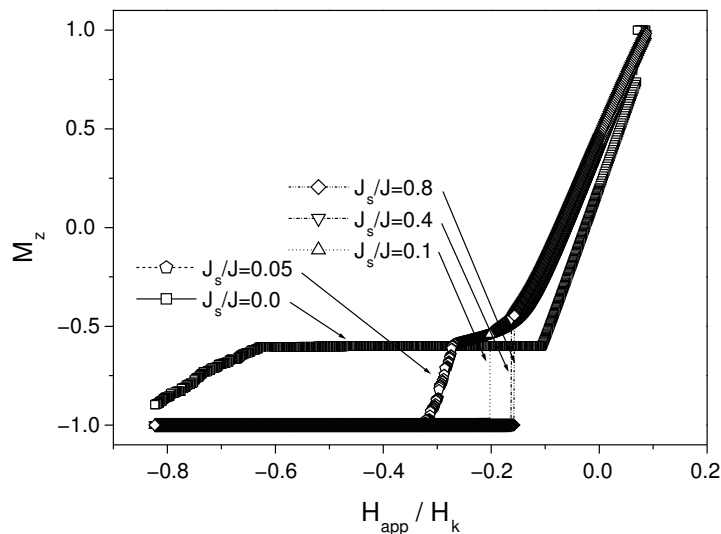


**Figure 3.27:** Hysteresis cycles of the continuous 12 nm FeRh/ granular 3 nm FePt thin film multilayer for  $K^{FePt} = 7 \cdot 10^7 \text{ erg/cm}^3$  and  $J_1^{FePt}/J = 0.001$ .

takes place in one single jump suggesting that the reversal process is determined in this case by the depinning field of the exchange spring and not by the individual switching field of each magnetic grain. For this case the FePt grains are coupled effectively through the continuous FeRh. Finally, we consider granular FePt medium on granular FeRh medium with perfect grain matching. We should note here that as was pointed out in Ref. [Thiele 04b], the growth of such grains would present crucial difficulties. The FeRh is considered with reduced intergranular exchange parameter

$J_1^{FeRh}$ . Fig. 3.28 compares the loops for a thin FePt layer and continuous and granular thick FeRh layer. The granularity of FeRh, avoiding the effective coupling through the soft material, allows the distribution of the switching fields in FePt, which is reflected in the form of the hysteresis loop.

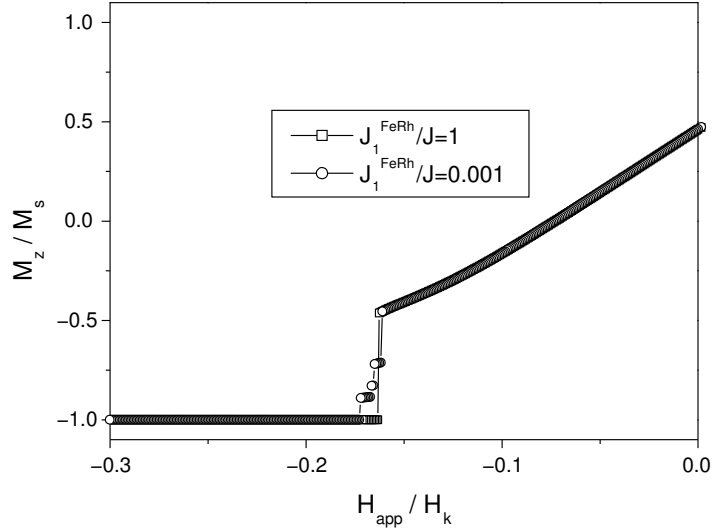


**Figure 3.28:** Hysteresis cycles of 12 nm FeRh continuous ( $J_1^{FeRh}/J = 1$ ) and granular ( $J_1^{FeRh}/J = 0.001$ )/ granular 3 nm FePt thin film multilayer for  $K^{FePt} = 7 \cdot 10^7 \text{ erg/cm}^3$ ,  $J_1^{FePt}/J = 0.001$  and  $J_s/J = 0.4$ . The grain size in FePt is 6 nm

### 3.7 Magnetization dynamics of an FePt/FeRh bilayer

In the magnetic recording, the writing process of a bit requires the application of a field of opposite direction to invert the magnetization. The recovery of the magnetization after the field pulse has to last few nano seconds and phenomena as ringing [Crawford 00] are completely undesired. A realistic simulation of magnetic media needs the inclusion of the writing head. However, we will include an homogeneous applied field to the study the dynamical switching, which is by itself an interesting question. We have simulated an FePt/FeRh thin film under a constant magnetic field using the LLG equation. The parameters of the LLG equation are: the damping  $\alpha = 0.05$  and the integration time step  $\Delta t = 1.56564 \cdot 10^{-16} \text{ s}$ . This time step does not allow to simulate large system sizes and in this case we have chosen the in-plane dimensions  $45 \text{ nm} \times 45 \text{ nm}$  (periodic boundary conditions) and the thicknesses  $15 \text{ nm}$  FePt and  $30 \text{ nm}$  FeRh. The interfacial exchange parameter is  $J_s/J = 0.1$  and the anisotropy  $K^{FePt} = 2 \cdot 10^7 \text{ erg/cm}^3$ . The field can not take

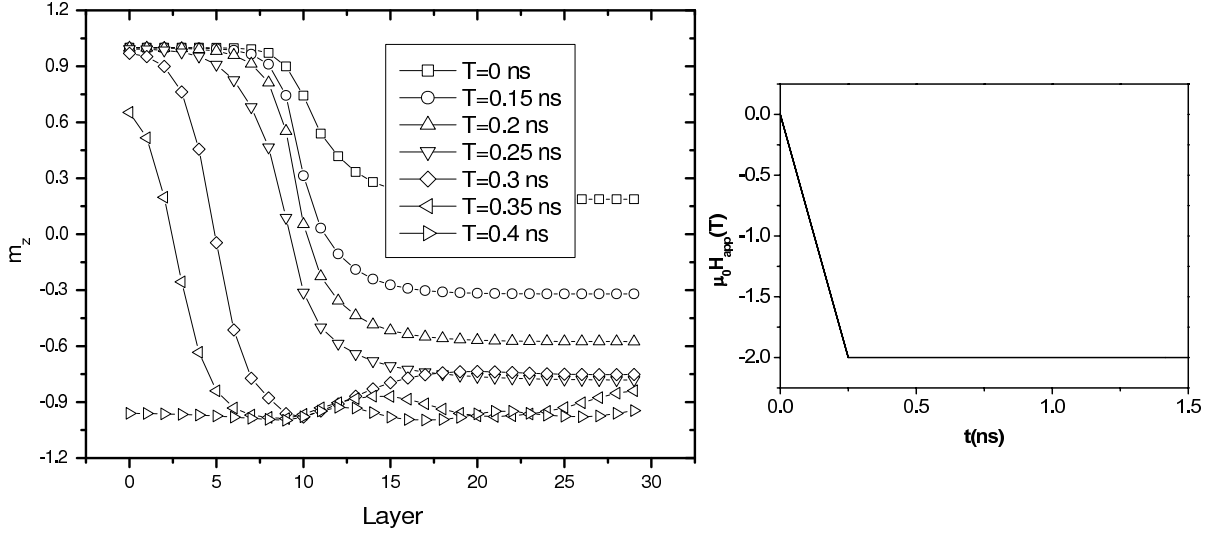


**Figure 3.29:** Magnetization profile in an FePt/FeRh film under a field pulse for different times. The field rise is plotted in the right figure.

any value immediately, due to physical limitations, and needs some time to reach its final value. The field rise time of the pulse was  $0.25 \text{ ns}$  and the maximum field  $H_{max} = 0.55H_k = 2 \text{ T}$ , which is slightly larger than the corresponding static coercivity for the film. To compare, the maximum field obtained from the current writing heads is  $1.7 \text{ T}$  [Kanai 05].

Fig. 3.29 represents the temporal evolution of the magnetization of the film. Before applying the field the initial state is the remanence, which includes a  $90^\circ$  domain wall, with the magnetization of the FePt pointing in the Z positive direction. The magnetization reversal process is found to essentially involve domain wall propagation, but is somewhat complex, and takes place in three distinct stages. In stage 1 there is a gradual propagation of the domain wall into the hard FePt phase. During this stage, the domain wall slowly changes its nature from  $90^\circ$  to  $180^\circ$  domain wall. The complete reversal of the FeRh layer, which is equivalent to the  $180^\circ$  domain wall, is not necessary to induce propagation of the domain wall into the FePt phase. During the second stage of the magnetization reversal process the magnetization in the FePt becomes more negative than that in the FeRh. This establishes a reverse domain wall, which propagates back into the FeRh layer, resulting in complete reversal of the whole system. The third stage consists in the relaxation of the magnetization to its new equilibrium value. In case the field is removed, this last stage includes the creation of a domain wall. The duration of this last stage has to be minimized in order to design a good magnetic recording media.

Additionally, the soft/hard bilayer presents very interesting dynamic properties. For example, if for a particular mode or spin-wave in one material there are no modes in the coupled material, then the interface between the two materials acts to

pin that particular mode in the first material, reducing the amplitude and changing the mode profile. This effect is known as dynamic pinning [Hoffmann 70] and can be tuned with an applied field. However, the study of spin waves in composite media is beyond the scope of this thesis and will be the focus of future work.

### 3.8 Generic Soft/Hard material: one grain simulation

The potential usage of the exchange spring media for magnetic recording applications requires the evaluation of both coercive field reduction and thermal energy barrier. The parameters of the system have to be chosen with the goal of maximizing both quantities. However, the number of such parameters, including the intrinsic material ones, does not allow the systematic search to obtain the best choice. Other parameters, as for example the grain size, are limited by the current growing techniques. In this section we will consider a generic soft/hard grain and study the effect of several combinations of saturation magnetization in the overall exchange spring performance. We considered the grain sizes  $6 \text{ nm} \times 6 \text{ nm}$  with the grain height  $7.5 \text{ nm}$  soft and  $7.5 \text{ nm}$  hard material. The anisotropy constants are  $K_{Hard} = 2 \cdot 10^7 \text{ erg/cm}^3$  and  $K_{Soft} = 0$ . The exchange interactions were taken from the models I and II for the FePt described in Section 3.3. For the saturation magnetization in the hard material we used the value of FePt,  $M_{Hard} = 1100 \text{ emu/cm}^3$ , and alternatively, a low value  $M_{Hard} = 250 \text{ emu/cm}^3$ , representing an hypothetical magnetic recording media. Accordingly, in the soft material we varied the saturation magnetization, starting from that of FeRh,  $M_{Soft} = 1270 \text{ emu/cm}^3$ , and decreasing it up to a low value  $M_{Soft} = 200 \text{ emu/cm}^3$ .

First, we will use the model I for the exchange interactions. Fig. 3.30 presents the coercivity field reduction as a function of interfacial exchange parameter  $J_s$ . First of all, we note that changing the saturation magnetization value in the soft magnetic material, we change its domain wall width since it is determined by the magneto-static interaction. Consequently, the coercivity mechanism undergoes a transition between two types of behavior. In the first case (high  $M_s^{soft}$ ) the exchange spring is formed. In the second case (low  $M_s^{soft}$ ), the magnetization reversal is homogeneous in each grain and can be represented by two-macrospins. The same type of transition was observed in Section 3.4 changing the thickness of the soft layer (see Fig. 3.13). In the low  $M_s^{soft}$  case we can distinguish also two types of behaviors. For low interfacial exchange the soft magnetic moment rotates and exerts an additional torque to the hard magnetic moment. For larger values of  $J_s$  the soft material will eventually be so coupled to the hard material that will be unable to rotate inde-

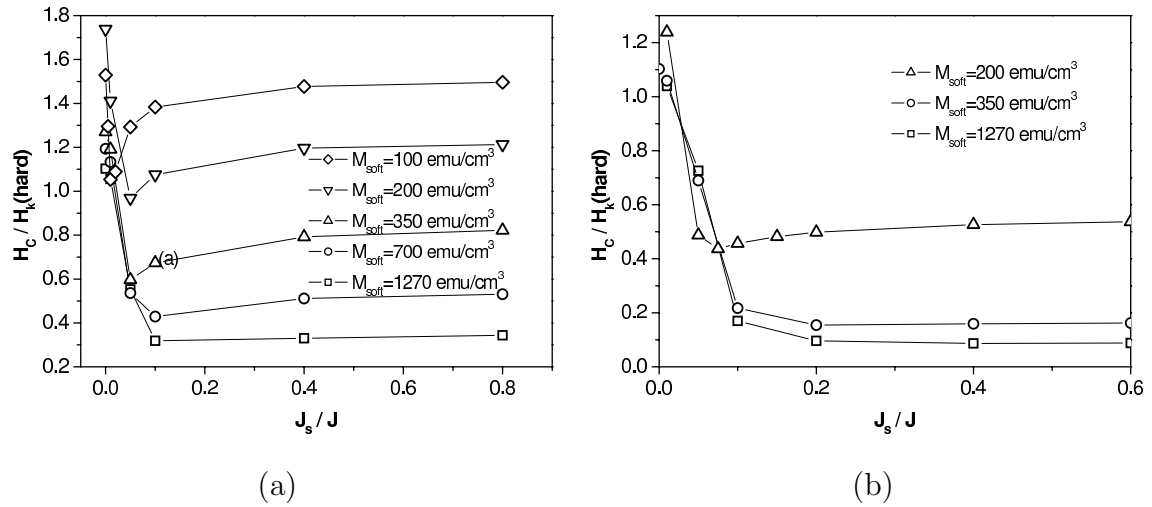


**Figure 3.30:** Coercivity of a soft/hard grain in model I as a function of the interfacial exchange  $J_s$  for different values of  $M_{\text{Soft}}$  corresponding to: (a)  $M_{\text{Hard}} = 1100 \text{ emu/cm}^3$  and (b)  $M_{\text{Hard}} = 250 \text{ emu/cm}^3$

pendently and the behavior will be collective. The corresponding demagnetization curves are shown in Fig. 3.31. This crossover of behaviors in the two-macrospins mechanism results in a minimum and, posteriorly, larger coercivity with increasing interfacial exchange as in Ref. [Richter 06]. This minimum has been observed experimentally in an exchange spring medium based on FeSiO(Soft) and CoPd(Hard) in Refs. [Wang 05a, Wang 05b]. In these experiments the variation of interfacial exchange is achieved through the interposition of a non magnetic material of different thicknesses, resulting in reduction of interfacial exchange with increasing thickness. From Fig. 3.30 it is clearly seen that the exchange spring formation is much more efficient in the coercive field reduction than the two macro-spins mechanism. In the exchange spring the coercivity reduction is saturated for the value of the interfacial exchange higher than 10%. This situation is favorable for an experiment since the field reduction is achieved for low exchange value and no tuning of the coupling parameter is necessary. In the opposite situation, the coercive field reduction is less, presents a narrow minimum for interfacial exchange values below 10% and the coercivity reduction experiences slight increase for higher  $J_s$  values. To have an optimum coercivity reduction, the value of the exchange should be tuned to this value which is experimentally hardly affordable. The qualitative behavior does not change, if in the hard material we consider large or low magnetization, Fig. 3.30(a) and Fig. 3.30(b) respectively, although the minimum in the coercivity for small  $M_{\text{Soft}}$  becomes less pronounced. Finally, Fig. 3.32 shows the calculation in model II. The two mechanisms are also present, but the interfacial exchange needed for saturation

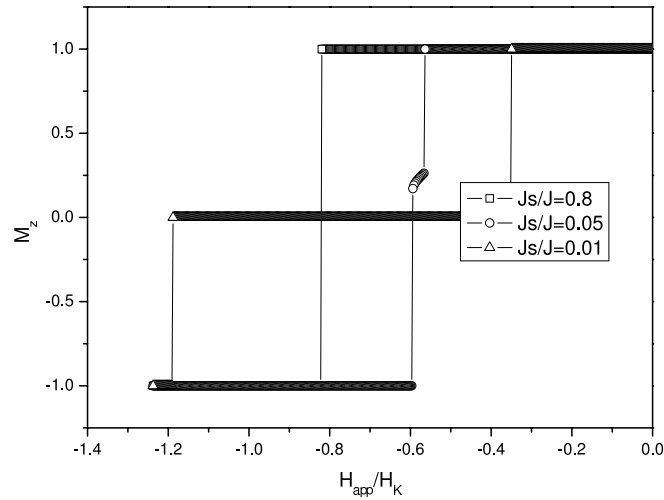


**Figure 3.31:** Hysteresis loops in a soft/hard grain simulated with the model I for  $M_{Hard} = 1100 \text{ emu/cm}^3$  and  $M_{Soft} = 350 \text{ emu/cm}^3$ .

is 20 – 40% of the bulk exchange, which is more difficult to reach. Additionally, the minimum, although present, is very shallow.

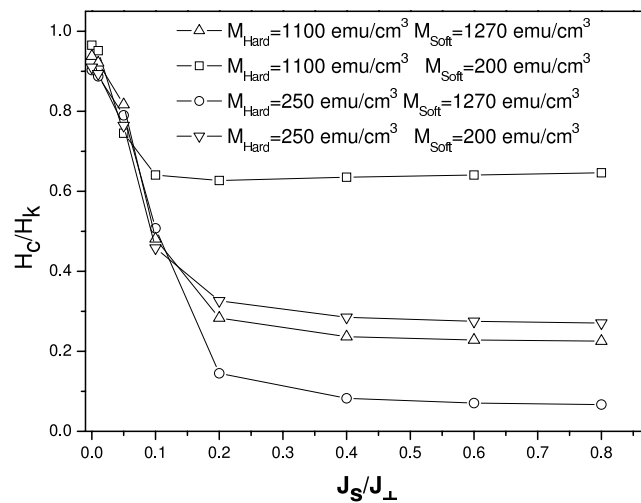


**Figure 3.32:** Coercivity of a soft/hard grain, normalized to the anisotropy field ( $2K_{hard}/M_{Hard}$ ) of the hard magnetic phase, in model II as a function of the interfacial exchange  $J_s$  for different values of  $M_{Soft}$  and  $M_{Hard}$ .

### 3.9 Energy barriers of individual grains

The requirement of large thermal stability of the recording media implies large energy barriers. Therefore, the next step is their evaluation for the grains of the

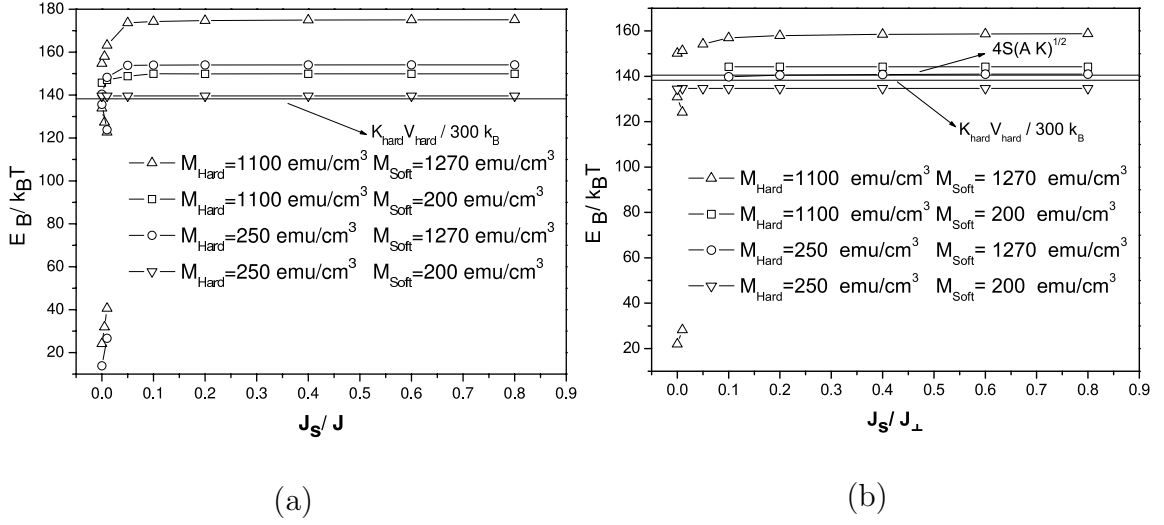


**Figure 3.33:** Energy barrier dependence on the interfacial exchange for different values of  $M_{Soft}$  and  $M_{Hard}$  in model I (a) and in model II (b)

previous section. For this purpose we used the Lagrange multiplier method presented in Section 2.3.6. Fig. 3.33 shows the energy barrier calculation for both model I and II as a function of the (perpendicular) interfacial exchange. Initially, the system is considered in the minimum that corresponds to all the moments aligned and to the coordinates  $\theta_{Hard} = \theta_{Soft} = 0$  in the energy landscapes plotted in Figs. 3.34 and 3.35. Recall that  $\theta$  is the average magnetization polar angle. The final state will be the equivalent minimum but with the moments pointing in the opposite direction, namely,  $\theta_{Hard} = \theta_{Soft} = \pi$ . For small values of the interfacial exchange, there is an intermediate minimum (see Fig. 3.34) and, therefore, additional reversal modes and saddle points. In this situation the soft grain can switch first with very low energy barrier and the hard magnetic material will follow with a reduced energy barrier value. However, the energy barrier corresponding to the inverse process, namely, returning to the original minimum, is very small and the probability of the inverse process to take place is high. Fig. 3.34 shows the effective energy landscape and relevant configurations. The saddle points configurations are curled to minimize the magnetostatic energy of the soft material. For interfacial exchange energy higher than 5% of the bulk exchange in all cases, the energy barrier values saturate as a function of  $J_s$  and correspond to collective reversal. The collective modes are different for the two models. In model I the thermal mode is almost coherent (see Fig. 3.36(a)). The maximum energy barrier value is determined by the quantity  $\Delta E_B^{max} = K_{eff} V \approx (K_{hard} + \pi M_{Soft}^2 + \pi M_{Hard}^2) V_{Hard}$ . In the model II, the value of the energy barrier coincides with the domain wall energy in the hard magnetic material as observed by D.Suess [Suess 05b] and the saddle point is a domain wall centered in the hard material (see Fig. 3.36(b)). These differences can be appreciated in the effective energy Fig. 3.35. If the point  $\theta_{Hard} = \theta_{Soft} = \pi/2$

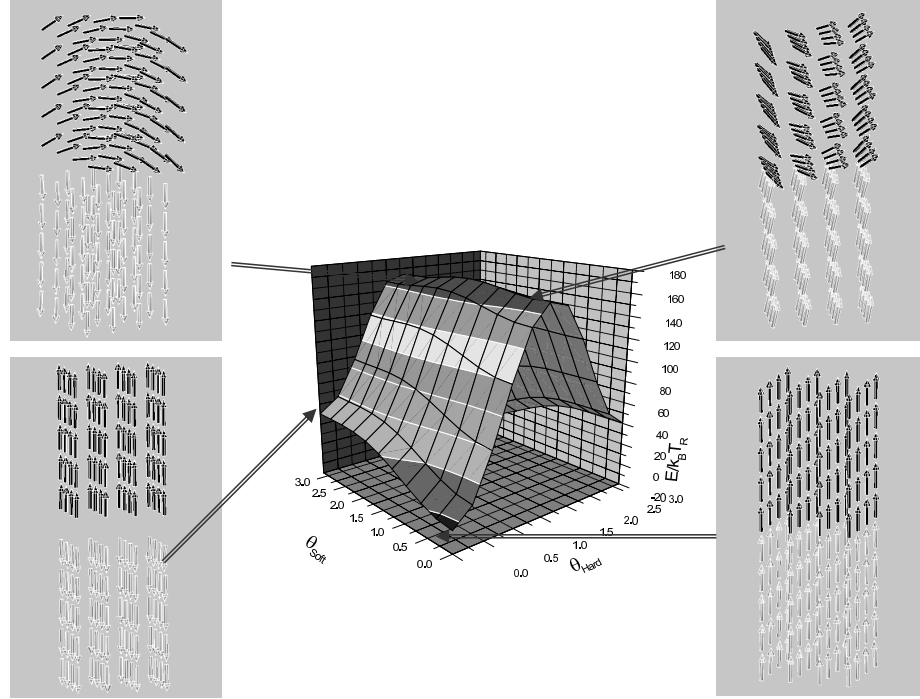


**Figure 3.34:** Effective energy landscape and magnetic moment configurations in the model I for  $M_{Hard} = 1100 \text{ emu/cm}^3$ ,  $M_{Soft} = 1270 \text{ emu/cm}^3$  and  $J_s/J = 0.01$  and corresponding configuration for saddle points and minima.

is the saddle point, the energy barrier corresponds to coherent rotation. For a non-homogeneous mode the saddle point has to be elsewhere as in Fig. 3.35(b).

To get a better understanding of the energy barriers in a soft/hard material, we can examine the case of model I for  $M_{Hard} = 1100 \text{ emu/cm}^3$ ,  $M_{Soft} = 1270 \text{ emu/cm}^3$  with a model similar to that of Ref. [Victoria 05a]. The model supposes a macro-spin for each material. In such a model the energy is:

$$E = -K_1 V \cos^2 \theta_1 - K_2 V \cos^2 \theta_2 - J_s N_{at} \mathbf{m}_1 \cdot \mathbf{m}_2 \quad (3.8)$$

where  $K_1 = K_{Hard} + \pi M_{Hard}^2$  and  $K_2 = \pi M_{Soft}^2$  are the effective anisotropy constants,  $N_{at} = 529$  is the number of atoms in the surface,  $V = 6 \times 6 \times 7.5 \text{ nm}^3$  is the volume of each material and finally  $\mathbf{m}_1 = (\cos \phi_1 \sin \theta_1, \sin \phi_1 \sin \theta_1, \cos \theta_1)$  and  $\mathbf{m}_2 = (\cos \phi_2 \sin \theta_2, \sin \phi_2 \sin \theta_2, \cos \theta_2)$  are the unit vector of the macrospin of each grain. To analyze the problem, we have to consider the energy gradient and the Hessian matrix. For large values of  $J_s$  there is only one energy barrier corresponding to the point  $\theta_1 = \theta_2 = \pi/2$  which value is  $\Delta E_B = K_1 V + K_2 V$ . For small interfacial exchange, there are additional barriers and saddle points similar to the ones plotted

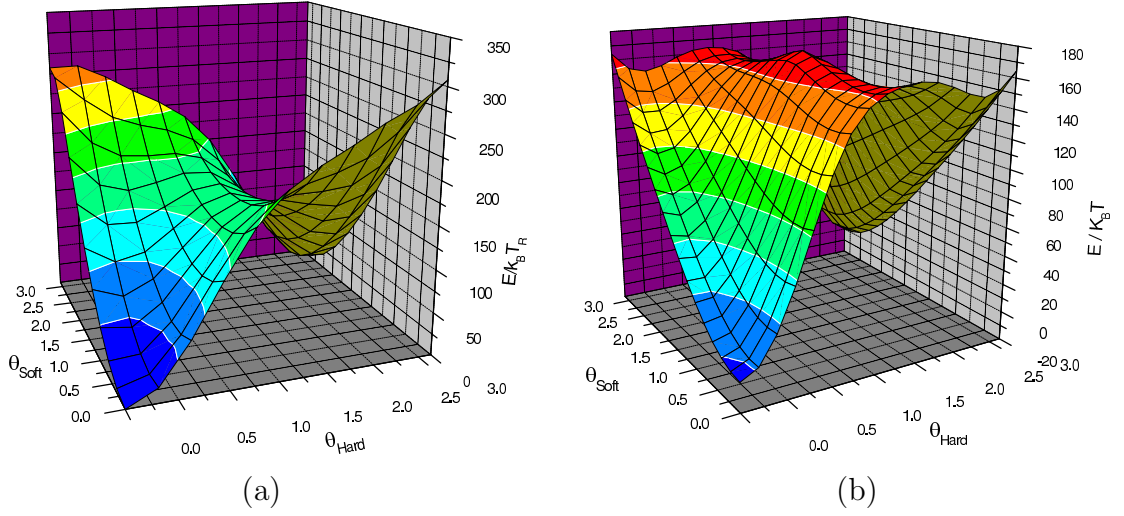


**Figure 3.35:** Effective energy landscapes : (a) Model I  $M_{Hard} = 250 \text{ emu/cm}^3$ ,  $M_{Soft} = 1270 \text{ emu/cm}^3$  and  $J_s/J_{\perp} = 0.4$  (b) Model II  $M_{Hard} = 250 \text{ emu/cm}^3$ ,  $M_{Soft} = 1270 \text{ emu/cm}^3$  and  $J_s/J_{\perp} = 0.2$ .

in Fig. 3.34. The critical exchange for the crossover between the region is:

$$J_{red,crit} = \frac{2K_1K_2}{N_{at}J(K_1 + K_2)}. \quad (3.9)$$

In our system  $J_{red,crit} = 0.0553838$ . Finally, we can compare the analytical results with our simulations for the same values of the constants. From Fig. 3.37, it is clear that there is a good quantitative and qualitative agreement. These results indicate that the two macro-spins is a good approximation for small interfacial

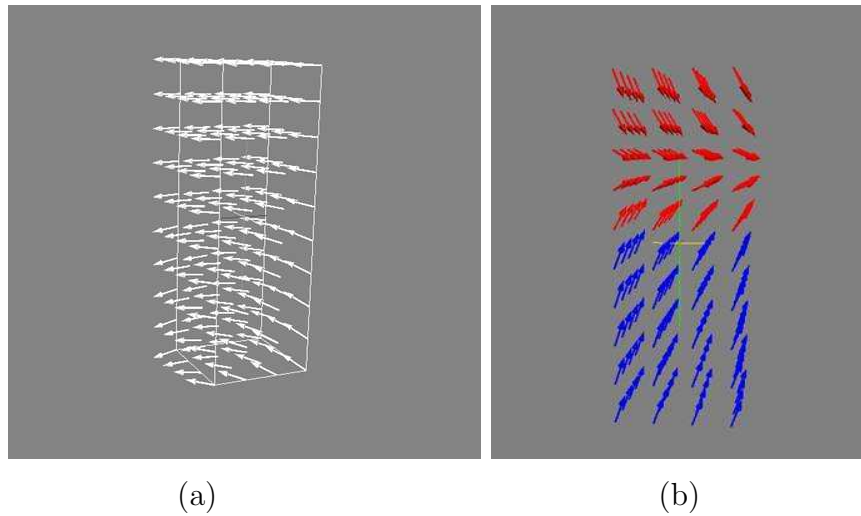


**Figure 3.36:** Saddle point configuration for different mechanism: (a) Coherent rotation (Model I) (b) Domain wall (Model II).

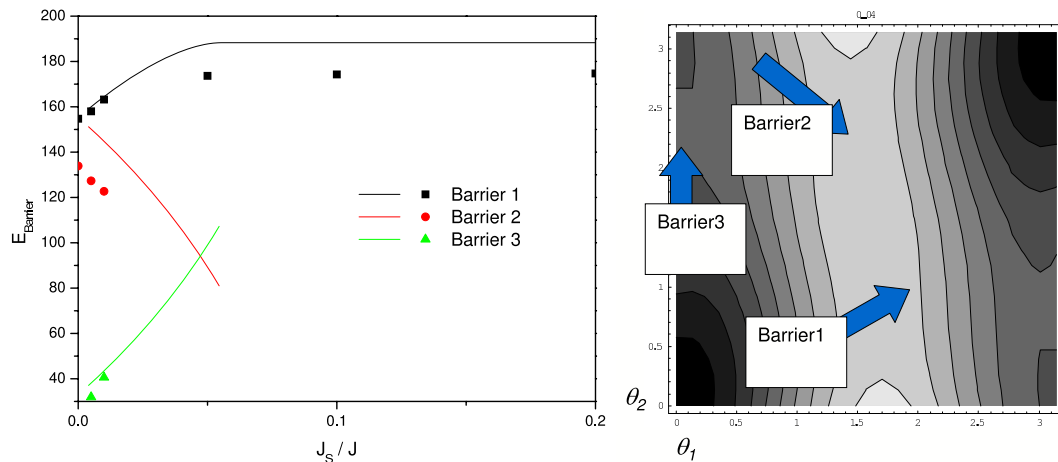


**Figure 3.37:** (a) Comparison between the analytical model (solid lines) and numerical calculations (symbols) for  $M_{\text{Hard}} = 1100 \text{ emu/cm}^3$  and  $M_{\text{Soft}} = 1270 \text{ emu/cm}^3$  in model I. (b) Energy contour plot from Eq. (3.8) for  $J_s/J = 0.05$ .

exchange. Nevertheless, this model is not valid for large exchange, where highly nonhomogeneous modes are expected.

### 3.10 Multigrain simulations in generic soft/hard magnetic material

The single grain of the previous sections is, somehow, an unrealistic system but can represent isolated grains as those present in patterned media. In the case of conventional perpendicular recording thin film, the real sample will be a collection of magnetostatically and exchangeably coupled grains. In previous works on composite media, the influence of other grains inside the film on a particular grain have been studied on the bases of an approach similar to the mean-field approximation [Suess 07]. In order to include the magnetostatic interaction between grains in a multigrain thin film we have modeled a system of  $3 \times 3$  grains with periodic boundary conditions in X and Y. We have used the model II for the exchange interactions. The grains are supposed to be exchangeably decoupled  $J_{\text{int}} = 0.0$ . The energy barrier is calculated constraining only the hard layer of the central grain and relaxing the whole system.

Fig. 3.38 shows the energy barrier and the coercivity as a function of the interfacial exchange in the film. The coercivity behavior is very similar to that of the single grain (see Fig. 3.32), but with an easy-plane anisotropy due to magnetostatics, which results in additional reduction of coercivity for small interfacial exchange. Compared with the isolated grain (see Fig. 3.33(b)), the energy barrier

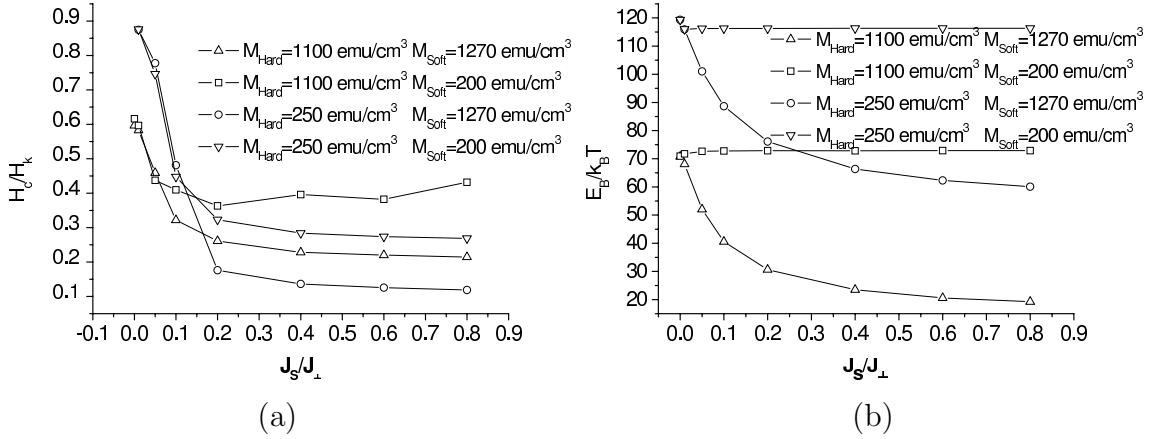


**Figure 3.38:** (a) Coercive field, normalized to the anisotropy field ( $2K_{Hard}/M_{Hard}$ ), and (b) energy barrier as a function of the interfacial exchange parameters for composite multigrain magnetic media.

of the grain inside the film is drastically reduced. Furthermore, the energy barrier value decreases with increasing the interfacial exchange. The explanation to these facts can be found in the magnetization distribution shown in Figs. 3.39 and 3.40. The remanent state in the film is a wall centered at the interface and the saddle point is a wall centered in the hard grain. In the ideal case of a infinitely long wire P. Loxley [Loxley 01] derived an expression for the energy barrier:

$$E_B = 4S\sqrt{AK_{Hard}} - 4S\sqrt{AK_{Soft}} \quad (3.10)$$

where  $S$  is the area of the interface. To derive this expression the original minimum

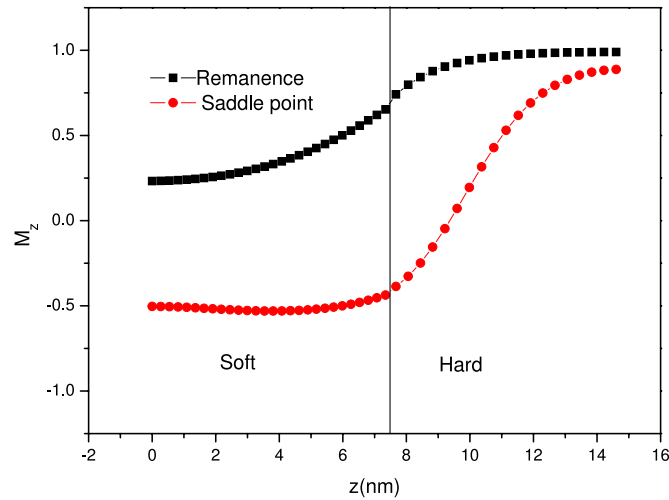


**Figure 3.39:** Saddle point and remanence magnetization (minimum) profiles for a central grain in a multigrain film with  $K_{Hard} = 2 \cdot 10^7$  erg/m<sup>3</sup>,  $M_{Hard} = 1100$  emu/cm<sup>3</sup>,  $M_{Soft} = 1270$  emu/cm<sup>3</sup> and  $J_s/J_{\perp} = 0.8$ .

was considered to be a domain wall centered in the soft layer. If the minimum of the system corresponds to the situation when all the moments are aligned with the easy axis, the energy barrier is  $E_B = 4S\sqrt{AK_{Hard}}$ , which coincides with the case of the domain wall mechanism of the previous section. The magnetic configurations that appear in our calculations are different from these two cases. In our case the domain wall does not fit into the soft magnetic material and, consequently, the domain wall in the minimum configuration is centered at the interface. However, Eq. (3.10) can give an insight into the physical origin of the reduced energy barrier: the shape anisotropy originated from the inclusion of the isolated grain in a film leads to the minimum different from that of the saturated state and reduces the energy barrier. Due to the dipolar origin of the anisotropy in the studied case, this reduction is less pronounced for small magnetization values as seen in Fig. 3.38. The reduction of the energy barrier with increasing exchange is due to the fact that the domain wall formation is more effective with more exchange coupling.

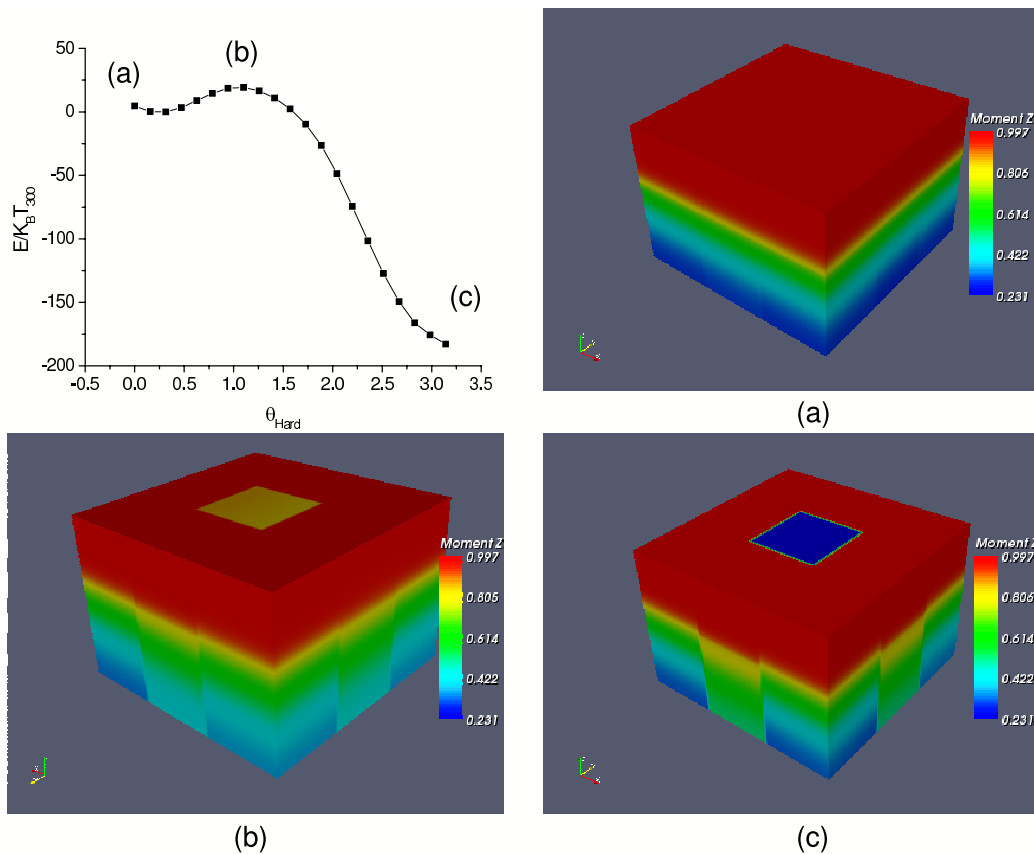


**Figure 3.40:** Effective energy plot (top left) and corresponding minima (a),(c) and saddle point (b) for a multigrain composite media with  $M_{Hard} = 1100 \text{ emu/cm}^3$  and  $M_{Soft} = 1270 \text{ emu/cm}^3$ .

In the configurations represented in Fig. 3.40 we can see clearly how the mo-

ments configurations of other grains are affected by the central grain, due to the magnetostatic interaction. This effect is neglected in the mean-field approximation implemented in Ref. [Suess 07], which reduces the applicability of that approach. From Fig. 3.40 we can see that the final minimum, which is not equivalent to the initial one, is deeper because this form of flux closure allows more alignment with the easy axis with the cost of relatively low magnetostatic energy. The energy barrier reduction is an effect not desirable in magnetic recording. Possible solutions are a soft material with non-zero perpendicular anisotropy or a small saturation magnetization value. These solutions will affect the coercivity reduction of the bilayer.

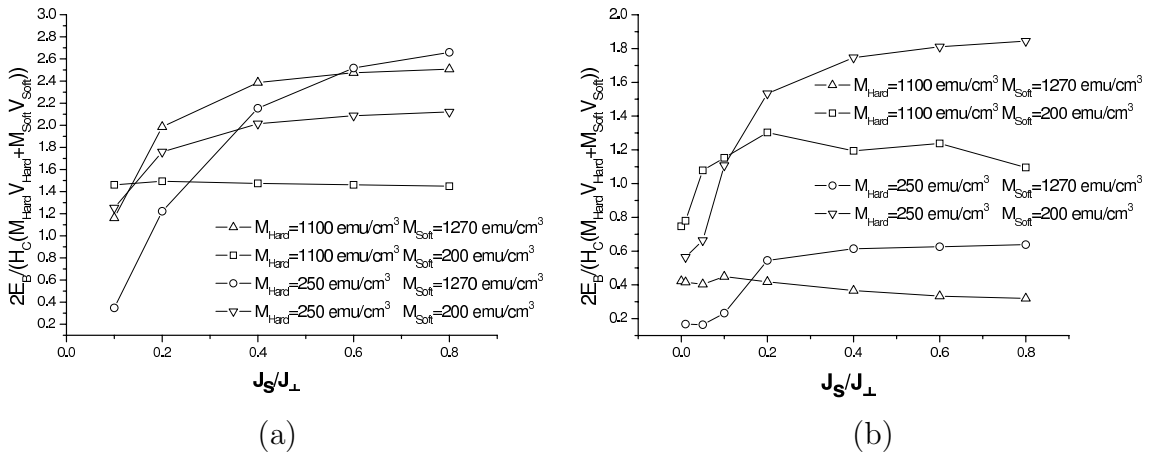


**Figure 3.41:** Figure of merit  $2E_B / [H_c \sum_i M_s^i V_i]$  as a function of the interfacial exchange parameters for composite magnetic media in the case of: (a) individual magnetic grain and (b) multigrain magnetic media.

### 3.11 Figures of merit

In magnetic recording applications the energy barrier value has to be maximized in order to obtain large thermal stability, whereas the coercivity has to be minimized in order to be below the writing head maximum field. To compare the performance of different media R. Victora [Victora 05a] proposed a figure of merit, considering the ratio between both quantities defined by  $2E_B / [H_c \sum_i M_s^i V_i]$ . According to the requirements, this figure of merit has to be maximized to obtain an optimum recording media. With this definition, the performance is compared with a bilayer in which both materials rotate coherently, which has the coercive field given by Eq. (3.1) and the energy barrier by Eq. (3.2). This bilayer has a figure of merit of 1. The maximum value of this figure of merit is 4 [Lu 07]. In Fig. 3.41 we present for comparison the figure of merit for different media calculated in the previous sections

in the case of an individual grain and a multigrain system (see Figs. 3.32, 3.33 and 3.38).

In the case of one-grain system, the best performance for  $J_s/J_\perp > 0.2$  corresponds to the media with high soft and hard layers magnetization mostly due to the additional shape anisotropy. The media with low magnetization hard layer and high magnetization soft layer is unfavorable for small and intermediate exchange but has the best performance for completely coupled system. As could be noticed here, the best performance in the case of multigrain systems corresponds clearly to the case of small magnetization soft and hard layers. However, this combination is benefited from the inclusion of the saturation magnetization in the denominator of the figure of merit. More than 20 – 40% of the exchange is necessary in this case in order to maximize the figure of merit. The behavior in all the cases does not reach saturation. The difference in the best media for multigrain and one grain systems stresses the importance of performing realistic granular simulations to obtain the parameters that optimize the composite media.

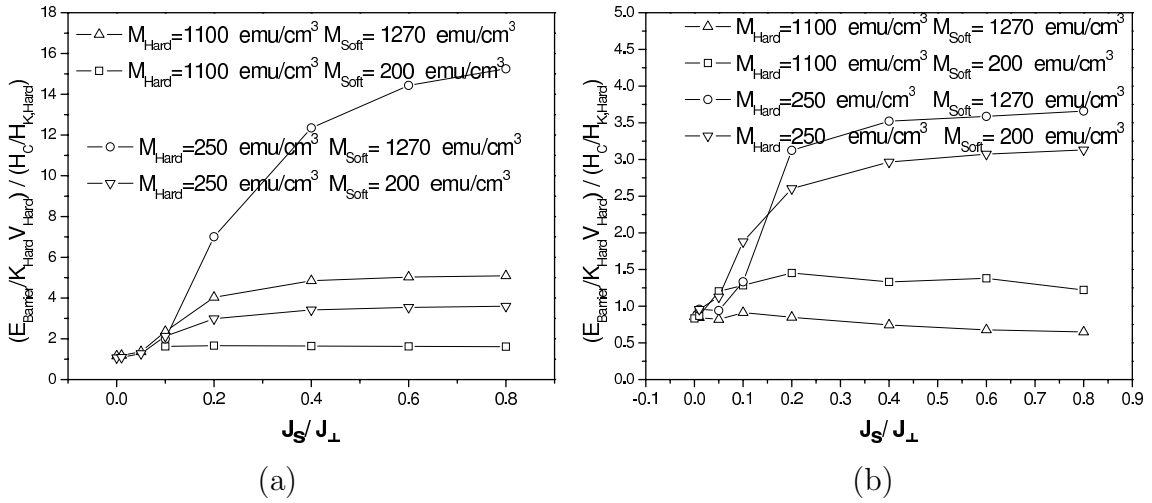


**Figure 3.42:** Figure of merit  $(E_B/K_{Hard}V)/(H_c/H_{k,Hard})$  as a function of the interfacial exchange parameters for composite magnetic media in the case of: (a) individual magnetic grain and (b) multigrain magnetic media.

We can also evaluate the media performance using a different figure of merit that normalize the quantity to the parameters of the hard layer:  $(E_B/K_{Hard}V)/(H_c/H_{k,Hard})$  (see Fig. 3.42). Both figures of merit are equivalent for single media. This way, we compare the bilayer with a hard phase grain (with the same volume than the hard phase in the bilayer) that switches coherently. From this new point of view, the combination that obtains the largest figure of merit is  $M_{Hard} = 250 \text{ emu/cm}^3$  and  $M_{Soft} = 1270 \text{ emu/cm}^3$  in both multigrain and one-grain cases.

Finally, there is an intrinsic limitation in the optimization of two quantities

only based on their ratio. The obtained set of parameter can optimize one of the magnitudes, while the other could have an unrealistic value. Additionally, the way the figure of merit is constructed could favor one or another material parameter combination and give different final conclusion. The two figures of merit of this section favor the combinations with small saturation magnetization in the hard layer, partially, because its presence in the denominator. Figs. 3.32, 3.33 and 3.38 represent a better picture of the media performance because they represent energy barriers and coercivity in real units. These values should be optimized to get in real units the switching fields below  $1.7 T$  and energy barriers higher than  $60 k_B T$ .

### 3.12 Conclusions

In summary, we have studied the field and thermal magnetization switching in soft/hard bilayers for magnetic recording application. Both can consist in a complex reversal mechanism involving the penetration of an exchange spring from the soft into the hard magnetic material. Special attention has been given to the case when the hard material is FePt and the soft material is FeRh. From our results we can conclude the following:

- The atomistic model indicates that penetration to the length scale of few atomic units may be sufficient to induce the domain wall propagation in a hard material. However, the latter is not allowed in the micromagnetic model due to the lack of discretization and this limitation is responsible for the failure of the micromagnetic model to predict the coercivity at low interfacial exchange. This emphasizes the necessity of atomistic and, in general, multiscale models to describe properly the role of interfaces in the magnetization reversal process. The result may have a general importance for all cases where the influence of small exchange on the switching properties is considered, such as two-phase permanent magnets [Fischer 98, Schrefl 94].
- From the point of view of an FePt/FeRh bilayer we have demonstrated that a small amount of interfacial exchange could suffice to decrease the coercivity of FePt by up to 2 – 5 times. The prediction of coercivity saturation at relatively low interfacial exchange energy is of practical significance. Clearly, the production of bilayer systems with this level of exchange energy is necessary in order to maximize the reduction in coercivity. A further consideration arises from the fact that the reduction in  $H_c$  is very rapid for small  $J_s/J$ . This means that in this region any local fluctuations in the exchange energy strength will give a contribution to the switching field distribution (SFD) over and above those arising from the dispersion of the intrinsic properties, principally, the

anisotropy and the grain volume. Given that a narrow SFD is required for good recording properties, it would appear to be desirable to develop bilayers with exchange energy in the saturation region. The degree of exchange energy in real experimental bilayer systems is not well known and difficult to quantify. However, the interfacial exchange is generally rather small, and it may be that even such relatively small values as  $J_s/J = 0.04$  may be beyond the abilities techniques such as sputtering, and thus it may be possible that successful composite media may require molecular-beam epitaxy or some other advanced technique.

- The granular structure of FePt necessary for magnetic recording application does not modify this conclusion, at least provided that the grain size of the soft material is much larger than that of FePt. However, continuous soft layers are shown to give rise to an effective exchange coupling within the grains of the hard FePt layer.
- The domain-wall assisted mechanism (high  $M_s^{soft}$ ), in agreement with the previous predictions [Dobin 06], is demonstrated to be more efficient in the reduction of the coercivity than the two-macrospin rotation mechanism (low  $M_s^{soft}$ ), considered in Ref. [Victora 05a].
- The differences between an isotropic model for exchange (Model I) and the one with more realistic parameters for the hard phase ( $L1_0$  FePt) (Model II) in the energy barrier calculations demonstrate the importance of using correct material properties for simulations of composite media. This again emphasizes the role of multiscale modeling, when the ab-initio results are incorporated into micromagnetics.
- We also showed that in the generic bilayer some moderate exchange amount (20 – 40%) is necessary in order to achieve low coercivity and the maximum figure of merit via the exchange spring effect. This differs from the FePt/FeRh case showing that the exchange saturation value depends on the real material parameters.
- The direct calculation of the magnetostatic interactions in a multigrain film, more realistic than the mean-field approximation, confirmed that in conventional perpendicular thin film recording the use of low-magnetization hard phase is necessary and that the state of the neighboring grains is altered by the state of the central one.

### 3.13 Conclusiones en castellano

En resumen, hemos estudiado la inversión de la imanación tanto térmica como por campo externo en bicapas magnéticas blando/duro para la grabación magnética. Ambos fenómenos pueden consistir en un complejo mecanismo, incluyendo la penetración de un muelle de canje desde el material blando hacia el duro. Se ha dado especial atención al caso en el cual el material duro es FePt y el material blando es FeRh. De nuestros resultados se puede concluir lo siguiente:

- El modelo atomístico indica que una penetración del orden de pocas unidades atómicas puede ser suficiente para inducir la propagación de la pared hacia el material duro. Sin embargo, esto último no está permitido en el modelo micromagnético debido a la falta de discretización y esta limitación es responsable del fallo del modelo micromagnético a la hora de predecir la coercitividad para bajo valor del acoplo en la intercara. Esto enfatiza la necesidad de modelos atomísticos y en general, modelos multiescala para describir apropiadamente el papel de la intercara en el proceso de inversión de la imanación. Este resultado puede ser de importancia general para todos aquellos casos donde se considera la influencia de un pequeño parámetro de intercambio en la coercitividad, tales como imanes permanentes compuestos de dos fases [Fischer 98, Schrefl 94].
- Desde el punto de vista de una bicapa de FePt/FeRh hemos demostrado que un pequeño valor del intercambio en la superficie puede ser suficiente para reducir la coercitividad hasta entre 2 y 5 veces. La predicción de la saturación de la coercitividad para valores pequeños de intercambio en la intercara es de importancia práctica. Sin duda, la producción de sistemas bicapa con este nivel de valor de intercambio es necesaria para conseguir maximizar la reducción de la coercitividad. Otra consideración adicional surge del hecho que la reducción de  $H_c$  es muy rápida para valores pequeños  $J_s/J$ . Esto significa que en esta región cualquier tipo de fluctuación local de la intensidad del valor de intercambio dará una contribución a la distribución de campos coercitivos por encima y por debajo de aquellas originadas por la dispersión de las propiedades, principalmente la anisotropía y el volumen del grano. Dado que una distribución estrecha de campos coercitivos es necesaria para obtener buenas propiedades, sería deseable crear bicapas con intercambio interfacial en la región de saturación. El valor del parámetro de intercambio interfacial no está bien establecido y es difícil de cuantificar. Sin embargo, el intercambio interfacial es normalmente bastante pequeño y puede ser que incluso un valor de  $J_s/J = 0.04$  esté por encima de las capacidades de técnicas como sputtering y por lo tanto puede ser posible que el medio pueda requerir crecimiento epitaxial por haz molecular u otras técnicas avanzadas.

- La estructura granular necesaria para aplicaciones de grabación magnética no modifica la anterior conclusión, siempre y cuando el tamaño de grano en el material blando es mucho más largo que en el FePt. No obstante, capas continuas de material blando dan lugar a un acoplo de intercambio efectivo dentro de los granos de la capa de material duro.
- El mecanismo asistido por pared de dominio, correspondiente a un valor elevado de  $M_s^{soft}$ , confirmando las predicciones previas, es mucho más eficiente en la reducción de la coercitividad que el mecanismo de rotación de dos macrospines, correspondiente a un valor pequeño de  $M_s^{soft}$  y considerado en Ref. [Victoria 05a].
- Las diferencias entre un modelo isotrópico del intercambio (Model I) y otro basado en parámetros más realistas para la fase dura ( $L1_0$  FePt) (Model II) en el cálculo de barreras de energía pone de relieve la importancia de usar parámetros correctos para las propiedades del material en simulación de medios compuestos de dos fases. Esto otra vez enfatiza el papel de los modelos multiescala, donde resultados ab-initio son incorporados en el micromagnetismo.
- También hemos demostrado que en una bicapa basada en materiales genérico una intensidad moderada del intercambio (20 – 40%) es necesaria para lograr baja coercitividad y la máxima figura de merito usando el efecto de muelle de canje.
- El cálculo directo de la interacción magnetostática en una lámina compuesta de granos, más realista que la aproximación de dicha interacción entre granos mediante campo medio, confirma que en películas delgadas para la grabación magnética perpendicular el uso de fases duras con pequeña imanación es necesario y que el estado de los granos vecinos es afectado por el estado del grano central.

## Bibliography

- [Asti 06] G. Asti, M. Ghidini, R. Pellicelli, C. Pernechele, M. Solzi, F. Albertini, F. Casoli, S. Fabbrici and L. Pareti. *Magnetic phase diagram and demagnetization processes in perpendicular exchange-spring multilayers*. Phys. Rev. B, vol. 73, page 094406, 2006.
- [Coehoorn 89] R. Coehoorn, D. B. De Mooij and C. De Waard. *Meltspun permanent magnet materials containing  $Fe_3B$  as the main phase*. J. Magn. Magn. Mater., vol. 80, pages 101–104, 1989.
- [Crawford 00] T. M. Crawford, P. Kabos and T. J. Silva. *Coherent control of precessional dynamics in thin film permalloy*. Appl. Phys. Lett., vol. 76, pages 2113–2115, 2000.
- [Dobin 06] A. Yu. Dobin and H. J. Richter. *Domain wall assisted magnetic recording*. Appl. Phys. Lett., vol. 89, page 062512, 2006.
- [Fischer 98] R. Fischer and H. Kronmüller. *Importance of ideal grain boundaries of high remanent composite permanent magnets*. J. Appl. Phys., vol. 83, pages 3271–3275, 1998.
- [Fullerton 98] E. E. Fullerton, J. S. Jiang, M. Grimsditch, C. H. Sowers and S. D. Bader. *Exchange-spring behavior in epitaxial hard/soft magnetic bilayers*. Phys. Rev. B, vol. 58, pages 12193–12200, 1998.
- [Garcia-Sanchez 06] F. Garcia-Sanchez, O. Chubykalo-Fesenko, O. N. Mryasov and R. W. Chantrell. *Multiscale models of hard-soft composite media*. J. Magn. Magn. Mater., vol. 303, pages 282–286, 2006.
- [Goto 65] E. Goto, N. Hayashi, T. Miyashita and K. Nakagawa. *Magnetization and switching characteristics of composite thin magnetic films*. J. Appl. Phys., vol. 36, pages 2951–2958, 1965.
- [Goto 04] T. Goto, H. Ogata, T. Sato, K. Yamaguchi, T. Shima and H. Yoshida. *Growth of FeRh thin films and magnetic properties of FePt/FeRh bilayers*. J. Magn. Magn. Mater., vol. 272-276, pages E791–E792, 2004.
- [Guslienko 04] K. Yu. Guslienko, O. Chubykalo-Fesenko, O. Mryasov, R. Chantrell and D. Weller. *Magnetization reversal via perpendicular exchange spring in FePt/FeRh bilayer films*. Phys. Rev. B, vol. 70, page 104405, 2004.

- [Hernando 92] A. Hernando, I. Navarro and J. M. Gonzalez. *On the role of intergranular exchange coupling in the magnetization process of permanent-magnet materials*. Europhys. Lett., vol. 20, pages 175–180, 1992.
- [Hoffmann 70] F. Hoffmann. *Dynamic pinning induced by nickel layers on Permalloy films*. Phys. Status Solidi (b), vol. 41, pages 807–813, 1970.
- [Hsia 02] Y.-T. Hsia and T. McDaniel. Proceedings of the ASME tribology symposium. Cancun, Mexico: ASME, 2002.
- [Jiang 02] J. S. Jiang and S. D. Bader. *Magnetic reversal in thin film exchange-spring magnets*. Scripta Materialia, vol. 47, pages 563–568, 2002.
- [Kanai 05] Y. Kanai, S. J. Greaves, K. Yamakawa, H. Aoi, H. Muraoka and Y. Nakamura. *A single-pole-type head design for 400 Gb/in<sup>2</sup> recording*. IEEE Trans. Mag., vol. 41, pages 687–695, 2005.
- [Kneller 91] E. F. Kneller and R. Hawig. *The exchange-spring magnet: a new material principle for permanent magnets*. IEEE Trans. Mag., vol. 27, pages 3588–3600, 1991.
- [Kouvel 66] J. S. Kouvel. *Unusual nature of the abrupt magnetic transition in FeRh and its pseudobinary variants*. J. Appl. Phys., vol. 37, pages 1257–1258, 1966.
- [Kronmüller 02] H. Kronmüller and D. Goll. *Micromagnetic theory of the pinning of domain walls at phase boundaries*. Physica B, vol. 319, pages 122–126, 2002.
- [Loxley 01] P. N. Loxley and R. L. Stamps. *Theory of domain wall nucleation in a two section magnetic wire*. IEEE Trans. Mag., vol. 37, pages 2098–2100, 2001.
- [Loxley 06] P. N. Loxley and R. L. Stamps. *Theory for nucleation at an interface and magnetization reversal of a two-layer nanowire*. Phys. Rev. B, vol. 73, page 024420, 2006.
- [Lu 07] Z. Lu, P. B. Visscher and W. H. Butler. *Domain wall switching: optimizing the energy landscape*. IEEE Trans. Mag., vol. 43, pages 2941–2943, 2007.
- [Mryasov 05] O. N. Mryasov, U. Nowak, K. Y. Guslienko and R. W. Chantrell. *Temperature-dependent magnetic properties of FePt: Effective spin Hamiltonian model*. Europhys Lett., vol. 69, pages 805–811, 2005.

- [Okamoto 02] S. Okamoto, N. Kikuchi, O. Kitakami, T. Miyazaki, Y. Shimada and K. Fukamichi. *Chemical-order-dependent magnetic anisotropy and exchange stiffness constant of FePt(001) epitaxial films*. Phys. Rev. B, vol. 66, page 24413, 2002.
- [Richter 06] H. J. Richter and A. Yu. Dobin. *Analysis of magnetization processes in composite media grains*. J. Appl. Phys., vol. 99, page 08Q905, 2006.
- [Ruigrok 00] J. J. M. Ruigrok, R. Coehoorn, S. R. Cumpson and H. W. Kesteren. *Disk recording beyond 100 Gb/in.<sup>2</sup>: Hybrid recording?* J. Appl. Phys., vol. 87, pages 5398–5403, 2000.
- [Schrefl 94] T. Schrefl, J. Fidler and H. Kronmüller. *Remanence and coercivity in isotropic nanocrystalline permanent magnets*. Phys. Rev. B, vol. 49, pages 6100–6110, 1994.
- [Suess 05a] D. Suess, T. Schrefl, R. Dittrich, M. Kirschner, F. Dorfbauer, G. Hrkac and J. Fidler. *Exchange spring recording media for areal densities up to 10 Tbit/in.<sup>2</sup>*. J. Magn. Magn. Mater., vol. 290-291, pages 551–554, 2005.
- [Suess 05b] D. Suess, T. Schrefl, S. Fahler, M. Kirschner, G. Hrkac, F. Dorfbauer and J. Fidler. *Exchange spring media for perpendicular recording*. Appl. Phys. Lett., vol. 87, page 012504, 2005.
- [Suess 06] D. Suess. *Multilayer exchange spring media for magnetic recording*. Appl. Phys. Lett., vol. 89, page 113105, 2006.
- [Suess 07] D. Suess. *Micromagnetics of exchange spring media: Optimization and limits*. J. Magn. Magn. Mater., vol. 308, pages 183–197, 2007.
- [Thiele 03] J.-U. Thiele, S. Maat and E. E. Fullerton. *FeRh/FePt exchange spring films for thermally assisted magnetic recording media*. Appl. Phys. Lett., vol. 82, pages 2859–2861, 2003.
- [Thiele 04a] J.-U. Thiele, M. Buess and C. H. Back. *Spin dynamics of the antiferromagnetic-to-ferromagnetic phase transition in FeRh on a sub-picosecond time scale*. Appl. Phys. Lett., vol. 85, pages 2857–2859, 2004.
- [Thiele 04b] J.-U. Thiele, S. Maat, J. L. Robertson and E. E. Fullerton. *Magnetic and structural properties of FePt-FeRh exchange spring films for thermally assisted magnetic recording media*. IEEE Trans. Mag., vol. 40, pages 2537–2542, 2004.

- 
- [Victora 05a] R. H. Victora and X. Shen. *Composite media for perpendicular magnetic recording*. IEEE Trans. Mag., vol. 41, pages 537–542, 2005.
- [Victora 05b] R. H. Victora and X. Shen. *Exchange coupled composite media for perpendicular magnetic recording*. IEEE Trans. Mag., vol. 41, pages 2828–2833, 2005.
- [Wang 05a] J.-P. Wang, W. Shen and J. Bai. *Exchange coupled composite media for perpendicular magnetic recording*. IEEE Trans. Mag., vol. 41, pages 3181–3186, 2005.
- [Wang 05b] J.-P. Wang, W. K. Shen, J. M. Bai, R. H. Victora, J. H. Judy and W. L. Song. *Composite media (dynamic tilted media) for magnetic recording*. Appl. Phys. Lett., vol. 86, page 142504, 2005.



## Chapter 4

# Magnetization reversal in textured Fe particles with different aspect ratios

### 4.1 Experimental motivation

The nanostructuring methods offer an important possibility to vary some of the extrinsic parameters, like shape and size of the elements composing the sample, to systematically study their effect on the magnetic behavior. The properties exhibited by the nanostructured materials can differ significantly from the bulk properties. An example of such system is Fe nanoribbons fabricated through an extrusion process [Biselli 96]. The wire shaped Cu-15 vol% Fe composite alloy samples were produced by the heavy working of spray-deposited billets. With the proceeding of the cold working, the spheroidal Fe particles having about 1  $\mu m$  in diameter and originally embedded into the Cu matrix, were drawn into highly elongated, flattened ribbons (see Fig. 4.1), which according to the X-rays diffractograms were oriented along (110) direction. Also, the high and positive enthalpy of mixing that characterizes the Fe-Cu system allows to exclude the formation of any FeCu solid solution. Due to this and the reduced Fe content, the samples consisted of close to isolated Fe particles embedded into Cu matrix. Transmission electron microscopy showed that the thickness of the Fe ribbons present in the cold drawn samples decreased with the increase of the drawing strain from 14  $nm$  down to 3.5  $nm$ , while the ribbons width dropped from 260  $nm$  down to 27  $nm$ . As for the length of the particles, the microscopy study was not conclusive due to both the wire geometry of the samples (which together with the particle texture favored the observation of the particle cross sections) and the possible deterioration of the elongated particles continuity induced by the thinning the samples for those observations. The best direct estimate of that

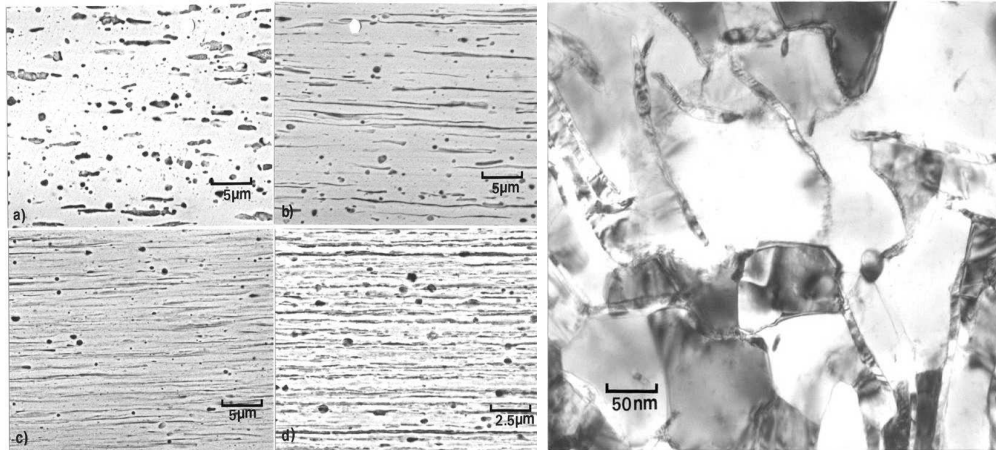


**Figure 4.1:** SEM and TEM images of heavily cold drawn Cu-15 vol% Fe prepared in the Centro Nacional de Investigaciones Metalúrgicas (CENIM) by the group of D.G. Morris

quantity was obtained from scanning electron microscopy images of fresh fracture surfaces and yielded a value of the order of a few units of  $\mu m$ .

The magnetic characterization of samples has been performed by the group of A. Hernando, J.M. González in the Instituto de Magnetismo Aplicado (IMA). The magnetization decrease with temperature of the nanoribbons deviated from the typical  $T^{3/2}$  bulk behavior, as observed by P. Crespo et al. [Crespo 04]. For small enough cross section dimensions this dependence becomes linear as shown in Fig. 4.2. It appears that the reduced size of the nanoribbons modifies the dispersion relation of the magnetic excitations (magnons). The magnons with wave length longer than the ribbon size can not propagate. From a model describing the magnons in the nanoribbons the value of  $2 \mu m$  was obtained as an indirect estimate of the average particle length for the sample in which the average cross section was  $4 nm \times 46 nm$  [Crespo 04]. Furthermore, the variation of the ribbon cross section modifies the shape anisotropy resulting from its elongated shape. Due to the large aspect ratio appearing in some samples, this anisotropy can surpass the bcc Fe magnetocrystalline anisotropy (intrinsic parameter). Therefore, the magnetization reversal mechanism and the coercivity will be affected by the change of the particle dimension as observed experimentally. The hysteresis loops were obtained by vibrating sample magnetometer, cycling between  $5 T$  and  $-5 T$  a magnetic field, which was applied along the long axis of the wire-shaped samples (the cold work direction coinciding with the Fe particles axes and the crystallographic (110) directions). In Fig. 4.3 the coercive field is presented as a function of the average width of the particles.

The present chapter is devoted to the micromagnetic simulations performed to analyze the magnetization reversal process taking place in those highly textured Fe nanoparticles. Our aim is to find the correspondence between experimental results

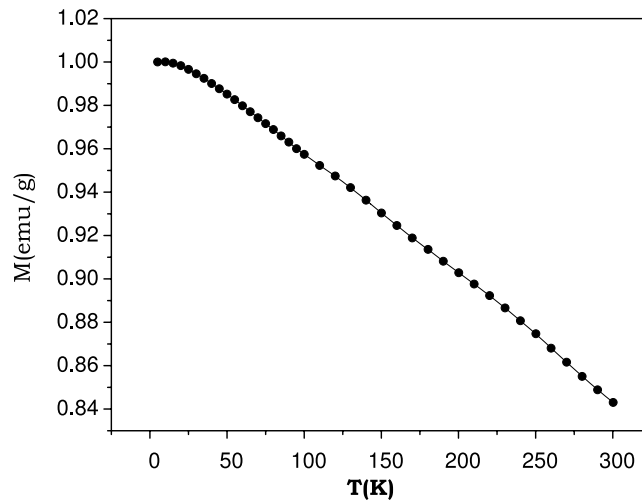


**Figure 4.2:** Temperature dependence of the magnetization for the bcc-Fe ribbons with cross section  $3.5 \text{ nm} \times 27 \text{ nm}$  (measured in the Instituto de Magnetismo Aplicado (IMA) by P. Crespo et al. [Crespo 04]).

and those obtained from simulations in which the local properties are systematically varied in plausible ranges. This stimulated us to attempt to go beyond traditional micromagnetics, trying to include into consideration several major contributions that are not easy to estimate, arising from the nanostructuring and fabrication process, for example residual stress or imperfect shapes, or the broken symmetry at the nanoribbon surface. In this chapter we consider, in addition to the macroscopic values of exchange, magnetization and magnetocrystalline anisotropy, different values of surface magnetocrystalline and magnetoelastic anisotropies, and the occurrence of different textures on the crystalline orientation of the nanoribbons. We also study the thermal reversal process and its possible influence on the coercivity.

## 4.2 Simulational model

We have modeled the field induced reversal processes taking place in Fe particles having dimensions in the range  $4 \text{ nm}$  (thickness)  $\times 30 - 250 \text{ nm}$  (width)  $\times 400 \text{ nm}$  (length). The particle dimensions range, although not covering completely the experimentally observed particle size scale, is affordable from the point of view of the computing time. Due to the above mentioned isolated character of the Fe ribbons, we assume that the behavior of the samples can be well represented by that of an isolated simulated ribbon. We considered the occurrence in the particles of a (110) texture and, therefore, easy axes oriented along directions forming  $45^\circ$  with the applied field direction and the ribbon long axis (see Fig. 4.4). The particles were discretized in elements of size  $1.29 \text{ nm}$  (1/10 of the exchange correlation length of

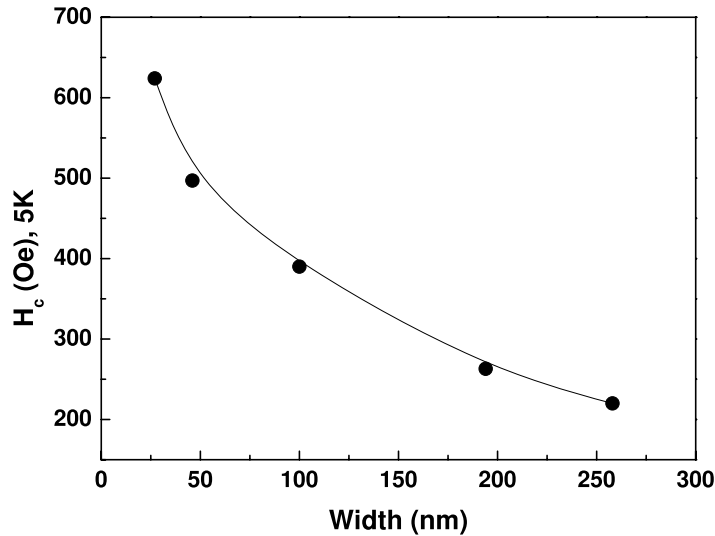


**Figure 4.3:** Experimental saturation coercive force dependence on the average width of the Fe nanoribbons (measured in the Instituto de Magnetismo Aplicado (IMA) by A. Martínez).

Fe,  $l_{ex,Fe} = 12.88 \text{ nm}$ ). A particular relaxation stage was terminated when achieved a value lower than  $10^{-4}$  for the error (see Section 2.2.3). The hysteresis cycles were followed by starting with the application of a  $2 \text{ T}$  field which was always enough to achieve the saturation. The field was varied through variable size increments which were large in the saturation region and of the order of  $5 \cdot 10^{-4} \text{ T}$  in the coercive force region. The considered Fe parameters were biaxial anisotropy value  $K = 5 \cdot 10^4 \text{ J/m}^3$ , micromagnetic exchange value  $A = 8.3 \cdot 10^{-12} \text{ J/m}$  and saturation magnetization value  $\mu_0 M_s = 2.15 \text{ T}$  and were taken from [Skomski 99, Page 158].

### 4.3 Magnetization reversal in ideal Fe elongated particles

Fig. 4.5 presents the results obtained from our simulation for the hysteresis cycles of ribbons having different widths and bulk biaxial magnetocrystalline anisotropy exclusively. The magnetic moment configuration (see Figs. 4.6 and 4.8) occurring during these processes allowed us to identify two different reversal modes associated to the particles having large and small aspect ratio, respectively.

An initial result, observed at all the applied field values and in all the simulated particles, was the fact that the orientation of the magnetic moments did not depend on the position along the system thickness. That result could be “a priori” expected from the particle thickness value which was below the Fe exchange correlation length,

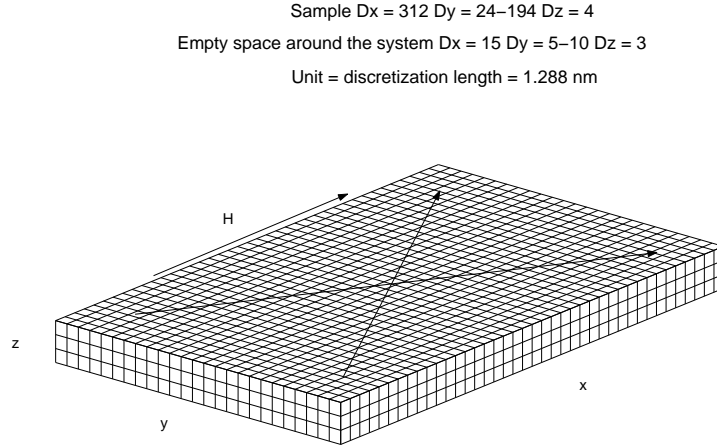


**Figure 4.4:** Schematic picture showing the system geometry and the cubic anisotropy easy axes in the simulations.

$l_{ex,Fe}$ . Thus, in the following we will discuss all the moment configurations present in the modeled systems in terms of 2D moment distributions corresponding to planes parallel to the two largest dimensions of the particles.

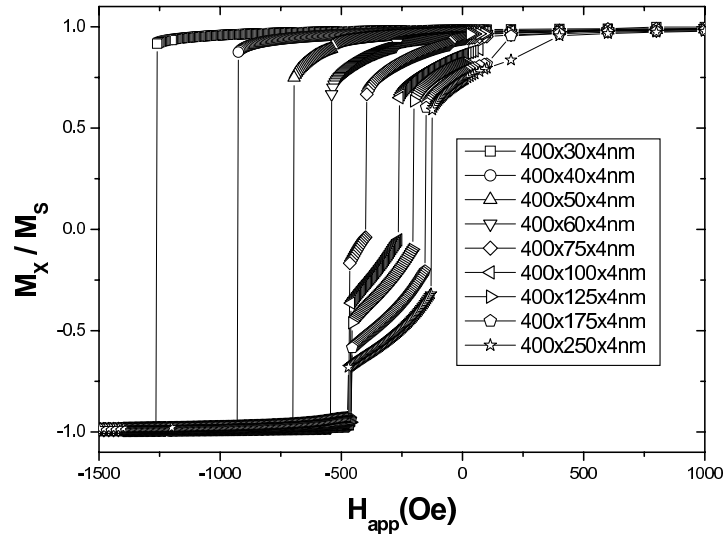


**Figure 4.5:** Hysteresis loops for different particle sizes, varying their width.

In the case of the particles having the largest aspect ratios (see the complete reversal sequence in Fig. 4.6, where data corresponding to the particle having  $400 \text{ nm} \times 40 \text{ nm} \times 4 \text{ nm}$  are presented) the remanent state corresponded to the well known “S-type” configuration, which only differs from the single domain one in the quasi-parallel-to-the-surface moment structures present at the particle ends. Those structures are a result of the minimization of the magnetostatic energy and their presence results in the spreading of the magnetic poles that should be local-

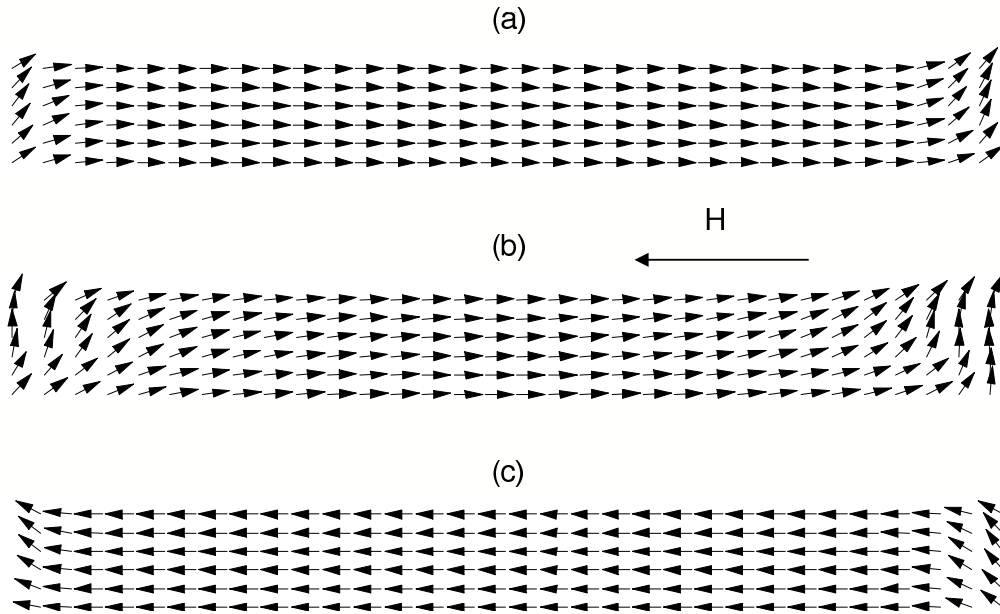


**Figure 4.6:** X-Y view of the magnetic moments configuration for  $400 \times 40 \times 4 \text{ nm}^3$  particle: (a) Remanent state, (b) Applied field  $H = 925 \text{ Oe}$  and (c) Applied field  $H = 930 \text{ Oe}$ . Every arrow represents  $10 \times 6$  cells.

ized at the particle surfaces in the case of the uniform magnetization configuration. The “S-type” configuration evolves with the increase of the demagnetizing field to the formation of closure-like domains at both ends of the particle and finally to a collective irreversible rotation which leads to a “S-type” state symmetric to that corresponding to the magnetizing field remanence. The hysteresis loops presented in Fig. 4.5 evidence that the coercive force decreases with the decrease of the aspect ratio value see (Fig. 4.7).

The field at which the reversal occurs can be compared to the classical shape anisotropy field associated to the particle dimensions. For that purpose we can consider the demagnetizing field model for thin films discussed in [O’Handley 00, Pages 42-43]. If the dimensions of the system are  $w$  (width)  $>$   $h$  (height)  $>$   $t$  (thickness), then the demagnetizing factors,  $N_w$  and  $N_h$ , associated to the two larger dimensions are in SI units:

$$N_w \approx \frac{2t}{\pi w}, N_h \approx \frac{2t}{\pi h} \quad (4.1)$$

and the corresponding anisotropy field,  $H_s$

$$H_s = M_s(N_w - N_h). \quad (4.2)$$

In the case of the particle having the larger aspect ratio,  $w = 400 \text{ nm}$ ,  $h = 30 \text{ nm}$ , and  $t = 4 \text{ nm}$ , this results in a shape anisotropy field of  $H_s = 0.172 \text{ T}$ , which is sig-

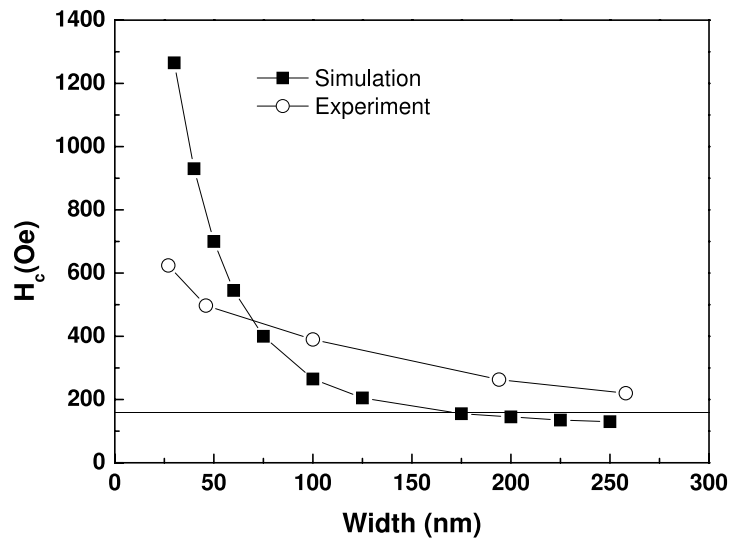


**Figure 4.7:** Comparison of the experimental and the simulational data obtained by exclusively considering bulk biaxial magnetocrystalline anisotropy. The line corresponds to the value predicted for the Stoner-Wohlfarth model with cubic anisotropy.

nificantly larger than our simulational result for the coercive force ( $H_c = 0.1265 T$ ). This fact is related to the moment configurations obtained from our micromagnetic simulations at the remanence and, more concretely, to the inhomogeneous moment structures present at the ends of the particles.

In the case of the particles having smaller aspect ratios, both the reversal mode and the associated moment configurations are more complex than those previously discussed. At the saturation remanence (see Fig. 4.8(a)), the moments at a layer close to the surface of the particles point essentially parallel to that surface, whereas those at the inner core of the particles are oriented along the direction of one of the magnetocrystalline (100) easy axes. The transition from the “S-type” configuration characteristic of the elongated particles to that present in the small aspect ratio ones is illustrated in Fig. 4.9 in which we have plotted the evolution with the aspect ratio of the orientation of the moment present at the center of the system. These data allow to know that only for particle widths above 200 nm the inner moments point parallel to the magnetocrystalline easy axis.

The next steps of the magnetization reversal of these small aspect ratio particles are shown in Fig. 4.8. From this figure it is possible to see how the first partially reversed region is the particle core which moments rotate irreversibly from their direction at the remanence to that of the closest easy axis forming the smallest angle with the applied demagnetizing field. For a field slightly below that corresponding to this rotation the particle exhibits uniform magnetization domains separated by charged 45 walls. Since for the particles having small aspect ratio most of the volume

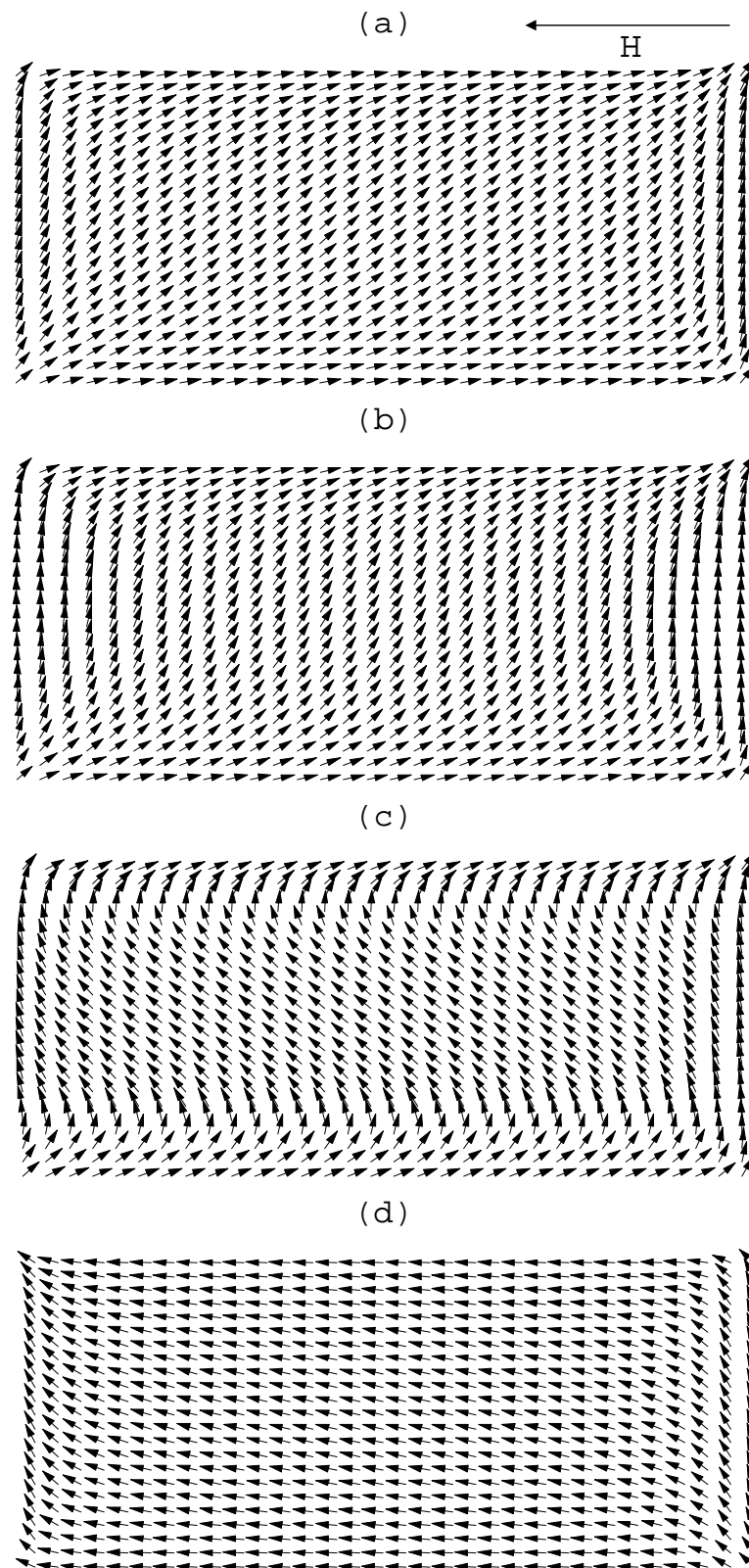


**Figure 4.8:** X-Y view of the magnetic moments configuration for  $400 \times 175 \times 4 \text{ nm}^3$  particle: (a) Remanent state, (b) Applied field  $H = 150 \text{ Oe}$ , (c) Applied field  $H = 155 \text{ Oe}$  and (d) Applied field  $H = 460 \text{ Oe}$ . Every arrow represents  $10 \times 6$  cells.

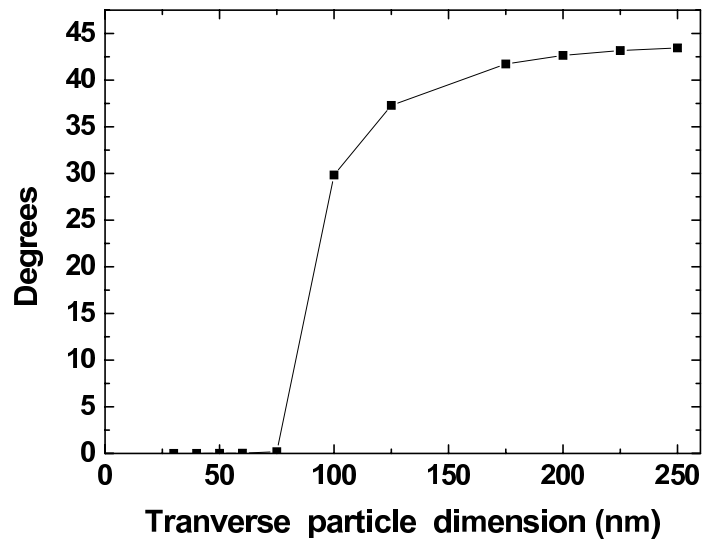


**Figure 4.9:** Angular deviation at the remanence from the applied direction at the center of the particle.

of the particle corresponds to the core moments their reversal governs the coercive force value (evaluated from the  $M_x = 0$  condition).

It is interesting to point out that the field corresponding to the particle core reversal approaches for sufficiently small aspect ratios the value corresponding to the Stoner-Wohlfarth (SW) model discussed in Section 5.3.2 (see Fig. 4.7 where we show the width dependence of the core reversal field and the corresponding SW field). Thus, for these conditions the surface layer minimizes the stray fields linked to the finite size of the particles and, very interestingly, the system behaves globally as an infinite one, reversing through a coherent rotation mechanism.

Once the particle core experiences the low field irreversible rotation their moments rotate reversibly towards the field direction. In the large width particles and for a field just above that corresponding to the rotation, the wall-like structure allowing the transition from the core moments direction to the orientation of the moments in the long axis uniform magnetization surface layer, sweeps an angle of ca.  $135^\circ$ . Further reorientation of the core moments towards the applied field reduces both the swept angle and the width of this wall. The reversal process is completed by the annihilation of the core-surface wall. This process occurs at a field approximately independent from the sample size and through the irreversible rotation of the surface moments. Immediately after that annihilation the system moment configuration is of the “S-type”.

The efficiency of the surface structures to minimize the magnetostatic energy contribution is also relevant from the point of view of the analysis of the interparticle dipolar interactions that should here be largely reduced in comparison to a case in

which the surface moment structures were absent. However, it is not clear that the pole avoidance is the best way to minimize the total energy of the many particles. An efficient compensation of charges in neighboring particles can be more advantageous than their avoidance.

Finally, in Fig. 4.7 is plotted, for comparison, the simulational and experimental coercivity. Whereas for reduced widths the simulational results are up to two times larger than the experimental ones (which is in principle plausible due to the absence in the model of different types of defects, i.e.: morphological, associated to reduced crystallinity regions, etc., that could help to reduce the coercivity) for widths larger than ca. 70 nm the experimental data are slightly larger than the simulational ones, clearly suggesting that mechanisms different from the presence of the mentioned defects should account for the differences between the experimental and the simulational data. Note also that in experimental situations the irreversible jumps of the hysteresis cycles are normally smoothed due to slight distribution of geometrical and magnetic parameters between different objects.

#### 4.4 Angular dependence of coercivity

One of the largest possible differences between experimental situation and the model is the misalignment between the particle axis and the applied field. To include this into consideration, we first have calculated the angular dependence of the demagnetization process, applying the field with an angle  $\beta$  with respect to the long axis of the particles. We can again distinguish two types of behavior as shown in Fig. 4.10. In the small aspect ratio case the angular dependence of the coercivity is

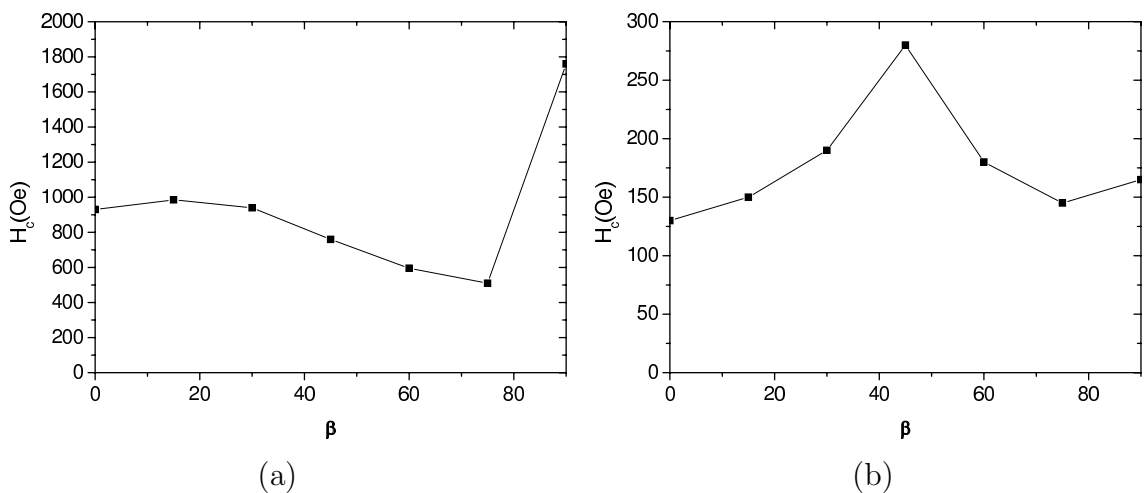


**Figure 4.10:** Simulated coercivity as a function of the angle of the applied field  $\beta$  for particles with dimensions: (a)  $400 \times 40 \times 40 \text{ nm}^3$  and (b)  $400 \times 250 \times 40 \text{ nm}^3$ .

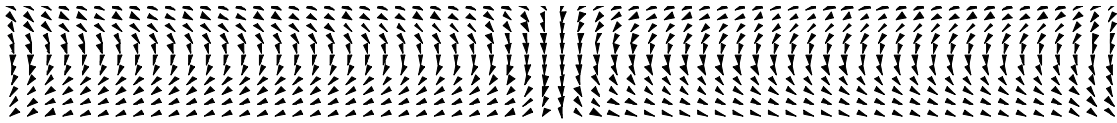


**Figure 4.11:** Remanence configuration of  $90^\circ$  hysteresis loop for the  $400 \times 40 \times 40 \text{ nm}^3$  particle.

proper to the biaxial anisotropy. For the particles with smaller widths the angular coercivity is determined by the strong shape anisotropy and the characteristics of the moment configurations corresponding to the remanence do not depend on the saturating field orientation for  $\beta < 90^\circ$ . Differently from this, in the case  $\beta = 90^\circ$  both the remanence configuration and the reversal process occurred through moment configurations clearly different from those previously discussed, see Fig 4.11. The configuration at the remanence corresponded to the disappearance of the close-to-uniform moment configuration observed at the particle core which is substituted by the two Néel-like walls with a cross-tie domain wall between them.

Finally, we evaluated the influence on the model system coercivity of the occurrence of misalignment between the orientations of the nanoribbons, present in the measured samples. In Fig. 4.12 we plot the calculated ribbon coercivity as a function of their widths for a non-interacting set of ribbons. We assumed the geometrical orientations, distributed according to a Gaussian distribution centered at  $30^\circ$  or  $45^\circ$  with the direction of the applied field and having a width  $dv$ . The result is the convolution of the gaussian distribution with the corresponding coercivity as a

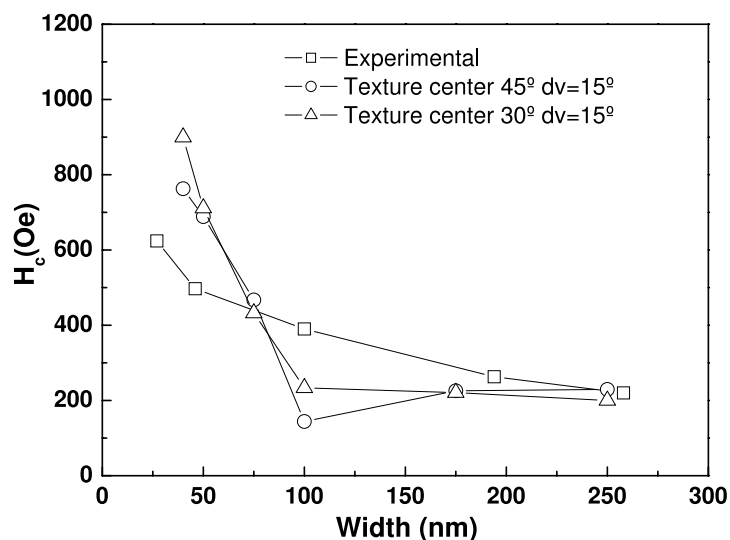


**Figure 4.12:** Ribbon width dependence of the coercivity of a set of non-interacting ribbons having distributed orientations.

function of the angle. As it is possible to observe from the Figure, the consideration of ribbon misorientation reduces, with respect to the absence of it, the differences between the experimental and the simulational results.

## 4.5 Coercivity of Fe particles with surface anisotropy

The contribution of surface anisotropy to the reversal process can not be “a priori” ruled out considering the simulated system dimensions. In Fig. 4.13 we present the results of our simulations corresponding to the consideration into the system energy of a surface magnetocrystalline anisotropy term. The local easy axes at the surfaces were considered to be parallel to the simulated system surfaces normals and replacing the anisotropy of the surface cubes by an effective anisotropy. Our results show that, for the considered surface anisotropy constants (taken from [Lorenz 96]) the coercivity of the thin ribbons is in reasonable agreement with the experiment but that this is not the case for the ribbons having the smaller aspect ratios. This difference can be related to the fact that the direction of the surface anisotropy easy axis favors the orientation of the moments perpendicular to the ribbon surface and consequently the reduction of the thickness of the Néel wall-like structures originated at the lateral surfaces by the minimization of the magnetostatic energy. Since the ribbon coercivities are linked to the creation of these structures (that process coincides with the rotation of the magnetization of the core of the ribbons towards the easy axis direction closest to the demagnetizing field direction) their reduction

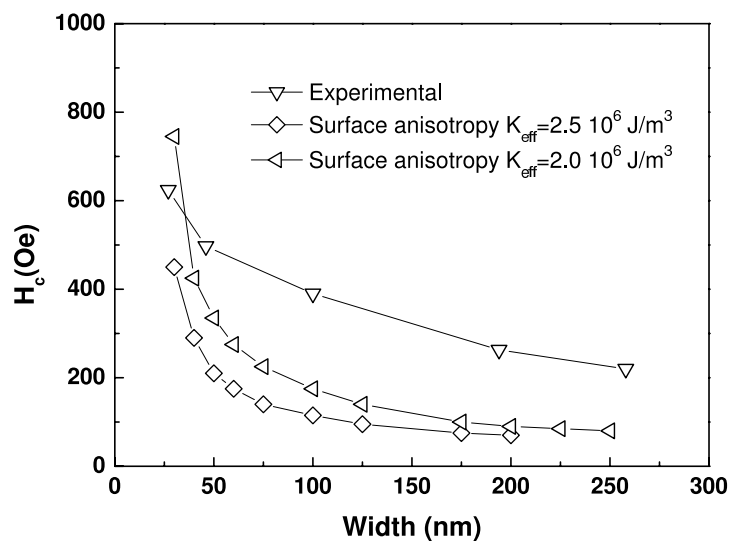


**Figure 4.13:** Comparison with the experimentally measured values of the simulated data obtained for the ribbon width dependence of the coercive force in ribbons having different values of the surface anisotropy.

should be related to the easiest formation of the Néel wall-like structures in systems having significant surface anisotropy.

## 4.6 Coercivity of Fe particles with magnetoelastic anisotropy

Due to the extreme large plastic deformations originated during the samples cold work, residual stresses can be present in the matrix containing the nanoribbons. These stresses originate lattice distortions that generate an additional term in the energy of the nanoribbons. Clearly, this effect can modify the final coercivity of the nanoparticles. The expression for the magnetoelastic energy is:

$$E = -\frac{3}{2}\lambda_{100}\sigma(\alpha_1^2\gamma_1^2 + \alpha_2^2\gamma_2^2 + \alpha_3^2\gamma_3^2) - 3\lambda_{111}\sigma(\alpha_1\alpha_2\gamma_1\gamma_2 + \alpha_2\alpha_3\gamma_2\gamma_3 + \alpha_3\alpha_1\gamma_3\gamma_1) \quad (4.3)$$

where  $\sigma$  is the stress magnitude,  $(\alpha_1, \alpha_2, \alpha_3)$  and  $(\gamma_1, \gamma_2, \gamma_3)$  are respectively the magnetization unit vector and the cosine director of  $\sigma$  in the system of reference given by the lattice axes, and  $\lambda_{100}$  and  $\lambda_{111}$  are the magnetoelastic constant. In the case of the nanoribbons the lattice is rotated  $45^\circ$  with respect to the long axis and supposing that the stress is applied along the long axis of the particles we have  $(\alpha_1, \alpha_2, \alpha_3) = ((m_x - m_y)/\sqrt{2}, (m_x + m_y)/\sqrt{2}, m_z)$   $(\gamma_1, \gamma_2, \gamma_3) = (\frac{1}{\sqrt{2}}, \frac{1}{\sqrt{2}}, 0)$ . For Fe the magnetoelastic constants are  $\lambda_{111} = -21 \cdot 10^{-6}$  and  $\lambda_{100} = 21 \cdot 10^{-6}$  [Bai 04]. The magnetoelastic energy is then equivalent to an additional uniaxial anisotropy (magnetoelastic) with easy axis in the Y direction and the value:

$$K_{Mag,elas} = \frac{3}{2}\lambda_{100}\sigma. \quad (4.4)$$

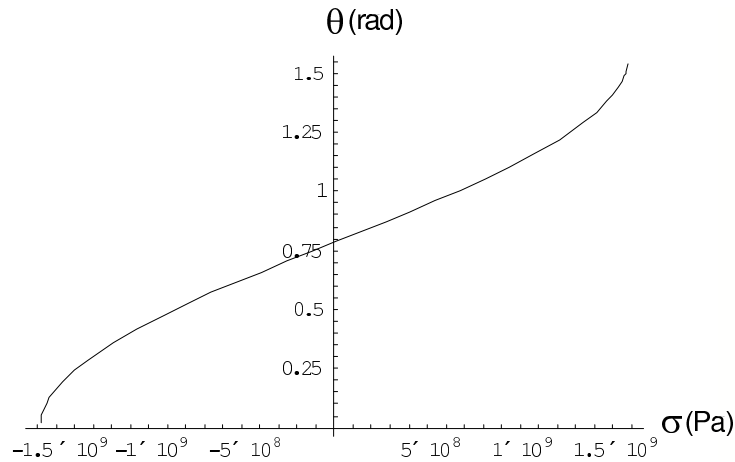


**Figure 4.14:** Position of the minimum of the energy with respect to the X axis as a function of the stress for a SW particle with only biaxial magnetocrystalline and magnetoelastic anisotropies.

The minimization of magnetocrystalline and magnetoelastic anisotropy in the SW particle gives us the preferred direction of the magnetization for the resulting mixed anisotropy. Fig 4.14 shows the magnetization angle with the long axis of the particle as a function of the stress  $\sigma$ . The original position of the minimum ( $\sigma = 0$ ) is at  $45^\circ$ . For traction (positive values of  $\sigma$ ) the preferred direction tends to  $90^\circ$  (Y axis) and for compression (negative values of  $\sigma$ ) the preferred direction moves toward  $0^\circ$  (X axis).

In Fig. 4.15 we present our simulational data for a ribbon, including both surface anisotropy (having an effective constant  $K_{eff} = 2.5 \cdot 10^6 \text{ J/m}^3$ ) and a magnetoelastic anisotropy arising from uniaxial compression  $\sigma = -2 \text{ GPa}$ . The magnetoelastic anisotropy in this case was directed parallel to the ribbon axis. From the Figure it is clear that this two-parameter ( $K_{eff}$  and  $\sigma$ ) fitting renders the set of data providing a better description of the experimental ones. Nevertheless, without independent evaluation of at least one of the considered parameter our simulation can not be used to evaluate the second one.

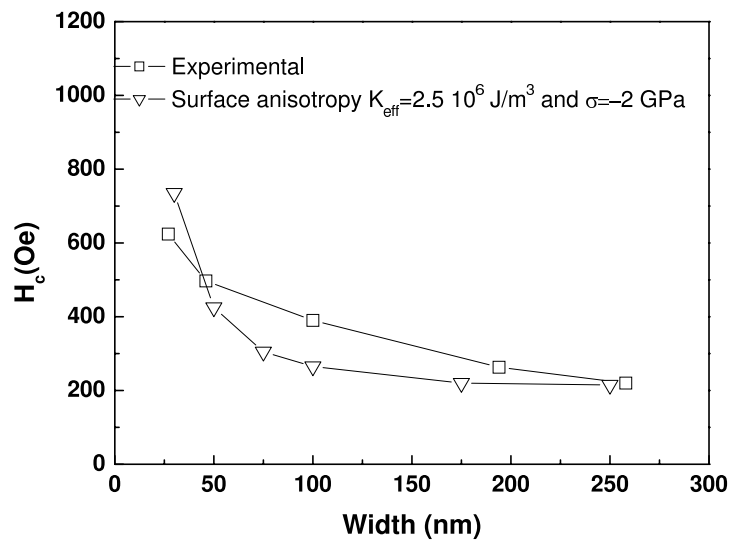


**Figure 4.15:** Measured ribbon width dependence and the calculated dependence of the coercive field including surface anisotropy and magnetoelastic anisotropy resulting from compression.

## 4.7 Thermal switching mechanism in Fe particles

Thermal effects can also contribute to reduce the switching fields. The dynamic dependence of the coercivity is usually analyzed using the Sharrock law [Sharrock 90], which is derived from the Arrhenius-Néel law. The application of the Sharrock law requires the energy barrier dependence on the applied field. In

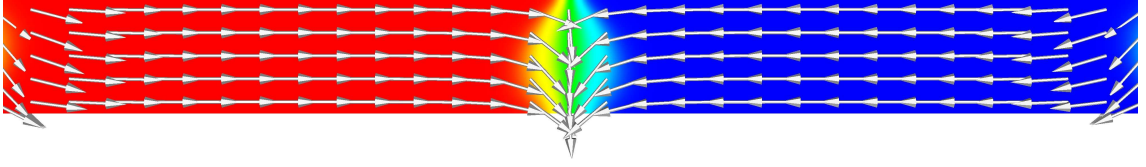


**Figure 4.16:** Saddle point configuration for the  $400 \times 40 \times 4 \text{ nm}^3$  particle.

in this section we evaluate that dependence and study the thermal switching mechanism. We have calculated the energy barrier values using the Lagrange multiplier method discussed in Section 2.3.6, but in this case we have used the constraint  $\langle m_x \rangle = m_{x0}$ , where  $\langle m_x \rangle$  is the average magnetization x component. This constraint has the advantage of having the form of an applied field in the X direction, allowing to obtain the energy barrier of an arbitrary applied field from the zero field energy barrier value [Lu 07].

The saddle points as well as the energy barrier vary with the applied field. Therefore, in this section we will refer to zero field saddle points as, simply, saddle points. As in the field switching, the thermal switching mechanisms are also different for different particle widths. For the large aspect ratio particles the thermal switching proceeds through a  $180^\circ$  domain wall, as a saddle-point configuration shown in Fig. 4.16. The nucleation of the domain wall starts from the structures that are created by the magnetostatics in the particle ends (see Fig. 4.6). In the small aspect ratio particles the saddle point configuration consists of two domains, which point in one of the local directions of the biaxial anisotropy, as shown in Fig. 4.17. The domain wall is not located at the center of the particle since the domain wall is stabilized in

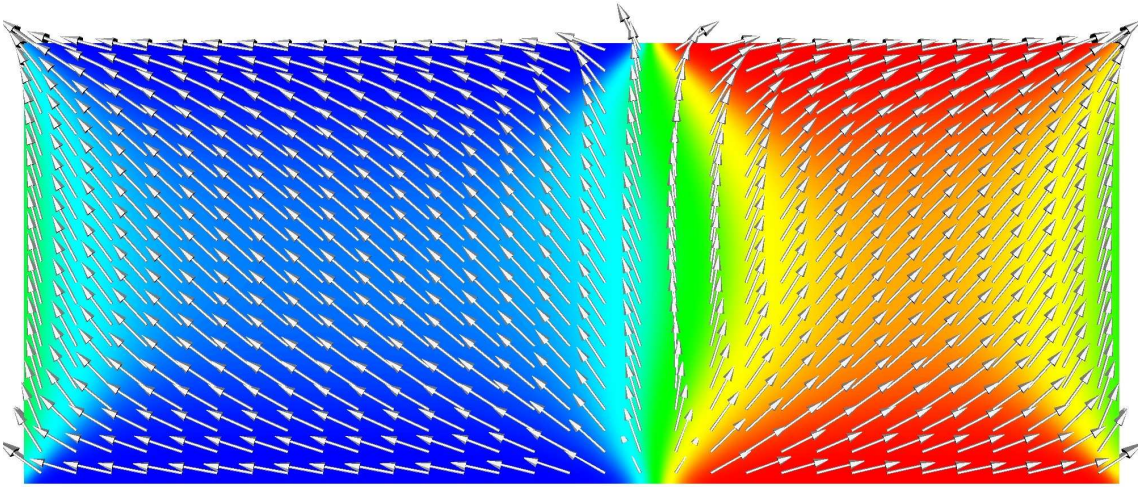


**Figure 4.17:** Saddle point configuration for the  $400 \times 175 \times 4 \text{ nm}^3$  particle.

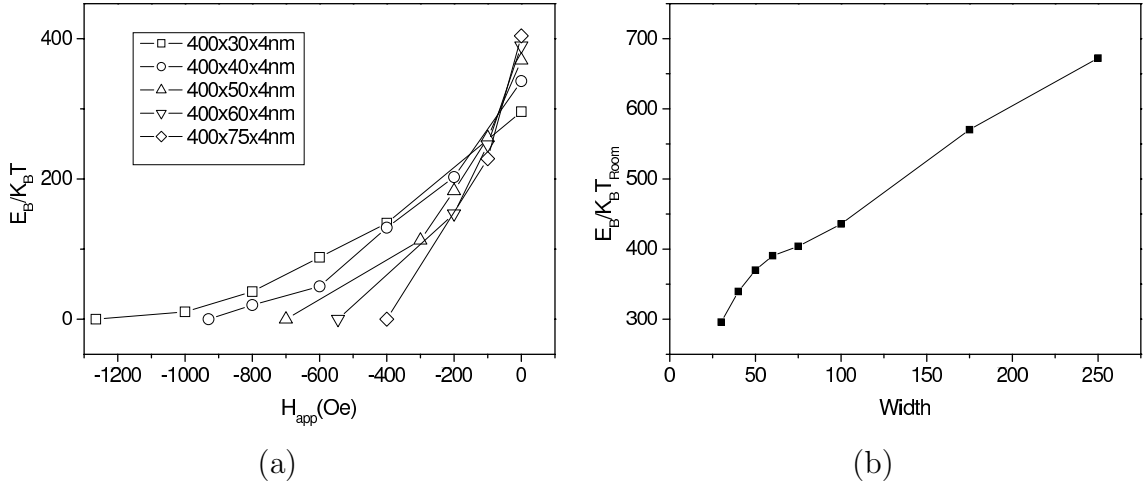


**Figure 4.18:** Energy barriers: (a) as function of the applied field for different particle sizes and (b) for zero applied field as a function of the particle width.

the center of the particle and such configuration is a shallow minimum of the energy. This minimum is not present if the particle presents any imperfection. As in the hysteresis loops, the change of behavior is for a width ca.  $75 \text{ nm}$  and is related to the length of the structures that minimize the magnetic charges. The zero field energy barrier as a function of the particle width is plotted in Fig. 4.18(b). The domain wall mechanism yields a linear dependence with the cross section. In our case there is a change in the slope due to the different effective anisotropy, being this slope larger for thinner particles due to their large shape anisotropy. Finally, for small aspect ratio the effective anisotropy is not dependent on the particle width obtaining a linear dependence of the energy barrier.

In Fig. 4.18 (a) the energy barrier values are shown as a function of the applied field value and the particle width. Several authors [Skomski 06] have found the applied field dependence of the energy barrier value to be:

$$E_B = E_0 \left(1 - \frac{H}{H_c}\right)^n \quad (4.5)$$

where  $E_0$  is the zero field energy barrier value and  $n$ -the scaling factor. As shown in Fig. 4.19, in the case of the domain wall thermal switching our simulations fit perfectly to a scaling factor  $n = 2$ . This factor also appears in other systems like in the case of a Stoner-Wohlfarth particle.

From the scaling of the energy barrier value and the Arrhenius-Néel law, M.P. Sharrock [Sharrock 90] obtained the following expression for the thermal dependence of the coercivity, due to thermal relaxation during the hysteresis process:

$$H_c(T) = H_c \left[1 - \left[\frac{k_B T}{E_0} \ln \left(\frac{f_0 t_0}{\ln 2}\right)\right]^{1/n}\right] \quad (4.6)$$

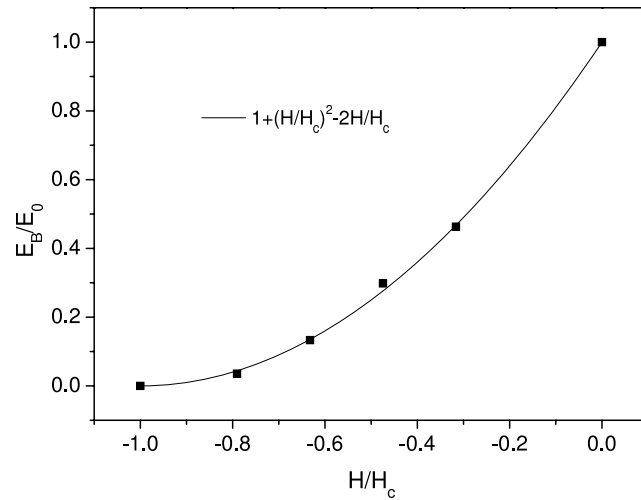


**Figure 4.19:** Energy barrier value normalized to the zero field value as a function of the normalized applied field for the  $400 \times 30 \times 4 \text{ nm}^3$  particle.

where  $f_0$  is the attempt frequency and  $t_0$  the time scale of the measure. From Fig. 4.18(a), the thermal activation in the timescale of a magnetometer measure will be only appreciable in the case of large aspect ratio particles. From all this results we can calculate the thermal dependence of the coercivity applying the Sharrock law, considering a time of measure  $0.1 \text{ s}$  and  $f_0 = 10^{10} \text{ Hz}$ . The results for the particle with cross section  $3.5 \text{ nm} \times 27 \text{ nm}$  are shown in Fig. 4.20. The dependence obtained from simulations is not in agreement with the experiment but indicates the existence

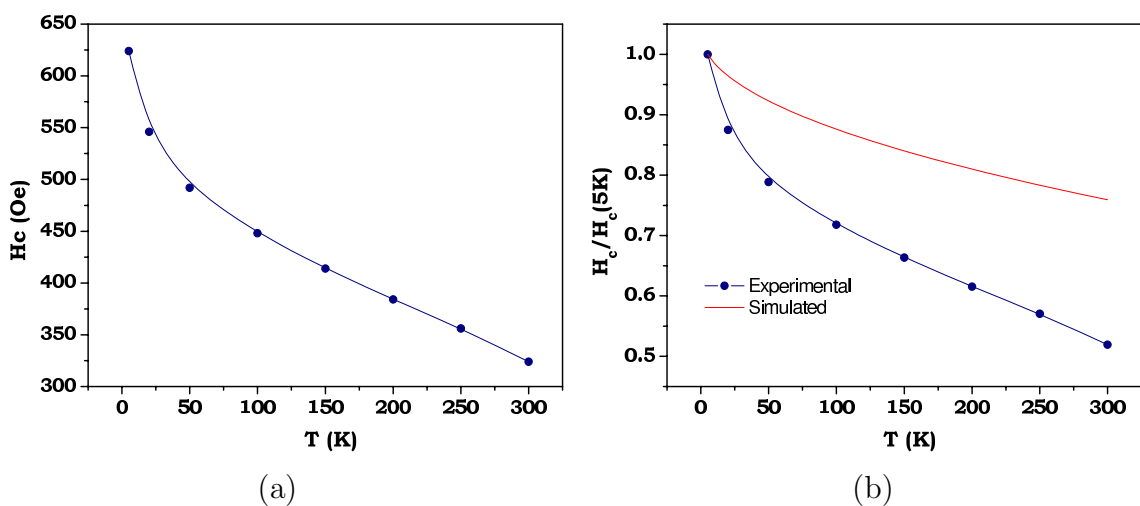


**Figure 4.20:** (a) Temperature dependence of the coercivity for the bcc-Fe ribbons with cross section  $3.5 \text{ nm} \times 27 \text{ nm}$  (measured in the Instituto de Magnetismo Aplicado (IMA) by A. Martínez). (b) Comparison of experimental and simulational results for the temperature dependence of the coercivity normalized to the  $5 \text{ K}$  value.

of appreciable thermal activation in the samples. However, in order to obtain the real dependence of the coercivity the thermal dependence of the magnetization has to be taken into account in the simulation. These could be obtained from the experimental dependence of the magnetization as shown in Fig. 4.2. This simulation using temperature dependent parameters will be subject of future work.

## 4.8 Conclusions

In summary we have compared experimental coercivity data obtained in highly elongated Fe ribbons with the micromagnetic modeling results, which included surface and magnetoelastic anisotropies and ribbon misorientation, in addition to bulk biaxial magnetocrystalline anisotropy. From our results it is possible to conclude:

- The occurrence of different coercivity mechanisms for different particle width ranges. In the case of the thinner particles demagnetization occurs in a single process from a S-type remanent state. In that of the wider particles, two demagnetization stages are clearly distinguishable: an initial one which for large enough particles is similar to an irreversible SW rotation between two in-plane easy axes and a high field stage corresponding to the reversal of a close-to-the-surface layer, appearing in order to minimize dipolar energy.
- Our results, including exclusively biaxial anisotropy reproduce qualitatively the size dependence of the coercivity. However, the obtained coercivity values are higher than those measured experimentally in the thin particles and smaller in the case of thick ones, suggesting the possibility of additional contributions to the magnetic energy.
- The consideration of a surface anisotropy, the inclusion of some ribbon misalignment and the combination of surface magnetocrystalline and magnetoelastic anisotropies in the model yield a better agreement, but still far from matching exactly the values actually measured in the samples. Two additional difficulties appear. First, the estimation of the intrinsic parameters in the sample is experimentally complicated. Second, these parameters can intrinsically be dependent on the sample size.
- Regarding the thermal switching, there exist two different possible mechanisms for large and small aspect ratio particles. For the former one the mechanism is a  $180^\circ$  domain wall. In the case of small aspect ratio particles the saddle point configuration is a  $90^\circ$  domain wall that allows the maximum alignment of the local magnetic moment with the anisotropy axis. The experimental coercivity dependence on temperature of long particles could not be explained by simple

consideration of temperature dependence of magnetization, which suggests the importance of the thermal switching in these particles as confirmed by the simulations.

## 4.9 Conclusiones en castellano

En resumen, hemos comparado datos experimentales de coercitividad obtenidos en cintas magnéticas de Fe altamente elongadas con cálculos micromagnéticos que incluían anisotropías de superficie y magnetoelástica y desviación de la orientación de las cintas, además de la anisotropía magnetocristalina cúbica del Fe masivo. De nuestros resultados es posible concluir:

- La aparición de diferentes mecanismos de inversión de la imanación para diferentes rangos de anchura de las partículas. En el caso de las partículas más delgadas consiste en un único proceso desde una estructura en remanencia tipo S. Para las partículas más anchas, se pueden observar claramente dos etapas: una inicial que para las partículas suficientemente anchas es similar a una rotación irreversible tipo Stoner-Wohlfarth entre dos ejes fáciles contenidos en el plano y una etapa que tiene lugar a campo alto correspondiente a la inversión de la capa cercana a la superficie que aparece para minimizar la energía dipolar.
- Nuestros resultados que incluyen exclusivamente la anisotropía cúbica reproducen cualitativamente la dependencia con la anchura de la coercitividad. Sin embargo, los valores obtenidos son más altos que aquellos medidos experimentalmente para partículas delgadas y más pequeños en el caso de las partículas más gruesas, sugiriendo la posibilidad de contribuciones adicionales a la energía magnética.
- La simulaciones en las que se incluyen anisotropía de superficie, distribución de orientaciones de las cintas y la combinación de anisotropía de superficie y magnetoelástica obtienen un mejor acuerdo pero todavía lejos de los datos medidos en las muestras. Hay presentes dos dificultades adicionales. Primero, la estimación de los parámetros intrínsecos en la muestra es experimentalmente complicada. Además, puede existir una dependencia intrínseca de estos parámetros con respecto al tamaño la partícula.
- Con respecto a la inversión térmica, existen dos posibles mecanismos para partículas con grande y pequeña relación de aspecto. Para las primeras el mecanismo involucra una pared de  $180^\circ$ . En el caso de las partículas con pequeña relación de aspecto la configuración del punto de silla contiene un par de dominios en los cuales los momentos se orientan en la dirección de los ejes de anisotropía. La dependencia experimental de la coercitividad en las partículas largas no puede ser explicada considerando simplemente de la variación de la imanación con la temperatura, lo cual indica que la inversión térmica en

estas muestras es importante, tal como indican también los resultados de los cálculos.

## Bibliography

- [Bai 04] D. Z. Bai, J.-G. Zhu, W. Yu and J. A. Bain. *Micromagnetic simulation of effect of stress-induced anisotropy in soft magnetic thin films*. J. Appl. Phys., vol. 95, pages 6864–6866, 2004.
- [Biselli 96] C. Biselli and D. G. Morris. *Microstructure and strength of Cu-Fe in situ composites after very high drawing strains*. Acta Materialia, vol. 44, pages 493–504, 1996.
- [Crespo 04] P. Crespo, J. M. González, A. Hernando and F. J. Yndurain. *Spin-wave excitations in ribbon-shaped Fe nanoparticles*. Phys. Rev. B, vol. 69, page 012403, 2004.
- [Lorenz 96] R. Lorenz and J. Hafner. *Magnetic structure and anisotropy of thin Fe films on Cu(001) substrates*. Phys. Rev. B, vol. 54, pages 15937–15949, 1996.
- [Lu 07] Z. Lu, P. B. Visscher and W. H. Butler. *Domain wall switching: optimizing the energy landscape*. IEEE Trans. Mag., vol. 43, pages 2941–2943, 2007.
- [O’Handley 00] R. C. O’Handley. *Modern magnetic materials*. New York: Wiley-Interscience, 2000.
- [Sharrock 90] M. P. Sharrock. *Time-dependent magnetic phenomena and particle-size effects in recording media*. IEEE Trans. Mag., vol. 26, pages 193–197, 1990.
- [Skomski 99] R. Skomski. *Permanent magnetism*. Bristol: Institute of Physics Publishing, 1999.
- [Skomski 06] R. Skomski, J. Zhou, R. D. Kirby and D. J. Sellmyer. *Micromagnetic energy barriers*. J. Appl. Phys., vol. 99, page 08B906, 2006.

# Chapter 5

## Modeling of hysteresis processes in antidot Fe films

### 5.1 Introduction

A type of nanostructure made available by the current microfabrication techniques is the inclusion of an array of nonmagnetic regions (holes) defined within a magnetic thin film (see Fig. 5.1). These magnetic elements are known, in opposition to dots, as antidots. The magnetic thin film dipolar energy associated with the magnetic poles present at the surfaces of the array motifs can override the magnetocrystalline anisotropy and largely determine the global demagnetization of the system. Hence, the coercivity of the antidot film can present a substantial increase compared to that of a continuous film. Additionally, the symmetry of the array determines that of the induced magnetic anisotropy, for example square and hexagonal arrays give respectively fourfold and sixfold anisotropies [Wang 06]. The use of different lithographic techniques, which include electron beam [Adeyeye 97], ultraviolet [Wang 06], focused ionic beam [Toporov 00], x-ray [Ruiz-Feal 02] or interferometric lithography [Vavassori 99], and anodic aluminium oxide membranes [Xiao 02] makes possible to fabricate highly regular antidot arrays with antidot sizes and interantidot distances with values going from a few tens of  $nm$  up to the units of  $\mu m$ . The imprinted motifs found in the literature are square [Heyderman 06], rectangular [Wang 04], elliptical [Guedes 00] and circular [Ruiz-Feal 02] holes. The techniques that allow to systematically vary the geometrical parameters (i.e size, shape and symmetry) and the dependence of the magnetic behavior on such parameters open the interesting possibility of tailoring the coercivity.

Besides the engineering of the coercivity, the use of antidots arrays has been suggested for magnetic recording applications. The antidots films have been proposed as potential recording media, where the bits are stored in the interantidot

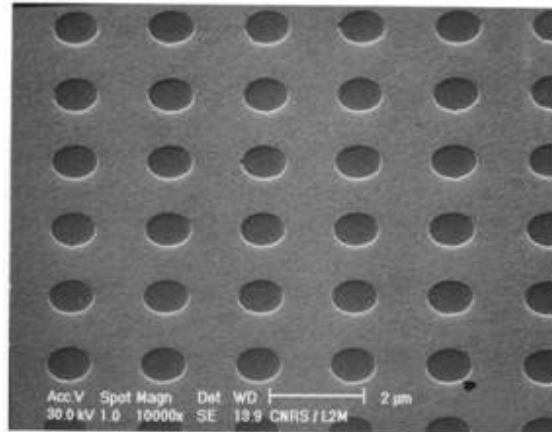


**Figure 5.1:** SEM image of an antidot Fe film from the Ph. D. thesis of J.M. Torres [Torres 05].

region [Cowburn 97] (see Fig. 5.2). This implementation is favored by the absence of any superparamagnetic effect, due to the large volume that is relatively strongly coupled, compared to the set of nearly isolated grains that constitute conventional media. The main disadvantage of the use of antidots arrays is linked to the potentially high noise-to-signal ratio originated by the bit transition, which should have in these arrays a width of the order of the material exchange correlation length [Jalil 03]. In fact, the potential recording media in order to be promising enough have to be not obsolete compared with the current technology when the candidate would reach production stages. Another proposal for the use of such structures is the Percolated Perpendicular Media [Zhu 07]. The medium consists of exchange

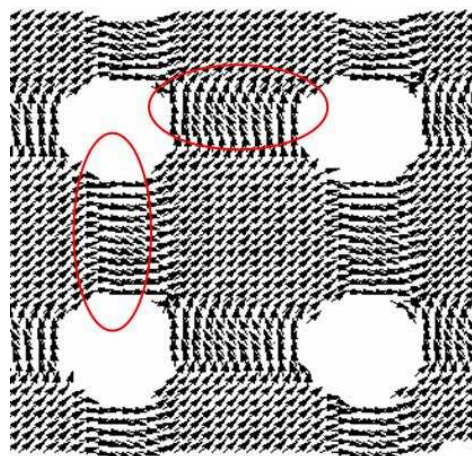


**Figure 5.2:** Magnetization distribution in closely packed antidot film. The circles indicate where the bits would be stored in the proposal of magnetic recording in Ref. [Cowburn 97].

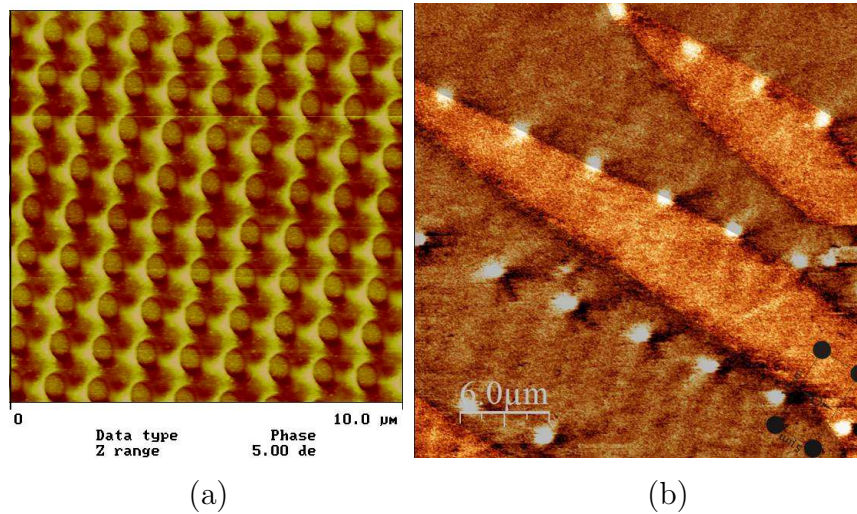


**Figure 5.3:** (a) MFM image of an antidot Fe film in the concentrated regime from the Ph. D. thesis of J.M. Torres [Torres 05]. (b) MFM image of a  $Co_{73}Si_{27}$  film patterned with circular holes where the pinning of the domain wall by the line of antidots is observed (from G. Rodríguez Rodríguez of the Universidad de Oviedo).

coupled grains and densely distributed nonmagnetic columns (antidots). The non-magnetic inclusions act as pinning centers and yield smooth transition boundaries, thus reducing transition noise while the thermal stability is not degraded. Another possible application is related to the implementation of different types of stress and magnetic field sensing devices for which the occurrence of reversible magnetization variations in large field ranges is desirable [Gonzalez 05].

Regarding the relation between the density of antidots and the magnetic behavior of the thin film, we can clearly distinguish two extreme regimes:

- Concentrated regime. The antidots are close enough that the magnetization structures that are created by the antidot surface occupy the antidot region and create a highly inhomogeneous domain structure (the antidots “interact”, see Figs. 5.2 and 5.3(a)). The magnetic anisotropy is dominated by the induced anisotropy resulting from the spatial preference of the created structure.
- Diluted regime. In this regime the antidots are far enough to be considered isolated and do not appreciably alter the magnetic anisotropy as can be observed in Fig. 5.4. The effect of the dots is to act as pinning centers for the domain walls propagating through the sample, which is shown in Fig. 5.3(b) [Pérez-Junquera 06].

The length of the magnetic structures created around the antidots is determined by the exchange length in the considered material. Therefore, in the diluted region the separation between antidots is several times larger than this quantity.

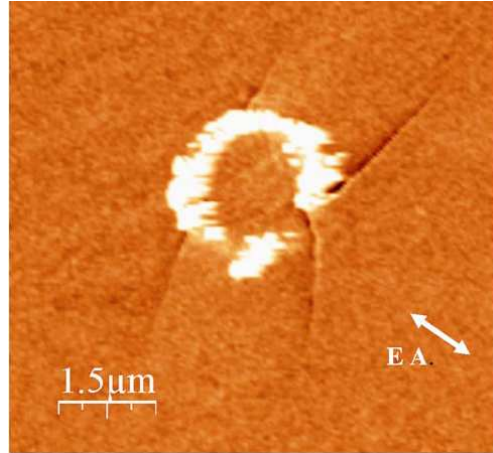


**Figure 5.4:** MFM image of a  $Co_{86}Zr_{14}$  film patterned with circular holes extracted from the Ref. [Pérez-Junquera 06].

One of the main problems raised by the patterned films is that related to the understanding of their demagnetization processes and, especially, the relationship between those processes and the array geometry and dimensions. Due to the dipolar energy minimizing structures at the antidots surfaces, the films can exhibit significant spatial inhomogeneities in the magnetic moment distribution, which can largely influence the global behavior of the system and make difficult the description in simple terms of the magnetization reversal. In this chapter we will analyze the magnetization reversal in patterned films on the basis of a comparison between the micromagnetic simulations and the experimentally measured coercivity in Fe antidots films.

## 5.2 Coercivity dependence on the geometrical parameters

Due to its large saturation magnetization and relatively low magnetocrystalline anisotropy, the Fe films are ideal systems to observe the effects of antidots. In this section we will study the effects of the geometrical parameters in the coercivity in a square array of circular antidots on an Fe film. These parameters are the antidot diameter  $D$  and the interantidot distance  $\lambda$  (see Fig. 5.5). In the examined case the sides of the unit cell of the array are oriented parallel to the  $(1\ 1\ 0)$  Fe film directions, i.e. the unit cell diagonals are parallel to the Fe film crystallographic easy axes. In this geometry the easy axis of the induced anisotropy will coincide with the diagonals of the array square. The dipolar interaction prefer to separate the magnetic poles appearing on the surface. This is achieved aligning the magnetization with the

diagonal of the array. Therefore, this geometry will produce a biaxial anisotropy that coincides in characteristics and disposition with the intrinsic Fe anisotropy. The thereafter examined geometry is the one from the samples that were initially studied and measured by J.M. Torres as reported in his Ph.D. thesis [Torres 05].

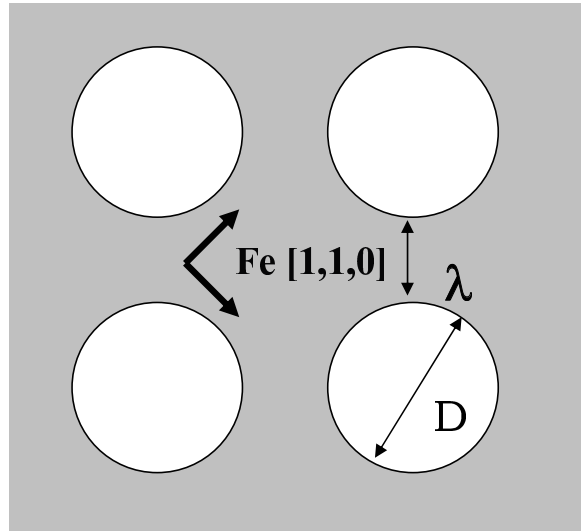


**Figure 5.5:** Diagram representing the geometric parameters: antidot diameter  $D$  and interantidot distance  $\lambda$ . In the graph the easy axis of the Fe biaxial anisotropy is also represented. The shape anisotropy easy axis corresponds also to the diagonals of the square formed by the antidots.

### 5.2.1 Experimental results

The coercivity of series of Fe antidot arrays was studied by J. M. Torres [Torres 05]. The arrays were produced by using X-ray lithography on a 30 nm thick Fe(001)/GaAs film grown by Molecular Beam Epitaxy in the group of Prof. J.A.C. Bland in the Cavendish Laboratory (Cambridge). The lithographed region covered a 0.8 mm × 0.8 mm area out of a 2 mm × 2 mm film. The samples prepared had the following set of diameters and separation (D,λ): (2 μm, 2 μm), (1 μm, 1 μm), (2 μm, 0.2 μm) and (1 μm, 0.1 μm). The coercivity was measured in the easy axis and hard axis configurations using an alternating gradient field magnetometer (AGFM) in the Instituto de Ciencia de Materiales de Aragón. The samples presented two jump in the hysteresis loops in both configurations: the first jump had a very similar value to that of the samples before the lithography procedure. This jump corresponds to the switching of the non-lithographed area. The second jump corresponds to the interantidot area. That later jump value can be several times higher than the former. This fact can be assigned to the stabilizing role of the antidots. Both processes can not be considered “a priori” independent, since the switching of the antidot region

can be caused by the external region. As expected, the obtained coercivities in easy axis configuration are larger than the hard axis ones. Plotting the value of this second jump as a function of  $\lambda$  a hypothesis of the linear dependence with the inverse of  $\lambda$  was suggested (see Fig. 5.6) [Ruiz-Feal 02]. From that, the coercivity was supposed to follow a simple scaling law with the inverse of  $\lambda$ . Generally speaking, the geometrical parameters  $\lambda$  and  $D$  of every sample were different, and, therefore, the coercivity can not be plotted as a variation of a single parameter. Nevertheless, there is a increase of the coercivity with the reduction of the distance  $\lambda$ , but this dependence can be more complex than the one shown in Fig. 5.6. More ample series of sample are needed in order to verify the scaling law. Series in which one of the parameters is kept constant are specially interesting.

### 5.2.2 Previous simulations

Trying to check the validity of the scaling law, in collaboration with J.M. Torres [Torres Bruna 05] we performed micromagnetic simulations, varying the geometrical parameters. It is this kind of problems where the utility of micromagnetic simulations is revealed, allowing to study the magnetic behavior where the experimental data are not available. Unfortunately, the sizes of the sample make impossible to reach, within the available resources, the real dimensions of the sample. A single periodicity cell was used but with periodic boundary conditions. The results obtained from that simulation showed two different types of behavior, each corresponding to a different concentration regime. For small values  $\lambda$ , concentrated regime, there is a

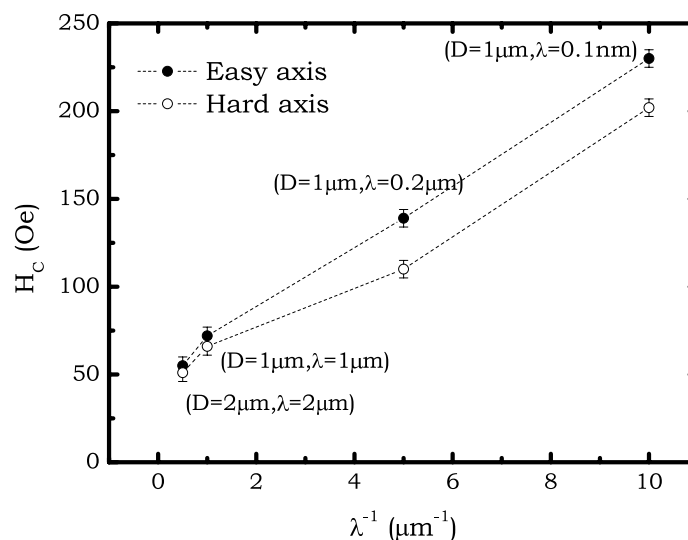


**Figure 5.6:** Measured coercivity of different samples plotted versus the inverse of the interantidot distance (extracted from the Ph. D. thesis of J.M. Torres [Torres 05]).

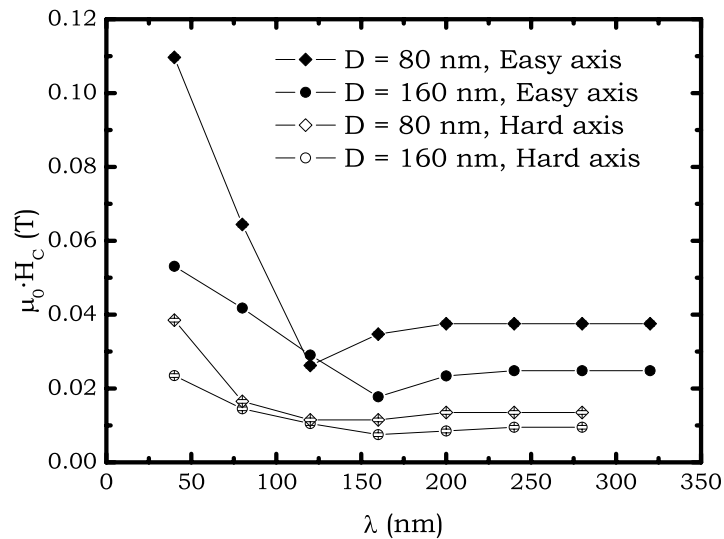


**Figure 5.7:** Calculated coercive force dependence on the interantidot distance  $\lambda$ , for  $D = 80$  and  $160$  nm (easy, EA, and hard, HA, axis data) from the calculations in the Ph. D. thesis of J.M. Torres [Torres 05].

strong dependence on  $\lambda$  of the coercivity. The corresponding magnetic configuration is shown in Fig. 5.8(c), where clearly a domain structure is formed. For large values of  $\lambda$ , diluted regime, the coercivity becomes independent of  $\lambda$ . In this case the flux closure structures occupy a small portion of the film as in Fig. 5.8(a). A minimum of coercivity is obtained in the crossover between the two types of behavior. This corresponds to the case where the magnetic structures of closest antidots join each other (see Fig. 5.8(b)). In the simulations a similar behavior to the experimental one is observed if only small  $\lambda$  region is taken into account, but for simulated sizes much smaller than in real samples.

In real samples the demagnetization process can be determined by the nucleation of a domain wall in the exterior region, specially in the diluted regimen. In the simulations of periodic structure this domain wall was absent, but can be included using open boundary conditions in one of the in-plane directions. The influence of the external zone was analyzed using the same range sizes [Gonzalez 05]. The presence of the external domain wall reduced the coercivity but the qualitative behavior was preserved. The pinning of the domain wall by the outer antidots was also observed.

### 5.2.3 Damaged zone simulations

There are several reasons for the disagreement between the simulations and the experiments regarding the sizes where the non trivial dependence of the coercivity appears. The magnetic parameters,  $A$ - exchange constant,  $K$ - magnetic anisotropy

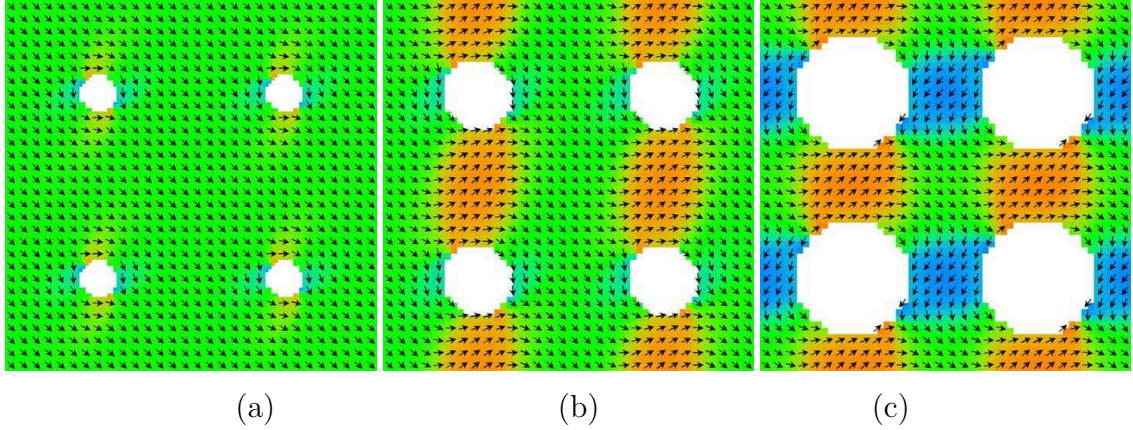


**Figure 5.8:** Magnetic moment configuration slightly before the array magnetization reversal for  $D = 80 \text{ nm}$  and the following parameter values: a)  $H = -0.036 \text{ T}$  and  $\lambda = 280 \text{ nm}$ , b)  $H = -0.025 \text{ T}$  and  $\lambda = 120 \text{ nm}$ , and c)  $H = -0.097 \text{ T}$  and  $\lambda = 40 \text{ nm}$  from the calculations in the Ph. D. thesis of J.M. Torres [Torres 05].

or  $M_s$ -saturation magnetization, that determine the magnetic processes and the characteristic lengths can be different to that considered in the simulations. The characteristic lengths determine the size of the minimizing structures and from that point of view, these lengths could be larger in the experiment than the obtained from the values used in the simulations. The reason for this fact can be that in reality the film may be polycrystalline instead of a single crystal structure.

Additionally, the X ray lithography can damage the structure of the region sur-

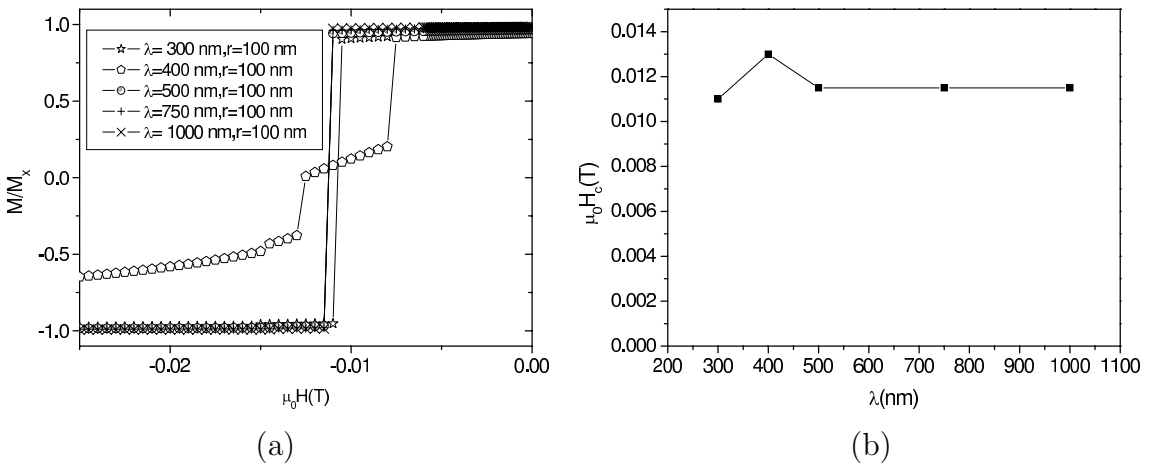


**Figure 5.9:** (a) Simulated hysteresis loops corresponding to antidot film with a region of width  $r = 100 \text{ nm}$  of reduced anisotropy and antidot diameter  $D = 1000 \text{ nm}$  for different separations  $\lambda$  and (b) simulated coercive force dependence of the interantidot distance  $\lambda$  for the same system.

rounding the antidots. This fact would effectively reduce the interantidot distance extending the zone where the coercivity presents appreciable variation. We will suppose, in the simulations of this section, that there is a region around the antidots of width  $r = 100 \text{ nm}$  in which the magnetic anisotropy values equal to zero. Due to the large in-plane anisotropy of the Fe film, we consider a 2D model. Periodic boundary conditions are applied in order to model a large array. The intrinsic parameters of the Fe film are the same used in the previous chapter. The discretization length is  $4 \text{ nm}$  that is less than the exchange correlation length. The antidot diameter is  $1 \mu\text{m}$  and different separations  $\lambda$  are considered. The obtained coercivity for the easy axis configuration adding the damaged region is independent of  $\lambda$  in a broad range of separations  $\lambda$  (see Fig. 5.9). This indicates that the considered interantidot distances range corresponds to the diluted regime of the antidots.

### 5.3 Angular dependence of coercivity

In this section we will study the angular dependence of the magnetization reversal in the antidot film using two different micromagnetic models. The first one assumes that the reversal takes place fully inside the array. In the second model we artificially introduced a domain wall outside the antidot region that governs the magnetization reversal. The aim is to compare the results of simulations with the magnetization processes observed by means of magneto-optic techniques.

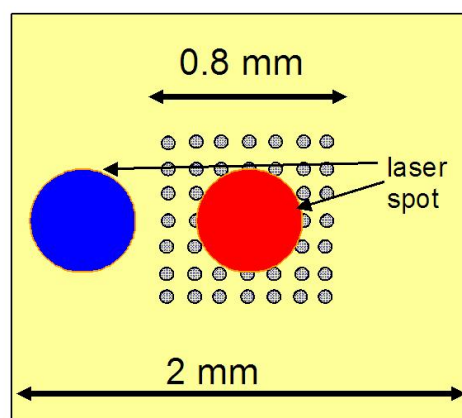
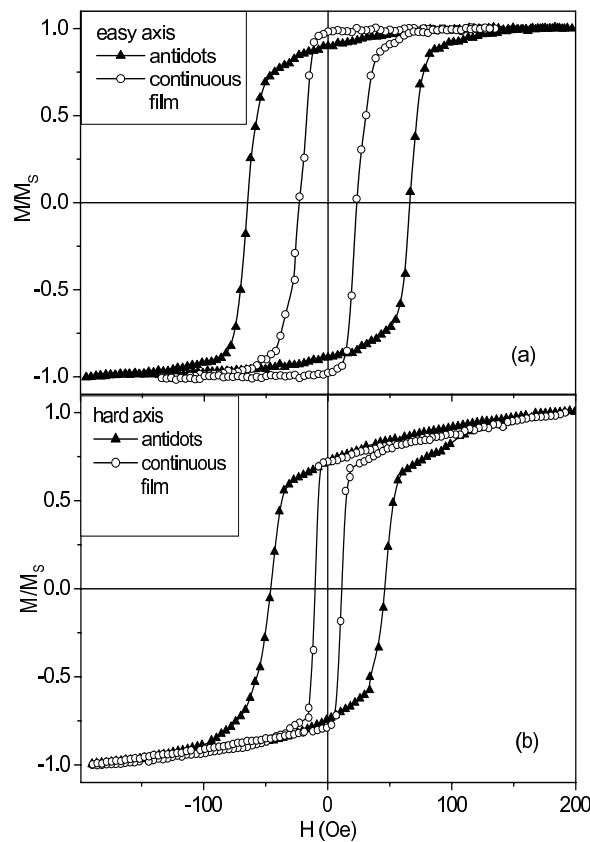


**Figure 5.10:** Experimental geometry to measure Kerr signal in Fe antidot film in the external region and in the antidots region.

### 5.3.1 Experimental Results

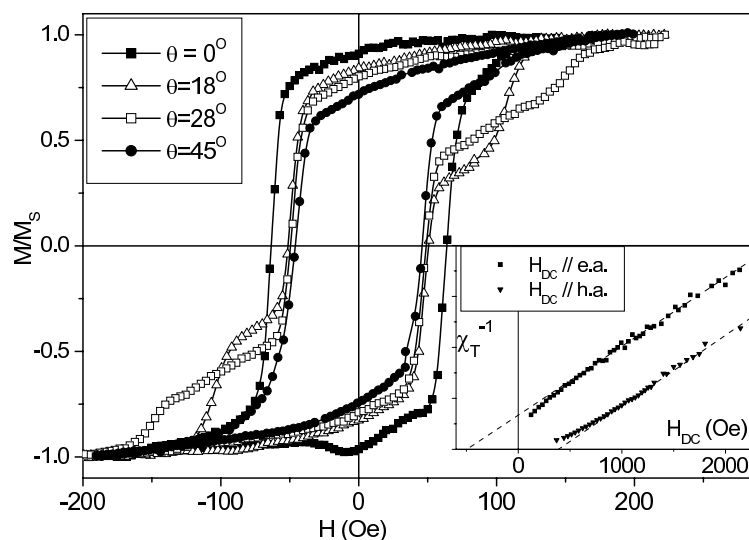
The same Fe antidots film was magnetically characterized at room temperature by F. Cebollada and F. Pigazo in the EUIT Telecomunicacion UPM using a magneto-optic Kerr effect device. The examined sample had diameter  $D = 1 \mu m$  and interantidot distance  $\lambda = 1 \mu m$ . The Kerr device is adapted to measure the angular dependence of the hysteresis loops and also the transverse initial susceptibility (TS). This technique yields the effective anisotropy field  $H_K$  of a sample and consists of generating small amplitude magnetization oscillations in a saturated sample by simultaneously applying a large (saturating) DC field  $H_{DC}$  -along either the e.a. or the h.a.- and a small AC field  $h_{ac}$ , perpendicular to  $H_{DC}$  [Hoffmann 64]. The laser beam was collimated to  $0.4 mm$ . Due to the size of lithographed area, this allows to measure independently the demagnetization loops in the external Fe film and in the antidots region (see Fig. 5.10).

Fig. 5.11 shows the hysteresis loops corresponding to the antidots region and to the continuous film measured in the film plane along the e.a (a) and the hardest



**Figure 5.11:** Hysteresis loops measured in the continuous film and antidots regions along the (a) easy and (b) hard axes. Measured in the EUITT UPM by F. Pigazo and F. Cebollada.

in-plane axis (b) of the sample. The measured coercivity is congruent with the result obtained by J.M. Torres using AGFM, including the different values for the external and the antidots region. The TS measurements obtained in the array region along both the e.a. and in-plane h.a. (inset in Fig. 5.12) yielded an anisotropy field close to  $500 \text{ Oe}$  that, by considering the bulk Fe magnetization value, corresponds to a first order anisotropy constant value  $K_1 = 4.3 \cdot 10^4 \text{ Jm}^{-3}$ , very similar to the corresponding bulk Fe magnetocrystalline anisotropy constant. The TS results confirm that the patterning process preserves the original four-fold symmetry but do not show any increase of the anisotropy constant with respect to that of the bulk Fe. This can be related to the fact that the magnetization oscillations induced during the TS measurements do not result in significant variations of the dipolar energy of the moment structures at the antidots surfaces. As for the angular dependence of the reversal process, the loops measured in the antidot region with the field applied along a direction at an angle  $\theta$  with respect to the Fe e.a. (Fig. 5.12 shows the loops measured at  $\theta = 0^\circ, 18^\circ, 28^\circ$ ; and  $45^\circ$ ) present two irreversible jumps at fields  $H_{S1}$  and  $H_{S2}$ , with the only exceptions of those measured along the e.a. ( $\theta = 0^\circ$ ) and the in-plane h.a. ( $\theta = 45^\circ$ ), which present a single jump. Therefore, for these angles the total film magnetization presents three jumps: two corresponding to the antidot region and the other one to the non-lithographed film. Fig. 5.13 shows the evolution of  $H_{S1}$  and  $H_{S2}$  with  $\theta$ : while  $H_{S1}$  slowly decreases,  $H_{S2}$  increases sharply with the increase of  $\theta$ .



**Figure 5.12:** Hysteresis loops measured in the antidots region with the field applied at different angles  $\theta$  with respect to the e.a. The inset shows the transverse susceptibility dependence on the saturating field value  $H_{DC}$ . Measured in the EUITT UPM by F. Pigazo and F. Cebollada.

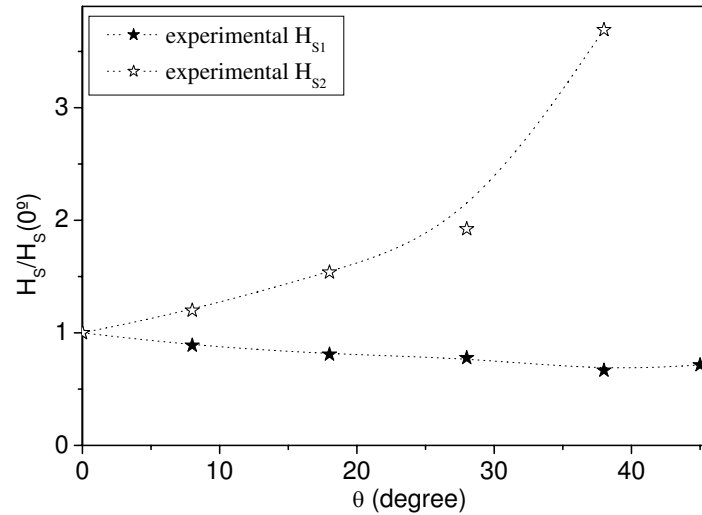


**Figure 5.13:** Experimental angular dependence of the switching fields of the array, normalized to  $H_S(0^\circ)$ . Measured in the EUITT UPM by F. Pigazo and F. Cebollada.

### 5.3.2 Coherent Reversal Model

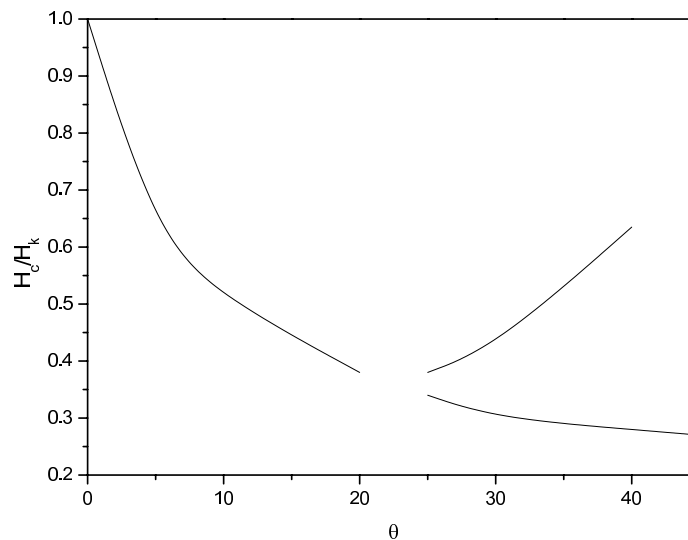


**Figure 5.14:** Angular dependence of the switching field for the coherent rotation model.

As a first approach we can use a simple model of an Fe film to compare with the results in the lithographed film. This simple model is equivalent to the Stoner-Wohlfarth model for uniaxial anisotropy particles, replacing the uniaxial anisotropy with the Fe twofold anisotropy. We consider only in-plane magnetization and do not allow in-plane magnetization variations, so that coherent reversal is supposed. As a consequence the energy can be expressed as a function of a single coordinate

$\vartheta$ , the angle between the magnetization and the applied field direction:

$$E/V = -M_s(\mathbf{m} \cdot \mathbf{H}_{\text{app}}) + K\alpha_1^2\alpha_2^2, \alpha_1 = \cos(\vartheta + \theta), \alpha_2 = \sin(\vartheta + \theta) \quad (5.1)$$

where  $\theta$  is the angle between the easy axis and the applied field direction. The magnetization will evolve through a reversible rotation, until the state of the magnetization becomes an inflexion point of the energy function and another solution branch becomes the minimum. We can only find analytic solution in the case of applied field in the direction of the easy axis or the hard axis. For an easy or hard axis loop the energy derivative becomes:

$$\frac{\partial}{\partial \vartheta} \frac{E}{2KV} = h \sin \vartheta \mp \sin^3 \vartheta \cos \vartheta \pm \cos^3 \vartheta \sin \vartheta. \quad (5.2)$$

The hysteresis loop can be calculated verifying the stability of the zeroes of Eq. (5.2). The rest of the cases have to be solved numerically. In Fig. 5.14 we show the dependence of the magnetization jumps on the angle  $\theta$ . The model predicts two jumps for angles larger than a critical value  $22.5^\circ$ , except for the hard axis configuration in which only one jump appears. The existence of two jumps is the consequence of the biaxial anisotropy. When the minimum opposite to the field direction becomes unstable an intermediate minimum still exists that does not correspond to the alignment with field. In fact the system finds the next relative minimum along the angle  $\vartheta$  but not the absolute minimum. The second jump will occur when this intermediate minimum becomes also unstable. In Fig. 5.15(a) the alternative minimum is shown for an easy axis loop. This minimum does not exist when the branch corresponding to the magnetization saturated along the positive direction is unstable and, therefore, the magnetization will never be in such state during hysteresis

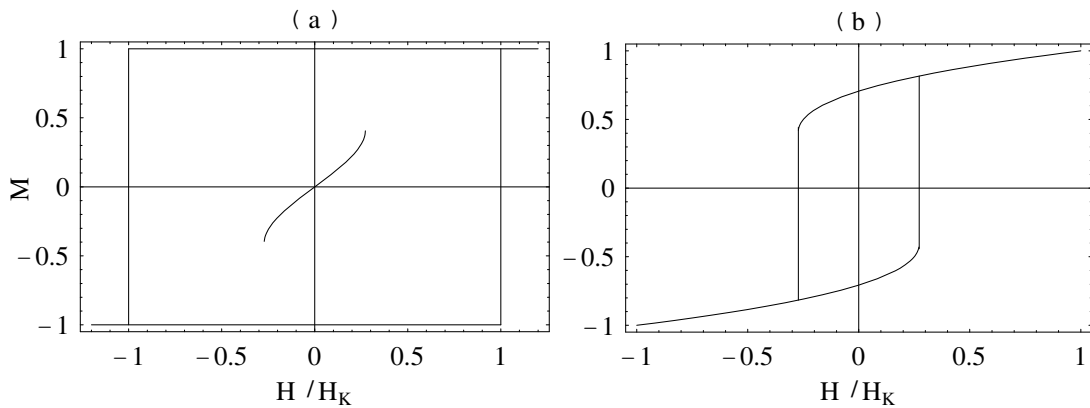


**Figure 5.15:** Hysteresis loops for the coherent rotation model of biaxial anisotropy for the applied field in (a) the easy axis direction and (b) the hard axis direction. In the easy axis plot the applied field values for which an alternative minimum exists and the corresponding magnetization are shown.

processes. The model predicts the occurrence of two coercive fields, observed experimentally. However, in the experimental situation such fields existed for all applied field angles. Clearly, the model does not include the possibility of inhomogeneous magnetization reversal.

### 5.3.3 Periodic Model

To get a deeper insight into the mechanisms involved in the angular dependence of hysteresis we have performed micromagnetic simulations considering two different models. In both of them the computational region was discretized in a two-dimensional square mesh of 4 nm single layer units. In our first model, which will be referred as “periodic model”, we have considered an infinite array of antidots, corresponding to periodic boundary conditions along X and Y directions and a  $2 \mu\text{m} \times 2 \mu\text{m}$  modeled region including a circular antidot with  $D = 1 \mu\text{m}$ . The remanent state was very similar to the saturation in the easy axis direction except for the presence of inhomogeneous moment structures similar to closure domains at the regions of the antidot surfaces (see Fig. 5.16). The thickness of these regions, measured along the average moment direction, was of the order of two times the exchange length of Fe. In the antidot perimeter the magnetization is parallel to the surface except in two small zones where it is parallel to the easy axes. The magnetization at remanence in the center between the antidots is almost directed in the easy axis direction for any applied field angle and the expected  $\cos \theta$  behavior

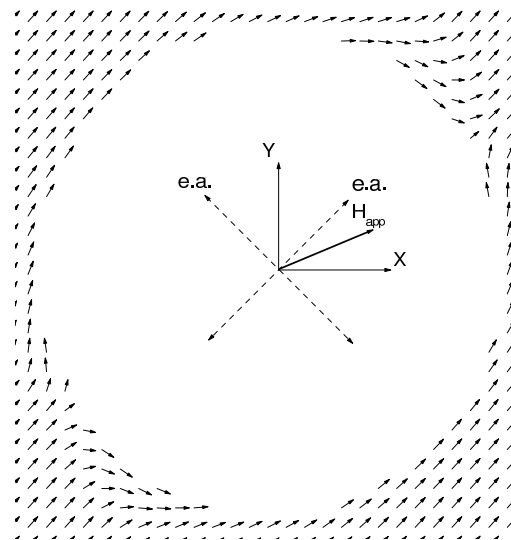


**Figure 5.16:** The magnetization distribution at remanence calculated in the periodic array of antidots for the external field applied at  $\theta = 22.5^\circ$  to the easy axis direction and showing the occurrence of magnetic inhomogeneities at the antidot surfaces. Every arrow gives the average direction of a group of  $10 \times 10$  moments.

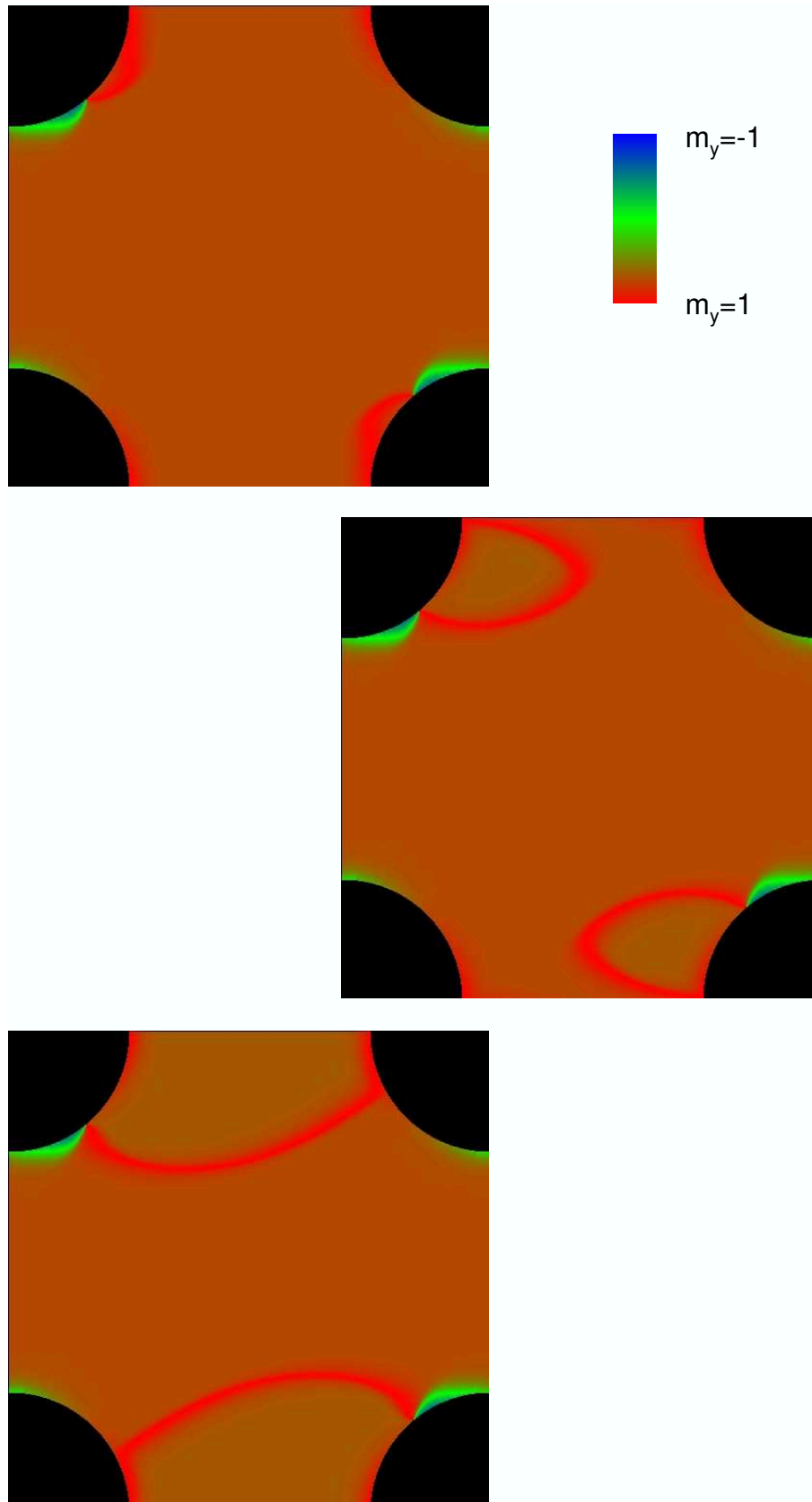


**Figure 5.17:** Sequence of non-equilibrium magnetization configurations calculated in the domain wall model for the external field applied at  $\theta = 0^\circ$  corresponding to the first jump of the hysteresis loop.

is verified for the normalized remanence  $M(H = 0)/M_s$  as a function of the applied field angle  $\theta$ .

The angular dependence of the demagnetization is governed by the occurrence of a nucleation-propagation sequence starting from those inhomogeneous magnetic moments structures present at the antidot surfaces and resulting from the magneto-static energy minimization. The process is shown in Fig. 5.17. The results obtained within this model show the presence of two magnetization jumps (see Fig. 5.18 (a)) for almost all applied field angles (the exceptions are the directions close to the h.a.) and switching field values similar to those observed experimentally. However, the calculated behavior of the angular dependence of the first switching field (see Fig. 5.18(b)) is qualitatively different from that experimentally observed.

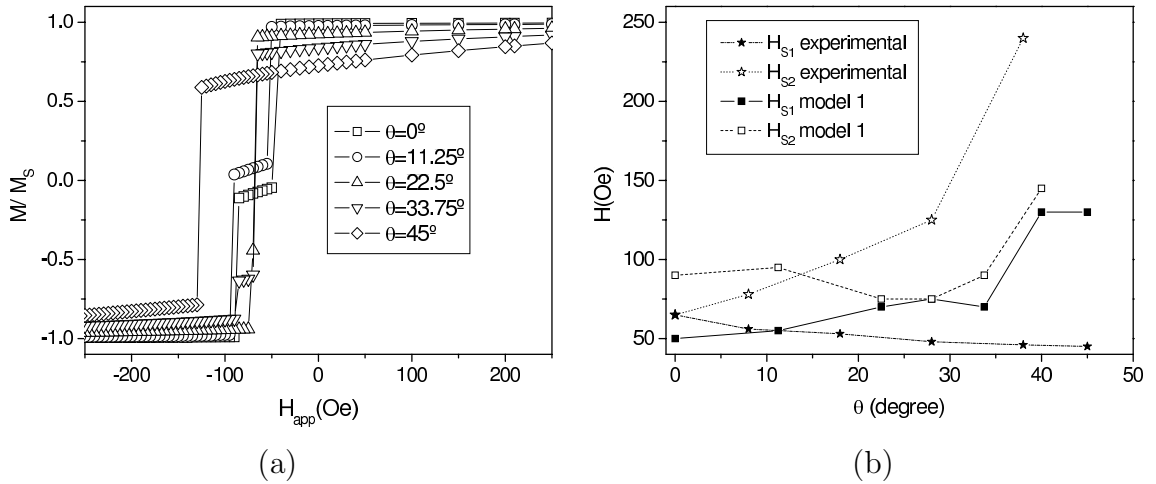


**Figure 5.18:** (a) Hysteresis loops and (b) angular dependence of the switching fields in the antidots arrays simulated in the periodic model in comparison to the experimentally measured values.

### 5.3.4 Domain Wall Model

Our second model, which will be referred as “domain wall model”, consists of a  $4 \mu m \times 4 \mu m$  system with a centered array of  $4 \times 4$  antidots of diameters  $D = 480 \text{ nm}$ , separated by  $\lambda = 480 \text{ nm}$ . In order to implement a more realistic approach to the experimental situation, we artificially introduced a domain wall outside the antidots region allowing to analyze the influence on the antidots magnetization reversal of the lower field reversal of the perimetral region. To introduce the domain wall, the anisotropy constant was set to be zero in two regions of size  $240 \text{ nm}$  parallel and next to two of the simulated square sides (like a half frame). This domain wall exists already at the remanence and subsequent negative field values. This is a realistic assumption since the reversal field of the external region in experiment

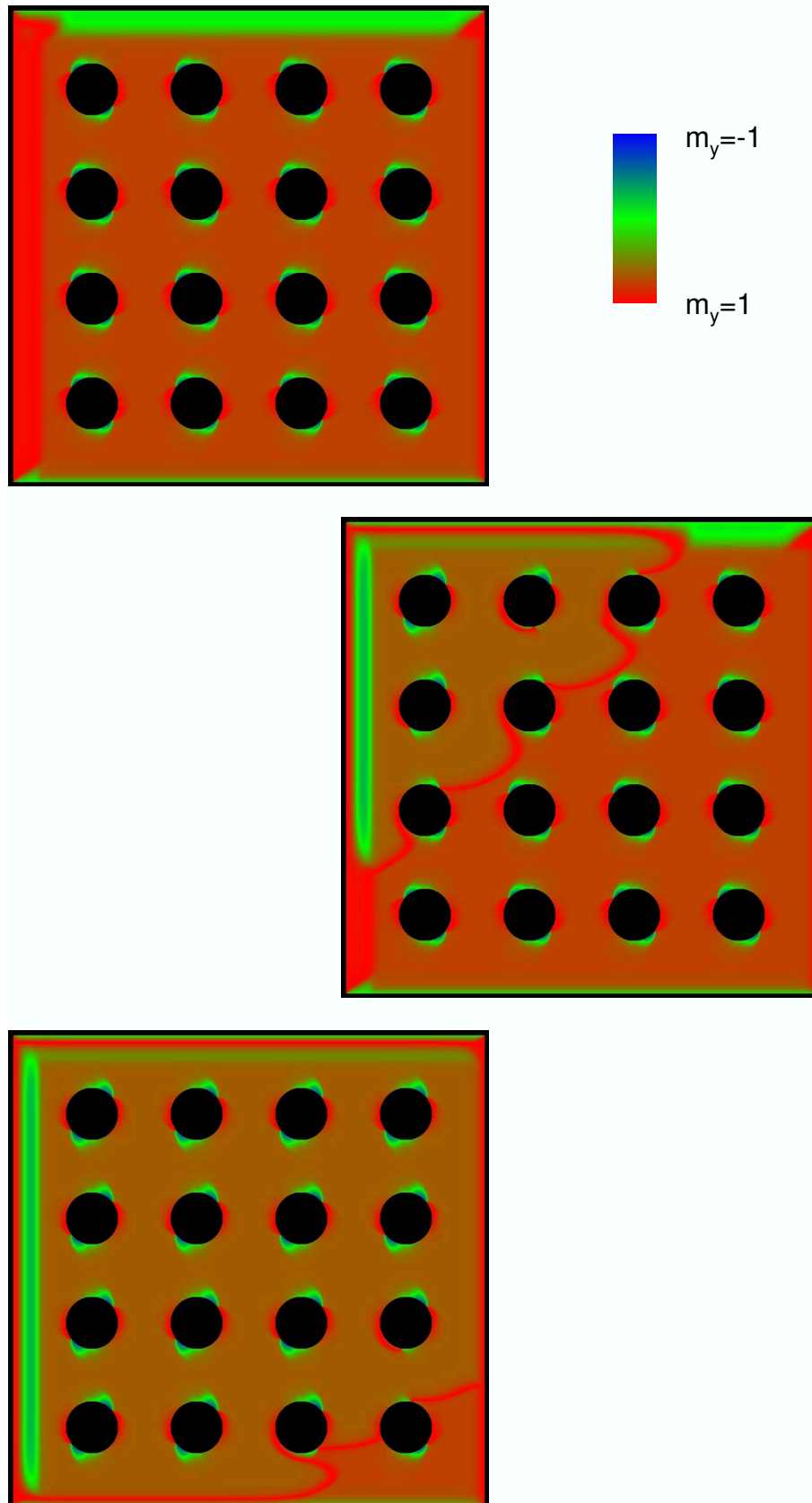


**Figure 5.19:** Sequence of non-equilibrium magnetization configurations calculated in the domain wall model for the external field applied at  $\theta = 11.25^\circ$  corresponding to the first jump of the hysteresis loop.

is several times inferior to that of the antidot-induced demagnetization processes. The remanence magnetization configuration in the interantidot region is similar to the obtained in the periodic model and the  $\cos\theta$  dependence of the normalized remanence is also obtained. As experimentally, we observe two jumps except in the hard and easy axes configuration (see Fig. 5.20(a)). For a given field value the created domain wall triggers an additional domain wall that reverses all the sample as shown Fig. 5.19. As the domain wall passes by the different antidots, the magnetization changes to the intermediate easy axis direction and does not align in the field direction. The external zone has completely reversed but the antidot zone is aligned in the intermediate easy axis direction and that fact creates a domain wall in the outer region pinned at the antidot structure. After the first jump the magnetization rotates reversibly to the field direction. The process corresponding to the second jump is also an inhomogeneous process initiated in the outer line of antidots nearest to the external domain wall.

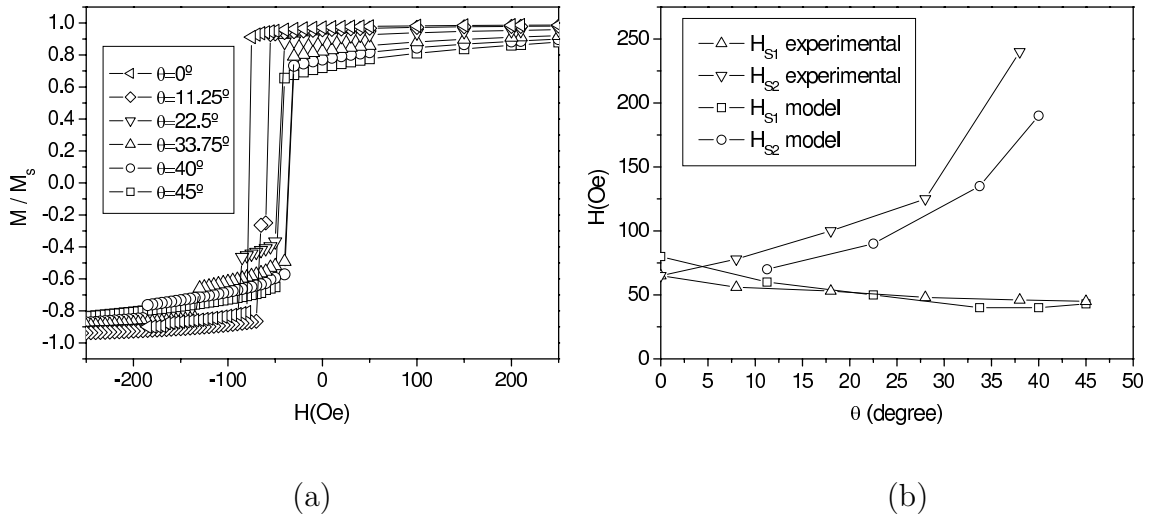


**Figure 5.20:** (a) Hysteresis loops and (b) angular dependence of the switching fields in the antidots arrays simulated in the domain wall model in comparison to the experimentally measured values.

Alternatively, the nucleation of the external domain wall was also implemented by assuming a triangular region, 320 nm wide, with null anisotropy located at one of the system corners. Only one jump in the magnetization was obtained for all the angles using that implementation. Regarding the angle dependence of the field values for the jumps appearing in the magnetization, the simulation with the “half frame” model and the experimental values are in very good agreement both in quality and in magnitude (see Fig. 5.20 (b)) indicating that the reversal in the antidot regions involves a domain wall created by the reversal of the external zone. The occurrence of only one jump when the domain wall is created at the corner is due to the fact that the event there is triggered for field values larger than the

ones necessary to observe the second jump. In these simulations the nucleation in the antidot region, equivalent to that of the periodic model (see Fig. 5.18), is also absent, presumably because the simulation size in this case is different to the simulated in Section 5.3.3.

In the examined cases the antidot demagnetization process is not determined by the antidot itself but by the defects and nucleation sites in the non-lithographed area. The existing possibilities for a nucleation-propagation-pinning sequence are multiple and may be influenced by the presence of defects of different types whose nature is determined by the deposition or lithography techniques. This is a non desirable effect since we can not control the presence of the defects and the aim of the antidots was to externally control the coercivity of the film. On the other hand, we have seen that even in this case, due to the presence of the antidots, the coercivity of the film is enhanced.

## 5.4 Conclusions

In summary we have studied the geometric and the angular dependence of the coercivity in antidots Fe films. From our micromagnetic models we can conclude:

- The characteristic lengths for geometric scaling of coercivity resulting from the use of standard Fe material constants in simulations do not coincide with the experimental observations.
- The present implementation of a zone damaged by the lithography near antidots can not explain the difference between previous simulations and experimental results.
- Our micromagnetic simulations indicate that the hysteresis process is determined by the nucleation-propagation sequence triggered either by inhomogeneities present on the antidot surface or by externally nucleated domain wall. The results of the simulations suggest that the angular dependence of coercivity is sensitive to the type of nucleation present in the system.
- The magnetization reversal of the antidot region is influenced by the reversal of the external region. The results of the simulation of this influence in relation to the angular dependence of the coercivity coincide with the experimental behavior and seems to confirm the presence of the external domain wall. Additionally, the biaxial nature of the film determines the presence of two magnetization jumps in the demagnetization process.

## 5.5 Conclusiones en castellano

Para resumir hemos estudiado la dependencia de los procesos de imanación con respecto a la geometría y al ángulo del campo aplicado en láminas de Fe con redes de agujeros. Desde el punto de vista micromagnético podemos concluir:

- Las longitudes características para el escalado de la coercitividad obtenidas con las constantes estándar para el Fe no coinciden con las observadas experimentalmente.
- La implementación de una zona dañada por la litografía cerca de los agujeros no puede explicar la diferencia entre las simulaciones previas para el mismo sistema y los resultados experimentales
- Nuestras simulaciones micromagnéticas indican que el proceso de histéresis está determinado por la secuencia de nucleación-propagación activadas bien por las inhomogeneidades presentes en la superficie del agujero o por una pared de dominio nucleada externamente. Los resultados de la simulación sugieren que la dependencia angular de la coercitividad es sensible al tipo de nucleación presente en el sistema.
- La inversión de la imanación en la región con agujeros se ve influenciada por la de la región externa. Los resultados de la simulación de esta influencia coinciden con el comportamiento experimental de la dependencia angular de la coercitividad lo cual parece confirmar la presencia de la pared externa. Adicionalmente, la naturaleza cúbica de la lámina determina la presencia de dos saltos en la imanación durante el proceso desimanador.

## Bibliography

- [Adeyeye 97] A. O. Adeyeye, J. A. C. Bland and C. Daboo. *Magnetic properties of arrays of “holes” in  $Ni_{80}Fe_{20}$  films*. Appl. Phys. Lett., vol. 70, pages 3164–3166, 1997.
- [Cowburn 97] R. P. Cowburn, A. O. Adeyeye and J. A. C. Bland. *Magnetic domain formation in lithographically defined antidot permalloy arrays*. Appl. Phys. Lett., vol. 70, pages 2309–2311, 1997.
- [Gonzalez 05] J. M. Gonzalez, O. A. Chubykalo-Fesenko, F. Garcia-Sanchez, J. M. Torres Bruna, J. Bartolomé and L. M. García Vinuesa. *Reversible magnetization variations in large field ranges associated to periodic arrays of antidots*. IEEE Trans. Mag., vol. 41, pages 3106–3108, 2005.
- [Guedes 00] I. Guedes, N. J. Zaluzec, M. Grimsditch, V. Metlushko, P. Vavassori, B. Ilic, P. Neuzil and R. Kumar. *Magnetization of negative magnetic arrays: Elliptical holes on a square lattice*. Phys. Rev. B, vol. 62, pages 11719–11724, 2000.
- [Heyderman 06] L. J. Heyderman, F. Nolting, D. Backes, S. Czekaj, L. Lopez-Diaz, M. Kläui, U. Rüdiger, C. A. F. Vaz, J. A. C. Bland, R. J. Matelon, U. G. Volkmann and P. Fischer. *Magnetization reversal in cobalt antidot arrays*. Phys. Rev. B, vol. 73, page 214429, 2006.
- [Hoffmann 64] H. Hoffmann. *Quantitative calculation of the magnetic ripple of uniaxial thin permalloy films*. J. Appl. Phys., vol. 35, pages 1790–1798, 1964.
- [Jalil 03] M. B. A. Jalil. *Bit isolation in periodic antidot arrays using transverse applied fields*. J. Appl. Phys., vol. 93, pages 7053–7055, 2003.
- [Pérez-Junquera 06] A. Pérez-Junquera, G. Rodríguez-Rodríguez, M. Vélez, J. I. Martín, H. Rubio and J. M. Alameda. *Néel wall pinning on amorphous  $Co_xSi_{1-x}$  and  $Co_yZr_{1-y}$  films with arrays of antidots in the diluted regime*. J. Appl. Phys., vol. 99, page 033902, 2006.
- [Ruiz-Feal 02] I. Ruiz-Feal, L. Lopez-Diaz, A. Hirohata, J. Rothman, C. M. Guertler, J. A. C. Bland, L. M. Garcia, J. M. Torres, J. Bartolome, F. Bartolome, M. Natali, D. Decanini and Y. Chen. *Geometric coercivity scaling in magnetic thin film antidot arrays*. J. Magn. Magn. Mater., vol. 242-245, pages 597–600, 2002.

- [Toporov 00] A. Yu. Toporov, R. M. Langford and A. K. Petford-Long. *Lorentz transmission electron microscopy of focused ion beam patterned magnetic antidot arrays*. Appl. Phys. Lett., vol. 77, pages 3063–3065, 2000.
- [Torres Bruna 05] J.M. Torres Bruna, J. Bartolomé, L. M. García Vinuesa, F. García Sanchez, J. M. Gonzalez and O. A. Chubykalo-Fesenko. *A micromagnetic study of the hysteretic behavior of antidot Fe films*. J. Magn. Magn. Mater., vol. 290-291, pages 149–152, 2005.
- [Torres 05] J. M. Torres. *Propiedades magnéticas de sistemas nano y micrométricos: multicapas de nanopartículas de cobalto y redes de agujeros en hierro*. PhD thesis, Universidad de Zaragoza-CSIC, 2005.
- [Vavassori 99] P. Vavassori, V. Metlushko, R. M. Osgood, M. Grimsditch, U. Welp, G. Crabtree, W. Fan, S. R. J. Brueck, B. Ilic and P. J. Hesketh. *Magnetic information in the light diffracted by a negative dot array of Fe*. Phys. Rev. B, vol. 59, pages 6337–6343, 1999.
- [Wang 04] C. C. Wang, A. O. Adeyeye and C. C. Lin. *Magnetic properties of lithographically defined rectangular antidot permalloy arrays*. J. Magn. Magn. Mater., vol. 272-276, pages E1299–E1300, 2004.
- [Wang 06] C. C. Wang, A. O. Adeyeye and N. Singh. *Magnetic antidot nanostructures: effect of lattice geometry*. Nanotechnology, vol. 17, pages 1629–1636, 2006.
- [Xiao 02] Z. L. Xiao, C. Y. Han, U. Welp, H. H. Wang, V. K. Vlasko-Vlasov, W. K. Kwok, D. J. Miller, J. M. Hiller, R. E. Cook, G. A. Willing and G. W. Crabtree. *Nickel antidot arrays on anodic alumina substrates*. Appl. Phys. Lett., vol. 81, pages 2869–2871, 2002.
- [Zhu 07] J.-G. Zhu and Y. Tang. *Micromagnetics of percolated perpendicular media*. IEEE Trans. Mag., vol. 43, pages 687–692, 2007.

# List of publications of F. García Sánchez

- [1] O. A. Chubykalo-Fesenko, F. García-Sánchez and R. W. Chantrell. *Implementation of the “Hyperdynamics of infrequent events” method for acceleration of thermal switching dynamics of magnetic moments*. IEEE Trans. Mag., vol. 40, pages 2140-2142, 2004.
- [2] F. García-Sánchez, O. Chubykalo-Fesenko, P. Crespo, A. Hernando and J. M. González. *Magnetization reversal in textured Fe nanoparticles having different aspect ratios*. J. Magn. Magn. Mater., vol. 290-291, pages 479-481, 2005.
- [3] J. M. Torres Bruna, J. Bartolomé, L. M. García Vinuesa, F. García-Sánchez, J. M. González and O. A. Chubykalo-Fesenko. *A micromagnetic study of the hysteretic behavior of antidot Fe films*. J. Magn. Magn. Mater., vol. 290-291, pages 149-152, 2005.
- [4] O. V. Usatenko, O. A. Chubykalo-Fesenko and F. García-Sánchez. *Adiabatic dynamics of small ferromagnetic particles*. J. Appl. Phys., vol. 97, page 10A711, 2005.
- [5] F. García-Sánchez, O. Chubykalo-Fesenko, O. Mryasov, R. W. Chantrell and K. Yu. Guslienko. *Exchange spring structures and coercivity reduction in FePt/FeRh bilayers: A comparison of multiscale and micromagnetic calculations*. Appl. Phys. Lett., vol. 87, page 122501, 2005.
- [6] F. García-Sánchez, O. Chubykalo-Fesenko, O. Mryasov, R. W. Chantrell and K. Yu. Guslienko. *Multiscale versus micromagnetic calculations of the switching field reduction in FePt/FeRh bilayers with perpendicular exchange spring*. J. Appl. Phys., vol. 97, page 10J101, 2005.
- [7] J. M. González, O. Chubykalo-Fesenko, F. García-Sánchez, J. M. Torres-Bruna, J. Bartolomé and L. M. García Vinuesa. *Reversible magnetization variations in large field ranges associated to periodic arrays of antidots*. IEEE Trans. Mag., vol. 41, pages 3106-3108, 2005.
- [8] F. Pigazo, F. García-Sánchez, F. J. Palomares, J. M. González, O. Chubykalo-Fesenko, F. Cebollada, J. M. Torres Bruna, J. Bartolomé and L. M. García Vinuesa. *Experimental and computational analysis of the angular dependence of the hysteresis*

- processes in an antidots array.* J. Appl. Phys., vol. 99, page 08S503, 2006.
- [9] F. García-Sánchez, O. Chubykalo-Fesenko, O. Mryasov and R. W. Chantrell. *Multiscale models of hard-soft composite media.* J. Magn. Magn. Mater., vol. 303, pages 282-286, 2006.
- [10] O. V. Usatenko, O. A. Chubykalo-Fesenko and F. García-Sánchez. *Nonlinear adiabatic dynamics of small ferromagnetic particles.* Int. J. Mod. Phys. B, vol. 20, pages 5391-5404, 2006.
- [11] F. García-Sánchez, O. Chubykalo-Fesenko, O. Mryasov and R. W. Chantrell. *Multiscale modelling of hysteresis in FePt/FeRh bilayer.* Physica B, vol. 372, pages 328-331, 2006.
- [12] E. Paz, F. García-Sánchez and O. Chubykalo-Fesenko. *Numerical evaluation of energy barriers in nano-sized magnetic elements with Lagrange multiplier technique.* Physica B, accepted.
- [13] F. García-Sánchez, O. Chubykalo-Fesenko, O. Mryasov, P. Asselin and R. W. Chantrell. *Switching and thermal stability properties of bi-layer thin films: single vs. multi-grain cases.* J. Appl. Phys., accepted.
- [14] F. García-Sánchez, O. A. Chubykalo-Fesenko, A. Martínez and J. M. González. *Hysteresis in Fe particles with surface and magnetoelastic anisotropies: experiment and micromagnetic modeling.* Physica B, accepted.

# Agradecimientos

Antes de nada debo agradecer a mi directora de tesis Oksana Fesenko por sus esfuerzos para la realización y finalización de esta tesis. Agradezco a todos los miembros del grupo su ayuda para el desarrollo de este trabajo así como los agradables ratos pasados durante estos años: a los seniors J.M. González, F. Cebollada, J. Palomares y a los juniors R. Yanes, E. Paz, U. Atxitia, F. Pigazo, R. Cuadrado y J. Haba. Del mismo modo ha sido agradable el tiempo pasado trabajando con la gente que ha visitado el grupo entre quienes están O. Usatenko, I. Gerasymchuk y G. Rodríguez. También debo acordarme de toda la gente que ha poblado el laboratorio 155 Ligia, German, Aldo y otra vez Unai. También dar las gracias a Sonia por sus alegres saludos y sus dulces.

Agradezco a Seagate Research la provisión de la beca que ha hecho posible esta tesis. También debo agradecer la estancia de tres meses en su sede de Pittsburgh y otras visitas anteriores. Especialmente agradecido estoy sobre todo a la gente que allí me he encontrado: O. Mryasov, quien me abrió las puertas de su casa, P. Asselin quien me enseñó sobre métodos matemáticos, y sobre todo a mi compañera de despacho Ninfang, sin su afición al café no sé que hubiera hecho todo ese tiempo. También quisiera agradecer a Roy Chantrell sus discusiones sobre magnetismo y su contagiante optimismo.

No quisiera tampoco olvidar los buenos momentos durante la tesis que he pasado con mis compañeros de planta y gente del fútbol K. Pirola, D. Navas, K. García, J. Torrejón, M. Vázquez, M. Provencio, G. Badini, W. Rosa, J. Caperos, R. Sanz, C. Luna y otros muchos. De igual modo he pasado buenos ratos a la hora de la comida con J. Mendez, J. Iribas, I. Jimenez, A. Baró, I. Reguera, M. Moreno y F. López.

Quisiera agradecer a J.M. Rodríguez Puerta su ayuda técnica, sobre todo en la compilación de software esotérico. Aunque su método de resolver los problemas es primero romperlo todo, sin su ayuda no hubiera podido continuar los cálculos.

Fuera del entorno científico quisiera dar las gracias a Scott Adams por las sonrisas diarias que han hecho más fácil el día a día.

No podría acabar sin agradecer a J.M. Torres por ayudarme durante el inicio de este trabajo. A partir de su código inicial he llegado a crear un auténtico engendro. A pesar de quedarme cerca, no he conseguido mi objetivo inicial de demostrar que

su tesis era completamente errónea. Espero sepa perdonarme tantas preguntas y tan parecidas.

Y antes de finalizar, debo por supuesto agradecer el cariño y el apoyo de mis padres, a pesar de que no entendían muy bien a qué se dedicaba su hijo.